

UNIVERSITÉ LIBRE DE BRUXELLES
FACULTÉ DES SCIENCES



Thèse

Search for new massive resonances
decaying to dielectrons or
electron-muon pairs with the CMS
detector

Présentée par

Thomas REIS

En vue de l'obtention du grade de
Docteur en Sciences

Bruxelles, Février 2015

Jury de thèse

	Prof. Arnd MEYER	RWTH Aachen
	Prof. Sam James HARPER	RAL
	Prof. Steven LOWETTE	VUB
Président	Prof. Jean-Marie FRÈRE	ULB
Secrétaire	Prof. Pascal VANLAER	ULB
Promoteur	Prof. Barbara CLERBAUX	ULB

Abstract

This thesis describes searches for new massive resonances that decay to a pair of electrons or to an electron-muon pair. The data was collected by the CMS experiment in the 2012 proton-proton run at a center-of-mass energy of 8 TeV at the Large Hadron Collider (LHC). After a short introduction to the standard model of elementary particle physics and theories that go beyond, the LHC and the CMS detector are described. The reconstruction of particles produced in the collisions is discussed afterwards, with a special emphasis on electrons and muons with high energies. Two separate analysis of the data are performed.

The first one is the search for a new narrow resonance in the dielectron invariant mass spectrum above the Z resonance, dominated by events from the Drell–Yan process. Such resonances are predicted by a variety of models that incorporate Grand unified theories or extra dimensions. The event selection for two electrons with high energies is optimised for a high efficiency, in order not to lose eventual signal events. Since the background from standard model processes is low in the search region, already a localised excess of few events could lead to a discovery. The analysis relies partly on simulated samples for the background estimation. A data driven approach for validating the simulation of the subleading background processes with prompt electrons in the final state is used, which utilises the electron-muon invariant mass spectrum. No excess over the standard model expectation is observed in the dielectron invariant mass spectrum, and 95% confidence level upper limits are set on the ratio of production cross section times branching ratio of a new resonance to the one from the Z boson. With this, lower limits can be set on the mass of several spin 1 and spin 2 particles predicted by theories beyond the standard model.

The second analysis uses the electron-muon invariant mass spectrum to search for new resonances therein. Such resonances would violate the lepton flavour conservation of the standard model, which is predicted by several theories. Among them is a model with two extra spatial dimensions which predicts the existence of new heavy bosons. The event selection includes a high energy electron like in the dielectron analysis, and a muon with high transverse momentum. As for the dielectron analysis, the search for a narrow resonance makes the statistical analysis insensitive to uncertainties in the absolute normalisation of the continuously falling electron-muon spectrum from the standard model background processes. Since there is no significant excess over the standard model prediction, 95% confidence level upper limits are set on the production cross section times branching ratio. Owing to the small production cross section of the lepton flavour violating boson, the amount of data analysed is not sufficient to set lower limits on the boson mass for the specific model under study. Nevertheless, the analysis represents a first direct search for a new resonance decaying with lepton flavour violation to an electron-muon pair, with the CMS experiment.

Résumé

Le sujet de cette thèse porte sur la recherche de nouvelles résonances massives se désintégrant en une paire d'électrons ou une paire électron-muon avec le détecteur CMS, installé auprès du Grand Collisionneur du Hadrons (LHC) au CERN. Les données analysées correspondent à l'ensemble des collisions proton-proton enregistrées par le détecteur en 2012 à une énergie dans le centre de masse de 8 TeV. Après une brève introduction au modèle standard des particules élémentaires et à quelques unes des théories allant au-delà, le LHC et le détecteur CMS sont présentés. La reconstruction des différentes particules créées lors des collisions, en particulier des électrons et muons de haute énergie, est ensuite discutée. Deux analyses séparées sont menées.

La première consiste en la recherche d'une nouvelle résonance étroite, plus massive que le boson Z, dans le spectre de masse invariante des paires d'électrons, dont la principale contribution, dans le modèle standard, provient du processus de Drell–Yan. De telles résonances sont notamment prédites par des modèles dits de grande unification ou à dimensions spatiales supplémentaires. Le bruit de fond provenant des processus du modèle standard étant réduit dans la région étudiée, quelques événements localisés peuvent suffire pour mener à une découverte, et la sélection des électrons est optimisée afin de ne perdre aussi peu d'événements que possible. Les différentes contributions des bruits de fond sont partiellement estimées à partir de simulations. Une méthode basée sur le spectre de masse invariante des paires électron-muon mesuré dans les données est développée pour valider la contribution du second bruit de fond en terme d'importance. Aucun excès n'est observé par rapport aux prédictions du modèle standard et des limites supérieures à 95% de niveau de confiance sont placées sur le rapport entre la section efficace de production multipliée par le rapport de branchement d'une nouvelle résonance et celle au pic du boson Z. Ces limites sont ensuite converties en limites inférieures sur la masse de différentes particules hypothétiques de spin 1 ou de spin 2.

La seconde analyse consiste en une recherche de résonances massives et étroites dans le spectre de masse invariante des paires électron-muon. De telles résonances briseraient la conservation du nombre leptonique tel que prédit par le modèle standard. Cette possibilité existe cependant dans certains modèles de nouvelle physique. C'est notamment le cas pour un modèle à dimensions supplémentaires où apparaissent des nouveaux bosons neutres lourds. La sélection des événements demande un électron de haute énergie comme dans l'analyse précédente, et un muon de grande impulsion transverse. La stratégie de recherche est similaire au cas des paires d'électrons : le fait de rechercher un signal étroit rend l'analyse statistique très peu sensible aux erreurs systématiques affectant la normalisation absolue du spectre de masse électron-muon. Comme aucune déviation significative n'est observée par rapport aux prévisions du modèle standard, des limites supérieures sur la section efficace multipliée par le rapport de branchement sont établies pour le modèle à dimensions spatiales supplémentaires. Étant données les faibles valeurs théoriques de la section efficace de production des résonances violant la conservation de la saveur dans ce modèle, la quantité de données analysées ne permet pas d'en déduire une limite inférieure sur leur masse. Cette analyse représente néanmoins la première recherche directe avec l'expérience CMS, de bosons massifs, se désintégrant avec violation du nombre leptonique, en une paire électron-muon.

Acknowledgements

During four years of doctoral studies, I came in contact with many people that helped me on the way to achieve the final goal, which manifests itself in this thesis.

First, I want to thank my thesis advisor Barbara Clerbaux for accepting me as a doctoral student and then for her support, advice and patience along the way. She always took the time to discuss my, certainly many, questions, and gave me guidance and suggestions to solve them. Furthermore, I would like to thank her for going through the first versions of my thesis manuscript, making comments on where to polish and improve the text.

I would also like to thank the other members of my jury, Jean-Marie Frère, Sam Harper, Steven Lowette, Arnd Meyer, and Pascal Vanlaer for valuable comments on the draft version of the thesis presented at the private defense.

I am very grateful that I could spend my time in the IIHE amongst the many pleasant colleagues. Thanks to all of you.

Special thanks go to Laurent, whom I shared an office with from the day of my interview until almost the end of my thesis. Also out of the office he became a good friend during this time. I like to think back to the time spent on countless interesting discussions over countless beers, and not to forget the indispensable lessons in French.

I also want to thank my other office mates and friends from the lab, Aidan, Giuseppe, David, Cécile, Erik, Tomislav, Luca, Alexandre, Florian, Thierry (Tu as perdu.), Michael, Arnaud and Vincent. I enjoyed the time with you at and off work, in summer schools and on conferences.

I wish good luck to Giuseppe, my successor in the Z' analysis, for the rest of his doctoral studies. Hopefully, you have more luck in finding the bump than I had.

Good luck for the upcoming hunting season also for the rest of the HEEP analysis team I had the pleasure of being a part of. This time you have to go beyond orange. I would like to thank my $e\mu$ analysis group, especially Andreas and Manny, and wish good luck to Andreas for the finishing of his PhD thesis.

At CERN, I want to thank especially Sam, Andre and Matteo for their advice on physics analysis, on how to perform my service tasks, and for the help in finding my way through the labyrinth of the CMS software.

Audrey deserves special thanks for solving many of my organisational problems and setting up the reception after the thesis defense.

For his help with the implementation of the lepton flavour violating Z' model in MADGRAPH, and answering my questions on event generation, I would like to thank Kentarou.

Thanks go to all my friends from home who kept in contact over the long distance, and especially Peter for standing by to take the blame.

Although they were physically far away, I felt always supported by my family during my time here and also all the time before. I know that they were always believing in my success, and I want to thank all of them, because with this knowledge in my back it certainly became easier.

When I came to Brussels I planned to gain a doctor in sciences. I did not know that I would find much more than that. Ludivine, I want to thank you for sharing your life with me over the last years. You have been a great help in finishing this thesis. It is good to know that there is someone who understands the highs and lows of this time and even better if that person takes part of it as well.

Thomas Reis
Brussels, February 25, 2015

This thesis was supported by the IISN fund of the FNRS Belgium.

Contents

Acknowledgements	vi
Introduction	1
1 Standard model	3
1.1 Matter and its interaction	3
1.2 Symmetries of the standard model	7
1.3 The proton	8
1.3.1 Parton distribution function	8
1.4 Drell–Yan process	10
2 Beyond the standard model	15
2.1 Motivations for physics beyond the SM	15
2.2 New massive resonances decaying to lepton pairs	17
2.2.1 Supersymmetry	18
2.2.2 Grand unified theories	18
2.2.3 Sequential standard model	19
2.2.4 Extra dimensions	20
2.2.5 Current experimental limits	21
2.3 Lepton flavour violating Z' models	22
3 Large Hadron Collider	25
3.1 CERN accelerator complex	26
3.2 Luminosity	30
3.3 LHC schedule	31
3.4 Proton-proton interactions at the LHC	32
4 CMS detector	35
4.1 General CMS layout	35
4.2 Coordinate system	35
4.3 Magnet system	36
4.4 Subdetectors	37
4.4.1 Inner tracker	37
4.4.2 Electromagnetic calorimeter	39
4.4.3 Hadronic calorimeter	42

4.4.4	Muon system	42
4.5	Trigger	45
4.5.1	Level-1 trigger	45
4.5.2	High level trigger	45
5	Event reconstruction	49
5.1	Electron reconstruction	49
5.1.1	Energy measurement	49
5.1.2	Track seed selection	50
5.1.3	Tracking	51
5.1.4	Track-supercluster matching	51
5.1.5	Charge and momentum measurement	51
5.2	Muon reconstruction	52
5.2.1	Standalone muon tracks	52
5.2.2	Global muon tracks	53
5.2.3	Tracker muon tracks	53
5.2.4	Track momentum assignment	53
5.2.5	High transverse momentum muon tracks	54
5.3	Jet and missing transverse energy reconstruction	54
5.3.1	Jet reconstruction	54
5.3.2	Missing transverse energy reconstruction	55
6	Search for new physics in dielectron events	57
6.1	Event selection	58
6.1.1	Datasets	58
6.1.2	Simulated samples	59
6.1.3	Trigger	60
6.1.4	Electron selection	67
6.1.5	Dielectron event selection	70
6.1.6	Acceptance times efficiency	70
6.2	Electron energy scale factor measurement	70
6.2.1	Event selection	72
6.2.2	Signal model	72
6.2.3	Fit	73
6.2.4	Results	74
6.3	High mass resolution	79
6.3.1	Method	79
6.3.2	Results	80
6.4	Backgrounds	85
6.4.1	Drell–Yan background	86
6.4.2	Jet background	86
6.4.3	Reducible dielectron background	90
6.4.4	Background fit	91
6.5	$e\mu$ method	91

6.5.1	Event selection	93
6.5.2	SM signals and backgrounds	95
6.5.3	$e\mu$ invariant mass spectrum	97
6.6	Invariant mass spectrum	101
6.7	Statistical interpretation	104
6.7.1	Limit setting method	107
6.7.2	Input for the limit calculation	109
6.7.3	Limit results	110
6.8	Summary	113
7	Search for new physics in $e\mu$ events	115
7.1	Dataset and simulated background samples	115
7.1.1	Datasets	115
7.1.2	Simulated SM samples	116
7.2	Signal samples	117
7.3	Event selection	121
7.3.1	Trigger	121
7.3.2	Electron selection	124
7.3.3	Muon selection	125
7.3.4	Electron-muon pair selection	125
7.3.5	Acceptance times efficiency	125
7.4	Muon p_T and $e\mu$ mass resolution	126
7.4.1	Muon p_T resolution	126
7.4.2	$e\mu$ mass resolution	129
7.5	Backgrounds	132
7.5.1	Prompt lepton background	132
7.5.2	Background with misidentified leptons	134
7.6	Comparisons between data and simulation	137
7.6.1	Number of primary vertices	137
7.6.2	Lepton kinematics	137
7.7	Invariant mass spectrum	141
7.7.1	Opposite sign mass spectrum asymmetry	141
7.8	Uncertainties	147
7.8.1	Systematic uncertainties on the background	147
7.8.2	Systematic uncertainties on the signal	151
7.8.3	Statistical uncertainties	152
7.9	Statistical interpretation	153
7.9.1	Limit calculation	153
7.9.2	Signal model	154
7.9.3	Background model	155
7.9.4	Limit results	155
7.10	Summary	157
	Conclusions	159

A Dielectron invariant mass resolution fits	163
B Muon p_T and $e\mu$ invariant mass resolution fits	170
B.1 Muon p_T resolution fits	170
B.2 $e\mu$ mass resolution fits	170
C Electron and muon selection variables	175
C.1 High Energy Electron Pair selection variables	175
C.2 High- p_T muon selection variables	175
C.3 Additional variables	175
Bibliography	183

Introduction

The universe, in all its variety and complexity, is made of a remarkably small number of fundamental constituents. Most of what we observe in nature can be described with a handful of elementary particles and a very powerful theory called the standard model of elementary particle physics. By studying these elementary particles and their interactions in high energy collisions, the accuracy of the standard model can be tested with precision.

It is known however, that the standard model does not describe the nature completely. Certain observations are not included in the model, and extensions beyond the standard model are necessary to accommodate the unexplained phenomena. To solve the problems of the standard model, many of those extensions predict new physics at an energy scale that can be probed with today's most powerful colliders. The Large Hadron Collider (LHC) at CERN has the highest proton-proton center-of-mass energy ever achieved, and many different searches for new phenomena are performed by the experiments built at the four interaction points of the machine. One of those experiments is the Compact Muon Solenoid (CMS) detector, one of the two general purpose experiments at the LHC. In 2012, the CMS experiment, in parallel with the ATLAS experiment, discovered the last missing piece of the standard model: the long searched for scalar boson, predicted by the Brout–Englert–Higgs (BEH) mechanism in 1964. With the dataset of proton-proton collisions at a center-of-mass energy of 8 TeV recorded in 2012 by the CMS experiment, searches for new physics beyond the standard model are performed as well.

This thesis is about the search for new massive particles decaying to dielectrons¹ or electron-muon pairs. Such new particles would manifest themselves as a narrow resonance in the invariant mass spectra of the lepton pairs in the final state. The production cross section of the new massive particles is very small compared to the one from the Z boson, but already a few reconstructed events at a similar mass, on top of the small non-resonant background contribution from standard model processes, can lead to a discovery. The leptonic channels with electrons and muons have the advantage that the reconstruction of those leptons is very well understood, leading to a low background from misreconstructed lepton candidates. Furthermore, for the dielectron final state, the Z resonance provides an excellent candle for the calibration of the analysis in the mass range between 60 and 120 GeV. Both searches are designed to be as inclusive as possible, which means that a high selection efficiency

¹In this thesis the term *electrons* describes both electrons and positrons, unless stated otherwise.

was an important point in the event selection. Emphasis is laid as well on an accurate simulation of the background contributions. No excess over the prediction of the standard model contribution is observed in both channels and upper limits are set on the production cross section times the branching ratio to the studied final states.

The thesis is organised as follows. The standard model of elementary particle physics is introduced in Chapter 1, including a discussion of the known elementary particles, the proton and the symmetries of the model. A detailed description of the Drell–Yan process concludes the chapter. Chapter 2 lists the shortcomings of the standard model and presents various theories going beyond the standard model. In particular, new models that predict additional massive resonances decaying to dielectrons or electron muon pairs are presented. The experimental setup is introduced in Chapter 3 and Chapter 4, where the design and operational parameters of the LHC and the CMS detector are discussed, respectively. The reconstruction of particle candidates from registered signals in the CMS detector is the topic of Chapter 5. Chapter 6 presents in detail the object and event selection, energy scale and resolution measurement, background estimation and validation, invariant mass spectra and statistical interpretation of the search for new resonances in the dielectron channel. The results of the analysis presented in Chapter 6 are part of a publication that has been submitted to JHEP in December 2014 [1]. The search for new resonances in the electron-muon pair channel, which is performed for the first time with data from the CMS experiment, is exposed in Chapter 7. The chapter contains detailed descriptions on the signal sample generation, object and event selection, resolution measurements, background estimation and statistical interpretation of the invariant mass spectrum. The work shown in Chapter 7 is expected to be published as a paper of the CMS collaboration in the future [2].

Chapter 1

Standard model

This chapter introduces the standard model (SM) of elementary particle physics. The elementary particles and the fundamental forces are described in Section 1.1. In Section 1.2 the group structure of the SM is discussed. Properties of the proton as a composite particle made of partons, and the parton distribution function (PDF) are discussed in Section 1.3. Finally, in Section 1.4 the cross section of a specific process, the Drell–Yan production, is derived using the formalism of the SM.

1.1 Matter and its interaction

Most of the visible matter that surrounds us consists of atoms. The theory that everything is made of very small building blocks exists already for a long time and the word atom comes from the Greek *atomos* which means indivisible. Since the end of the nineteenth century, research done by many individuals has shown that the atom is by no means indivisible, but consists of even smaller particles. Today we know that atoms are made of a positively charged nucleus consisting of at least one positively charged proton and zero or more electrically neutral neutrons. Surrounding the nucleus are as many electrons as there are protons to give an electrically neutral atom. While in the SM of elementary particle physics the electron is considered as an elementary particle with no substructure, the proton and neutron are made from so-called quarks, which are also believed have no substructure. The number of electrons and protons of an atom determines its chemical behaviour. Since the proton and the neutron are both made of quarks, there should be at least two different types of quarks with different electric charges. Electrons, protons and neutrons, all have a half-integer spin and follow the Fermi–Dirac statistic. Particles that follow this statistic are called fermions. Since the proton and the neutron are made of quarks, the quarks must be fermions as well. If one assumes the proton and the neutron to be a composite of quarks, the smallest number of quarks that give a total half-integer spin is three. The proton should be made of two so-called up quarks with an electric charge of $+2/3e$, where e is the elementary charge, and one so-called down quark with an electric charge of $-1/3e$. For the neutron the numbers of up and down quarks are reversed. The electric charges for the quarks were found to be such that

the combination in a proton and a neutron gives a positively charged proton with the same absolute charge than the electron and an electrically neutral charge for the neutron.

In order to keep energy, momentum and spin conserved in the nuclear beta decay, Wolfgang Pauli proposed the existence of a neutral particle that was later called the electron neutrino. Electron and electron neutrino belong to the group of particles called leptons where the electron is counted as charged lepton and the electron neutrino as neutral lepton. The electron and the electron neutrino form two different so-called flavours of leptons. With the discovery of the muon, which behaves like a heavy version of the electron, in cosmic rays in the thirties of the last century, another lepton flavour was found. In 1975 another charged lepton, the tau particle, has been found and to each charged lepton a corresponding neutrino was discovered as well. The lepton group consists now of six flavours arranged in three generations, with electron and electron neutrino forming the first generation, muon and muon neutrino forming the second generation and tau and tau neutrino forming the third generation.

Also, two further generations of quarks have been found with the charm and strange quark flavours forming the second generation and the top and bottom quarks forming the third generation. The charm quark and the top quark have the same electric charge as the up quark and the strange quark and the bottom quark have the same electric charge as the down quark. Beside their electric charge, quarks also carry another charge, which can have three different values that are often referred to by the colours red, green and blue. The names for the colour charges are arbitrary and only reflect the three different states possible.

According to the SM of elementary particle physics, the elementary particles are the six lepton flavours and the six quark flavours. However, Dirac's theory tells us that every particle should have its own antiparticle which is characterised as having the same mass as the corresponding particle but opposite charge. This doubles the number of elementary particles. The antiparticle of the electron is the positron and for all the other particles the antiparticle simply has the prefix "anti" in the name. The antiparticles of the quarks, the antiquarks, carry the anti-colour charges that are usually named anti-red, anti-green and anti-blue, in correspondence to the choice for the names of the colour charges. The question whether the electrically neutral neutrinos are their own antiparticles (Majorana particles) or not (Dirac particles) remains open to date. Table 1.1 lists the elementary fermions of the SM and some of their properties¹.

Composite particles like protons and neutrons, which are made of several quarks are called hadrons. Since hadrons do not carry a colour charge, the sum of the quarks colour charges must vanish. While the proton and the neutron, being built of three quarks, are part of the so called baryon family within the hadrons, there is another family of hadrons called the mesons, which is made of one quark and one antiquark. The mesons are bosons because they are made of two fermions, and they do not

¹In this thesis $\hbar = c = 1$ is chosen. This means that energy, momentum and mass have the same unit.

Table 1.1 – The elementary fermions of the SM. Numerical values taken from [3].

Generation	Name	Symbol	Mass	Charge Q_f
Leptons				
1 st	Electron	e^-	511 keV	-1
	Electron neutrino	ν_e	< 2 eV	0
2 nd	Muon	μ^-	106 MeV	-1
	Muon neutrino	ν_μ	< 2 eV	0
3 rd	Tau	τ^-	1.78 GeV	-1
	Tau neutrino	ν_τ	< 2 eV	0
Quarks				
1 st	Up	u	2.3 MeV	2/3
	Down	d	4.8 MeV	-1/3
2 nd	Charm	c	1.28 GeV	2/3
	Strange	s	95 MeV	-1/3
3 rd	Top	t	173.5 GeV	2/3
	Bottom	b	4.18 GeV	-1/3

carry a colour charge, because the combination of colour charge of the quark and anti-colour of the antiquark leaves a colourless state.

In order for the particles of matter to interact with each other, forces have to act between them. These forces are mediated by particles with an integer spin, the so-called bosons, that follow the Bose–Einstein statistic. There are four fundamental interactions in nature, however, they do not act on all matter particles.

Electromagnetic force

All electrically charged particles are subject to electromagnetic interactions. The massless and chargeless photon is the carrier particle of the electromagnetic force and, owing to its masslessness, the electromagnetic force is a long range force with a $1/r$ potential. The theory describing the electromagnetic interactions is called quantum electrodynamics (QED).

Strong force

The strong interactions are responsible for the attracting force between quarks. It is mediated by the gluons which are massless spin one particles. Gluons exist as a colour octet between a colour and an anti-colour and upon interaction with the quarks change their colour charge. Gluons can also interact with themselves and, thus, the theory of quantum chromodynamics (QCD), which describes the strong interaction must be a non-Abelian theory. The potential between the quarks follows a Coulomb potential at small distances but rises linearly with the distance at larger distances. This means that when the distance between two quarks becomes too large, it is energetically better to produce a quark-antiquark pair to shorten the distance between quark and antiquark. Therefore, it is not possible to observe a quark as a free particle. This is known as confinement.

Weak force

Even though weak interactions take place between all leptons and quarks, they are usually not relevant at energies well below 100 GeV, since the strong or electromagnetic interactions have couplings that are orders of magnitude larger than the weak coupling. However, for processes where the electromagnetic interactions and the strong interactions are forbidden because of some conservation law for a quantum number, the weak interaction becomes significant. Such interactions can involve neutrinos which have no electric and colour charge and, therefore, do not interact with the photon or gluons. Other processes involve the changing of quark flavour which is not allowed with the strong interaction. Contrary to the photon and the gluons, the bosons exchanged in a weak interaction are heavy compared to most elementary particles in the SM. There exists a charged and a neutral version of the vector bosons that mediate the weak force, called W^\pm and Z^0 . The range of the weak interactions is very small because of the high mass of the bosons involved.

Gravitational force

All particles are affected by the gravitational force. However, even though it is the dominant force on an astronomical scale, on a microscopic scale where elementary particle physics is happening, it is negligible. The graviton G , a hypothetical, massless and chargeless elementary particle of spin two, would be the carrier of the gravitational force in a quantum field theory that involves gravity. However, such a theory is difficult to construct, as will be explained in Chapter 2, and is not part of the SM.

The SM bosons that mediate the fundamental interactions are listed in Table 1.2 with numerical values taken from [3], if not stated otherwise.

The last line in Table 1.2 shows the last discovered particle of the SM, first observed in 2012 by the CMS and ATLAS experiments [6, 7]. It is the scalar boson, mediating the Brout–Englert–Higgs field, that was proposed in 1964, independently by Brout and Englert [8] and Higgs [9], to explain the mass of the other elementary particles. The coupling of the massive particles to the BEH field is proportional to the mass of the particles.

Table 1.2 – The elementary bosons of the SM.

Interaction	Name	Symbol	Mass	Charge	Spin	Decay width Γ
Electromagnetic	Photon	γ	$< 1 \times 10^{-18}$ eV	0	1	stable
Strong	Gluon	g	0 (theoretical)	0	1	
Weak	W boson	W^\pm	80.4 GeV	± 1	1	2.1 GeV
	Z boson	Z^0	91.2 GeV	0	1	2.5 GeV
	Scalar boson	H^0	125.0 GeV [4]	0	0	< 22 MeV [5]

1.2 Symmetries of the standard model

In the SM, symmetries play an important role. It was shown by Emmy Noether that every continuous symmetry in the theory gives rise to a conserved quantity [10]. For example, the energy and momentum conservation follows from the symmetry of the action under translations in time and space. A symmetry is defined as global when the corresponding transformation is independent of spacetime, whereas a symmetry under spacetime dependent transformations is called a local symmetry. Generally, a symmetry that leaves the Lagrangian invariant under a group of transformations is called a gauge symmetry. In quantum electrodynamics for example the Lagrangian is invariant under the group of local phase rotations,

$$\psi(x) \rightarrow e^{i\alpha(x)}\psi(x), \quad A_\mu \rightarrow A_\mu - \frac{1}{e}\delta_\mu\alpha(x), \quad (1.1)$$

which means that the group of QED is an Abelian unitary $U(1)$ gauge group, with only one vector field involved and the phase as a scalar quantity. Ultimately, this leads to a conserved current and to the electric charge. If the phase rotation in Equation (1.1) is replaced with the non-commuting Pauli spin operators, that are the Pauli matrices, one ends up with the non-Abelian $SU(2)$ group, which is the group of the isospin quantum number that distinguishes the up quark and the down quark. The isospin symmetry is a global symmetry. In QCD there exists also an additional quantum number, often called the colour charge, which can have three different values and leads to the gauge symmetry of the $SU(3)_c$ group, where the c subscript stands for colour. While one representation of the generators of the $SU(2)$ symmetry were the Pauli matrices, with some additional factor, a representation of the generators of the $SU(3)$ symmetry are the eight 3×3 Gell-Mann matrices, as well with some factor.

Symmetries exist also in the electroweak (EW) theory, which unifies the electromagnetic interaction and the weak interaction. In the electroweak theory two quantum numbers are introduced, the weak isospin I_W , which belongs to the $SU(2)$ gauge group, and the hypercharge Y which comes from a $U(1)$ gauge group. One can group the fermions of the SM by their chirality, which can be left-handed or right-handed and is defined with the projection operators $(1 - \gamma^5)/2$ and $(1 + \gamma^5)/2$ ², respectively. Left-handed fermions form doublets, while right-handed fermions form singlets. The left-handed quark doublets consist of up-type and down-type quarks and the left-handed lepton doublets of a charged lepton and its neutrino. Up to now right-handed neutrinos have never been observed. The weak interaction only acts on left-handed particles and, thus, violates parity, which is the invariance under mirror operation at the origin in space.

The Lagrangian of the electroweak theory is invariant under transformations in $SU(2)_L \times U(1)$, where the L subscript stands for left-handed, and together with the colour group of the QCD theory the Lagrangian of the SM is invariant under $SU(3)_c \times SU(2)_L \times U(1)$.

² $\gamma^5 = i\gamma^0\gamma^1\gamma^2\gamma^3$, where γ^i are the Dirac matrices.

1.3 The proton

In Section 1.1 it was shown that the proton is a composite particle made from two up-type quarks and one down-type quark. These three quarks are called the valence quarks and their rest mass makes up about 1% of the proton mass of 938.3 MeV. The quarks are held together by gluons that are interacting with them and exchange the colour charge between them. However, at higher loop order the gluon exchanged between two quarks can interact with other gluons in the proton or produce a quark-antiquark pair that annihilates shortly afterwards. Such quarks and antiquarks produced from gluons are called sea quarks.

1.3.1 Parton distribution function

When two protons collide some of their partons, that is their quarks and gluons, can interact with each other. The probability density $f_p(x_p, Q^2)$ to find a parton p, with the fraction x of the longitudinal proton momentum in the proton-proton center-of-mass frame, depends on the squared four-momentum transfer Q^2 between the partons of the collision, and is described by the parton distribution function (PDF). The PDF is different for each type of parton. An example for parton distribution functions is shown in Figure 1.1 for two different scales of the invariant momentum transfer Q^2 between the partons. The PDF depend on the energy scale at which the interaction between the partons takes place, as can be seen in Figure 1.1. For low Q^2 the proton

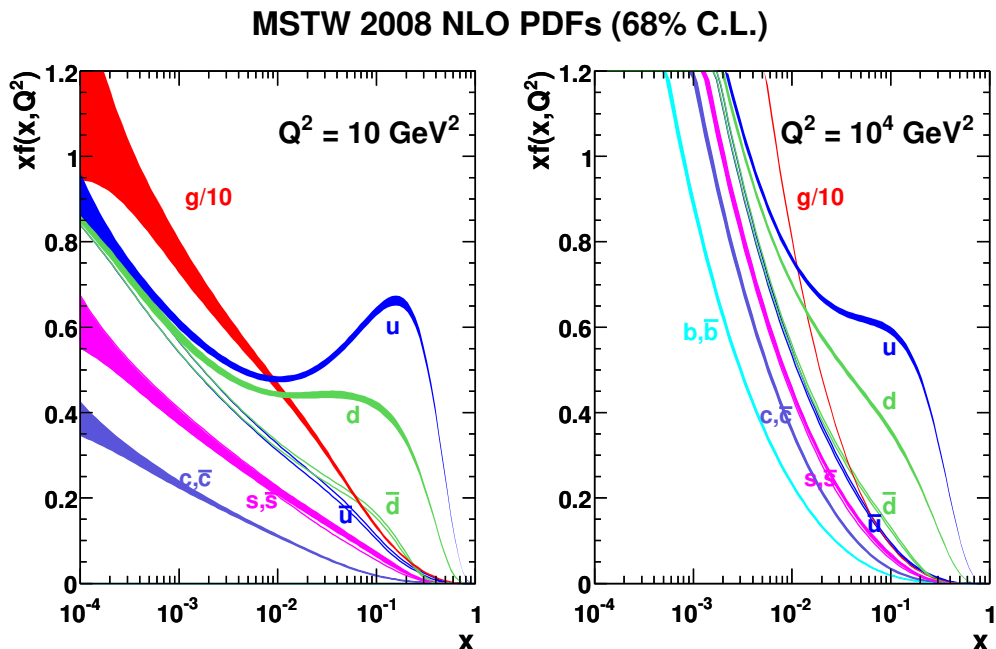


Figure 1.1 – PDFs, including the one sigma uncertainty bands, for the partons in a proton for two different invariant momentum transfers Q^2 [11].

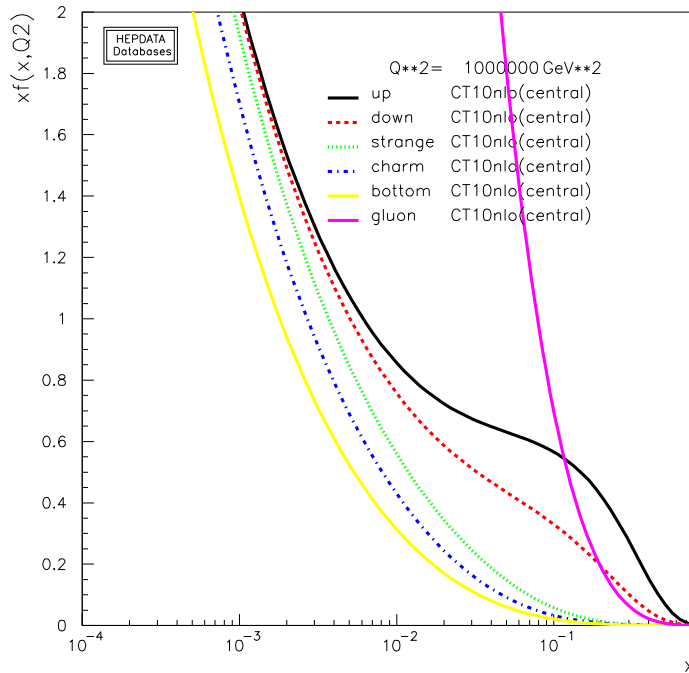


Figure 1.2 – PDFs for different partons in a proton, obtained with the CT10 parametrisation [12]. Q^2 is chosen for physics studies at the TeV scale. The plot was generated with the tool from the HepData project [13].

can be described as consisting of the three valence quarks. For interactions with high Q^2 the sea quarks and gluons can be probed as well, and have to be added to the valence quarks in the description of the proton. To probe physics at a certain energy scale, the value for Q^2 has to be taken in the range of the squared invariant mass M^2 of the system. If, e.g. the Z boson should be studied, M^2 is in the order of the squared Z boson mass of 91.2 GeV, and Q^2 is taken as 10^4 GeV as in the right plot of Figure 1.1. A relation of this mass to the momentum fractions x_1 and x_2 , carried by the two colliding partons, is given by

$$M = \sqrt{x_1 x_2 s}, \quad (1.2)$$

where s is the squared center-of-mass energy of the colliding protons. This means, e.g. that to study physics at the TeV scale, with a collider with $\sqrt{s} = 8$ TeV, the average x of the partons has to be around 0.1. From the corresponding PDF in Figure 1.2 it can be seen that at such values the up quark and down quark content shows an excess over the other quarks, which means that the interactions are dominated by the valence quarks and the gluons.

PDF can be experimentally measured by deep inelastic scattering (DIS) of leptons on hadrons, as is, e.g. done by the HERA electron-proton collider [14]. With the help of the Dokshitzer–Gribov–Lipatov–Altarelli–Parisi (DGLAP) equation [15–17], the PDF obtained at one scale μ_0^2 can be extrapolated to a different scale μ^2 , called the factorisation scale. Several different collaborations such as CTEQ [12, 18], MSTW [11] or NNPDF [19] provide sets of PDF.

1.4 Drell–Yan process

One process of particular interest for this thesis is the production of an electron-positron pair from proton-proton collisions, by the Drell–Yan (DY) [20] process. Generally, the DY process describes the production of a pair of oppositely charged leptons from the interaction of a quark-antiquark pair. The interaction between the two fermion pairs can be mediated by a virtual photon γ^* or a Z^0 boson as can be seen in the Feynman diagrams in Figure 1.3. Taking into account that the quark-antiquark

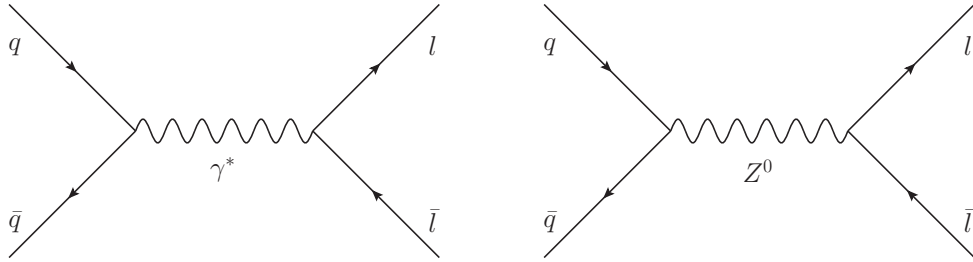


Figure 1.3 – Feynman diagrams taking part in the DY process. Left: Virtual photon exchange. Right: Neutral Z^0 boson exchange.

pair comes from colliding protons, the Feynman diagram of the complete process looks like the one showed in Figure 1.4. There, the incoming protons are called P_A

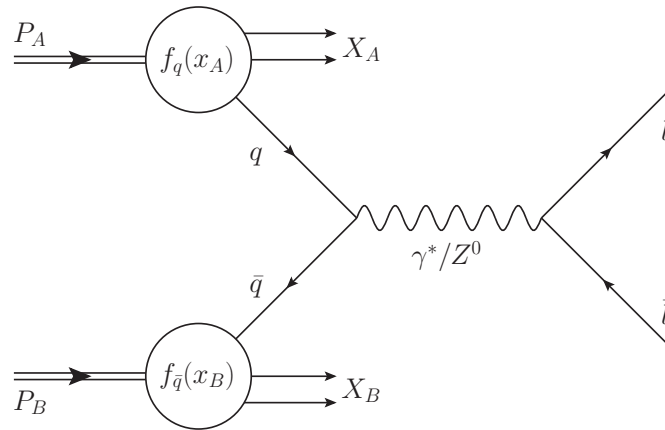


Figure 1.4 – Lepton-antilepton production with the DY process in an hadron collider. The proton remnants after the collision are denoted X_A and X_B , and $f_q(x_A)$ and $f_{\bar{q}}(x_B)$ are the PDFs for the quark and antiquark, respectively.

and P_B , and the proton remnants after the collision are denoted X_A and X_B . Since the quarks that take part in the DY process carry only a fraction x_A or x_B of the proton momentum, the PDFs of the quark and the antiquark, respectively, $f_q(x_A)$ and $f_{\bar{q}}(x_B)$, have to be taken into account. The formula³ for the total cross section

³Natural units $\hbar = c = \epsilon_0 = 1$ are chosen for the calculation.

is then

$$\sigma(\text{pp} \rightarrow \gamma^*/Z^0 \rightarrow \bar{l}l + X) = \int_0^1 dx_A \int_0^1 dx_B \sum_{q,\bar{q}} f_q(x_A) f_{\bar{q}}(x_B) \sigma_{DY}(x_A p_A, x_B p_B), \quad (1.3)$$

where $\sigma_{DY}(x_A p_A, x_B p_B)$ is the partonic cross section of the DY process, as a function of the momentum fraction of the proton momentum carried by the quark and antiquark, with dileptons in the final state.

To calculate the partonic cross section the quark-antiquark center-of-mass frame is chosen. The coordinate system is defined with the incoming quark and antiquark flying in the positive and negative z direction, respectively, and the x - z plane spanned between the quarks and leptons, where θ is the angle between the quark and the lepton. Figure 1.5 illustrates the coordinate system. In the quark-antiquark center-

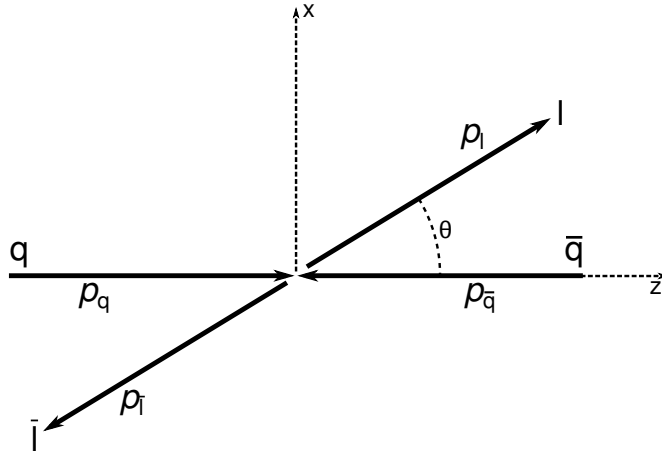


Figure 1.5 – Coordinate system used for the cross section calculation. Particles are set in normal font, variables in italic font and the coordinates in small letters. The solid lines with arrows mark the direction of the particles.

of-mass frame, the differential cross section for a $q\bar{q}$ pair going into a lepton-antilepton pair is

$$d\sigma(q\bar{q} \rightarrow \bar{l}l) = \frac{1}{2E_q 2E_{\bar{q}} |v_q - v_{\bar{q}}|} \frac{d^3\mathbf{p}_l}{(2\pi)^3 2E_l} \frac{d^3\mathbf{p}_{\bar{l}}}{(2\pi)^3 2E_{\bar{l}}} (2\pi)^4 \delta^{(4)}(p_q + p_{\bar{q}} - p_l - p_{\bar{l}}) |\mathcal{M}|^2, \quad (1.4)$$

where E_a , \mathbf{p}_a and p_a , with $a \in \{q, \bar{q}, l, \bar{l}\}$, are the energy, three-momentum and four-momentum of fermion a , and $|v_q - v_{\bar{q}}|$ is the velocity difference between quark and antiquark, defined as

$$|v_q - v_{\bar{q}}| = \frac{1}{E_q E_{\bar{q}}} \sqrt{(p_q p_{\bar{q}})^2 - (m_q m_{\bar{q}})^2}. \quad (1.5)$$

The matrix element \mathcal{M} is defined by the Feynman diagrams in Figure 1.3. The phase

space integrals can be partially evaluated and give

$$d\sigma(q\bar{q} \rightarrow \bar{l}l) = \frac{1}{2E_q 2E_{\bar{q}} |v_q - v_{\bar{q}}|} \frac{|\mathbf{p}_l| d\Omega}{(2\pi)^2 4\sqrt{s'}} |\mathcal{M}(q\bar{q} \rightarrow \bar{l}l)|^2, \quad (1.6)$$

where $d\Omega$ is an infinitesimal element of the solid angle and $\sqrt{s'}$ is the center-of-mass energy of the quark-antiquark pair. For very high energies the masses of the fermions can be neglected, which means that $E_q = E_{\bar{q}} = E_l = E_{\bar{l}} = \sqrt{s'}/2$, simplifying Equation (1.6) to the differential cross section

$$\frac{d\sigma(q\bar{q} \rightarrow \bar{l}l)}{d\Omega} = \frac{|\mathcal{M}(q\bar{q} \rightarrow \bar{l}l)|^2}{64\pi^2 s'}. \quad (1.7)$$

In addition to the contributions from the Feynman diagrams, the matrix element for the DY process has some additional factors, since the participating fermions have a spin and the incoming quarks and antiquarks have also a colour charge. For the incoming quarks one has to sum over all the quark flavours and multiply by a factor of three since the quark-antiquark pair has to form a colourless boson. Two additional factors of $1/3$ come from the averaging over the colour states of the initial quark and antiquark. Since the initial and final states of the process have unknown polarisation, one has to sum over all the possible spin combinations of the fermions and average over the spins of the incoming quark and antiquark. The matrix element that needs to be computed is then

$$\frac{1}{3} \frac{1}{2} \sum_{s_q} \frac{1}{2} \sum_{s_{\bar{q}}} \sum_{s_l} \sum_{s_{\bar{l}}} |\mathcal{M}(q(p_q, s_q), \bar{q}(p_{\bar{q}}, s_{\bar{q}}) \rightarrow l(p_l, s_l), \bar{l}(p_{\bar{l}}, s_{\bar{l}}))|^2, \quad (1.8)$$

with s_a denoting the spin states of the fermions.

With the Feynman rules for a fermion-photon vertex and a photon propagator, the left diagram in Figure 1.3 leads to the matrix element for the photon exchange, and gives at leading order⁴

$$i\mathcal{M}_\gamma = i \frac{Q_l Q_q e^2}{s'} \bar{\psi}_l \gamma^\mu \psi_l \bar{\psi}_{\bar{q}} \gamma_\mu \psi_q, \quad (1.9)$$

with e being the elementary charge, and Q_l and Q_q the fraction of the elementary charge for lepton and quark. This matrix element gives no contribution for outgoing neutrinos since they have $Q_l = 0$.

Combining two fermion-Z boson vertices⁵ with the propagator for the Z boson gives the matrix element for the exchange of a massive vector boson

$$i\mathcal{M}_Z = i \frac{g^2}{4 \cos^2 \theta_W} \frac{1}{s' - M_Z^2 + i s' \frac{\Gamma_Z}{M_Z}} \bar{\psi}_l \gamma^\mu (g_{V_l} - g_{A_l} \gamma^5) \psi_l \bar{\psi}_{\bar{q}} \gamma_\mu (g_{V_q} - g_{A_q} \gamma^5) \psi_q, \quad (1.10)$$

⁴Greek indices run from 0 to 3. The Einstein summation convention is used ($a^\mu b_\mu = a^0 b_0 + a^1 b_1 + a^2 b_2 + a^3 b_3$). The signature of the Minkowski metric is chosen to be $sign(g^{\mu\nu}) = (1, -1, -1, -1)$.

⁵To simplify the writing down of the equations, the 0 of the neutral Z^0 boson will be omitted.

where $g = e/\sin\theta_W$ is the weak coupling constant, θ_W the weak angle and M_Z and Γ_Z , respectively, the mass and total width of the Z boson. The vectorial and axial coupling constants g_V and g_A can be written as a function of the third component of the weak isospin I_W^3 , the weak angle and the charge of the fermion in units of e .

$$g_A = I_W^3 \quad g_V = I_W^3 - 2Q_f \sin^2 \theta_W \quad (1.11)$$

For neutrinos and up-type quarks $I_W^3 = 1/2$, and for charged leptons and down-type quarks $I_W^3 = -1/2$.

The cross section is proportional to the square of the sum of the two matrix elements \mathcal{M}_γ and \mathcal{M}_Z . One gets three different components, where $|\mathcal{M}_\gamma|^2$ and $|\mathcal{M}_Z|^2$ are the contributions from the virtual photon and Z boson exchange, respectively, and $\mathcal{M}_\gamma\mathcal{M}_Z^* + \text{c.c.}$ ⁶ is the contribution from the interference. With the abbreviations

$$\mathcal{R} = \frac{1}{Q_1 Q_q \sin^2 2\theta_W} \frac{s'}{s' - M_Z^2 + is' \frac{\Gamma_Z}{M_Z}}, \quad (1.12)$$

$$c_1^Z = (g_{V_1}^2 + g_{A_1}^2) (g_{V_q}^2 + g_{A_q}^2) + 4g_{V_1}g_{A_1}g_{V_q}g_{A_q}, \quad (1.13)$$

$$c_2^Z = (g_{V_1}^2 + g_{A_1}^2) (g_{V_q}^2 - g_{A_q}^2) + 4g_{V_1}g_{A_1}g_{V_q}g_{A_q}, \quad (1.14)$$

$$c_1^{\text{int}} = g_{V_1}g_{V_q} + g_{A_1}g_{A_q}, \quad \text{and} \quad (1.15)$$

$$c_2^{\text{int}} = g_{V_1}g_{V_q} - g_{A_1}g_{A_q} \quad (1.16)$$

one gets for the three components

$$\frac{1}{4} \sum_s |\mathcal{M}_\gamma|^2 = \frac{Q_1^2 Q_q^2 e^4}{2} (1 + \cos^2 \theta), \quad (1.17)$$

$$\frac{1}{4} \sum_s |\mathcal{M}_Z|^2 = \frac{Q_1^2 Q_q^2 e^4}{2} |\mathcal{R}|^2 [c_1^Z (1 + \cos \theta)^2 + c_2^Z (1 - \cos \theta)^2], \quad (1.18)$$

$$\frac{1}{4} \sum_s (\mathcal{M}_\gamma \mathcal{M}_Z^* + \text{c.c.}) = \frac{Q_1^2 Q_q^2 e^4}{2} \Re(\mathcal{R}) [c_1^{\text{int}} (1 + \cos \theta)^2 + c_2^{\text{int}} (1 - \cos \theta)^2], \quad (1.19)$$

where the sum over s indicates the sum over the spins of all involved fermions, as written in Equation (1.8), and $\Re(\mathcal{R})$ denotes the real part of \mathcal{R} . This leads, with the formula from Equation (1.7), to the differential cross section

$$\frac{d\sigma (q\bar{q} \rightarrow \gamma^*/Z^0 \rightarrow \bar{l}l)}{d\Omega} = \frac{\alpha^2 Q_1^2 Q_q^2}{12s'} [c_1 (1 + \cos^2 \theta) + c_2 \cos \theta], \quad \text{with} \quad (1.20)$$

$$c_1 = 1 + |\mathcal{R}|^2 (g_{V_1}^2 + g_{A_1}^2) (g_{V_q}^2 + g_{A_q}^2) + 2\Re(\mathcal{R})g_{V_1}g_{V_q}, \quad (1.21)$$

$$c_2 = 8|\mathcal{R}|^2 g_{V_1}g_{A_1}g_{V_q}g_{A_q} + 4\Re(\mathcal{R})g_{A_1}g_{A_q}, \quad \text{and} \quad (1.22)$$

$$\alpha = \frac{e^2}{4\pi}, \quad \text{the fine structure constant.} \quad (1.23)$$

⁶c.c. stands for complex conjugate.

Finally, to get the total cross section, the differential cross section is integrated over the complete sphere and gives

$$\begin{aligned}\sigma(\text{q}\bar{\text{q}} \rightarrow \gamma^*/Z^0 \rightarrow \text{l}\bar{\text{l}}) &= \frac{\alpha^2 Q_1^2 Q_q^2}{12s'} \int_0^{2\pi} d\phi \int_0^\pi \sin\theta d\theta [c_1 (1 + \cos^2\theta) + c_2 \cos\theta] \\ &= \frac{4\pi\alpha^2 Q_q^2}{9s'} c_1,\end{aligned}\tag{1.24}$$

where ϕ denotes the angle in the x - y plane and $Q_1 = 1$.

Chapter 2

Beyond the standard model

While Chapter 1 introduced the SM of elementary particle physics, the currently best model to describe most phenomena of elementary particle physics, this chapter deals with theories that go beyond the standard model (BSM). In Section 2.1 the motivations for theories beyond the standard model are presented. Section 2.2 describes theories that lead to heavy resonances that decay to lepton/antilepton pairs and Section 2.3 introduces a theory that leads to a new heavy boson that decays to a lepton/antilepton pair, where the lepton and the antilepton do not have the same flavour.

2.1 Motivations for physics beyond the SM

The SM of elementary particle physics is a very successful theory that is able to describe most of the known phenomena with very high precision. However, the SM is usually seen as a low energy approximation of a more general theory. Indeed, there are some observations which can not be explained by the SM, as explained below.

Gravitational interaction From the four fundamental forces, gravity is the only one not included in the SM. The theory of general relativity based on classical physics describes gravitational effects. To combine the quantum theory of the SM with general relativity, a quantum theory of gravity is necessary, which could be obtained by adding a particle carrying the gravitational force, called a graviton. This proves to be difficult because of the way that gravity interacts with the geometry of spacetime. A quantum gravity, where the graviton is a spin 2 particle, is non-renormalisable. Loop corrections involving gravitons become ultraviolet divergent and can not be renormalised to give a finite result. The strength of the gravitational force is much lower than the ones from the other three fundamental forces. While those have a similar strength that shows an effect at the electroweak scale of $\mathcal{O}(100 \text{ GeV})$, the energy at which gravitational interactions become relevant is at the order of the Planck scale of $E_{\text{Pl}} = 10^{19} \text{ GeV}$, which is defined by the Planck mass, $M_{\text{Pl}} = \sqrt{\hbar c/G}$, with G being the gravitational constant. The huge difference between the electroweak

scale and the Planck scale is also known as a hierarchy problem.

Fine-tuning of the scalar boson mass The hierarchy problem implies that the mass of the scalar boson should be of the order of the Planck scale. In order for the observed mass value to be 125 GeV, a fine-tuned cancellation of the bare mass and the contribution from Feynman diagrams involving loops, so called loop corrections, both of $\mathcal{O}(10^{19}$ GeV), is necessary.

Matter content of the universe Astronomical observations show that the visible content of matter can only be approximately 5% of the total matter and energy content of our universe. The remaining part is assumed to consist of about 25% dark matter, which is typically assumed to not interact electromagnetically or by strong interactions, and 70% dark energy, which is thought to be responsible for the observed accelerated expansion of the universe, by introducing a repellent force. The SM, however, does not offer a good candidate for a dark matter particle.

Neutrino masses In the SM neutrinos have no mass. The fact that neutrinos can change from one flavour to another implies that they must have non-zero mass difference, and their mass eigenstates are different from their flavour eigenstates. A mass term for the neutrinos can be added to the SM, but it is not clear if the small masses that the neutrinos must have can arise from the same electroweak symmetry breaking mechanisms than the masses for the other particles of the SM.

Free parameters of the SM Lagrangian The SM contains 19 free parameters, listed in Table 2.1, that have to be measured. The parameters include the charged fermion masses, the mixing angles and the charge-parity (CP) violating phase of the Cabibbo–Kobayashi–Maskawa (CKM) matrix, the coupling constants of the three forces, and the mass and vacuum expectation value of the scalar boson. However, it is widely believed that some of these parameters at least should be related to each other from a mechanism that is not described by the SM. As an example one could consider the different masses of the quark and lepton generations that may arise from a common generation in a BSM theory, that has a spontaneously broken symmetry at the scale of the SM.

Convergence of the coupling constants The SM coupling constants of the electromagnetic interaction, the weak interaction and the strong interaction have a similar value at an energy scale of $\mathcal{O}(10^{16}$ GeV). However, they do not converge to a single value as shown in Figure 2.1. In order to unify the coupling constants, an extension of the SM is necessary that changes the evolution above the electroweak scale.

These problems of the SM with gravity and the matter content of the universe, as well as the other characteristics of the SM, indicate that there must be new physics at a scale beyond the electroweak scale. What is unknown, however, is the energy

Table 2.1 – The free parameters of the SM [3].

Quantity	Symbol	Value
Electron mass	m_e	511 keV
Muon mass	m_μ	105.7 MeV
Tau mass	m_τ	1.78 GeV
Up quark mass	m_u	2.3 MeV ($\mu_{\overline{\text{MS}}} = 2 \text{ GeV}$)
Down quark mass	m_d	4.8 MeV ($\mu_{\overline{\text{MS}}} = 2 \text{ GeV}$)
Strange quark mass	m_s	95 MeV ($\mu_{\overline{\text{MS}}} = 2 \text{ GeV}$)
Charm quark mass	m_c	1.28 GeV ($\mu_{\overline{\text{MS}}} = m_s$)
Bottom quark mass	m_b	4.18 GeV ($\mu_{\overline{\text{MS}}} = m_b$)
Top quark mass	m_t	173.5 GeV
CKM 12-mixing angle	θ_{12}	12.9°
CKM 23-mixing angle	θ_{23}	2.4°
CKM 13-mixing angle	θ_{13}	0.2°
CKM CP violating phase	δ_{13}	69°
W boson mass	m_W	80.4 GeV
Z boson mass	m_Z	91.2 GeV
Strong coupling constant	α_S	0.119 ($\mu_{\overline{\text{MS}}} = m_Z$)
QCD vacuum angle	θ_{QCD}	~ 0
Scalar boson vacuum expectation value	v	246 GeV
Scalar boson mass	m_H	125.0 GeV [4]

scale at which this new physics will manifest itself. It could be as high as the Planck scale, but this would mean that the hierarchy problem remains unsolved. Therefore, it is rather believed that there should be new physics at the TeV scale, at which a discovery with direct searches at the LHC could be possible.

2.2 New massive resonances decaying to lepton pairs

If there is new physics to be found at the TeV scale, then a promising search channel at a hadron collider is the dilepton invariant mass spectrum. New physics would manifest itself in a change of the high mass tail of this spectrum. Especially in the case of new heavy resonances, the low background and the resonance peak as a signal, in combination with the high accuracy of the lepton reconstruction, make the dilepton final state an experimentally well motivated channel. From a theoretical point of view, a new massive resonance that decays to a lepton/antilepton pair arises in many different types of BSM models. There exist supersymmetric models that predict a resonance with a spin 0 [22], while extensions of the SM gauge group in the framework of Grand Unification can lead to a new spin 1 resonance [23–25]. Models with extra dimensions can also lead to new particles, including spin 1 or spin 2 particles [26, 27]. Generically, for searches for new physics, all particles that can give rise to a resonance in the dilepton spectrum are called Z' . In the following

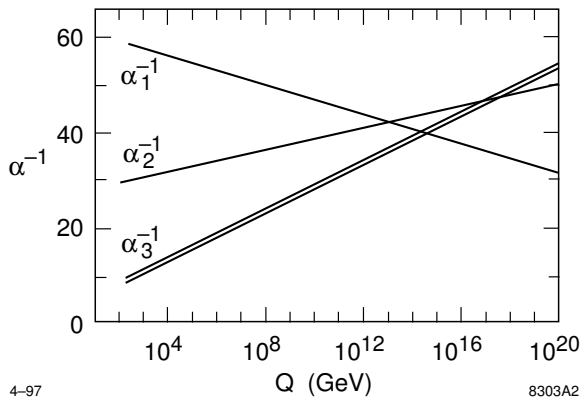


Figure 2.1 – Evolution of the SM couplings $\alpha_i = \frac{g_i^2}{4\pi}$ as a function of the energy scale. The plot is taken from [21].

the different classes of models that lead to a Z' resonance are described.

2.2.1 Supersymmetry

In Supersymmetry (SUSY) models every SM fermion has a SUSY partner particle which is a boson, and vice versa. The superpartner particles of fermions are called sfermions and have spin 0 and the gauge bosons superpartners are the gauginos with spin 1/2. In the SM the baryon number B and the lepton number L are conserved quantities defined as

$$B = \frac{1}{3} (n_q - n_{\bar{q}}) , \quad L = n_l - n_{\bar{l}} , \quad (2.1)$$

where n_q , $n_{\bar{q}}$, n_l and $n_{\bar{l}}$ are, respectively, the numbers of quarks, antiquarks, leptons and antileptons. This is generally not the case in a SUSY model, and a new quantum number called R -parity (R_p) is introduced

$$R_p = (-1)^{B-L+2s} , \quad (2.2)$$

where s is the spin of the particle, to restore the conservation laws found in experiments. With this definition all SM particles have $R_p = +1$ and all superpartners have $R_p = -1$. While many SUSY models are R -parity conserving and do not allow for the decay of a superparticle into an ordinary dilepton, there exist R -parity violating SUSY models where this is possible [22]. A spin 0 superpartner of a neutrino, a sneutrino ($\tilde{\nu}$), could decay to dileptons in these R -parity violating SUSY models. In order to be able to solve the fine-tuning problem of the SM, by canceling the SM loop corrections with the loop corrections involving superpartners, the masses of SUSY particles are expected to be in the TeV range.

2.2.2 Grand unified theories

Grand unified theories (GUT) are theories where the three gauge interactions from the strong, weak and electromagnetic force are unified in one single gauge interaction

at a high energy scale, referred to as the GUT scale. The motivation for this is the scale dependency of the coupling constants of the three forces, which in the SM converge almost at one value at a very high energy scale, as shown in Figure 2.1. It is hoped therefore, that the introduction of a larger symmetry modifies the couplings in such a way to unify them in one point at the GUT scale. This larger symmetry group, introduced by the unification, contains the symmetry group of the SM, which is $G_{\text{SM}} = SU(3)_c \times SU(2)_L \times U(1)$ as described in Section 1.2. Below the GUT scale the symmetry of the GUT group has to be broken to recover the SM. Introducing a new gauge group implies the existence of one or more new neutral gauge bosons.

The minimal extension of the SM gauge group is the $SU(5)$ group of unitary 5×5 matrices with determinant 1 [28]. For this group, the symmetry breaking scale for $SU(5) \rightarrow SU(3)_c \times SU(2)_L \times U(1)$ is of $\mathcal{O}(10^{16} \text{ GeV})$. However, models using the simple extension of the SM to the $SU(5)$ gauge group predict the decay of the proton to a positron and a neutral pion within a time shorter than the lower limit of current proton lifetime measurements ($\tau_p > 10^{33}$ years for this decay mode [3]).

Another extension is the $SO(10)$ group, defined by orthogonal 10×10 matrices, which contains the $SU(5)$ group. The symmetry of this group could be broken in a scheme

$$SO(10) \rightarrow SU(5) \times U(1)_\chi \rightarrow G_{\text{SM}} \times U(1)_\chi, \quad (2.3)$$

where χ denotes the charge of the new particle coming from the additional $U(1)_\chi$ group. While in the previously discussed $SU(5)$ extension, the mass of the new bosons must be of the order $\mathcal{O}(10^{16} \text{ GeV})$, the mass for bosons from the additional $U(1)_\chi$ can be in the TeV range. Therefore, particles coming from such an extension could be discovered with a TeV hadron collider like the LHC.

Popular classes of models are the E_6 models, which extend the $SO(10)$ group with another unitary group to the exceptional E_6 group, so that the symmetry can be broken following

$$E_6 \rightarrow SO(10) \times U(1)_\psi \rightarrow SU(5) \times U(1)_\chi \times U(1)_\psi \rightarrow G_{\text{SM}} \times U(1)_\chi \times U(1)_\psi. \quad (2.4)$$

For the linear combination of $U(1)_\theta = U(1)_\chi \cos \theta - U(1)_\psi \sin \theta$ only one is expected to be light and at the TeV scale, so that θ becomes a free parameter of the theory. The mixing angles where $\theta = 0, -\pi/2, \sin^{-1} \sqrt{3/8}$ and $-\sin^{-1} \sqrt{5/8}$ are called the ψ, χ, η and I modes, respectively, and give rise to the $Z'_\psi, Z'_\chi, Z'_\eta$ and Z'_I bosons that couple differently to quarks and leptons.

2.2.3 Sequential standard model

The sequential standard model (SSM) [23], is often used as a benchmark model for experimental Z' searches. A Z'_{SSM} is essentially a heavy copy of the Z of the SM with the same couplings.

2.2.4 Extra dimensions

Theories involving additional spatial dimensions represent a different class of models beyond the standard model. The aim of these models is to explain the weakness of the gravitational force compared to the other forces by allowing the graviton, as the carrier of the gravitational force, to propagate in the extra dimensions, while the other fields of the SM must remain in the usual 4-dimensional spacetime. The overlap of the wave functions of the SM particles with the graviton is, therefore, small, which would explain the observed weakness of the gravitational force.

Large extra dimensions

There exist models with large extra dimensions, proposed by Arkani-Hamed, Dimopoulos and Dvali [29], called ADD models, that try to explain the mass hierarchy. The idea is that gravity has not been tested to distances smaller than about $100 \mu\text{m}$. Therefore, below this distance n extra dimensions with radius R could exist, that would modify the gravitational potential to $1/R^n$ for distances much smaller than R . From this follows that the observed Planck mass in 4 dimensions is an effective mass that is defined by the fundamental Planck mass in $4 + n$ dimensions and R

$$M_{\text{Pl}}^2 \sim M_{\text{Pl}_{4+n}}^{2+n} R^n. \quad (2.5)$$

The fundamental Planck mass can, thus, be in the TeV range, which would solve the hierarchy problem. If one assumes the mass scale at 1 TeV, a condition for the size of the extra dimension arises

$$R \sim 10^{\frac{30}{n}-19} \text{ m}. \quad (2.6)$$

From this follows that there have to be at least two extra dimensions to arrive at an R that is below 1 mm. ADD models predict a large number of massive excitations, called Kaluza–Klein (KK) excitations or KK tower, of the graviton, where the mass difference between the different excitations is inverse proportional to R . For $M_{\text{Pl}_{4+n}}$ masses in the TeV range and two extra dimensions, this mass difference between the KK excitations is so small, that physics following this model would not appear as single resonances but as a continuous distortion of the measured dilepton spectrum. In the case that the SM bosons are also allowed to propagate in the extra dimensions, this gives rise to KK towers of these bosons as well.

Small extra dimensions

Another popular attempt, introduced by Randall and Sundrum [26, 27] to solve the hierarchy problem, uses only one small extra spherical dimension of radius $R = 1/10^{19} \text{ GeV}$ in a warped geometry. The metric of this geometry is given as

$$ds^2 = e^{-2kR|\phi|} \eta_{\mu\nu} dx^\mu dx^\nu + R^2 d\phi^2, \quad (2.7)$$

where k is an arbitrary scale and $\phi \in [-\pi, \pi]$ is the coordinate in the extra dimension, with periodic boundary conditions. The three normal spatial dimensions, also called

Table 2.2 – 95% C.L. limits on the Z' mass for various models, obtained from LEP data.

Z' model	Z'_χ	Z'_ψ	Z'_η	Z'_{SSM}
Lower limit on $M_{Z'}$ (GeV)	785	500	500	1760

the 3-brane, are located at $\phi = \pi$ and contain the SM bosons, while the graviton can propagate also in the extra dimension. The full space is often called the bulk, while a subset with p dimensions is denounced as p -brane. The Planck mass in four dimensions is related to the Planck mass in five dimensions by

$$M_{\text{Pl}}^2 = \frac{M_{\text{Pl}5}^3}{k} (1 - e^{-2kR\pi}) , \quad (2.8)$$

and the masses in the 3-brane at $\phi = \pi$ are related to the masses in five dimensions by an exponential factor

$$m = m_0 e^{-kR\pi} . \quad (2.9)$$

For the choice of an appropriate value of kR this gives rise to massive leptonically decaying KK gravitons in the 4-dimensional world, with masses at the TeV scale. The RS model is characterised by two free parameters: the mass of the first KK mode and the coupling parameter of the graviton to the SM, $c = k/M_{\text{Pl}}$.

2.2.5 Current experimental limits

Searches for new massive resonances have been done by various experiments. The electron-positron collision data from the Large Electron-Positron (LEP) collider at CERN allowed the setting of indirect limits, using leptonic and hadronic cross sections and leptonic forward-backward asymmetries, on the mass of a Z' [30]. About 700 pb^{-1} of data from collisions with center-of-mass energies ranging from 130 GeV to 209 GeV (LEP-II) were analysed, and the obtained limits are listed in Table 2.2.

Direct limits on spin 1 resonances in the dielectron channel have been set by the CDF [31] and D0 [32] collaborations, from 2.5 fb^{-1} (CDF) and 5.4 fb^{-1} (D0) of data collected at the Tevatron $p\bar{p}$ collider at a center-of-mass energy of 1.96 TeV. Limits on RS gravitons, using the dielectron and diphoton final states, have also been set by the two collaborations [33, 34]. D0 used 5.4 fb^{-1} of data in both channels for the search, while CDF analysed 5.7 fb^{-1} and 5.4 fb^{-1} of data in the dielectron and diphoton channels, respectively. The obtained limits for the two experiments are listed in Table 2.3.

From the first three years of data taking at the Large Hadron Collider at CERN, the ATLAS and CMS collaborations published results from pp collisions at $\sqrt{s} = 7 \text{ TeV}$ [35, 36], at a combination of $\sqrt{s} = 7 \text{ TeV}$ and early 2012 $\sqrt{s} = 8 \text{ TeV}$ [37], and at $\sqrt{s} = 8 \text{ TeV}$ [1, 38]. Since the resonances are very closely spaced in their masses in the ADD models, the experimental approach is not a search for a narrow resonance, but for a deviation of the shape of the invariant mass spectrum at high

Table 2.3 – 95% C.L. limits on the Z' or G_{RS} mass for various models, obtained from Tevatron data [31–34].

Z' model	Lower mass limit (GeV)			
	CDF		D0	
	expected	observed	expected	observed
Z'_χ	857	862	910	903
Z'_ψ	846	851	898	891
Z'_η	873	877	927	923
Z'_{SSM}	961	963	1024	1023
$G_{\text{RS}} (c/\overline{M}_{\text{Pl}} = 0.01)$		612		560
$G_{\text{RS}} (c/\overline{M}_{\text{Pl}} = 0.05)$		941		940
$G_{\text{RS}} (c/\overline{M}_{\text{Pl}} = 0.1)$		1058		1050

Table 2.4 – 95% C.L. limits on the Z' or G_{RS} mass for various models, obtained from about 20 fb^{-1} of $\sqrt{s} = 8 \text{ TeV}$ LHC data. The results were obtained by combining the dielectron and dimuon final state [1, 38].

Z' model	Lower mass limit (TeV)			
	ATLAS		CMS	
	expected	observed	expected	observed
Z'_χ	2.60	2.62		
Z'_ψ	2.46	2.51	2.57	2.57
Z'_{SSM}	2.87	2.90	2.90	2.90
$G_{\text{RS}} (c/\overline{M}_{\text{Pl}} = 0.01)$	1.28	1.25	1.38	1.27
$G_{\text{RS}} (c/\overline{M}_{\text{Pl}} = 0.05)$	2.25	2.28	2.35	2.35
$G_{\text{RS}} (c/\overline{M}_{\text{Pl}} = 0.1)$	2.67	2.68	2.73	2.73

mass. ATLAS [39] and CMS [40, 41] have published results for searches for signals from large extra dimensions. Table 2.4 lists the combined dielectron and dimuon lower limits for the mass of various heavy resonances, obtained from searches at the LHC with a center-of-mass energy of 8 TeV. Lower limits obtained separately in the dielectron and the dimuon final states are presented in Table 2.5.

2.3 Lepton flavour violating Z' models

The models that were introduced previously all lead to final states which are symmetric in lepton flavour. That means that, while electron-positron, muon-antimuon or tau-antitau final states are allowed, electron-antimuon or muon/antitau states, for example, are forbidden. In this section, a class of models predicting the existence of new resonances that can decay to final states with leptons from different flavours is introduced. One speaks of lepton flavour violating (LFV) models.

The LFV model that will be used in this thesis is explained in detail in [42–44]. It

Table 2.5 – Observed 95% C.L. limits in the dielectron and dimuon channels, on the Z' or G_{RS} mass for various models. The results were obtained from about 20 fb^{-1} of $\sqrt{s} = 8 \text{ TeV}$ LHC data, recorded in 2012 [1, 38].

Z' model	Lower mass limit (TeV)			
	ATLAS		CMS	
	dielectron	dimuon	dielectron	dimuon
Z'_ψ			2.34	2.39
Z'_{SSM}	2.79	2.53	2.67	2.73
$G_{\text{RS}} (c/\overline{M}_{\text{Pl}} = 0.01)$			1.25	1.13
$G_{\text{RS}} (c/\overline{M}_{\text{Pl}} = 0.05)$			2.13	2.12
$G_{\text{RS}} (c/\overline{M}_{\text{Pl}} = 0.1)$			2.50	2.56

introduces two extra spatial dimensions that are compactified on a sphere with radius R . The motivation for such a model is to explain the hierarchy of fermion masses in four dimensions as stemming from a single generation in six dimensions. In the model the three light generations in four dimensions are distinguished by different winding numbers on the spherical extra dimensions and the overlap of the fermion wave functions with the one from the scalar boson generates the hierarchy of the masses. With the approximation that there is no mixing between the fermions, the model shows also a conservation of the generation number, since each generation is associated with only one winding number.

Beside the flavour conserving KK modes, which give rise to Z' bosons that can decay to same flavour dileptons, flavour changing KK modes emerge if the gauge bosons are allowed to propagate in the bulk. When the extra dimensions are integrated out, an effective Lagrangian in four dimensions is obtained that contains vector fields Z'_{LFV} and a'_{LFV} that generate transitions between the generations, where the generation number changes by one. Examples for possible processes are

$$\begin{aligned}
d + \bar{s} &\rightarrow Z'_{\text{LFV}}/a'_{\text{LFV}} \rightarrow d + \bar{s} \\
d + \bar{s} &\rightarrow Z'_{\text{LFV}}/a'_{\text{LFV}} \rightarrow e^- + \mu^+ \\
d + \bar{s} &\rightarrow Z'_{\text{LFV}}/a'_{\text{LFV}} \rightarrow \mu^- + \tau^+
\end{aligned} \tag{2.10}$$

where the one with electrons and muons in the final state shall be studied further. A production process with inverted charges is also possible and can lead to a $e^+ + \mu^-$ final state. However, because of the proton structure which makes it necessary that both initial quarks come from the sea, this process has a cross section which is smaller by approximately one order of magnitude. In the case that a signal is discovered at a pp collider, this asymmetry could be used to distinguish this model from others that result in a resonance that is symmetric in the $e^- \mu^+$ and $e^+ \mu^-$ final states. The effective Lagrangians for the couplings of a Z'_{LFV} boson or a a'_{LFV} to the $e^\mp \mu^\pm$ final

state are [45]

$$\begin{aligned}\mathcal{L}_{Z'_{\text{LFV}}} &= -\frac{\kappa_{12}g}{2\cos\theta_W}\left[\frac{1}{2}\bar{\mu}\gamma_\mu\gamma_5e - \left(\frac{1}{2} - 2\sin^2\theta_W\right)\bar{\mu}\gamma_\mu e\right]\overline{Z'_{\text{LFV}\mu}} \\ \mathcal{L}_{a'_{\text{LFV}}} &= \kappa_{12}g\sin\theta_W\bar{\mu}\gamma_\mu e\overline{a'_{\text{LFV}\mu}},\end{aligned}\quad (2.11)$$

where g denotes the SM coupling, θ_W is the weak angle and κ_{12} is the factor from the overlap integral between generation one and generation two fermions. In the simplest case, without fermion mixing, all $\kappa_{ij} \sim \kappa \cdot \delta_{i,i+1}$.

Results from rare decay measurements with $K_L \rightarrow e^-\mu^+$ give some strong constraints on the mass scale of the models, leading to

$$M_{Z'_{\text{LFV}}/a'_{\text{LFV}}} \gtrsim \kappa_{12} \cdot 100 \text{ TeV}, \quad (2.12)$$

which translates in a constraint for the κ parameter for a given boson mass

$$\kappa \lesssim \frac{M_{Z'_{\text{LFV}}/a'_{\text{LFV}}}}{100 \text{ TeV}}. \quad (2.13)$$

The mass of the Z'_{LFV} and the a'_{LFV} bosons is not necessarily the same, but the separation between the two is small compared to the mass. At invariant masses in the TeV range, the mass resolution of the detector, is larger than what is expected for the separation between the two bosons. Therefore, only a single resonance peak is expected to be seen experimentally, and the contributions from Z'_{LFV} and a'_{LFV} can be added coherently.

By counting all the possible decay modes the decay width for a Z'_{LFV} and an a'_{LFV} are found to be

$$\begin{aligned}\Gamma(Z'_{\text{LFV}}) &\simeq \kappa^2 \frac{M_{Z'_{\text{LFV}}}}{M_Z} \cdot 1.8 \text{ GeV} \quad \text{and} \\ \Gamma(a'_{\text{LFV}}) &\simeq \kappa^2 \frac{M_{a'_{\text{LFV}}}}{M_Z} \cdot 1.3 \text{ GeV},\end{aligned}\quad (2.14)$$

which gives widths of 2.0 MeV and 1.4 MeV, respectively, for Z'_{LFV} and a'_{LFV} masses of 1 TeV. Thus, with the constraint for the κ factor, these models can be treated as predicting the existence of a narrow resonance in the $e\mu$ invariant mass spectrum at the TeV scale.

Results on the search for new spin 1 particles decaying to an electron-muon pair have been reported by the CDF collaboration [46] and the ATLAS collaboration [47]. Other searches, using the $e\mu$ final state in the context of R -parity violating SUSY, have been performed by the CDF [48], the D0 [49] and the ATLAS collaborations [50]. No interpretation of the full $e\mu$ invariant mass spectrum in the context of the LFV model, presented in this chapter, has been published up to now. In [51], upper limits for selected LFV resonance masses were calculated, using 3.35 fb^{-1} from 7 TeV collision data collected by CMS in 2011. A first publication of the CMS collaboration of a BSM resonance search in the $e\mu$ final state, involving also the interpretation of the results in the context of the LFV model described here, is in preparation.

Chapter 3

Large Hadron Collider

From all the fundamental particles known in the SM only the electron, the neutrinos and the photon are stable and observable as a free particle. However, since neutrino interaction with matter is characterised by a small cross section, they are very hard to detect and generally require very large detectors. The quarks are hidden in baryons and mesons because of the confinement, and from these hadrons only the proton is stable. A possible way to study elementary particles and their interactions is to design an experiment that provides collisions between these elementary particles, and then study the particle produced in the final state. For the production of the particles one can rely on natural sources such as cosmic rays, or artificially produced particle beams. In the later case a beam of charged particles is accelerated in an electric field, and then either directed on a fixed target, or brought into collision with another beam of particles that was accelerated in the opposite direction. These two methods are called, respectively, a fixed target experiment and a collider experiment. If the two beams of a collider experiment consist of particles with the same mass, the complete energy of the colliding particles is available for the production of new particles.

Notable colliders are the, now decommissioned, LEP collider at CERN in the Geneva area, which collided a beam of electrons with a beam of positrons in four interaction points around an underground storage ring of about 27 km circumference, the Tevatron proton-antiproton collider at Fermilab, and the LHC [52] that now occupies the tunnel which formerly housed the LEP collider and that collides two proton beams. A non-exhaustive list of other important existing or former colliders includes the HERA electron-proton collider at DESY in Germany, the Relativistic Heavy Ion Collider at Brookhaven National Laboratory in the USA, the BEPC II electron-positron collider in Beijing in the PRC, the KEKB electron-positron collider at KEK in Japan and the PEP-II electron-positron collider at SLAC in the USA. Section 3.1 presents the CERN accelerator complex and the LHC machine, which currently has the highest collision energy. The luminosity, as an important characteristic of an accelerator, is introduced in Section 3.2. Section 3.3 gives an overview of the schedule of the LHC and Section 3.4 details the processes that take place in a proton-proton collision.

3.1 CERN accelerator complex

CERN houses several particle accelerators that can accelerate protons or heavy ions, like lead, from being at rest to relativistic energies, where they are then used in various fixed target and collider experiments to produce other particles. The accelerators are chained together so that the beam coming out of one accelerator can be accelerated further by the next one. Figure 3.1 shows the CERN accelerator complex.

Protons, which are produced from hydrogen by stripping the electron in a duoplasmatron, are first accelerated to 50 MeV by a linear accelerator called the Linac 2. They are then fed into the Proton Synchrotron Booster (PSB), a machine of four synchrotron rings stacked above each other, to be accelerated to 1.4 GeV before being injected into the Proton Synchrotron (PS). During the process of the acceleration the particles form bunches as trailing particles are accelerated more and leading particles less than the center of the bunch. Lead ions (Pb^{29+}) are accelerated in the Linac 3 accelerator to an energy of 4.2 MeV/u¹, and then injected into the Low Energy Ion Ring (LEIR), which splits the bunch into four short bunches and accelerates them to 72 MeV/u before the transfer to the PS. Before being injected in the LEIR the bunches pass a carbon foil, which strips more electrons from the ions so that they enter the LEIR as Pb^{54+} . From the PS onward protons and lead nuclei are accelerated further in the same machines. The PS is a storage ring with a circumference of 628.3 m that started its operation in 1959 and is now used, in an upgraded version, to accelerate the protons and lead nuclei to 25 GeV and 5.9 GeV/u, respectively. After the PS the lead ions pass a second carbon foil, which ionizes them fully as Pb^{82+} . The particle bunches are then injected in the Super Proton Synchrotron (SPS), which has a circumference of 6.9 km and accelerates protons to 450 GeV and lead nuclei to 177 GeV/u. After this last stage of acceleration the bunches of particles are injected in the two beam pipes of the LHC, alternately in the clockwise and counter clockwise direction. Up to the SPS all ring accelerators use bending magnets operating at room temperature to keep the bunches on their path.

The LHC at CERN has a design energy per proton beam of 7 TeV, which results in a center-of-mass energy of $\sqrt{s} = 14$ TeV. Up to now however, this energy has not been reached because of concerns about the stability of the electrical interconnections between the 1232 superconducting dipole bending magnets, that force the beams on a circular track around the ring. In the years 2010 and 2011 the LHC was operated with proton beam energies of 3.5 TeV. In 2012, the beam energy of 4 TeV was reached, resulting in a proton-proton (pp) center-of-mass energy of 8 TeV. The maximal energy reached in heavy ion operation is 2.76 TeV/u, which results in a total center-of-mass energy of 1.15 PeV. In pp operation, the LHC is designed to have 2808 bunches per ring and the time between two bunch crossings in an interaction point (IP) is 25 ns, which spaces the bunches about 7.5 m apart along the beam axis. In the data taking period from 2010 to 2013 (LHC run 1), before the long shutdown one (LS1), only every second bunch space was filled, so that the bunch spacing was, with 50 ns, double

¹ MeV per nucleon

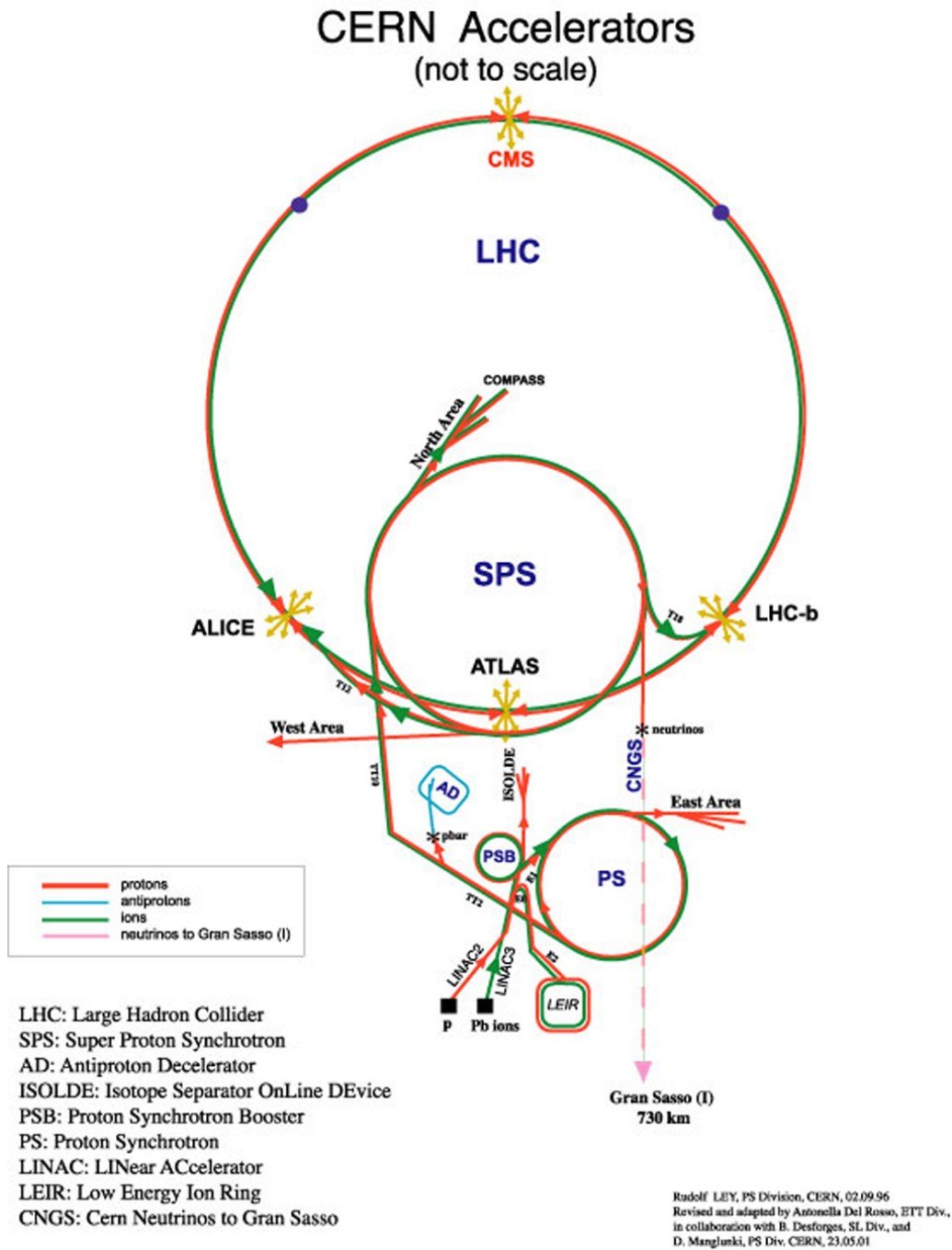


Figure 3.1 – The CERN accelerator complex [53].

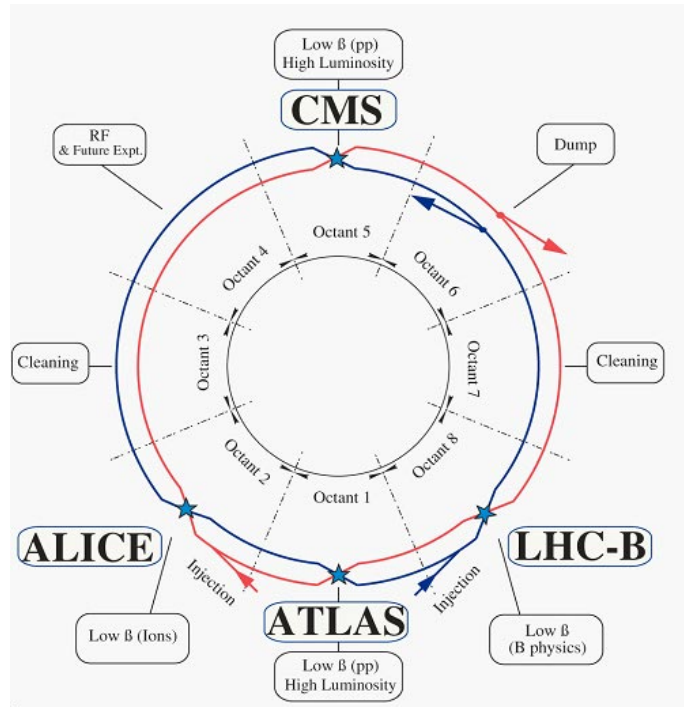


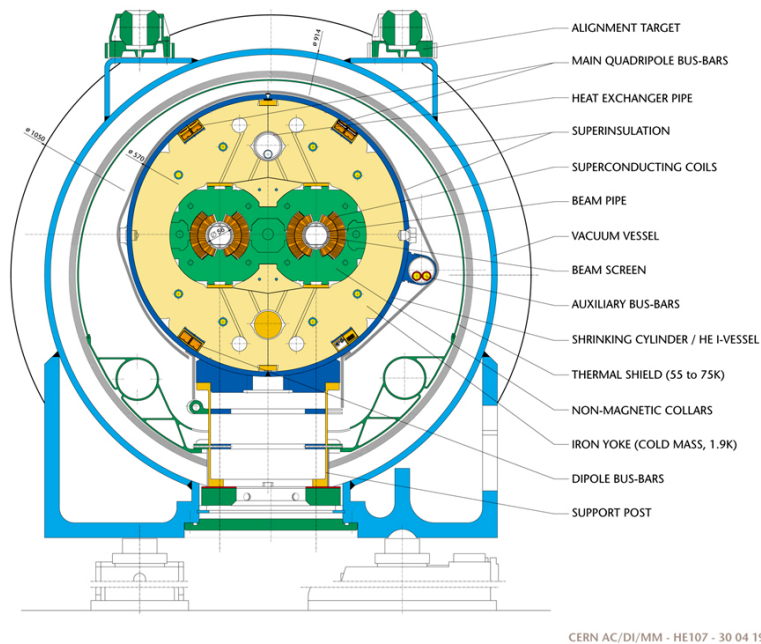
Figure 3.2 – Layout of the LHC. Beam 1 is the clockwise beam (in red). Beam 2 is the counter clockwise beam (in blue) [52].

the nominal one, and the number of colliding bunches was 1380. The design number of bunches in lead-lead (Pb-Pb) operation is 592 and a maximum of 356 colliding bunches was reached before LS1. In 2013 the LHC was running in a third mode of operation, colliding protons with lead ions (p-Pb).

It takes several injections from the PS storage ring to fill the SPS, and then in turn also several injections from the SPS to fill the LHC, so that the time to completely fill the LHC is approximately half an hour. During the time that the PS, SPS or LHC ring is fully filled and accelerating or colliding particles, the upstream accelerators can deliver beams to other experiments at CERN. When both rings are filled the beams are accelerated to the final energy, which takes approximately 20 minutes because of the slow increase of the current in the magnetic system. After the ramp up of the magnetic field, the two beams are adjusted and focused before brought to collision. The LHC is designed for a total stored energy of 362 MJ per beam.

The LHC is divided in eight arcs and eight straight sections, of which four house equipment needed for the accelerator and the other four contain the interaction points where the two beams are brought into collision in the four main experiments. The two general purpose experiments ATLAS (A Toroidal Apparatus) [54] and the Compact Muon Solenoid (CMS) [55] are located at the IP 1 and IP 5, respectively. IP 2 is the location of the heavy ion experiment ALICE (A Large Ion Collider Experiment) [56], and the b-physics orientated LHCb experiment [57] is located at IP 8. Figure 3.2 shows the general layout of the two LHC rings.

Interaction region 4 (IR 4) is the location of the radio frequency (RF) system, built

LHC DIPOLE : STANDARD CROSS-SECTION

CERN AC/DI/MM - HE107 - 30 04 1999

Figure 3.3 – Cross section of a main dipole of the LHC [52].

from eight superconducting cavities per beam, operating at 400 MHz, to accelerate the beam and compensate the losses from synchrotron radiation. The beam abort system is installed at IR 6, with two separate tunnels containing the beam dumps for the two beams. Finally, the two interaction regions IR 3 and IR 7 house equipment for beam cleaning for momentum and betatron, respectively.

The superconducting dipole and quadrupole magnets of the LHC use NbTi as a superconductor and produce a magnetic field up to 8.33 T. Because of the high magnetic field, the magnets have to be cooled down to 1.9 K with superfluid helium, instead of the usual 4.2 K, which allow only fields up to approximately 5 T. Since both beams consist of protons the bending magnets have two beam pipes with a field in opposite direction. A cross section of one of the main dipoles is shown in Figure 3.3. The total energy stored in the magnetic system reaches 11 GJ.

To keep beams from interacting with gas molecules, the two beam pipes are pumped down to an ultrahigh vacuum with a pressure of 10^{-10} mbar in the room temperature sections of the vacuum system. There are also two other vacuum systems for the insulation of the cryomagnets and the insulation of the helium distribution, respectively.

Table 3.1 – Machine parameters of the LHC [58].

	design	run 2012
Bunch spacing	25 ns	50 ns
n_b	2808	1380
N_b	1.15×10^{11}	1.7×10^{11}
f_{rev}	11245 Hz	
ϵ_n	$3.75 \mu\text{m}$	$\approx 2.5 \mu\text{m}$
β^*	0.55 m	0.6 m
F	0.84	0.76
\mathcal{L}	$1 \times 10^{34} \text{ cm}^{-2} \text{ s}^{-1}$	$7.7 \times 10^{33} \text{ cm}^{-2} \text{ s}^{-1}$
E_{beam}	362 MJ	$\approx 140 \text{ MJ}$

3.2 Luminosity

At the LHC, the number N of events that are produced of a process is proportional to the cross section σ

$$N = \sigma \mathcal{L}, \quad (3.1)$$

where \mathcal{L} is a machine dependent quantity called luminosity, which is defined as

$$\mathcal{L} = n_b \frac{N_1 N_2}{A} f_{rev}. \quad (3.2)$$

Here, N_1 and N_2 are the number of particles in the two colliding bunches, A is the overlap area of the two bunches transverse to the beam, n_b is the number of bunches in one beam and f_{rev} is the revolution frequency of one bunch. At the LHC both beams are made of the same type of particles and $N_1 = N_2 = N_b$. The maximum number of bunches per beam and the revolution frequency are defined by the circumference of the LHC, and amount to 2808 and 11 245 Hz, respectively. In order to get as many events of interest as possible, one can either increase the number of particles in a bunch or focus the two beams on a smaller area for the interaction.

Since the area of overlap is difficult to measure directly in an accelerator, one uses a different formula to calculate the luminosity, assuming circular beam profiles

$$\mathcal{L} = n_b N_b^2 f_{rev} \frac{\gamma}{4\pi\epsilon_n\beta^*} F, \quad (3.3)$$

where γ is the relativistic gamma factor, ϵ_n is the normalised transverse beam emittance from the injectors, β^* is the so called beta function at the IP, and F is a geometric luminosity reduction factor, due to the fact that the two beams cross each other at a small angle. The values for the LHC machine parameters are listed in Table 3.1.

During collisions, the number of particles in a bunch, and thus also the instantaneous luminosity, decreases exponentially from the initial peak luminosity. The peak luminosity for the first three years of running of the LHC is shown in Figure 3.4. After about ten hours the instantaneous luminosity has decreased so much that it is

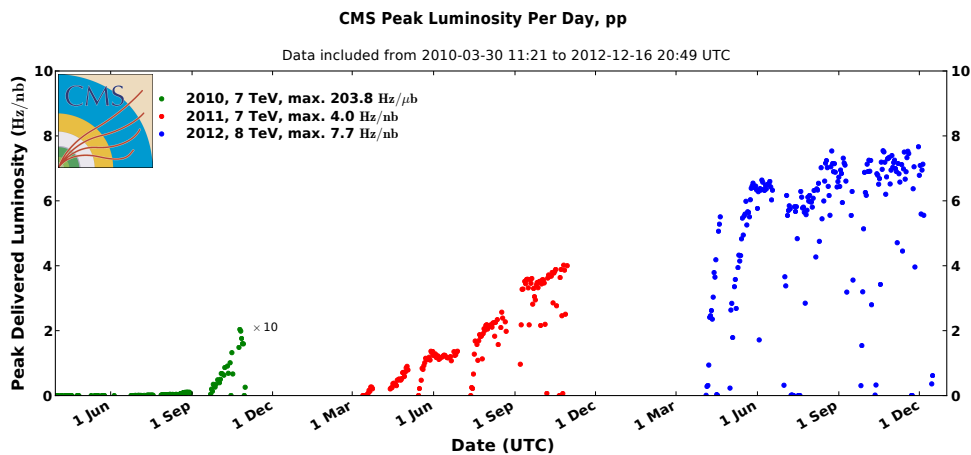


Figure 3.4 – Peak luminosities for the first three years of running of the LHC as measured by the CMS experiment [59].

more efficient to abort the fill and refill the machine with new beams. The integrated luminosity is the luminosity integrated over time, and is shown in Figure 3.5, cumulated for all the pp fills taken during run 1. Table 3.2 lists the integrated luminosity

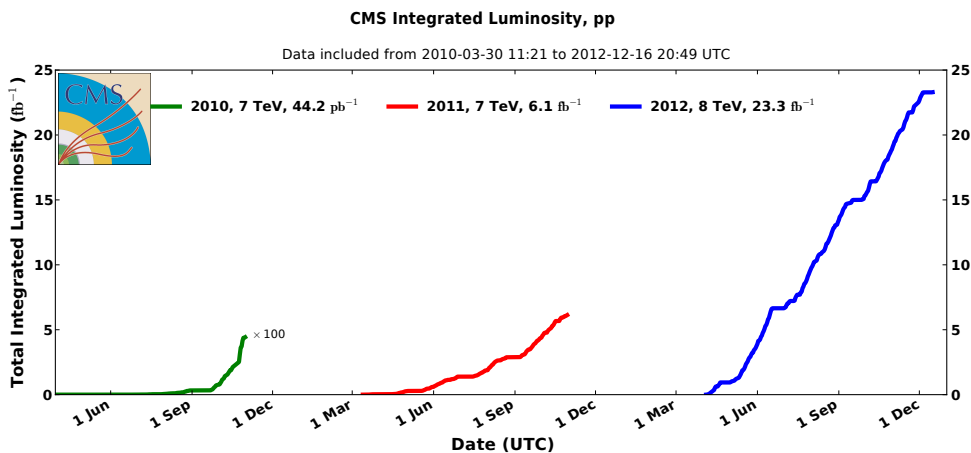


Figure 3.5 – Integrated luminosity for the first three years of running of the LHC, as measured by the CMS experiment [59].

delivered at IP 5 of the LHC, for the years from 2010 to 2012.

3.3 LHC schedule

The LHC is designed to run for many years, with short shutdowns at the end of every year and long shutdowns every couple of years. After the startup in 2010, the run 1 for pp collisions ended in 2012. From 2013 until May 2015 the long shutdown 1 takes place. During this time the LHC is being upgraded to run at higher center-of-mass

Table 3.2 – Total integrated luminosity from pp collisions, delivered at IP 5 by the LHC [59].

Year	Center-of-mass energy	Integrated luminosity
2010	7 TeV	44.2 pb ⁻¹
2011	7 TeV	6.1 fb ⁻¹
2012	8 TeV	23.3 fb ⁻¹

energies. The planned center-of-mass energy for pp collisions in 2015 is 13 TeV, and the bunch spacing is planned to be 25 ns. The expectation is to collect about 100 fb⁻¹ of pp collisions at 13 TeV or 14 TeV before the next long shutdown, planned in 2018. After the LS 2, a third run, delivering approximately 300 fb⁻¹ of pp collisions at 14 TeV, is planned until the end of the LHC phase 1, which is scheduled for 2022. In 2022 and 2023, a major upgrade for the machine is foreseen to the High Luminosity Large Hadron Collider (HL-LHC), with five times the nominal instantaneous luminosity of the LHC. Until the end of the program in 2035, about 3000 fb⁻¹ of pp collision data at 14 TeV are expected to be collected. Synchronised with the LHC shutdowns, the detectors will be upgraded as well to cope with the more challenging data taking conditions at higher instantaneous luminosity, and to replace detector components that degraded owing to the high radiation levels.

3.4 Proton-proton interactions at the LHC

In this thesis, a proton-proton interaction at the LHC is called an event. Depending on their cross section, different SM processes have different probabilities to occur in an event. The cross section for SM processes in an LHC event is shown in Figure 3.6.

The facts that a proton bunch of the beam contains many protons, and that the proton is a composite particle, result in several processes taking place in an event.

Hard interaction

When two protons collide, two of its partons can take part in a hard interaction, which is usually the interaction of interest. Which kind of hard interaction takes place cannot be known in advance, and the probability for one particular interaction depends on the cross section of that process. In the hard interaction secondary particles can be created, which in turn can decay to form the final state of an event that can be measured with a detector. An example for such a hard interaction is the DY process that was discussed in Section 1.4.

Initial state radiation and final state radiation

Before the two partons interact with each other they can radiate other partons. Similar to this process also the decay products of the hard interaction can radiate partons or photons. This radiation of particles is called initial state radiation (ISR) when it happens before the hard interaction, and final state

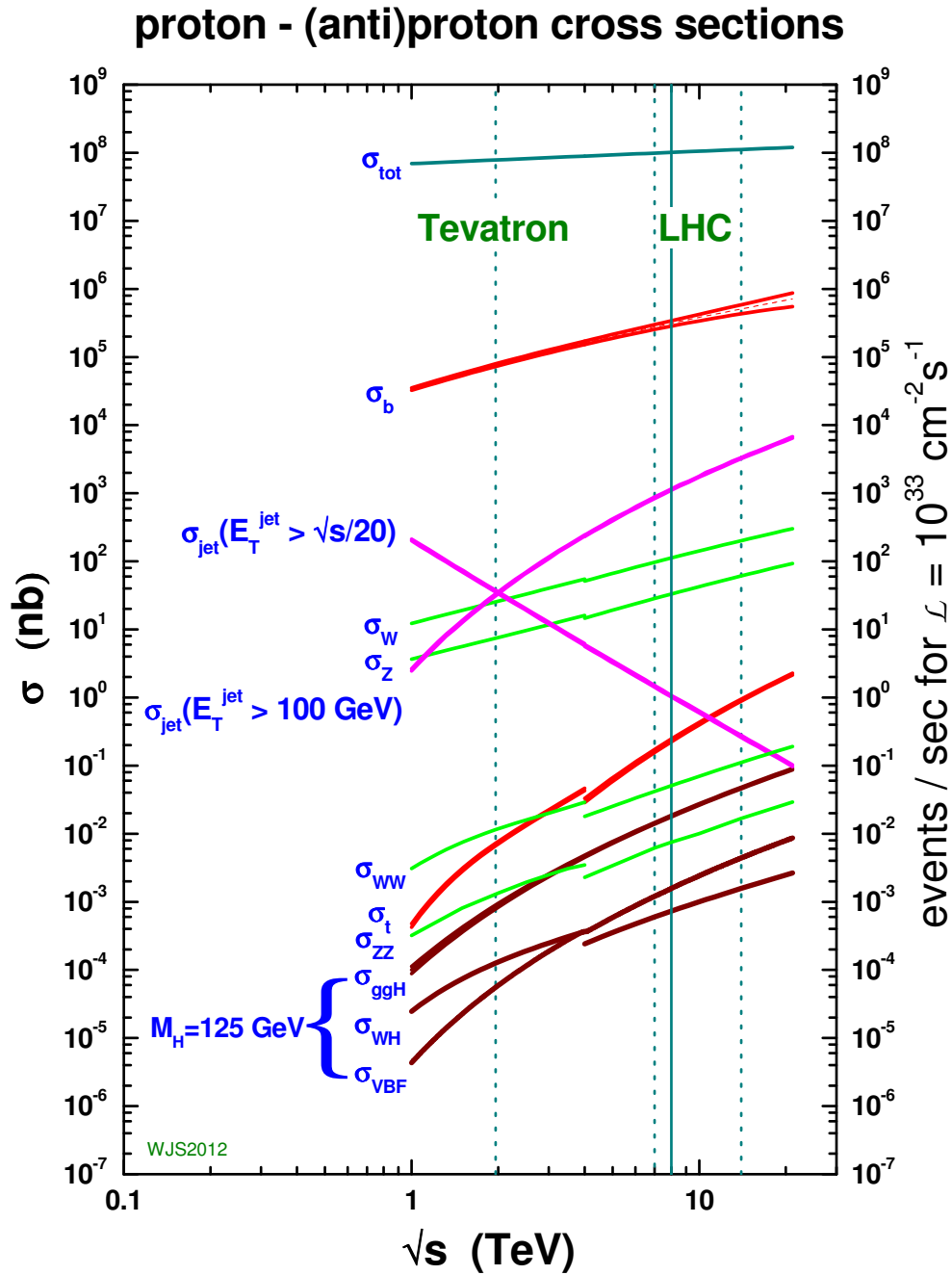


Figure 3.6 – Cross section of SM processes as a function of the pp center-of-mass energy. The vertical lines mark the center-of-mass energies of the Tevatron and the LHC [60].

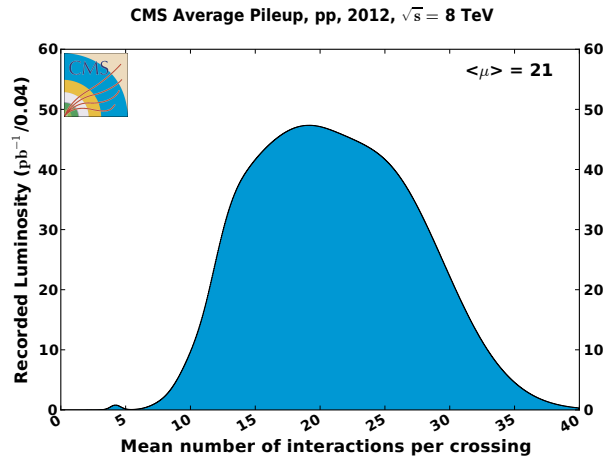


Figure 3.7 – Luminosity recorded as a function of the mean number of interactions per bunch crossing in the CMS experiment in 2012 [59].

radiation (FSR) if it occurs with the decay products of the hard interaction. When quarks and gluons are involved in the ISR and FSR, one speaks also of parton showering.

Hadronisation

If the final state of a hard interaction contains particles that carry a colour charge like e.g. quarks, they have to form new particles in order to become colour neutral. This process is called hadronisation and results in showers of particles that form a cone along the initial particles direction and are called jets. The exception to this is the top quark, which has a lifetime shorter than the timescale at which the hadronisation takes place, and, therefore, decays before it hadronises. If the particles created in ISR and FSR carry a colour charge they hadronise as well. After the hard interaction, the remnants of the two protons are not colour neutral anymore and have to hadronise as well, forming jets that fly along the beam axis.

Additional interactions

Several independent pp interactions take place in a bunch crossing in the IP. The interaction of two protons forms a primary vertex, from which the particles, that were created in the interaction, originate. How many primary vertices are created on average depends on the beam parameters, e.g. how many particles are in a bunch and how small is the focusing area. In 2012 the beam parameters at the LHC were tuned to have on average 20 interactions per bunch crossing. Figure 3.7 shows how much integrated luminosity was recorded in 2012 as a function of the mean number of interactions per bunch crossing, as measured by the CMS experiment. Having many primary vertices per bunch crossing presents a challenge for the event reconstruction, since the particles originating from different primary vertices are superimposed in the detector. Interactions besides the hard interaction that one wants to study are referred to as pileup.

Chapter 4

CMS detector

The CMS detector [55] is one of the two general purpose experiments at the LHC. This chapter presents the general layout of the experiment in Section 4.1. The coordinate system is described in Section 4.2. Section 4.3 details the superconducting solenoid magnet, and the various subdetectors are discussed in Section 4.4. The trigger system, responsible for the selection of events to be kept, is presented in Section 4.5.

4.1 General CMS layout

The CMS detector is located at IP 5 of the LHC ring in a cavern about 100 m underground. Figure 4.1 shows a cutaway drawing of the detector in its 2012 configuration with the subdetectors labeled. The detector has a cylindrical shape with an overall length of 28.7 m, of which 21.6 m make the main cylinder with a diameter of 15 m, and the rest of the length comes from the forward calorimeter. The total mass is 14000 t. The main detector is made of a central barrel section that is closed with an endcap section on both ends to cover most of the 4π solid angle. The central feature of the CMS detector is the superconducting solenoid magnet in the barrel part, producing a magnetic field of 3.8 T. Inside the 6 m diameter bore of the magnet, the silicon tracking system, the electromagnetic calorimeter (ECAL), and the hadronic calorimeter (HCAL) are located. Outside of the solenoid, the muon tracking system is sandwiched in between the layers of the steel return yoke for the magnetic field. The detector was assembled on the surface and then lowered in sections to the underground cavern.

4.2 Coordinate system

The origin of the coordinate system of the detector lies in the center at the nominal collision point. The x -axis points radially inward to the center of the LHC ring and the y -axis points vertically upward. The coordinate system is right-handed and so the z -axis points horizontally along the counter clockwise beam direction. Since the decay

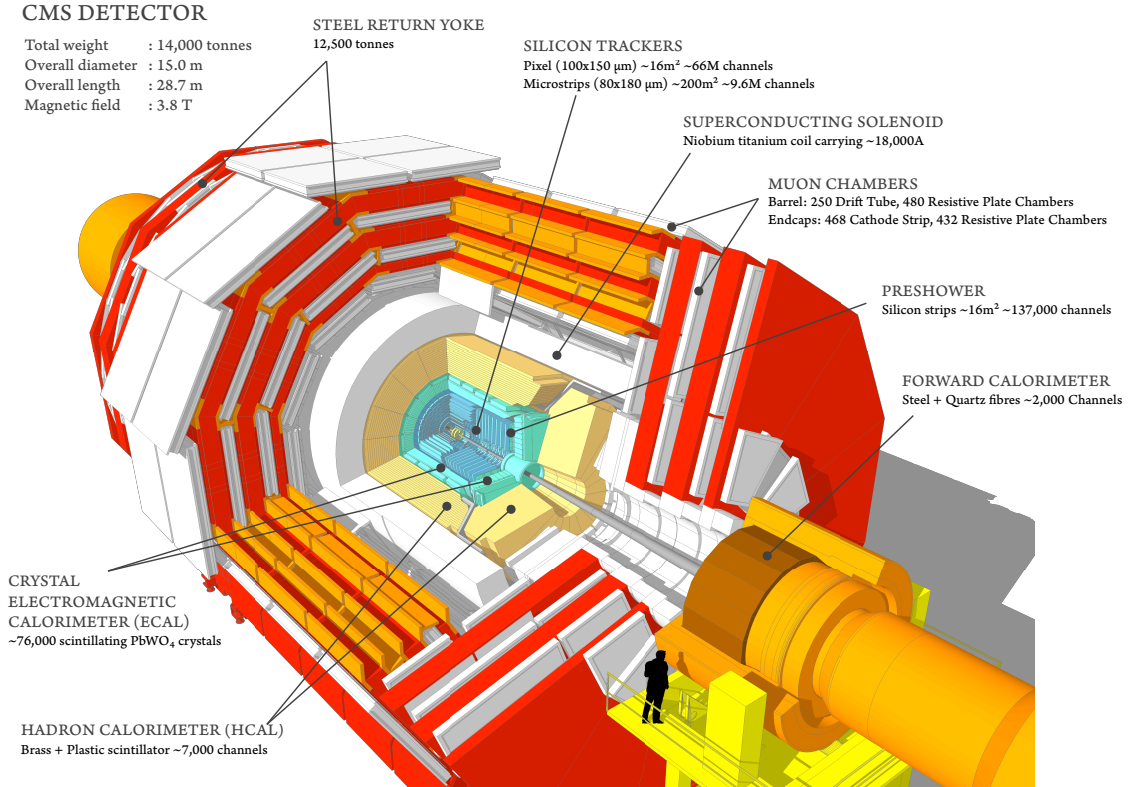


Figure 4.1 – Cutaway view of the CMS detector [61].

products of the collisions will fly outward from the collision point, it makes sense to use spherical coordinates for the description. The azimuthal angle ϕ is defined as the angle measured from the x -axis in the x - y plane. The radial coordinate r is also measured in the x - y plane. Finally, the polar angle θ is measured from the z -axis. Instead of the polar angle the pseudorapidity η , defined as

$$\eta = -\ln \left[\tan \left(\frac{\theta}{2} \right) \right], \quad (4.1)$$

is used, which is zero in the x - y plane and goes to positive and negative infinity, respectively, towards the positive and negative z -axis. The forward regions of the detector mean regions of higher $|\eta|$, close to the z -axis or about $|\eta| > 3$.

4.3 Magnet system

The superconducting magnet of the CMS detector, responsible for the bending of the trajectories of charged particles, has a length of 12.5 m and a diameter of the cold bore of 6.3 m. It is made from a 4-layer winding of NbTi cable reinforced with aluminium, weighting a total of 220 t, and kept at a temperature of 4.5 K with liquid helium. The inner bore of the solenoids cryostat has a diameter of 6 m. The magnet

was designed to produce a field of 4 T but was operated at a lower field of 3.8 T during run 1 of the LHC to prolong its lifetime. The 3.8 T magnetic field is obtained because of an 18 kA current circulation in the cables. The magnet system stores an energy of 2.5 GJ.

Outside of the solenoid, the magnetic field is returned by the steel return yoke with three layers, in between which the muon system is installed. The yoke is made of five rings in the barrel part, of which the central one holds the cryostat for the solenoid, and two endcaps. The magnetic field saturates a total of 1.5 m of iron with a mass of 10 kt. To open the detector, the endcaps and rings can be moved with a hydraulic strand jack system on air pads and grease pads. In Figure 4.2, a simulation of the magnetic field and the field lines within the CMS detector is shown.

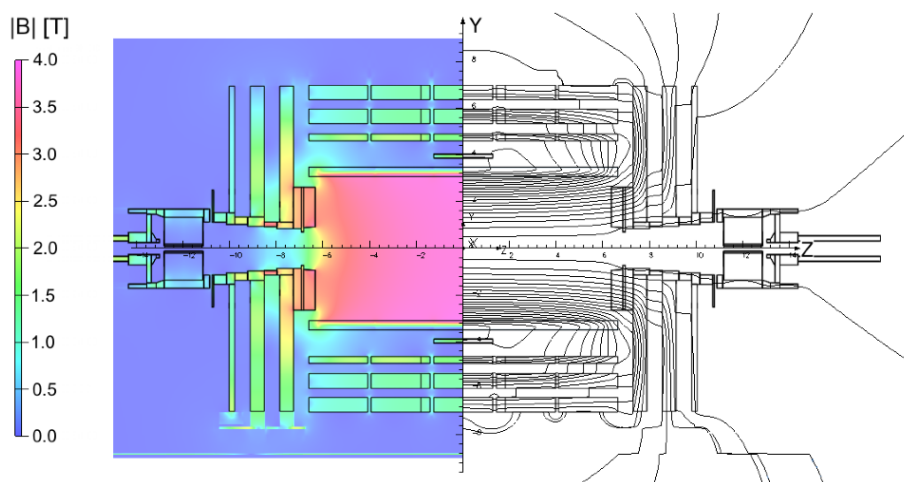


Figure 4.2 – Simulated magnetic field $|B|$ (left) and magnetic field lines (right) in the y - z plane of the CMS detector for a central field of 3.8 T. Between two field lines the magnetic flux changes by 6 Wb [62].

4.4 Subdetectors

The CMS detector is divided in several subdetectors, to measure the signatures of the different particles produced in the collisions. In the barrel part inside the solenoid, there are, from the IP outwards, the silicon pixel tracking detector followed by the silicon strip tracker, the ECAL and the HCAL. The endcaps hold an electromagnetic preshower detector in front of the endcap ECAL and HCAL detectors, that enter in the solenoid volume. Outside of the solenoid are the muon chambers in between the three layers of the steel return yoke of the barrel and endcaps.

4.4.1 Inner tracker

The inner tracking system sits completely in the solenoid volume of the barrel and is schematically shown in Figure 4.3. The aim of the tracking system is to measure the

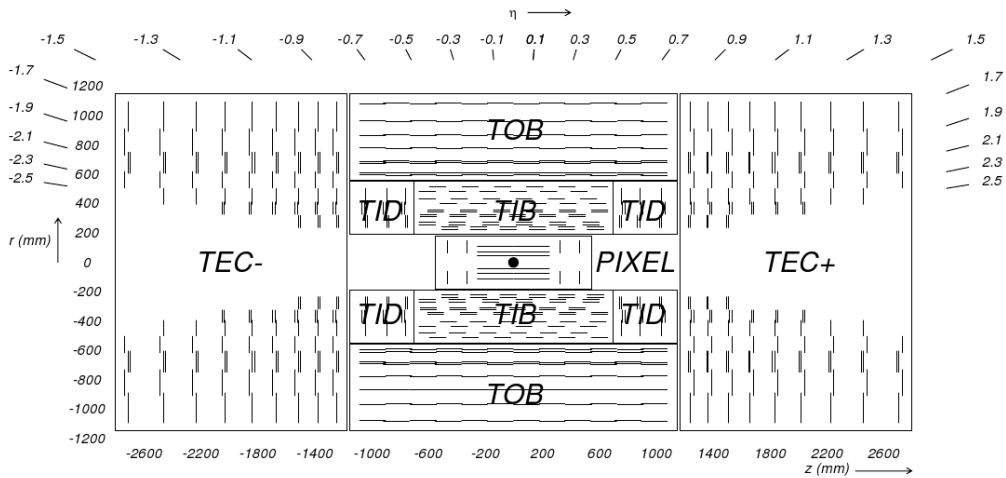


Figure 4.3 – Schematic overview of the inner tracker [55].

trajectories of charged particles, and reconstruct the positions of the primary and secondary vertices. The innermost tracker closest to the IP is made of three layers of silicon pixel detectors named barrel pixel detector (BPIX), ranging from 8.8 cm to 20.4 cm diameters, and two wheels of forward pixel detectors (FPix), covering the pseudorapidity range up to $|\eta| = 2.5$. BPIX and FPix contain 48 million and 18 million pixels, respectively. The pixels have a size of $100 \times 150 \mu\text{m}^2$ in $r-\phi$ and z directions. Because of the magnetic field, a Lorentz drift spreads the charge generated by a hit over more than one pixel. With a charge interpolation from the analog pulse heights, a spacial resolution of 15-20 μm (15 μm) can be achieved in the BPIX (FPix).

The silicon strip tracker is placed outside of the pixel tracker. The barrel part of the strip tracker is divided in the four layers of the tracker inner barrel (TIB) and the six layers of the tracker outer barrel (TOB). Coverage in the forward region is provided by the three tracker inner discs (TID), and the nine disks of the tracker endcap (TEC) on each side. The pitch of the strips varies between 80 μm in the innermost layers of the TIB, and 183 μm in the outer layers of the TOB. In the disks the pitch varies between 97 μm and 184 μm . Some layers of the TIB and the TOB, as well as some disks of the TID and the TEC, have two strip modules mounted back-to-back with an angle of 100 mrad, to provide a measurement of the second coordinate. In total, there are 9.3 million strips on 198 m² active silicon area. The single point resolution that can be achieved varies between 23 μm and 53 μm in $r-\phi$ in the TIB and TOB. The resolution for the z coordinate for the double sided modules is 230 μm and 530 μm for the TIB and the TOB, respectively.

The material budget for the whole inner tracker is shown in Figure 4.4, and lies between 0.4 and 2.0 radiation lengths X_0 .

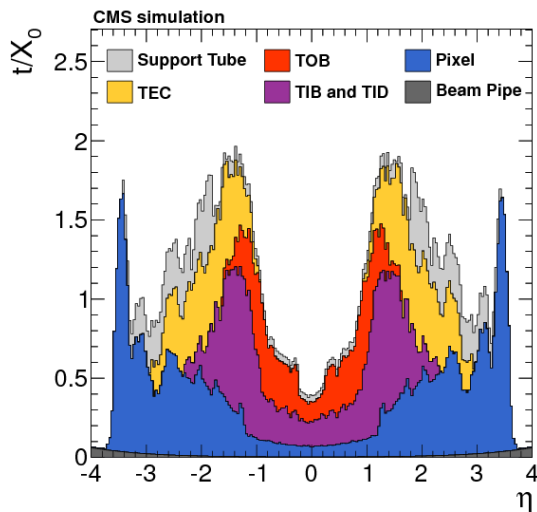


Figure 4.4 – Inner tracker material budget as a function of pseudorapidity in units of radiation length. Shown are the contributions from the different tracker subsystems, the tracker support tube and the beam pipe [63].

4.4.2 Electromagnetic calorimeter

The lead tungstate (PbWO_4) crystal ECAL of CMS is divided in a barrel part (EB) and two endcap parts (EE), one in each endcap of the CMS detector. It consists of 61 200 crystals in the barrel, covering a pseudorapidity range of $|\eta| < 1.479$, and 14 648 crystals in the endcaps, which cover pseudorapidities of $1.479 < |\eta| < 3.0$. In front of the EE there is a preshower detector (ES), covering the pseudorapidity region of $1.653 < |\eta| < 2.6$, to identify photons coming from neutral pion decays. Photons coming from neutral pion decays would be too close together to be separated in the EE detector. The preshower detector is a two layer sampling calorimeter with lead as a radiator, to initiate electromagnetic showers from incoming electrons and photons, and silicon strip detectors to measure the energy and transverse shower profile. The two silicon strip detectors of the ES are orientated such, that the strips of one detector are orthogonal to the strips of the other, to achieve a two dimensional position measurement of the electromagnetic shower with a resolution of typically $300 \mu\text{m}$ at 50 GeV.

A schematic view of the ECAL and the preshower detector is shown in Figure 4.5 and the geometry in a quadrant of CMS is shown in Figure 4.6.

Lead tungstate has a high density of 8.28 g/cm^3 and is optically clear, which, together with its radiation length of 0.89 cm and small Molière radius of 2.0 cm, makes it suitable as a material for the calorimeter. It emits blue-green scintillation light at on average 425 nm. The crystals in the CMS ECAL have the shape of a rod-like truncated pyramid, with three of the long sides polished to maximize light collection and maintain uniformity of the light collection. The front face for the barrel crystals measures $22 \times 22 \text{ mm}^2$ and their length is 23 cm, which is equivalent to 25.8 radiation

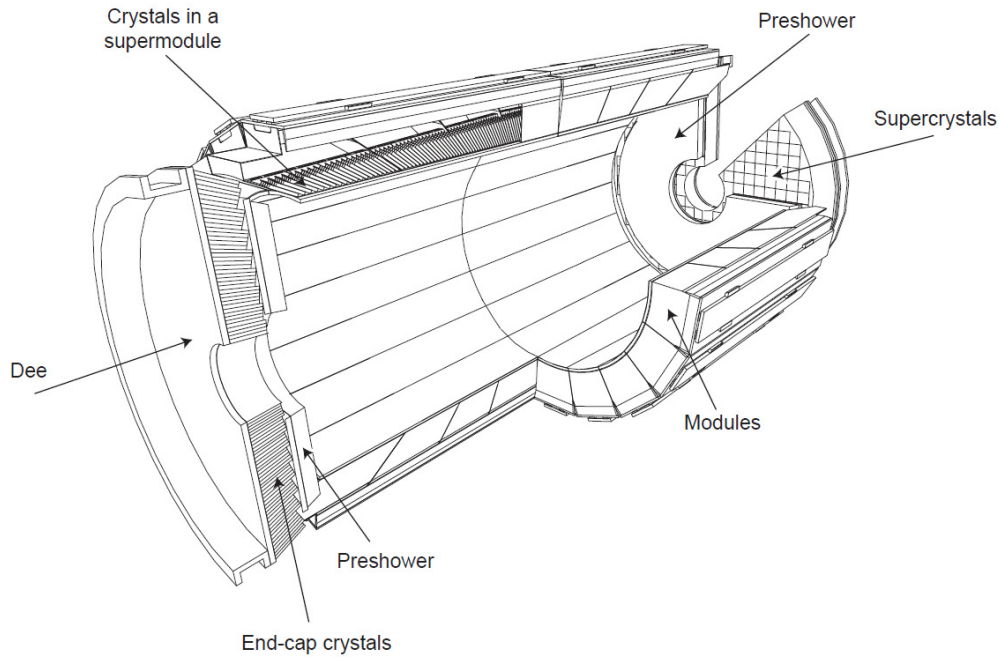


Figure 4.5 – Cutaway overview of the ECAL, with the preshower detector in front of the EE [55].

lengths X_0 . The endcap crystals have a front face of $28.62 \times 28.62 \text{ mm}^2$ and a length of 22 cm, or $24.7 X_0$. In the barrel, light is collected by two avalanche photodiodes (APD), and in the endcap a more radiation hard vacuum phototriode (VPT) is used, that collects on average 4.5 photoelectrons per MeV. The transparency of the material lowers during operation because of the radiation, but recovers partially during time without collisions. Especially in the forward region, the loss of transparency can reach tens of percent. This effect is measured by the injection of laser light in the crystals during the abort gap of the circulating beam, and the loss of transparency is corrected for. Since the crystals have a light yield that depends strongly on the temperature, and also the gain of the APD is temperature dependent, the operating temperature of the ECAL is kept constant at 18°C with a stability better than 0.05°C (0.1°C) in the EB (EE).

The barrel is divided in 360 crystals in the ϕ direction and 85 crystals in each η direction. In the endcaps the crystals are grouped in 5×5 matrices on two separate half-discs. The crystals are installed in a non-pointing geometry facing towards, but not exactly at the center of the detector. This geometry minimises the number of particles that escape through the crack between two crystals. In the transition region between the barrel and the endcap, for $1.479 < |\eta| < 1.566$, the precision is degraded owing to services for the tracker that have to enter between barrel and endcap, and shadow much of the first endcap trigger tower. This defines the gap region, which is usually not considered for analysis. In order to contain the whole electromagnetic shower in the crystals, the two crystals closest to the edge in the EB are also counted

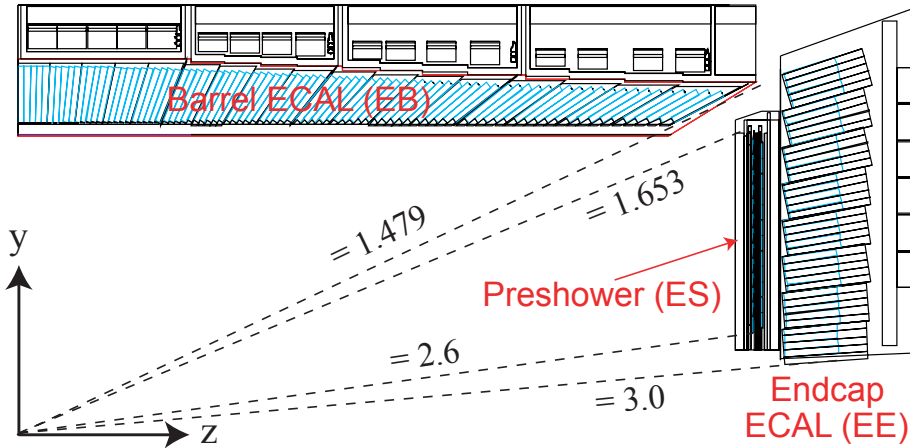


Figure 4.6 – Geometry of the ECAL and the preshower detector, for a quadrant of the CMS detector [64].

to the gap, which limits the EB to $|\eta| < 1.442$. At the forward edge of the preshower detector, a similar margin of two crystals is given for precision measurements, limiting the pseudorapidity range to $|\eta| < 2.5$. This coincides with the range of the inner tracker, which is needed to distinguish electron from photon signatures in the ECAL.

The relative resolution as a function of the energy E of the incoming particle is described by the quadratic sum of a stochastic term, a noise term and a constant term

$$\left(\frac{\sigma(E)}{E(\text{GeV})}\right)^2 = \left(\frac{S}{\sqrt{E(\text{GeV})}}\right)^2 + \left(\frac{N}{E(\text{GeV})}\right)^2 + C^2. \quad (4.2)$$

The parameters were measured in an electron test beam with a 3×3 crystal configuration [65].

Stochastic term ($S = 0.028 \text{ GeV}^{1/2}$)

Processes contributing to the stochastic term are the fluctuations in the lateral shower containment, and the photostatistics, that depends on the number of primary photoelectrons generated and the type of photodetector. Fluctuations of the energy that is deposited in the preshower detector contribute as well in the ECAL regions behind a preshower detector.

Noise term ($N = 0.12 \text{ GeV}$)

The noise term consists of electronic noise, digitisation noise, and noise from additional pp interactions. Pileup noise comes from the fact that the electrical signal from one hit extends over several bunch crossings. If other particles arrive during that time, their signal can overlap with the initial signal, changing the energy measurement.

Constant term ($C = 0.003$)

Contributions to the constant term come from the non-uniformity of the longi-

tudinal light collection of the crystals, the leakage of energy at the rear of the crystals, and from intercalibration errors.

4.4.3 Hadronic calorimeter

The HCAL of CMS is a sampling calorimeter with brass as absorber, plastic scintillator tiles as active medium, and wavelength shifting fibres to transfer the light to the detector. Most of the HCAL is located inside the bore of the cryostat, in a barrel (HB) that extends to $|\eta| < 1.4$, and two endcaps (HE) ranging from $1.3 < |\eta| < 3$. The region between $1.3 < |\eta| < 1.4$ is shared by the HB and HE. Since the absorber depth of the ECAL barrel and the HCAL barrel in the solenoid is not sufficient to contain the complete particle shower, an additional calorimeter (HO) is placed as a tail catcher outside the cryostat, using it as an additional absorber. In the central ring of the CMS barrel, the HO has two layers, one on each side of the first layer of iron of the yoke, while in the other four rings there is only one HO layer. Figure 4.7 shows a quadrant of the HCAL with the segmentation in calorimeter towers. Further away from the interaction point, at ± 11.2 m, the forward calorimeter (HF) extends the pseudorapidity range of the calorimetry up to $|\eta| < 5.2$. As the particle flux in this very forward region is extremely high, a radiation hard technology, using Cherenkov light in quartz fibers, was chosen with steel as an absorber. The HF detector is also used as a real-time monitor for the luminosity on a bunch-by-bunch basis.

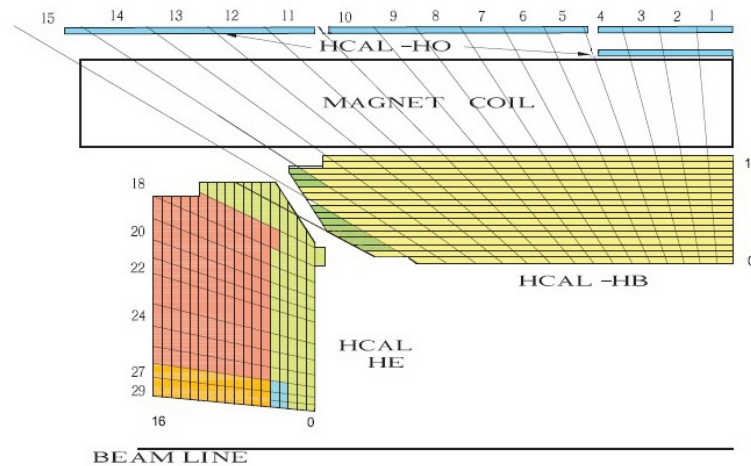


Figure 4.7 – A quadrant of the HCAL with the segmentation in calorimeter towers in the r - z plane [55]. The colours indicate the optical grouping of the readout channels.

4.4.4 Muon system

The CMS muon system is located outside the solenoid magnet in between the steel layers of the barrel and endcap yoke. It uses three different technologies of gaseous

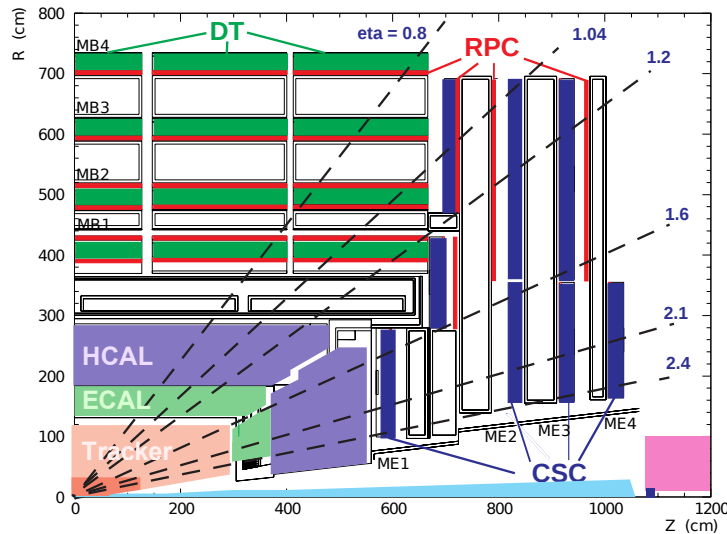


Figure 4.8 – A quadrant of the CMS detector with the different muon subdetectors highlighted [66].

detectors to identify muon tracks. In the barrel, where the muon rate and the neutron induced background are low, a combination of drift tubes (DT) and resistive plate chambers (RPC) is used. In the endcaps, more radiation hard cathode strip chambers (CSC) are installed, in addition to the RPC. Figure 4.8 shows a quadrant of the CMS detector with the different muon systems highlighted. The detectors are grouped in so called stations, in the magnetic field between the layers of the yoke.

Drift tubes

The DTs cover a pseudorapidity range up to $|\eta| < 1.2$. They use a gas mixture of 85% Ar + 15% CO₂, and are made of two or three super layers (SL), each consisting itself of four layers of drift cells. Some SL have their wires aligned parallel to the beam line to give a measurement in the r - ϕ bending plane of the track, while others have wires perpendicular to the beam to provide a measurement of the z -coordinate.

Cathode strip chambers

The coverage of the CSCs installed in the endcaps extends between $0.9 < |\eta| < 2.4$. In this region the rates for muons and background are high, and the magnetic field is non-uniform and large. Each endcap has four stations in which the strips point radially outward, providing a measurement in the r - ϕ plane, and, where the anode wires are almost perpendicular to the strips, allowing for a measurement in pseudorapidity. The chambers use a gas mixture of 40% Ar + 50% CO₂ + 10% CF₄.

Resistive plate chambers

RPCs are installed in the barrel and endcap stations, and extend to a pseudorapidity of $|\eta| < 1.6$. They have a lower spacial granularity than the other

two technologies used, but their better granularity in time makes them suited for triggering purposes, and to identify the bunch crossing to which the muon is assigned. The chambers are built with two gaps, filled with a gas mixture of 96.2% $C_2H_2F_4$ + 3.5% iC_4H_{10} + 0.3% SF_6 + water vapour, and a common read-out strip in between them.

The muon system provides a measurement of muon tracks up to $|\eta| < 2.4$ without gaps, since for a track coming from the interaction point the barrel and endcap muon chambers overlap.

The reconstruction of muon tracks can be done with only the information from the muon chambers in a standalone mode, with only the information from the inner tracker or by performing a global fit of the hits in the inner tracker and in the muon stations. For small muon momenta, the momentum resolution is mainly driven by the inner tracker, whereas at high muon momenta the combination with the muon system gives the best performance. The relative momentum resolution is shown in Figure 4.9 for a muon emitted in the central region and in the forward region.

The whole muon system is aligned using a laser system as well as tracks from cosmic muons, that travel through the detector.

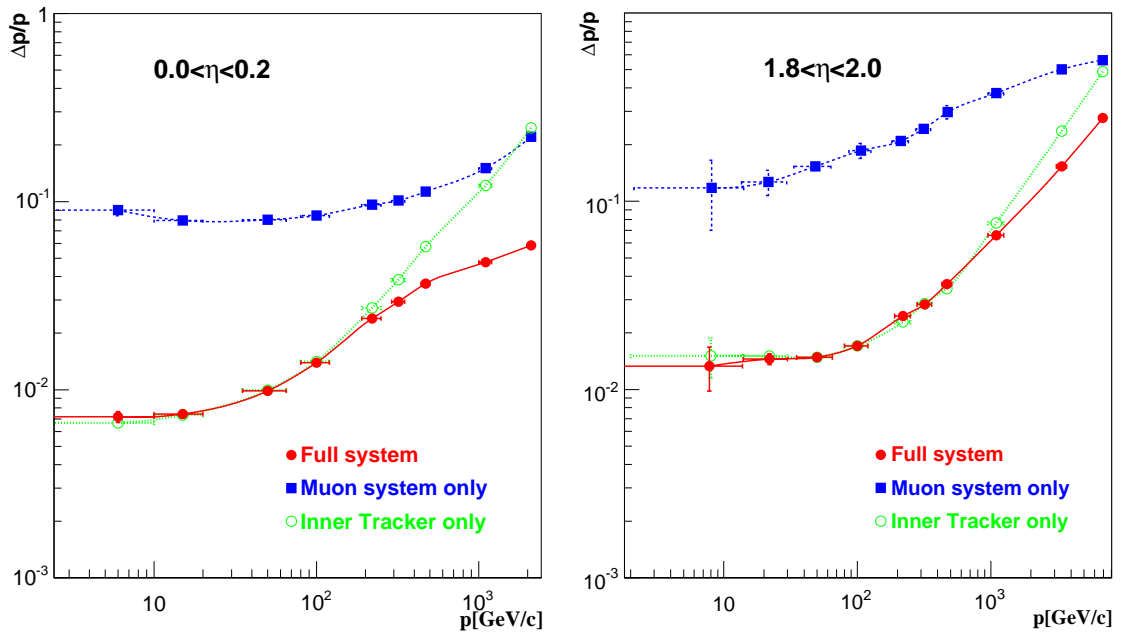


Figure 4.9 – Relative resolution of the muon momentum measurement for the reconstruction with the inner tracker only, the muon system only and for the combination of the inner tracker and the muon system [64].

4.5 Trigger

The LHC is designed to have a bunch spacing of 25 ns, which translates to a bunch crossing rate of 40 MHz. It is impossible to read out all the subdetector channels, to store and to reconstruct the amount of data that are produced at this rate. A sophisticated trigger system selects events of interest. The trigger of CMS is characterised by a two level design. First, a level-1 (L1) trigger, built from custom hardware, reduces the rate to a maximum of 100 kHz. A software high level trigger (HLT), running the CMS reconstruction software on a processor farm, performs higher level reconstruction, and reduces the rate of events selected by the L1 trigger to about 400 Hz, before the events are stored on disk.

4.5.1 Level-1 trigger

The L1 system is built from custom designed, programmable electronics, and is located underground, both in the service and the experiment caverns. Within a time budget of 3.2 μ s, it has to decide if an event is discarded or kept, and transfer this decision back to the subdetectors, which keep the high resolution data in memory in the meantime. The L1 is divided in a muon trigger and a calorimeter trigger, which classify and rank interesting event candidates, reconstructed from low resolution data read out from the subdetectors. The rank of a candidate is determined by energy or momentum, and quality of the data. Based on the input from the muon trigger and the calorimeter trigger, the global trigger calculates the final trigger decision. Up to 128 trigger algorithms can be executed in parallel to generate a decision. The high resolution data from the inner tracker are not used to generate the L1 decision, which means that there is no information about the vertices and no distinction between electrons and photons available at this level.

4.5.2 High level trigger

Once the L1 trigger has accepted an event, the data of this event are transferred from the buffer memory to the surface, where they are reconstructed in the HLT. The HLT is a special part of the CMS software and runs on a farm of several thousand processors. Each processor works on the reconstruction of one event at a time, to get to a trigger decision within on average 100 ms. Since the time budget for one event is much larger than at the L1 trigger, more complicated algorithms, including tracking, can be executed at the HLT. Once an event is accepted, it is stored on disk and fully reconstructed offline at a later time.

The HLT consists of approximately 400 trigger paths, which, starting from the seed of the L1 trigger, look for different objects and signatures in an event. One trigger path is built from reconstruction modules and filter modules. After some parts of the data are reconstructed, a filter module decides if the reconstructed objects pass the thresholds and the next step in reconstruction is started, or if the event is not accepted by the path. In the later case, the execution of the path is stopped and the

following reconstruction steps and filter steps are not performed to save computation time. Following this concept to save computation time, the less computation intense reconstruction steps, e.g. unpacking the data from the ECAL and measuring the energy deposit of a particle there, are done first. The reconstruction steps that take a lot of time, e.g. the tracking, are done at the end of a path for objects that have already passed the previous steps. If an event is not accepted by a path, it can still be accepted by a different path.

If, for some paths with low thresholds, the acceptance rate is too high, they can be prescaled to lower the rate. A prescale value of ten means, for example, that the path is executed only for every tenth event that was accepted by the L1 trigger, and, consequently, the trigger rate for that path is ten times smaller. The prescale value for one trigger path has several predefined levels, depending on the instantaneous luminosity of the LHC machine. During an LHC fill, the instantaneous luminosity decreases. The prescale values can be changed during a CMS run to keep the global trigger rate at an optimal level.

Electron trigger

In the HLT, electron events are reconstructed in several steps. After each reconstruction step, a filter selects the passing candidates. First, the L1 trigger decision is confirmed, and then the energy deposit in the ECAL is reconstructed for the L1 trigger seed. A filter step ensures that the trigger candidate has a small energy deposit in the HCAL tower behind the ECAL energy deposit, and that the shape of the shower in the ECAL passes some quality criteria. Optional steps are the calculation of the isolation of the energy deposits in the calorimeters, to avoid triggering on energy deposits from jets. These steps are identical with the ones for photon triggering. Then the tracker hit information is unpacked, and hits that are compatible with the ECAL energy deposit are searched in the pixel tracker layers. The search window for the hits is defined by the trajectories of a charged particle, under both charge hypothesis, from the beam spot position to the position of the energy deposit in the ECAL. Optionally, the information from the whole tracker is used to reconstruct the track. With the reconstructed track it is possible to apply filters on the difference of reciprocal calorimeter energy deposit and reciprocal track momentum, and compare the track position to the position of the energy deposit in the ECAL. Isolation requirements can also be made on the track.

Muon trigger

The muon trigger algorithm first reconstructs tracks in the muon detector system, taking the information from the L1 trigger as a seed. The trajectories in the muon system are extrapolated to the inner tracker, and hits in the tracker are searched for in a region of interest around the extrapolated trajectory. If hits are found, they serve as seeds for the reconstruction of tracks in the inner tracker, that can be matched to the outer muon tracks. In case a match is found, a global refit of the track parameters

is performed with the outer and inner tracks, which is the input for the final filter on kinematic variables of the track.

Chapter 5

Event reconstruction

The online reconstruction at the HLT only looks at regions of interest to save time and, therefore, does usually not reconstruct the full event. This task is done offline only, for the events that were triggered and stored before. For each event collections of particles are reconstructed, as well as jets, the missing transverse energy E_T^{miss} and the primary vertices. The offline electron reconstruction is described in Section 5.1, while Section 5.2 discusses the offline muon reconstruction. The reconstruction of jets and missing transverse energy is explained in Section 5.3.

5.1 Electron reconstruction

Electrons that are produced at the interaction point fly outwards on a trajectory bent by the magnetic field, leaving hits in the inner tracker and then deposit practically all their energy in clusters of ECAL crystals. As a first step the energy deposit in the ECAL is measured and after that follow the selection of track seeds, the tracking and the association of tracks to ECAL energy deposits. A more detailed description of the electron reconstruction can be found in [63, 67, 68].

5.1.1 Energy measurement

An electron interacting in the ECAL, will deposit in average 94% (97%) of its energy in a matrix of 3×3 (5×5) crystals around the crystal with the largest energy deposit, which is called the seed crystal. However, as shown in Figure 4.4, the material in front of the ECAL has a thickness between 0.4 and 2 radiation lengths. This means that the electrons lose energy because of bremsstrahlung in the material before they reach the ECAL crystals. At $\eta \sim 0$, on average 33% of the electron energy is lost before reaching the ECAL and in the direction of the largest material budget at $|\eta| \sim 1.4$ the loss is on average 86%. This energy, lost via radiated photons, has to be added to the energy deposited by the electron in the ECAL. This is done by the construction of a supercluster (SC) as defined below.

Since the trajectory of the electron is curved in r - ϕ plane, the energy deposit in the ECAL barrel coming from radiated photons is mainly spread in the ϕ direction.

To get the energy in a SC, dominoes of 5×1 crystals in $\eta - \phi$ are produced, extending for 17 crystals (0.3 rad) in the ϕ direction around the seed crystal, which must have a transverse energy of at least 1 GeV. If the energy of the domino exceeds a threshold of 0.1 GeV it is grouped with nearby dominoes to form a cluster. The clusters themselves have to have a seed domino that exceeds an energy of 0.35 GeV to be added to the SC.

In the endcaps, the energy deposit from bremsstrahlung follows a trajectory in η and ϕ . The energy is collected in a 5×5 matrix around a seed crystal that has to exceed a transverse energy threshold of 0.18 GeV. Around the seed crystal the energy is collected in 5×5 matrices along roads in η and ϕ . These roads have a range of ± 0.07 in η and ± 0.3 rad in ϕ around the seed crystal, and the transverse energy of the 5×5 cluster has to exceed 1 GeV if it is to be added to the SC. The energy collected in the preshower detector situated in front of the 5×5 matrix is also added to the SC energy.

As part of the particle flow (PF) reconstruction algorithm [69], which aims at identifying all particles present in an event by combining information from the different subdetectors, PF clusters are defined by adding neighbouring crystals around a seed crystal with $E_{seed} > 230$ MeV in the barrel, and $E_{seed} > 600$ MeV or $E_T^{seed} > 150$ MeV in the endcaps, depending on pseudorapidity. The crystals must have a signal that is 2σ above the electronic noise level of 80 MeV in the barrel and up to 300 MeV in the endcaps.

5.1.2 Track seed selection

Track seeds for electron tracks, which are the starting point for the electron track reconstruction, are built from doublets or triplets of hits in the pixel detector, combined with vertex positions calculated from general charged particle tracks. To select track seeds for electrons two methods are used, called ECAL driven and tracker driven.

For the ECAL driven seeding, one starts from an ECAL SC, with at least 4 GeV of transverse energy and a veto of 0.15 on the ratio of hadronic energy to SC energy. The hadronic energy is calculated from the HCAL towers in a cone of $\Delta R = 0.15$ ¹ around the direction of the electron. Hits in the first pixel layer are searched by back propagating the trajectory from the barycenter of the SC, under both charge assumptions. If a pixel hit is found in a relatively wide window around the prediction from the back propagation, the track is refitted with the position of the hit and a second hit in the next layers is searched for with a narrower window. If the first two hits are matched with the prediction from the SC the seed is selected.

Tracker driven seeds are selected from tracks that were reconstructed with the Kalman filter (KF) algorithm. This algorithm is not suited for electrons that emit bremsstrahlung as the curvature of the track changes in that case. All seeds of KF tracks that match a PF cluster in the ECAL and pass a matching criterion of the ratio between PF cluster energy and track momentum $E/p > 0.65$ (0.75), for track momenta $2 < p < 6$ GeV ($p \geq 6$ GeV), are selected.

¹ $\Delta R = \sqrt{\Delta\eta^2 + \Delta\phi^2}$

The seeds obtained with the ECAL driven method are combined with the tracker driven seeds.

5.1.3 Tracking

The tracking for electrons consists of the track building outward from the seed, for which a combinatorial KF method is used, and the track fitting which uses a Gaussian sum filter (GSF) method in a backward fit. For the track building, starting from the seed, the combinatorial track finding algorithm iteratively adds successive layers, using the Bethe–Heitler (BH) model [70] for the modeling of the electron losses. Owing to the possibility of emitted bremsstrahlung, a very loose requirement between the predicted hits and the found hits is applied. Not more than one layer can have no compatible hit found, and in case of multiple hits found up to five candidate trajectories are generated per layer.

The fractional loss of energy of an electron owing to bremsstrahlung when passing through a material is given by the Bethe–Heitler model. Since the distribution of the energy loss after the BH model is non-Gaussian, fitting the track with the KF algorithm that uses Gaussian distributions does not give good results. The GSF algorithm models the BH energy loss distribution as a sum of six Gaussian distributions with different mean, width and amplitude. After passing through a layer, six new trajectory components are generated with the weight according to the weight of the initial trajectory multiplied by the weight of the Gaussian component in the BH energy loss distribution estimation. To limit the maximal number of trajectories followed to 12, the ones with low weight are dropped or merged if they are similar. Finally, the track parameters obtained have their uncertainty distributed according to the sum of Gaussian distributions from the trajectory components. For the value of the track parameter the mode of the distribution is used.

5.1.4 Track-supercluster matching

In order to build GSF electron candidates, a track has to be associated to a SC. For ECAL driven tracks, the position of the SC is taken as the energy weighted position and the position of the track is the extrapolated position at the SC from the innermost track position. The difference should be smaller than 0.02 in the η direction and 0.15 rad in the ϕ direction. For tracker driven tracks a multivariate technique, using a boosted decision tree (BDT), is used, that combines track observables and SC observables to get a global identification variable. For a successful matching, the track-SC combination should be higher than a threshold of this variable.

5.1.5 Charge and momentum measurement

The charge of the electron candidate is defined by the majority of the charge estimation by three different methods. The first method measures the charge from the curvature of the GSF track. The second estimate comes from the curvature of the KF

track associated to the GSF track if they share at least one innermost hit. The third charge estimation comes from the comparison of the ϕ direction of the SC position as measured from the beam spot with the ϕ direction as measured from the first hit of the GSF track. Simulations predict a charge mis-identification rate of 1.2% for electrons with a transverse momentum $p_T \sim 35$ GeV.

The momentum of the electron candidates is measured by combining the momentum as measured by the tracking procedure with measurements from the ECAL. The weighting of the two measurements depends on the track parameters and the SC parameters. For electrons with high energies the precision of the energy measurement from the ECAL outweighs the one from the tracker, and the transverse momentum of the electron candidate is defined by the energy measurement from the ECAL SC E_{SC} and the polar angle of the track at the interaction point θ_{track} ,

$$p_T = E_{SC} \sin \theta_{track}. \quad (5.1)$$

Since the transverse momentum measurement for high energy electrons is based on the energy measurement from the ECAL, it is in the following called E_T .

5.2 Muon reconstruction

The muon reconstruction [66] is done with data collected by the muon system and the inner tracker. Muon candidates that are reconstructed using only information from the muon system are referred to as standalone muon candidates, while muon candidates reconstructed in the inner tracker outward to the muon stations are called tracker muon candidates. Global muon candidates are muon tracks that are reconstructed from the muon stations inwards to the inner tracker, by first assigning an inner track to a standalone muon track and then refitting the hits from both tracks with a KF algorithm to form the global track.

5.2.1 Standalone muon tracks

The reconstruction of muon tracks in the muon system starts from seeds, generated by the DTs and the CSCs from two track segments within two muon stations. The track parameters obtained from the seed are propagated to the innermost muon layer compatible with the track, and from there a first KF pre-filter is used to find track segments in the outward direction. After the pre-filter, a filtering step, using the same technique, performs a fit in the inward direction, using the individual hits of the track segments and a tighter criterion for the χ^2 of the projected position of a hit and the hit in the detector. For the propagation of the trajectory between the muon stations, energy loss from multiple scattering, ionisation and bremsstrahlung must be taken into account because of the large amount of material between the stations. Parametrisations are used to estimate these effects. A second tracking step is done in a similar way with the hits from the RPCs, with the difference that no track segments are generated in the RPCs but only the hits are used. The inclusion of the

RPC measurements improves the reconstruction of low momentum muons and muons that pass a gap between the DT or CSC detectors. At least two measurements, one of which coming from a DT or CSC station, must be in the fit for the trajectory to be accepted as a muon track. A standalone muon track is obtained by propagating the track from the muon stations to the closest approach to the beam, with a constraint to be close to the nominal interaction point.

5.2.2 Global muon tracks

Global muon tracks are obtained by propagating standalone muon track and tracks from the inner tracker onto a common surface. The tracks in the inner tracker are obtained using a combinatorial track finding algorithm with a KF similar to the method described under 5.1 for the electron tracking. The difference is that since the probability for bremsstrahlung is much lower, the use of a KF is sufficient.

Generally, there are many tracker tracks in a region of interest defined by the propagation of the standalone track towards the interaction point and the momentum of the tracks. The choice of common surface for the matching is defined by the momentum of the tracks, which at lower momentum favours the outermost tracker layer with a hit and at high momentum the innermost muon hit surface. For low p_T tracks the matching is done with the momentum parameters, while for high- p_T tracks the spatial coordinates are used. For each tracker track that matches the standalone track, a global track fit is performed using the hits from both tracks, and the fit with the best χ^2 is chosen as the global muon track candidate.

5.2.3 Tracker muon tracks

Tracker muon tracks are reconstructed by propagating tracks with sufficient (transverse) momentum from the inner tracker, first to the calorimeters and then to the muon system, to match them with signatures in those detectors. If at least one matching segment in a muon station is found, the tracker track is defined as a tracker muon track but no refitting with the muon station hits is done.

5.2.4 Track momentum assignment

The track momentum assigned to the muon candidate is selected from the global and the tracker only fit. If both fits give a $p_T > 200$ GeV and the ratio of charge and momentum agrees with each other within 2σ , the global fit is chosen. In all other cases the tracker muon momentum is selected. The p_T resolution in the p_T range between 20 GeV and 100 GeV is found to be better than 2% for muons in the barrel and 6% for muons in the endcaps [66].

5.2.5 High transverse momentum muon tracks

For muons with a very high transverse momentum of hundreds of GeV the energy loss because of bremsstrahlung and subsequent electromagnetic showers in the steel of the yoke is high. This lowers the performance of the fitting because of the change of the trajectory of the muon and owing to the additional hits in the muon chambers coming from the showers. To chose the best momentum assignment for high- p_T muons, two additional fits are performed with special aim at the showering muon events.

Tracker-Plus-First-Muon-Station (TPFMS) fit

As the name suggests, this is a refit of the global muon track with all tracker hits and the first muon station hit. This fit is less sensitive to muons showering after the first muon station.

Picky fit

Starting from the global muon fit, in chambers with high hit occupancy, only hits that have a good compatibility with the trajectory are kept. This reduces the sensitivity to chambers with showers, while keeping hits from chambers that are not affected by the shower.

The track parameters are chosen, for every muon, according to an algorithm called *Tune P*, which picks the best fit from the TPFMS and the picky fits, or the tracker muon track fit only. High- p_T muons get their track parameters assigned by one of the two high- p_T refits in most of the cases. Up to transverse momenta of 1 TeV the relative resolution remains better than 10% as measured from cosmic muons [66].

5.3 Jet and missing transverse energy reconstruction

5.3.1 Jet reconstruction

The cross section to produce jets is by far the largest in pp collisions in the LHC, and they represent background for many analysis, but are also used to perform analysis. A jet is reconstructed using the anti-kt jet clustering algorithm [71] with a cone size parameter of $R = 0.5$, or in some cases $R = 0.7$, in the $y - \phi$ space, where the rapidity of a jet is defined by its energy and momentum as

$$y = \frac{1}{2} \ln \left(\frac{E + p_z}{E - p_z} \right). \quad (5.2)$$

Three different types of jets are reconstructed, which depend on the way information from the subdetectors is combined [72].

- Calorimeter jets use information from the calorimeter towers in the HCAL and the corresponding ECAL crystals.

- Jet-plus-track (JPT) jets use the information from the tracker in addition to the calorimeter jets, to add tracks that are bent out of the cone defined by the calorimeter jets. The calorimeter jets parameters are corrected by taking into account these additional tracks.
- Particle flow jets are generated by the clustering of PF candidate particles and taking the vectorial sum of their four momenta.

The energy of the jet measured with the jet algorithm has to be corrected for pileup and other contributions to match the true energy of the jet. An uncertainty smaller than 3% has been found on the jet energy scale for jets with $|\eta| < 3$ and $p_T > 50$ GeV. The jet energy resolution (JER) is obtained by studying the energy resolution of jet energy scale corrected jets in data and simulation, using dijet and γ +jet events. The resolution is found to be about 10% for central PF jets with $|\eta| < 0.5$ and $p_T > 100$ GeV. Jets that originate from b-quarks are identified with several different techniques, referred to as b-tagging. b-tag methods make use e.g. of the small distance that a B meson, produced by the hadronisation of a b-quark, travels before it decays, which leads to a secondary vertex from which tracks originate.

5.3.2 Missing transverse energy reconstruction

Processes that involve neutrinos or hypothetical weakly interacting particles that escape the detector undetected show an imbalance of the total transverse momentum of all visible particles. The negative vectorial sum of the transverse momentum of all visible particles is referred to as missing transverse energy (E_T^{miss}) and can give information about the undetected particles. Three different methods of calculating the E_T^{miss} are used [73].

- Calo E_T^{miss} uses the energy deposits above the noise level in the calorimeters and its directions. Muons are included by taking into account their transverse momentum and not their small energy deposit in the calorimeters.
- TC E_T^{miss} uses the information from the calorimeters as Calo E_T^{miss} and adds information from the tracks in the inner tracker, removing the expected energy deposit of the tracks from the calorimeter energy.
- PF E_T^{miss} is defined as the negative vectorial sum of all PF candidate particles transverse momenta.

The E_T^{miss} is improved by including the corrected jet energies. Pileup interactions are like minimum bias events, which are average collision events dominated by low p_T QCD processes and triggered by minimal hadronic activity in the detector. Such interactions should lead to a value of zero for the E_T^{miss} , with the vectorial sum of the transverse momenta of charged particles equal to the one of neutral particles. However, because of non-linearities in the calorimeters and thresholds for the minimum energy, E_T^{miss} arises and points on average in the direction of the vectorial sum of the

transverse momenta of neutral particles. This effect is corrected by estimating the E_T^{miss} introduced by pileup events from the vectorial sum of the transverse momenta of charged particles that originate from pileup vertices.

Chapter 6

Search for new physics in dielectron events

In this chapter, the search for new heavy narrow resonances with spin 1 and spin 2, using the invariant mass spectrum of selected dielectrons from pp collisions at a center-of-mass energy $\sqrt{s} = 8$ TeV with the CMS detector, is described. As already discussed in Chapter 2, there exist many models beyond the SM that predict new heavy resonances at the TeV scale. The analysis presented here is not designed for a specific model, but to be as general as possible, so that the results can be interpreted in the context of many different models that predict spin 1 or spin 2 particles. Three common models have been chosen to act as benchmark interpretations. As spin 1 particles the Z'_{SSM} , from the sequential standard model (SSM) with SM-like couplings [23], and the Z'_ψ from grand unified theories with the E_6 gauge group [24, 25] are considered. As spin 2 particles RS gravitons, which are KK excitations in the Randall–Sundrum extra dimensional model [26, 27], are used. In the analysis the new resonance is denoted by a generic Z' particle.

The signal searched for has an electron and a positron in the final state, which would lead to a very clean signature in the detector. Furthermore, as there are no neutrinos involved that lead to missing energy, the invariant mass of an electron-positron pair would peak at the new resonance mass value, giving a clear signal over the background, which is smoothly falling in the high mass region above the Z peak.

The analysis has been submitted to JHEP for publication [1], in which also searches for non-resonant new physics from ADD models are included. Previous results have been published by the CMS collaboration on data at $\sqrt{s} = 7$ TeV collected in 2010 [74], on data at $\sqrt{s} = 7$ TeV recorded in 2011 [36], as well as on a combination of 2011 data at $\sqrt{s} = 7$ TeV and early 2012 data at $\sqrt{s} = 8$ TeV [37]. A similar search has been performed by the ATLAS experiment as well, at pp collision energies of 7 TeV [35] and 8 TeV [38]. At the Tevatron, the CDF and D0 experiments have searched for new massive resonances produced in $p\bar{p}$ collisions with a center-of-mass energy of $\sqrt{s} = 1.96$ TeV [31–34]. A list of the current limits for various Z' models is given in Table 2.4.

The event selection is described in Section 6.1, the measurement of the electron

energy scale factor at the Z peak is explained in Section 6.2 and the high mass resolution estimation in Section 6.3. The relevant backgrounds and the methods to estimate them are introduced in Section 6.4, followed by the detailed description of the $e\mu$ method used to check the prompt lepton background in Section 6.5. In Section 6.6 the invariant mass spectra are shown, and the statistical interpretation is presented in Section 6.7.

6.1 Event selection

The production of new heavy resonances decaying to an electron pair is characterised by a final state with two high energy electrons. Thus, the selection of the electron candidates must be optimised for high energies. It is also desirable to extend the energy range of the selected electron candidates to low values in order to reconstruct the Z resonance peak in the dielectron spectrum, which is useful for the normalisation of the background samples. Since the expected signal is a narrow peak over a rapidly falling, continuous background, already a few events are enough to discover new physics. Thus, the philosophy of the event selection is to have a very high efficiency of the trigger and the electron candidate selection, in order to not lose events, but keep a good purity at the same time. As the priority of the selection lies on the efficiency, it is essential that the background processes are well understood.

6.1.1 Datasets

The data recorded by CMS are stored in several different datasets. All events that are accepted by a specific set of high level triggers enter one specific dataset, so that the choice of a trigger for the analysis defines which dataset has to be used. The datasets contain a range of CMS runs that were collected in a run period, which is typically the period between two LHC technical stops. The triggers used stay the same during one run period but can change in between two run periods, so that a change of dataset can be necessary to use a specific trigger. During 2012 there have been four run periods labeled from A to D. The datasets used in the analysis are listed in Table 6.1, together with the run range and the part of the analysis where the dataset has been used. The datasets from the 22Jan2013 re-reconstruction campaign with the 5.3.7.patch5/6 versions of the CMS software [75] were used for the analysis, starting from run 190456 and ending with run 208686. Only runs that satisfy the data quality criteria were used in the analysis. These runs are listed in a file in the JSON format. The analysed data correspond to an integrated luminosity of $19.7 \pm 0.5 \text{ fb}^{-1}$ [76], from pp collisions at 8 TeV. The integrated luminosity is measured by counting pixel clusters in the pixel tracker for zero-bias events, that is for events that only require two bunches colliding in the IP. The uncertainty on the luminosity measurement consists of a 2.5% systematic uncertainty, added in quadrature to a 0.5% statistical uncertainty, to arrive at the combined uncertainty of 2.6%.

Table 6.1 – Reconstructed datasets used in the analysis together with the run range of the dataset.

Dataset	Run range	Usage
/DoublePhotonHighPt/Run2012B-22Jan2013-v1/AOD	193834 - 196531	main analysis
/DoublePhotonHighPt/Run2012C-22Jan2013-v1/AOD	198022 - 203742	
/DoublePhotonHighPt/Run2012D-22Jan2013-v1/AOD	203777 - 208686	
/DoubleElectron/Run2012A-22Jan2013-v1/AOD	190456 - 193621	trigger studies electron scale
/DoubleElectron/Run2012B-22Jan2013-v1/AOD	193834 - 196531	
/DoubleElectron/Run2012C-22Jan2013-v1/AOD	198022 - 203742	
/DoubleElectron/Run2012D-22Jan2013-v1/AOD	203777 - 208686	
/MuEG/Run2012A-22Jan2013-v1/AOD	190456 - 193621	$e\mu$ method
/MuEG/Run2012B-22Jan2013-v1/AOD	193834 - 196531	
/MuEG/Run2012C-22Jan2013-v1/AOD	198022 - 203742	
/MuEG/Run2012D-22Jan2013-v1/AOD	203777 - 208686	
/Photon/Run2012A-22Jan2013-v1/AOD	190456 - 193621	main analysis & fake rate
/SinglePhoton/Run2012B-22Jan2013-v1/AOD	193834 - 196531	
/SinglePhoton/Run2012C-22Jan2013-v1/AOD	198022 - 203742	fake rate
/SinglePhotonParked/Run2012D-22Jan2013-v1/AOD	203777 - 208686	

6.1.2 Simulated samples

Several Monte Carlo (MC) simulation samples were used for the background and signal estimations. The samples were generated using either the MADGRAPH5 [77], POWHEG [78, 79] or PYTHIA6 [80] generators, with the CT10 [12] or CTEQ6 [18] parton distribution functions. MADGRAPH5 and PYTHIA6 are leading order (LO) generators, and POWHEG is a next-to-leading-order (NLO) generator. Since MADGRAPH5 and POWHEG only generate the hard process PYTHIA6 is used for the parton shower, hadronisation and decay to the final state. In order to better model the decay of the τ -lepton, the TAUOLA [81] package is used for $t\bar{t}$, single top and diboson samples.

The particles that are generated by the event generators are then propagated through the detector with the GEANT4 [82] program, which simulates the detector response to these particles. Using a detailed model of the CMS detector including the geometries and materials, GEANT4 generates the hits and particle showers that would happen in the subdetectors and subsequently simulates the response of the detector electronics to these signals.

After the simulation by GEANT4, the data format of a simulated event is the same as for the data, so that, from this point onward, the same software can be used for the reconstruction of data and simulation. Pileup is included in the samples by mixing randomly chosen minimum bias events with the simulated events to achieve the expected PU distribution.

Table 6.2 lists the simulated SM samples used for the analysis, together with the cross sections, and Table 6.3 lists the signal samples. For the DY samples with $M_{\text{ij}} > 20$ GeV and for the W+jets sample, the respective next-to-next-to-leading-order (NNLO) cross sections, calculated with FEWZ [83], are used. The cross sections of the high mass DY samples are scaled to NNLO with the K-factor obtained from the NNLO-to-NLO difference of the DY sample with $M_{\text{ij}} > 20$ GeV. For the inclusive $t\bar{t}$ sample the NNLO cross section from [84] is used, and the high $M_{t\bar{t}}$ samples are

scaled to NNLO with the K-factor from the NNLO-to-NLO ratio of the inclusive $t\bar{t}$ sample. The NLO cross sections for the diboson samples were calculated with the MCFM [85] calculator, and the DIPHOX [86] calculator was used to obtain the $\gamma + \text{jets}$ NLO K-factor.

6.1.3 Trigger

As already indicated in Section 6.1.1, several different triggers are used for the analysis. Table 6.4 lists the used triggers with their respective L1 seeds and the area of usage. Most of the triggers are seeded by a L1 trigger that requires a localised deposit in the ECAL above a certain E_T threshold. One exception is the double electron trigger in the last row of Table 6.4, which requires two localised deposits in the ECAL with $E_T > 13 \text{ GeV}$ and $E_T > 7 \text{ GeV}$, respectively. The other exception is the muon-photon trigger, which needs a L1 muon candidate with $p_T > 3.5 \text{ GeV}$ together with a localised energy deposit in the ECAL of $E_T > 12 \text{ GeV}$. These two triggers are explained in detail in Section 6.2.1 and Section 6.5.1, respectively.

The main signal trigger requires two electron candidates with requirements as listed in Table 6.5. The trigger uses a single electron L1 seed, which means that the second electron candidate is not required to pass the L1 trigger. The electron candidates must have pixel hits matching to the SC, pass loose calorimeter identification (ID) requirements and very loose matching requirements between the SC and the GSF track.

Trigger efficiency

The tag-and-probe method [87–89] is used to measure efficiencies using pair produced objects, e.g. the electrons from the DY process. A tight selection is applied to one object, called the tag, and the efficiency is then measured with a second object, called the probe, which is selected with a loose selection. The efficiency is calculated as

$$\epsilon = \frac{N_{\text{pass}}}{N_{\text{tot}}}, \quad (6.1)$$

where N_{pass} is the number of probes passing the selection of which the efficiency should be measured, and N_{tot} is the number of all probes. The tag does not enter the efficiency calculation, but ensures that a sample of high purity is selected. For the efficiency measurements presented here, electrons from the Z resonance are used.

The efficiency for the double electron signal trigger consists of a product of three terms: the efficiency of the L1 trigger (SingleEG22), the online electron ID efficiency of the trigger and the turn on curve with respect to the supercluster E_T . The three terms are described below.

1. Since the double electron signal trigger is seeded by a L1 trigger requiring only one candidate, a tag-and-probe method can be used to determine the L1 efficiency. The tag is required to pass the L1 trigger and the last filter of the signal trigger, which is the loose matching of the SC to the GSF track

Table 6.2 – Simulated SM process samples used with the corresponding cross sections. The first block lists the samples of the irreducible DY background and the second block other DY samples. The third block lists processes involving top quarks and electroweak processes are listed in the fourth block. The last block lists γ +jet samples.

Process	Criteria	Generator	PDF	Cross section (pb)
DY $\rightarrow e^-e^+$	$M_{e^-e^+} > 20$ GeV	POWHEG + PYTHIA6	CT10	1915 (NNLO)
DY $\rightarrow e^-e^+$	$M_{e^-e^+} > 120$ GeV	POWHEG + PYTHIA6	CT10	12.16 (NLO \times 1.024)
DY $\rightarrow e^-e^+$	$M_{e^-e^+} > 200$ GeV	POWHEG + PYTHIA6	CT10	1.517 (NLO \times 1.024)
DY $\rightarrow e^-e^+$	$M_{e^-e^+} > 400$ GeV	POWHEG + PYTHIA6	CT10	0.1112 (NLO \times 1.024)
DY $\rightarrow e^-e^+$	$M_{e^-e^+} > 500$ GeV	POWHEG + PYTHIA6	CT10	0.04515 (NLO \times 1.024)
DY $\rightarrow e^-e^+$	$M_{e^-e^+} > 700$ GeV	POWHEG + PYTHIA6	CT10	0.01048 (NLO \times 1.024)
DY $\rightarrow e^-e^+$	$M_{e^-e^+} > 800$ GeV	POWHEG + PYTHIA6	CT10	0.005615 (NLO \times 1.024)
DY $\rightarrow e^-e^+$	$M_{e^-e^+} > 1000$ GeV	POWHEG + PYTHIA6	CT10	0.001837 (NLO \times 1.024)
DY $\rightarrow e^-e^+$	$M_{e^-e^+} > 1500$ GeV	POWHEG + PYTHIA6	CT10	1.744×10^{-4} (NLO \times 1.024)
DY $\rightarrow e^-e^+$	$M_{e^-e^+} > 2000$ GeV	POWHEG + PYTHIA6	CT10	2.259×10^{-5} (NLO \times 1.024)
DY $\rightarrow \mu^-\mu^+$	$M_{\mu^-\mu^+} > 20$ GeV	POWHEG + PYTHIA6	CT10	1915 (NNLO)
DY $\rightarrow \tau^-\tau^+$	$M_{\tau^-\tau^+} > 20$ GeV	POWHEG + PYTHIA6	CT10	1915 (NNLO)
t \bar{t}	inclusive	POWHEG-TAUOLA	CT10	245.8 (NNLO)
t \bar{t}	$700 < M_{t\bar{t}} < 1000$ GeV	POWHEG-TAUOLA	CT10	18.2 (NLO \times 1.17)
t \bar{t}	$M_{t\bar{t}} \geq 1000$ GeV	POWHEG-TAUOLA	CT10	3.4 (NLO \times 1.17)
tW	inclusive	POWHEG-TAUOLA	CTEQ6M	11.1 (NLO)
t \bar{t} W	inclusive	POWHEG-TAUOLA	CTEQ6M	11.1 (NLO)
WW	inclusive	PYTHIA-TAUOLA	CTEQ6L1	54.8 (NLO)
WZ	inclusive	PYTHIA-TAUOLA	CTEQ6L1	33.2 (NLO)
ZZ	inclusive	PYTHIA-TAUOLA	CTEQ6L1	17.7 (NLO)
W + jets $\rightarrow l\nu$	inclusive	MADGRAPH5	CTEQ6L1	36257 (NNLO)
W + jets $\rightarrow l\nu$	$50 < p_T^W < 70$	MADGRAPH5	CTEQ6L1	967.5 (NNLO)
W + jets $\rightarrow l\nu$	$70 < p_T^W < 100$	MADGRAPH5	CTEQ6L1	511.5 (NNLO)
W + jets $\rightarrow l\nu$	$p_T^W \geq 100$	MADGRAPH5	CTEQ6L1	273.0 (NNLO)
γ + jets	$15 < p_T < 30$ GeV	PYTHIA6	CTEQ6L1	260081 (LO \times 1.3)
γ + jets	$30 < p_T < 50$ GeV	PYTHIA6	CTEQ6L1	25912 (LO \times 1.3)
γ + jets	$50 < p_T < 80$ GeV	PYTHIA6	CTEQ6L1	4319.0 (LO \times 1.3)
γ + jets	$80 < p_T < 120$ GeV	PYTHIA6	CTEQ6L1	725.8 (LO \times 1.3)
γ + jets	$120 < p_T < 170$ GeV	PYTHIA6	CTEQ6L1	140.4 (LO \times 1.3)
γ + jets	$170 < p_T < 300$ GeV	PYTHIA6	CTEQ6L1	39.16 (LO \times 1.3)
γ + jets	$300 < p_T < 470$ GeV	PYTHIA6	CTEQ6L1	2.781 (LO \times 1.3)
γ + jets	$470 < p_T < 800$ GeV	PYTHIA6	CTEQ6L1	0.2755 (LO \times 1.3)
γ + jets	$800 < p_T < 1400$ GeV	PYTHIA6	CTEQ6L1	0.009201 (LO \times 1.3)
γ + jets	$1400 < p_T < 1800$ GeV	PYTHIA6	CTEQ6L1	5.863×10^{-5} (LO \times 1.3)
γ + jets	$p_T \geq 1800$ GeV	PYTHIA6	CTEQ6L1	2.427×10^{-6} (LO \times 1.3)

Table 6.3 – Simulated signal samples used with the corresponding cross sections at the LO. The first block lists the spin 1 Z' samples. The second block lists the spin 2 Randall–Sundrum graviton samples.

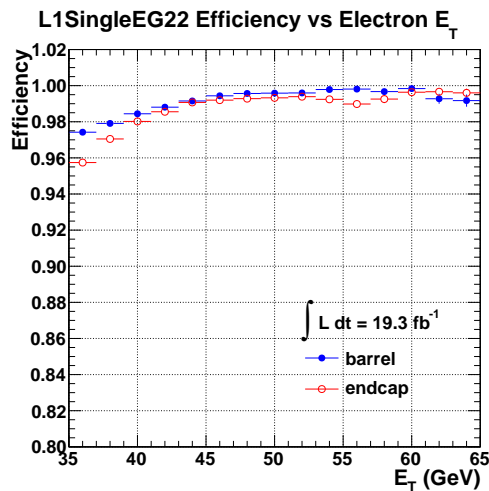
Signal process	Resonance mass	Generator	PDF	Cross section (pb)
$Z'_{\psi} \rightarrow e^{-}e^{+}$	$M_{Z'_{\psi}} = 750 \text{ GeV}$	PYTHIA6	CTEQ6L1	0.1328 (LO)
$Z'_{\psi} \rightarrow e^{-}e^{+}$	$M_{Z'_{\psi}} = 1000 \text{ GeV}$	PYTHIA6	CTEQ6L1	0.03933 (LO)
$Z'_{\psi} \rightarrow e^{-}e^{+}$	$M_{Z'_{\psi}} = 1250 \text{ GeV}$	PYTHIA6	CTEQ6L1	0.01196 (LO)
$Z'_{\psi} \rightarrow e^{-}e^{+}$	$M_{Z'_{\psi}} = 1500 \text{ GeV}$	PYTHIA6	CTEQ6L1	0.00437 (LO)
$Z'_{\psi} \rightarrow e^{-}e^{+}$	$M_{Z'_{\psi}} = 1750 \text{ GeV}$	PYTHIA6	CTEQ6L1	0.00168 (LO)
$Z'_{\psi} \rightarrow e^{-}e^{+}$	$M_{Z'_{\psi}} = 2000 \text{ GeV}$	PYTHIA6	CTEQ6L1	7.029×10^{-4} (LO)
$Z'_{\psi} \rightarrow e^{-}e^{+}$	$M_{Z'_{\psi}} = 2250 \text{ GeV}$	PYTHIA6	CTEQ6L1	2.895×10^{-4} (LO)
$Z'_{\psi} \rightarrow e^{-}e^{+}$	$M_{Z'_{\psi}} = 3000 \text{ GeV}$	PYTHIA6	CTEQ6L1	2.666×10^{-5} (LO)
$Z'_{SSM} \rightarrow e^{-}e^{+}$	$M_{Z'_{SSM}} = 2250 \text{ GeV}$	PYTHIA6	CTEQ6L1	0.001302 (LO)
$G_{RS} \rightarrow e^{-}e^{+}$	$M_{G_{RS}} = 250 \text{ GeV}$	PYTHIA6	CTEQ6L1	1.11 (LO)
$G_{RS} \rightarrow e^{-}e^{+}$	$M_{G_{RS}} = 500 \text{ GeV}$	PYTHIA6	CTEQ6L1	0.04303 (LO)
$G_{RS} \rightarrow e^{-}e^{+}$	$M_{G_{RS}} = 750 \text{ GeV}$	PYTHIA6	CTEQ6L1	0.005059 (LO)
$G_{RS} \rightarrow e^{-}e^{+}$	$M_{G_{RS}} = 1000 \text{ GeV}$	PYTHIA6	CTEQ6L1	9.653×10^{-4} (LO)
$G_{RS} \rightarrow e^{-}e^{+}$	$M_{G_{RS}} = 1250 \text{ GeV}$	PYTHIA6	CTEQ6L1	2.478×10^{-4} (LO)
$G_{RS} \rightarrow e^{-}e^{+}$	$M_{G_{RS}} = 1500 \text{ GeV}$	PYTHIA6	CTEQ6L1	7.303×10^{-5} (LO)
$G_{RS} \rightarrow e^{-}e^{+}$	$M_{G_{RS}} = 1750 \text{ GeV}$	PYTHIA6	CTEQ6L1	2.584×10^{-5} (LO)
$G_{RS} \rightarrow e^{-}e^{+}$	$M_{G_{RS}} = 2000 \text{ GeV}$	PYTHIA6	CTEQ6L1	9.288×10^{-6} (LO)
$G_{RS} \rightarrow e^{-}e^{+}$	$M_{G_{RS}} = 2250 \text{ GeV}$	PYTHIA6	CTEQ6L1	3.458×10^{-6} (LO)
$G_{RS} \rightarrow e^{-}e^{+}$	$M_{G_{RS}} = 3000 \text{ GeV}$	PYTHIA6	CTEQ6L1	2.368×10^{-7} (LO)

Table 6.4 – The triggers used by the analysis.

Trigger	L1 seed	Usage
HLT_DoubleEle33_CaloIdL_GsfTrkIdVL	L1_SingleEG22	Signal, tag-and-probe
HLT_Ele32_X_SC17_Mass50 with X = CaloIdT_CaloIsoT_TrkIdT_TrkIsoT	L1_SingleEG20 or L1_SingleEG22	tag-and-probe
HLT_DoublePhoton70	L1_SingleEG30	tag-and-probe, monitoring
HLT_Mu22_Photon22_CaloIdL	L1_Mu3p5_EG12	$e\mu$ method
HLT_PhotonY_CaloIdVL, with Y = 30, 50, 75, 90	L1_SingleEG20 or L1_SingleEG22	Fake-rate
HLT_Photon135	L1_SingleEG30	Fake-rate
HLT_Photon150	L1_SingleEG30	Fake-rate, sig. backup
HLT_Ele17_Z_Ele8_Z with Z = CaloIdL_CaloIsoVL_TrkIdVL_TrkIsoVL	L1_DoubleEG_13_7	Energy scale

Table 6.5 – Kinematic, ID and GSF track to SC matching requirements for the main signal trigger HLT_DoubleEle33_CaloIdL_GsfTrkIdVL.

2 Electron candidates		EB	EE
Kinematic	E_T	$> 33 \text{ GeV}$	
	$ \eta $	< 2.5	
CaloIdL	H/E	< 0.15	< 0.10
(loose calorimeter ID)	$\sigma_{i\eta i\eta}$	< 0.014	< 0.035
GsfTrkIdVL	$ \Delta\eta_{in} $	< 0.02	
(very loose GSF track ID)	$ \Delta\phi_{in} $	$< 0.15 \text{ rad}$	

Figure 6.1 – L1 trigger efficiency as a function of E_T for electrons passing the non-L1 seeded part of the signal trigger and the electron candidate selection described in Section 6.1.4 [90].

(GsfTrkIdVL). The probe has to pass the last filter of the signal trigger and must be in a different ECAL subdetector than the tag, to avoid an overlap of tag and probe in the L1 trigger. Both, tag and probe, must pass the electron candidate selection described in Section 6.1.4. Figure 6.1 shows the L1 trigger efficiency as a function of the supercluster E_T [90].

2. The online electron ID efficiency contains the efficiency of the shower shape criteria, the pixel hits matching and the matching of the GSF track with the SC. The efficiency is measured with the tag-and-probe technique, for events triggered by the HLT_Ele32_CaloIdT_CaloIsoT_TrkIdT_TrkIsoT_SC17_Mass50 tag-and-probe trigger. This trigger is prescaled with a prescale value between 5 and 7, and events are weighted by the prescale to ensure that they show the same behaviour as the signal trigger, regarding pileup and instantaneous luminosity. The requirements for the trigger are given in Table 6.6. The tag is required to pass the electron part of the tag-and-probe trigger and the L1 seeded part of the signal trigger. The probe has to pass the supercluster part

Table 6.6 – Kinematic, ID, isolation and combination requirements for the tag-and-probe trigger,

HLT_Ele32_CaloIdT_CaloIsoT_TrkIdT_TrkIsoT_SC17_Mass50.

First object (electron)			
Kinematic	E_T	$> 32 \text{ GeV}$	
	$ \eta $	< 2.5	
		EB	EE
CaloIdT	H/E	< 0.10	< 0.075
(tight calorimeter ID)	$\sigma_{i\eta i\eta}$	< 0.011	< 0.031
CaloIsoT	ECAL iso/ E_T	< 0.125	< 0.075
(tight calorimeter isolation)	HCAL iso/ E_T	< 0.125	< 0.075
TrkIdT	$ \Delta\eta_{in} $	< 0.008	
(tight tracker ID)	$ \Delta\phi_{in} $	$< 0.07 \text{ rad}$	$< 0.05 \text{ rad}$
TrkIsoT	Track iso/ E_T	< 0.125	< 0.075
(tight tracker isolation)			
Second object (supercluster)			
Kinematic	E_T	$> 17 \text{ GeV}$	
	$ \eta $	< 2.5	
Combination of first and second object			
Invariant mass	M_{inv}	$> 50 \text{ GeV}$	

of the tag-and-probe trigger and be in a different subdetector than the tag. It is furthermore required to have an online measured $E_T > 33 \text{ GeV}$ to pass that part of the signal trigger. Both, tag and probe, must pass the electron candidate selection described in Section 6.1.4. Figure 6.2 shows the efficiency for the probe to pass the non-L1 seeded part of the signal trigger as a function of E_T . In the barrel (endcaps) the efficiency is measured to be constant at $99.65 \pm 0.02\%$ ($99.61 \pm 0.02\%$) [90]. To improve the statistics for electron candidates with higher E_T , the normal tag-and-probe trigger is replaced by the HLT_DoublePhoton70 trigger, which requires two SC with $H/E < 0.15(0.1)$ in the barrel (endcaps). One of the two SC has to pass the L1 trigger. The efficiency as a function of the invariant mass for barrel-barrel and barrel-endcap pairs of electron candidates is shown in Figure 6.3. For barrel-barrel (barrel-endcap) pairs the efficiency is measured to be constant at $99.30 \pm 0.04\%$ ($99.26 \pm 0.02\%$) [90].

3. The turn on curve of the trigger is measured from data for the barrel and two endcap η regions, using as well the tag-and-probe method with events triggered by the HLT_Ele32_CaloIdT_CaloIsoT_TrkIdT_TrkIsoT_SC17_Mass50 trigger. The tag must pass the electron part of the trigger and the probe must be in a different subdetector than the tag. Both, tag and probe, must pass the electron selection, as described in Section 6.1.4. Depicted in Figure 6.4 is the efficiency turn on curve, for the probes passing the online requirement of

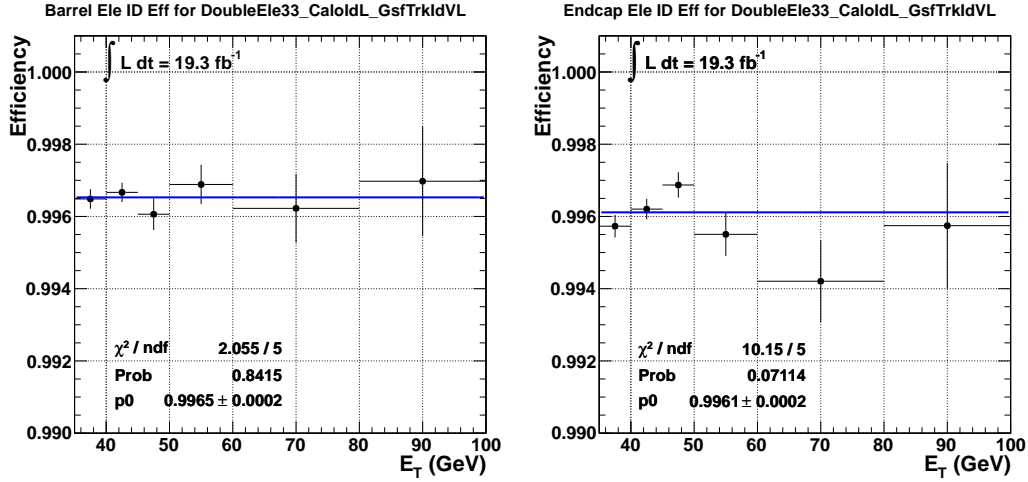


Figure 6.2 – Efficiency as a function of E_T for electron candidates passing the selection to pass the online electron ID criteria of the signal trigger. Efficiencies for barrel (endcap) electron candidates are shown in the left (right) plot [90].

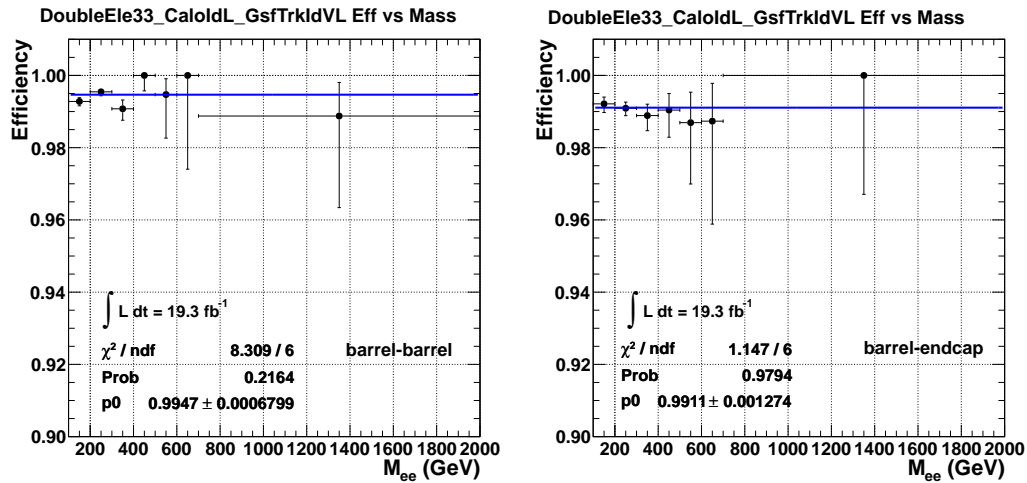


Figure 6.3 – Efficiency as a function of the invariant mass of two electron candidates passing the selection to pass the online electron ID criteria of the signal trigger. Efficiencies for barrel-barrel (barrel-endcap) pairs are shown in the left (right) plot [90].

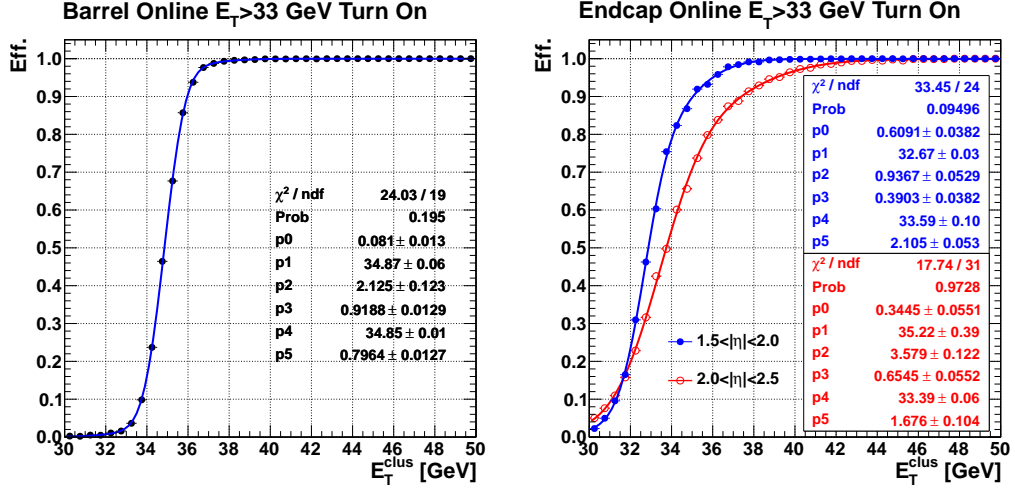


Figure 6.4 – Turn on curve for the signal trigger in the barrel (left) and the two endcap regions (right) as a function of the offline reconstructed E_T^{SC} [91].

Table 6.7 – The fitted parameters for Equation (6.2) as a function of E_T^{SC} . X_0 can be interpreted as the efficiency on the plateau, X_1 as the E_T value where the efficiency reaches half maximum and X_2 as the slope of the turn on curve, where X is A or B [91].

	barrel	endcap $ \eta \leq 2.0$	endcap $ \eta > 2.0$
A_0	0.081 ± 0.013	0.61 ± 0.04	0.345 ± 0.055
A_1	34.9 ± 0.1	32.67 ± 0.03	35.2 ± 0.4
A_2	2.13 ± 0.12	0.94 ± 0.05	3.58 ± 0.12
B_0	0.919 ± 0.013	0.39 ± 0.04	0.655 ± 0.055
B_1	34.85 ± 0.01	33.6 ± 0.1	33.39 ± 0.6
B_2	0.796 ± 0.012	2.11 ± 0.05	1.68 ± 0.10
χ^2/ndof	24.0/19	33.5/24	17.7/31

$E_T > 33$ GeV, as a function of the offline reconstructed SC E_T (E_T^{SC}), for the three η regions. Contrary to E_T , the E_T^{SC} is not measured with respect to the primary vertex, but to the origin of the detector.

A parametrisation as given in Equation (6.2), consisting of the sum of two turn on curves, was fitted to the measurements in the barrel and in two separate η regions of the endcaps. The sum of two turn on curves was chosen in order to better fit the measurements. The parameters of the fits are listed in Table 6.7.

$$f(E_T) = \frac{A_0}{2} \left[1 + \operatorname{erf} \left(\frac{E_T - A_1}{\sqrt{2}A_2} \right) \right] + \frac{B_0}{2} \left[1 + \operatorname{erf} \left(\frac{E_T - B_1}{\sqrt{2}B_2} \right) \right] \quad (6.2)$$

The turn on curve is used to weight the simulated events, taking the two electrons E_T^{SC} as parameters. Since the simulated events are weighted by the turn on curve obtained from data, the trigger simulation in the samples is not used.

Table 6.8 – The HEEP version 4.1 selection criteria. The first block defines the kinematic thresholds, geometric regions and the electron candidates seed. The second block are the ID criteria and the third block defines the isolation criteria in the calorimeters and the tracker.

Variable	Barrel	Endcap
E_T	$> 35 \text{ GeV}$	$> 35 \text{ GeV}$
$ \eta_{SC} $	< 1.442	$1.56 < \eta_{SC} < 2.5$
Seed	ECAL driven	ECAL driven
H/E	< 0.05	< 0.05
$E^{X \times 5}/E^{5 \times 5}$	$E^{2 \times 5}/E^{5 \times 5} > 0.94$ or $E^{1 \times 5}/E^{5 \times 5} > 0.83$	-
$\sigma_{in\eta}$	-	< 0.03
Missing inner hits	≤ 1	≤ 1
$ d_{xy} $	$< 0.02 \text{ cm}$	$< 0.05 \text{ cm}$
$ \Delta\eta_{in} $	< 0.005	< 0.007
$ \Delta\phi_{in} $	$< 0.06 \text{ rad}$	$< 0.06 \text{ rad}$
Isolation:	$< 2 \text{ GeV} + 0.03 \times E_T +$	$< 2.5 \text{ GeV} + \rho \times 0.28,$
ECAL + HCAL Depth 1	$+\rho \times 0.28$	for $E_T \leq 50 \text{ GeV}$ $< 1 \text{ GeV} + 0.03 \times E_T + \rho \times 0.28,$ for $E_T > 50 \text{ GeV}$
Track isolation: Track p_T	$< 5 \text{ GeV}$	$< 5 \text{ GeV}$

6.1.4 Electron selection

In this analysis the high energy electron pair (HEEP) selection is used for the selection of electron candidates. The main goal of the HEEP selection is to maintain a high efficiency for the electron candidate selection over a wide energy range, while remaining independent of the number of primary vertices. The HEEP selection follows a cut based approach with different thresholds for electron candidates in the barrel or endcaps. An electron candidate that passes the HEEP V4.1 selection, listed in Table 6.8 for the barrel and endcap regions, is called a HEEP electron candidate in the following. The transverse energy threshold value is chosen such that the trigger efficiency is close to the efficiency on the plateau. The HEEP electron candidates must be reconstructed as ECAL electron candidates since the energy resolution of the ECAL is much better for electrons with a high energy than the momentum resolution from the tracker.

The relative energy deposit in a cone of $\Delta R = 0.15$ in the HCAL behind the SC (H/E) must remain small, in order to avoid the misidentification of hadrons that have deposited some of their energy in the ECAL.

As selection criteria for the shower shape of an electron in the ECAL, two different approaches are used in the barrel and the endcaps, since the crystal arrangement and the shower shape are different. In the barrel the ratio of the energy of the most energetic 1×5 or 2×5 crystals in the η - ϕ -plane, centered in ϕ around the seed crystal, to the energy of the 5×5 crystals has to surpass a threshold. In cases where the electron hits the centre of a crystal the ratio $E^{1 \times 5}/E^{5 \times 5}$ is suitable, while for

electrons that enter close to the edge of a crystal the ratio $E^{2 \times 5} / E^{5 \times 5}$ is better. Allowing for a logical "or" of both requirements covers the two cases well [87]. In the endcaps the $\sigma_{in\eta}$ variable is used to discriminate the shower shape of electrons with respect to other particles. The variable measures the width that the energy deposit has in η , in a 5×5 crystal matrix around the seed crystal, in units of crystals.

In order to reject electrons that come from converted photons only one missing hit in the pixel detector is allowed. Allowing for one missing hit instead of none was necessary to avoid a discrepancy between data and simulation. To compensate the looser requirement on the missing inner hits, the track has to be close to the primary vertex position in the transverse plane ($|d_{xy}|$).

The variables $|\Delta\eta_{in}|$ and $|\Delta\phi_{in}|$ measure, respectively, the difference in η and ϕ , of the track position, calculated at the vertex and extrapolated to the ECAL, and the SC position. The distribution for $|\Delta\phi_{in}|$ is much wider than the one from $|\Delta\eta_{in}|$ because of bremsstrahlung, hence the looser requirement.

The HEEP electron candidates are required to be isolated in the tracker and the calorimeters. In the tracker the isolation variable is defined as the sum of the p_T of all tracks with $p_T > 700$ MeV and $|\Delta z| < 0.2$ cm in a cone of $\Delta R = 0.3$ around the candidate track, excluding an inner cone of $\Delta R = 0.04$. The distance Δz is the distance on the z -axis between the track and the HEEP electron candidate.

The isolation variable for the calorimeter isolation is a sum of energy deposits in the ECAL and in the HCAL. In the ECAL the isolation energy is calculated as the sum of energy deposits with $E > 80$ MeV ($E_T > 100$ MeV) in crystals in a cone of $\Delta R = 0.3$ around the electrons candidates position in the barrel (endcap). An inner cone of a radius of three crystals and a strip of three crystals in η is excluded. The HCAL depth 1 isolation energy is calculated from the transverse energy of the calorimeter towers in a cone of $\Delta R = 0.3$ around the electrons candidates position, with the exclusion of towers in a cone of $\Delta R = 0.15$. Depth 1 takes the complete towers 1-17, depth 1 of the towers 18-29 and depth 2 of the towers 27-29 as defined in Figure 4.7. The thresholds for the isolation variable are depending on the transverse energy of the electron candidate and the transverse energy density of the event because of pileup interactions ρ [92]. The ρ variable is calculated with the FastJet package [93], by looking at regions in the event where no particles or jets from the hard interaction are present, and taking the energy density in these regions as the one coming from pileup interactions. For the 2012 run ρ was on average $1 \text{ GeV} / \Delta\eta\Delta\phi$ per vertex. Since ρ is an energy density, the factor that it is multiplied with has the dimension of an area. This area is an effective area defined by the ratio of the slopes of the mean isolation energy and ρ as a function of the number of primary vertices N_{Vtx} ,

$$A_{\text{eff}} = \frac{\frac{d}{dN_{Vtx}} \overline{E_{\text{iso}}}}{\frac{d}{dN_{Vtx}} \rho}, \quad (6.3)$$

and is taken as a constant.

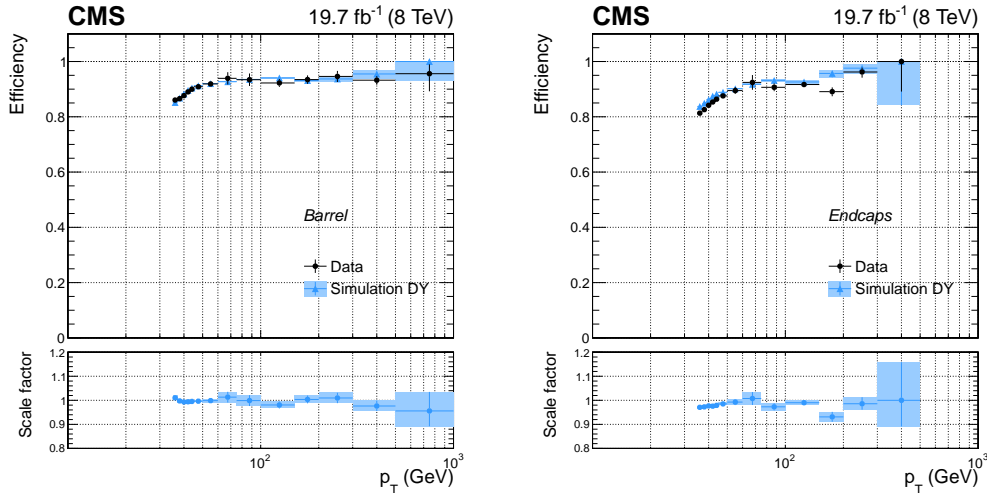


Figure 6.5 – Top: Efficiencies measured as a function of E_T for the barrel (left) and endcap (right) regions for GSF electron candidates to pass the HEEP selection. Bottom: The data to simulation scale factor for barrel (left) and endcaps (right). The error bars show statistical and systematic uncertainties [67].

Electron selection efficiency

The efficiency ϵ_{HEEP} of the HEEP electron candidate selection was measured for data and simulation, using the tag-and-probe technique with events from the Z resonance [87]. The tag needs to be a GSF electron candidate triggered by the signal trigger, pass the HEEP selection and, to reduce contamination of the sample from multijet events from QCD processes, must be in the barrel of the detector. The probe is a GSF electron candidate that passes the signal trigger. The invariant mass of the tag and probe pair must be $60 < M_{TP} < 120$ GeV. Efficiencies for the probe passing the HEEP selection were measured for the barrel and endcap regions, and for medium and high E_T electron candidates. The measured efficiencies for probes with $p_T > 35$ GeV are shown in Figure 6.5, for the barrel and the endcap regions. The bottom plots in Figure 6.5 show the data over simulation ratio. This ratio is called scale factor and is used to correct the simulations. The scale factors used for the analysis are listed in Table 6.9. For the extrapolation of the scale factor to electron momenta of the signal region ($p_T \approx 1$ TeV) a systematic uncertainty of 2% is assigned for HEEP electron candidates in the barrel and 4% in the endcaps, where lower statistics limits the precision.

Table 6.9 – Data/simulation scale factors for the HEEP selection efficiency for the barrel and endcap, and two different electron candidate E_T regions.

Electron E_T	barrel	endcap
$E_T > 35$ GeV	0.997 ± 0.000 (stat.) ± 0.007 (syst.)	0.979 ± 0.000 (stat.) ± 0.006 (syst.)
$E_T > 100$ GeV	0.985 ± 0.002 (stat.) ± 0.014 (syst.)	0.981 ± 0.006 (stat.) ± 0.004 (syst.)

Table 6.10 – Parametrisations for the acceptance times efficiency for spin 1 and spin 2 resonances for the barrel-barrel and barrel-endcap channels.

Resonance	Barrel-barrel	Barrel-endcap
Spin 1	$0.592 - \frac{2.91 \times 10^5}{m^2 + 7.45 \times 10^5}$	$0.0635 - \frac{159}{m+345} + \frac{7.304 \times 10^5}{m^2 + 1.81 \times 10^6}$
Spin 2	$0.571 - \frac{2.97 \times 10^4}{m^2 + 1.32 \times 10^5}$	$-0.238 - \frac{1.16 \times 10^4}{m + 3.52 \times 10^4} + \frac{6.58 \times 10^4}{m^2 + 7.54 \times 10^6}$

6.1.5 Dielectron event selection

To search for high mass resonances in the dielectron decay channel, events with two HEEP electron candidates are selected. The event must be triggered by the main signal trigger, which was unrescaled for the whole period of the 2012 data taking. One of the two electrons is required to be in the ECAL barrel to reduce the contamination from multijet events from QCD processes. There is no requirement for the charge of the two HEEP electron candidates, in order to not lose eventual high mass events where one charge is misreconstructed. To keep the analysis inclusive, no additional requirements that could reduce SM backgrounds, e.g. on the maximal number of jets or the maximal E_T^{miss} , are demanded. Instead, care is taken to verify the accurate modeling of the simulated backgrounds as good as possible. In case of more than two HEEP electron candidates, the two passing the selection and giving the highest invariant mass are chosen. The minimal invariant mass of the dielectron pair is 60 GeV.

6.1.6 Acceptance times efficiency

The product of geometrical acceptance and detection efficiency is estimated from simulations as a function of the generated dielectron invariant mass for the barrel-barrel and the barrel-endcap cases. For this the ratio of the selected dielectron pairs to all generated dielectron pairs is calculated. The resulting distributions are fitted with polynomial functions that serve as input to the final limit setting that will be discussed in Section 6.7. Since the geometric acceptance is different for a spin 1 and a spin 2 particle, two different sets of acceptance times efficiency distributions are generated. For the spin 1 particle distribution, the DY samples from Table 6.2 are used and for the spin 2 particles the RS graviton signal samples from Table 6.3 are taken. The results for spin 1 particles are shown in Figure 6.6 and the ones for spin 2 particles in Figure 6.7, together with the parameters for the polynomials. Table 6.10 lists the parametric functions used for the acceptance times efficiency.

6.2 Electron energy scale factor measurement

The Z resonance offers a good possibility to check and correct the behaviour of the simulation with the data, since it represents a very pure dielectron sample and has well known properties. At the Z resonance, shifts of the energy measurement, which

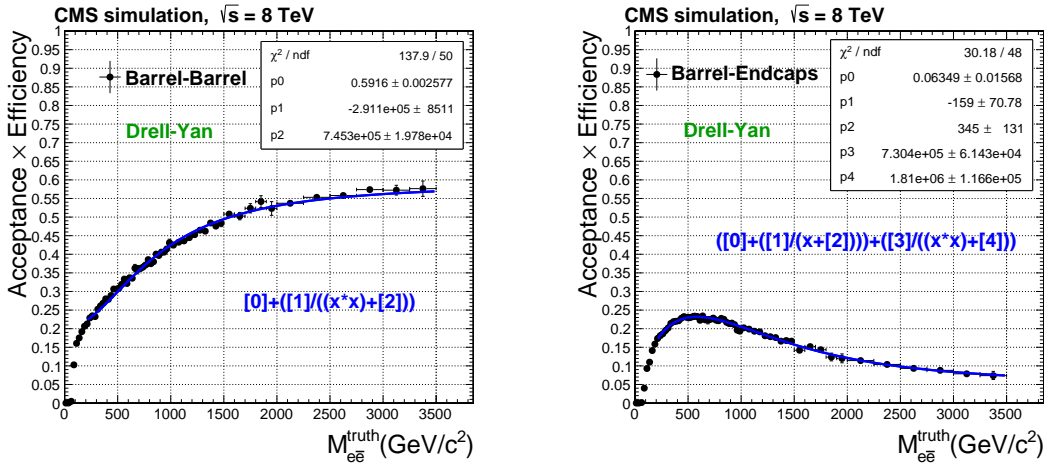


Figure 6.6 – Acceptance times efficiency for barrel-barrel dielectrons (left) and barrel-endcap dielectrons (right) for a spin 1 particle [87].

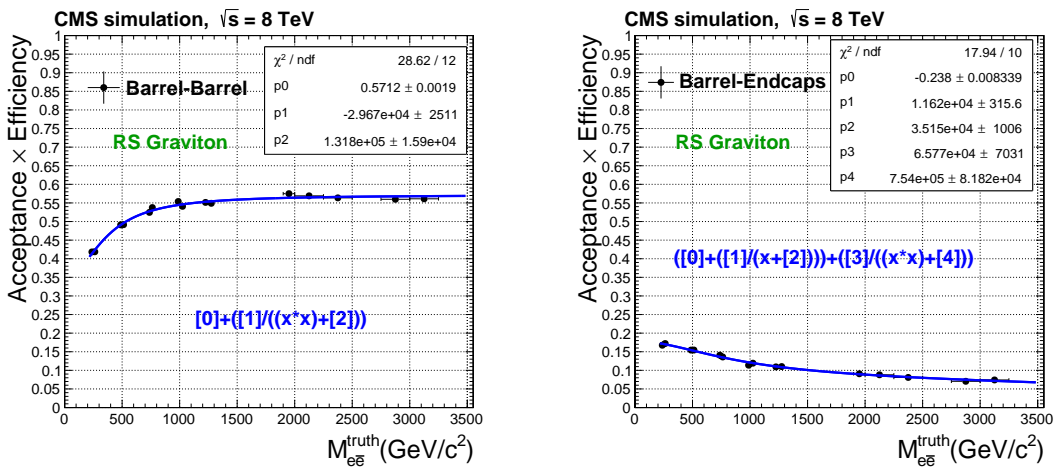


Figure 6.7 – Acceptance times efficiency for barrel-barrel dielectrons (left) and barrel-endcap dielectrons (right) for a spin 2 particle like an RS graviton [87].

lead to different invariant masses, and differences in the width of the peak can be measured. For this, a fit of a line shape, that models the intrinsic shape of the Z resonance and the detector effects, to the selected events in data and simulation is performed.

6.2.1 Event selection

In order not to lose events that form the low mass tail of the Z peak, the E_T requirement of the HEEP selection is loosened to $E_T > 25$ GeV. Since this is below the online requirement of $E_T > 33$ GeV of the main signal trigger, a different trigger with lower E_T thresholds is used. The HLT_Ele17_X_Ele8_X, where X stands for CaloIdL_CaloIsoVL_TrkIdVL_TrkIsoVL, trigger requires two online reconstructed electron candidates, one with $E_T = 17$ GeV and one with $E_T = 8$ GeV, that have the same loose calorimeter ID requirements (CaloIdL) as the signal trigger described in Table 6.5. The trigger has very loose isolation requirements in the ECAL (HCAL), relative to the E_T , of 0.2 for electron candidates in the barrel or in the endcaps (CaloIdL). Both online electron candidates KF tracks must satisfy very loose ID requirements of $\Delta\eta < 0.01(0.01)$ and $\Delta\phi < 0.15(0.10)$ in the barrel (endcaps) (TrkIdVL). Furthermore, the tracks must be very loosely isolated with a tracker isolation relative to E_T smaller than 0.2 in the barrel and endcaps (TrkIsoVL). Apart from these two items, the event selection is the same as described in Section 6.1. Dielectron events with an invariant mass between 60 GeV and 120 GeV are selected.

6.2.2 Signal model

The shape of the signal is modeled by the convolution of two functions: a Breit-Wigner (BW) distribution for the natural shape of the Z resonance and a distribution that describes the detector effects for the electron reconstruction as explained below.

Natural shape

The natural shape of the Z resonance is described by a BW distribution

$$f_{\text{BW}} = \frac{\Gamma_Z}{2\pi \left[(m - m_Z)^2 + \left(\frac{\Gamma_Z}{2}\right)^2 \right]}, \quad (6.4)$$

where m_Z is the mean and Γ_Z the full width at half maximum (FWHM) of the distribution. The parameters of the resonance were measured with great accuracy by the LEP experiments and the Stanford Linear Collider (SLC) [94], and the mean and width of the BW are set to the measured mass and width of the Z boson of $m_Z = 91.1876$ GeV and $\Gamma_Z = 2.4952$ GeV, respectively.

Detector effects

For the modeling of the detector effects several possibilities can be considered. A Gaussian lineshape does not model the data well, since the electrons lose energy because of bremsstrahlung, which is not always fully recovered by the superclustering algorithm. Therefore, the low mass tail in the dielectron invariant mass resolution distribution is much enlarged and does not follow a Gaussian shape but an exponential. A line shape that better models the energy loss due to bremsstrahlung is the Crystal Ball (CB) function, which is a combination of a Gaussian core with an exponential tail on one side. A threshold defines the beginning of the tail, and the function and its first derivative are continuous. An extension of the CB function is the double sided Crystal Ball (DCB), which has an exponential tail on both sides of the central Gaussian with independent thresholds and slopes. The double sided Crystal Ball is given in the form

$$f(m) = \begin{cases} \exp\left(-\frac{(m-m_0)^2}{2\sigma^2}\right), & \text{for } -|\alpha_L| \leq \frac{m-m_0}{\sigma} \leq |\alpha_R| \\ A_L \cdot \left(B_L - \frac{m-m_0}{\sigma}\right)^{-n_L}, & \text{for } \frac{m-m_0}{\sigma} < -|\alpha_L| \\ A_R \cdot \left(B_R - \frac{m-m_0}{\sigma}\right)^{-n_R}, & \text{for } \frac{m-m_0}{\sigma} > |\alpha_R| \end{cases} \quad (6.5)$$

with

$$A_x = \left(\frac{n_x}{|\alpha_x|}\right)^{n_x} \cdot \exp\left(-\frac{|\alpha_x|^2}{2}\right), \quad B_x = \frac{n_x}{|\alpha_x|} - |\alpha_x|, \quad \text{where } x \in \{L, R\},$$

where m_0 and σ are the mean and width of the central Gaussian. $\alpha_{L/R}$ and $n_{L/R}$ are, respectively, the cutoff parameters and powers for the exponential tails on the left and on the right. A second exponential tail on the high mass side of the Z peak appears as a consequence of the bremsstrahlung recovery in the SC algorithm. In some cases more than the actual value of the energy deposited by bremsstrahlung is recovered in the SC algorithm, leading to the appearance of a tail on the high mass side of the peak. For the analysis, the double sided Crystal Ball was chosen to model for the detector effects.

6.2.3 Fit

The RooFit extension [95] for the ROOT framework [96] was used to perform the unbinned maximum likelihood fit. Since RooFit offers only the CB function, the DCB class had to be built starting from the code for the CB class and extending it with a second exponential tail. The fit is performed independently for events with two barrel HEEP electron candidates, one barrel and one endcap HEEP electron candidate, and two endcap HEEP electron candidates. The inclusive POWHEG DY sample with a dielectron mass $M_{ee} > 20$ GeV is used as a reference and normalised to the number of selected data events, which are given in Table 6.11.

Figure 6.8 shows the results of the fit for the three different models of detector effects, the BW \otimes Gaussian, the BW \otimes CB and the BW \otimes DCB, for events with two barrel HEEP electron candidates. The same distributions for events with one barrel and one endcap candidate and events with two endcap candidates are given in Figure 6.9 and Figure 6.10, respectively. For better comparison of the fits at the peak

and in the tails, all plots are shown with a linear as well as a logarithmic y -axis. The variables Δm_{Gauss} , Δm_{CB} and Δm_{DCB} represent the shift of the mean of the central Gaussian of the fit functions with respect to the Z mass. One can see that the fit using a BW convoluted with a Gaussian as a model shows large discrepancies in the low invariant mass region. The fit model using a BW convoluted with a CB function shows much better behaviour in that region but still has some differences with the measurements in the high invariant mass region above the peak. The second exponential tail of the fit model that uses a BW convoluted with a DCB function gives fit results that also agree well with the high invariant mass side of the Z peak.

At the Z resonance, the selected event sample is very pure and contains mostly electron pairs from the DY process. However, there remains a small contamination background from other SM processes, especially at small invariant mass. These processes can be modeled as an exponentially falling background added to the fit function. The result of the addition of an exponential to the $\text{BW} \otimes \text{DCB}$ with floating normalisations between the two parts can be seen in the plots in Figure 6.11.

6.2.4 Results

The measured shifts from the Z mass are listed in Table 6.12, together with the uncertainties from the fits. Since the shift of the energy scale remains way below 1%, which is smaller than the resolution at that mass, no correction for the energy scale is performed for the analysis.

The width of the central Gaussian of the DCB function is taken as a measure for the resolution of the detector. As the width as measured from data is larger than the width measured from simulation an extra relative correction is calculated using the formula

$$\sigma_{\text{DCB}}(\text{extra}) = \sqrt{\sigma_{\text{DCB}}^2(\text{data}) - \sigma_{\text{DCB}}^2(\text{sim})}. \quad (6.6)$$

Table 6.13 lists the resolutions relative to the Z mass, measured from fits to data and simulation for three dielectron topologies. In addition, the extra relative correction calculated from these resolutions is listed. The listed uncertainties are the ones obtained from the fits.

Table 6.11 – Number of selected events in a dielectron invariant mass range from 60 GeV to 120 GeV, used in the unbinned maximum likelihood fit.

	Data	$DY \rightarrow ee$
Barrel-barrel	3143553	3878849
Barrel-endcap	1757252	2238407
Endcap-endcap	622148	777580

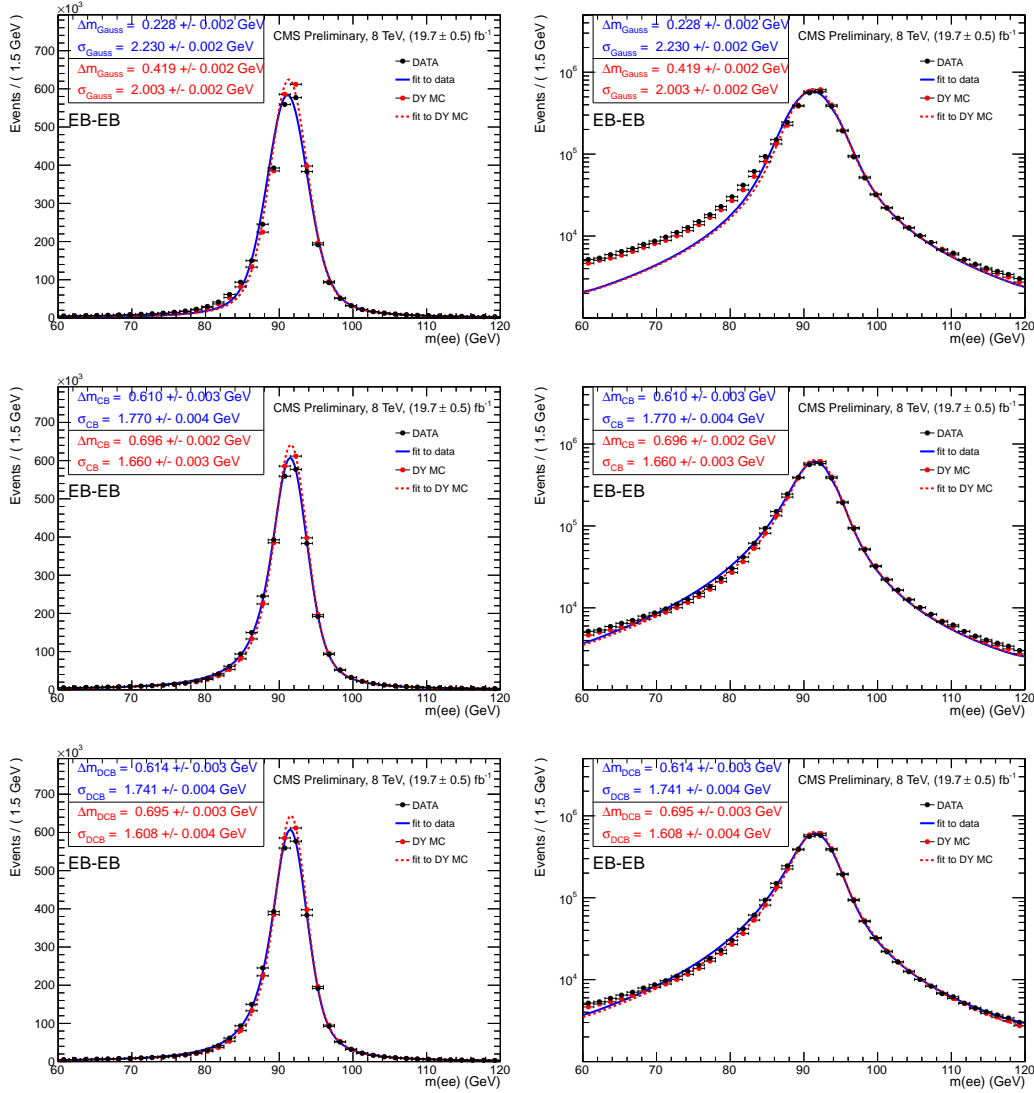


Figure 6.8 – Invariant mass spectrum of barrel-barrel (EB-EB) events around the Z peak for the data (black dots) and simulation (red dots). Overlaid are the fit results with a BW⊗Gaussian (top), a BW⊗CB (middle) and BW⊗DCB (bottom). Left: Linear y -axis scale. Right: Logarithmic y -axis scale.

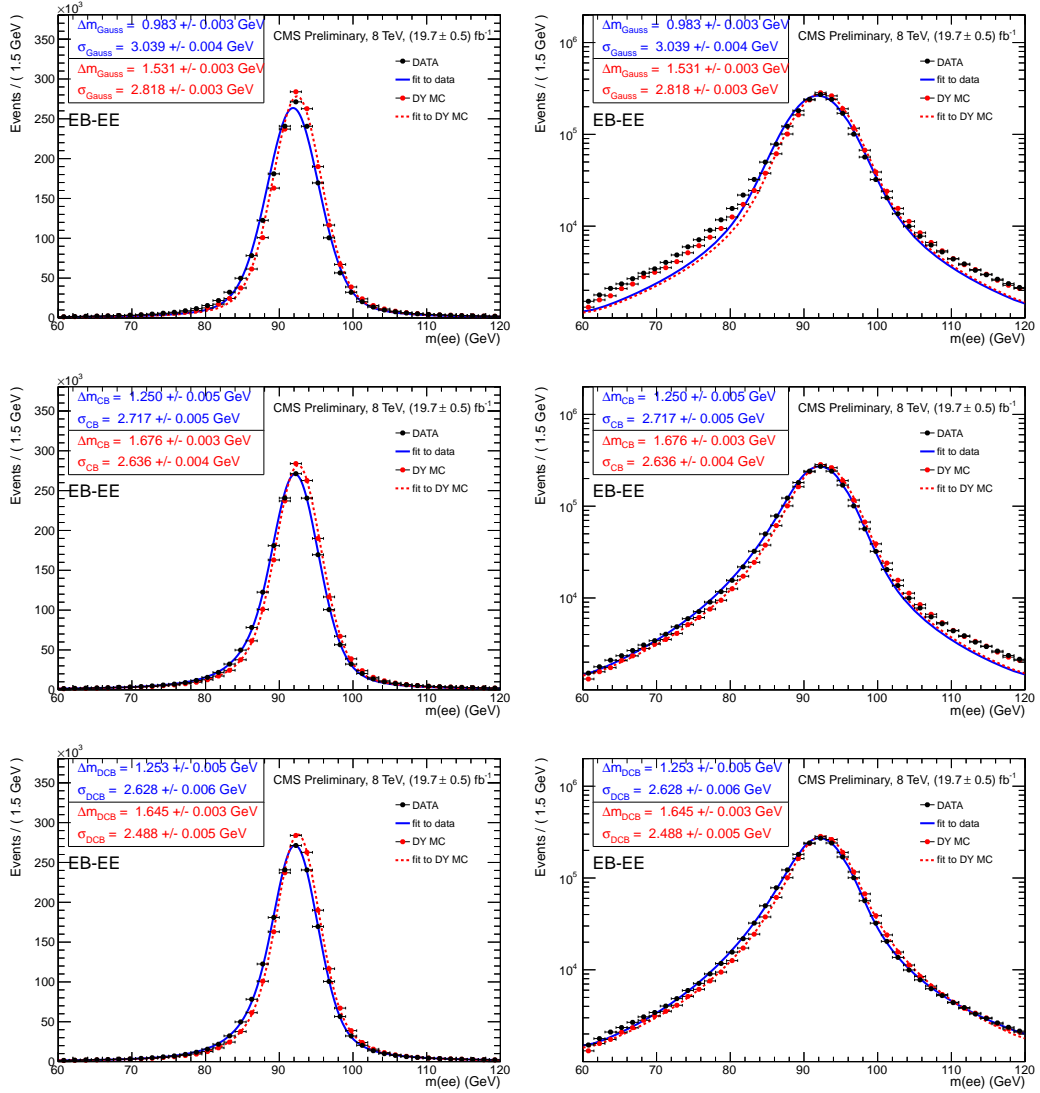


Figure 6.9 – Invariant mass spectrum of barrel-endcap (EB-EE) events around the Z peak for the data (black dots) and simulation (red dots). Overlaid are the fit results with a BW⊗Gaussian (top), a BW⊗CB (middle) and BW⊗DCB (bottom). Left: Linear y -axis scale. Right: Logarithmic y -axis scale.

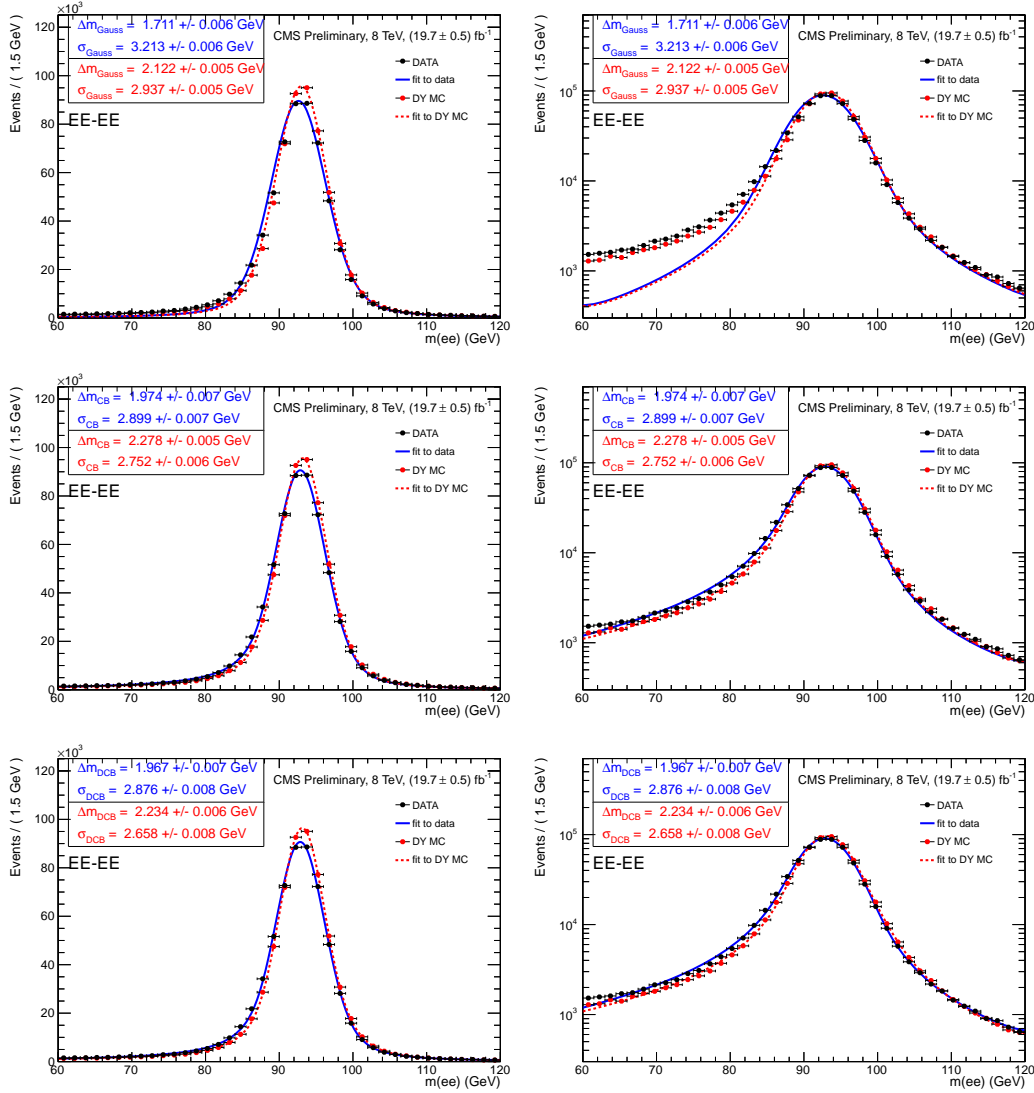


Figure 6.10 – Invariant mass spectrum of endcap-endcap (EE-EE) events around the Z peak for the data (black dots) and simulation (red dots). Overlaid are the fit results with a BW⊗Gaussian (top), a BW⊗CB (middle) and BW⊗DCB (bottom). Left: Linear y -axis scale. Right: Logarithmic y -axis scale.

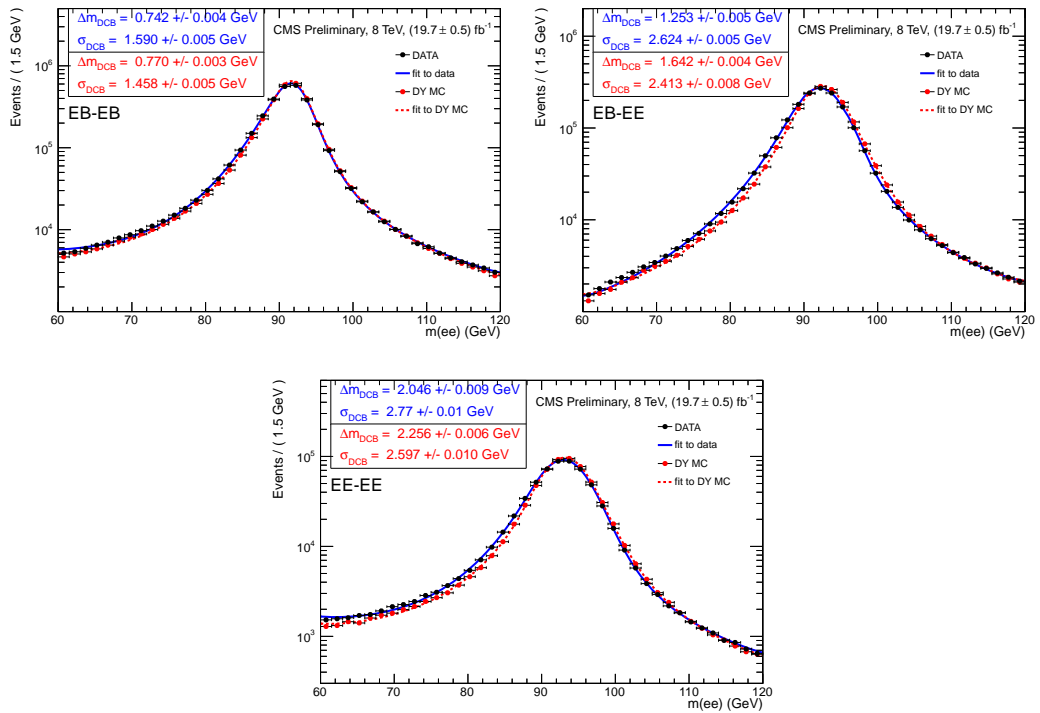


Figure 6.11 – Invariant mass spectra for the data (blue) and MC (red) overlaid with $\text{DCB} \otimes \text{BW}$ plus exponential fit results. Top left: Both HEEP electron candidates in ECAL barrel region (EB-EB). Top right: One HEEP electron candidate in ECAL barrel region and the other one in ECAL endcap region (EB-EE). Bottom: Both HEEP electron candidates in ECAL endcap region (EE-EE).

Table 6.12 – Deviations of the mean of the central Gaussian of a fit with a DCB \otimes BW from the Z mass value for different event topologies. The relative difference between the fits to the data and DY simulation is given in the rightmost column.

	$\Delta m_{DCB}(\text{data})$	$\Delta m_{DCB}(\text{sim})$	$\frac{\Delta m_{DCB}(\text{data}) - \Delta m_{DCB}(\text{sim})}{m(Z)}$
Barrel-barrel	$0.61 \pm 0.00 \text{ GeV}$	$0.70 \pm 0.00 \text{ GeV}$	$-0.09\% \pm 0.00\%$
Barrel-endcap	$1.25 \pm 0.01 \text{ GeV}$	$1.64 \pm 0.00 \text{ GeV}$	$-0.43\% \pm 0.01\%$
Endcap-endcap	$1.97 \pm 0.01 \text{ GeV}$	$2.23 \pm 0.01 \text{ GeV}$	$-0.29\% \pm 0.01\%$

Table 6.13 – Dielectron mass resolution relative to the Z mass, extracted from a fit of a DCB convoluted with at BW at the Z peak for different event topologies. The rightmost column give the extra correction to the resolution.

	$\frac{\sigma_{DCB}(\text{data})}{m(Z)}$	$\frac{\sigma_{DCB}(\text{sim})}{m(Z)}$	$\frac{\sigma_{DCB}(\text{extra})}{m(Z)}$
Barrel-barrel	$1.91\% \pm 0.00\%$	$1.76\% \pm 0.00\%$	$0.73\% \pm 0.01\%$
Barrel-endcap	$2.88\% \pm 0.01\%$	$2.73\% \pm 0.01\%$	$0.93\% \pm 0.01\%$
Endcap-endcap	$3.15\% \pm 0.01\%$	$2.92\% \pm 0.01\%$	$1.20\% \pm 0.01\%$

6.3 High mass resolution

The electron transverse energy measurement for the analysis uses the energy of the supercluster and the polar angle of the track at the primary vertex, as described in Equation (5.1). The characteristic of the crystal ECAL of CMS is that the resolution improves at higher energies until it reaches a plateau. This reflects itself as well in the dielectron invariant mass resolution, which follows the same model. In Section 6.2 the measurement of the invariant mass resolution at the Z peak was described. Since there are no candle events at high mass, the high mass resolution is estimated from simulated DY samples.

6.3.1 Method

Using simulated DY samples allows to access the true generated invariant mass m_{true} of the dielectron pair and compare it to the reconstructed invariant mass m_{RECO} , derived from a selected dielectron pair. The spectrum of $m_{\text{RECO}} - m_{\text{true}}$ is similar in shape to the invariant mass spectrum at the Z peak, with the difference that there is no natural width to the peak which is located around zero. The same double sided Crystal Ball function that was used for the energy scale measurement at the Z peak can be used as a fit function, but without the BW.

Events are selected with the HEEP selection, with electron $E_T > 25 \text{ GeV}$, like for the electron energy scale measurement, from all the DY $\rightarrow ee$ samples listed in Table 6.2. For all events that lie in a given true dielectron invariant mass range, the difference between reconstructed and simulated dielectron invariant mass is calculated and a DCB is fitted to the resulting distribution. For the barrel-barrel and barrel-endcap events, the fit range was chosen to be half of the mass window and for

the endcap-endcap events the fit range was the full mass window to give better fits to the wider peaks. This way the resolution for several mass ranges is taken from the width of the central Gaussian of the DCB shape. The same method is also performed with Z'_ψ and Z'_{SSM} signal samples with different resonance masses. For these samples the fit range is defined as 7.5% of the resonance mass around the resonance mass for barrel-barrel and barrel-endcap events, and 15% for endcap-endcap events.

Since these resolutions are determined from simulations, the estimated resolution in data is derived by adding the extra contribution measured at the Z peak, and listed in Table 6.13, in quadrature to the resolution obtained from the simulation. This is done under the assumption that the extra contribution is the same as at the Z peak at high mass. The resulting resolutions obtained from DY samples as a function of dielectron invariant mass are then fitted with a characteristic function of the ECAL mass resolution, given by

$$f(m_{ee}|N, S, C) = \sqrt{\frac{N^2}{m_{ee}^2} + \frac{S^2}{m_{ee}} + C^2}, \quad (6.7)$$

where N , S and C are the fit parameters for the noise term, stochastic term and constant term of the fit function, similar to the ECAL energy resolution function given in Equation (4.2).

6.3.2 Results

Figure 6.12 shows, respectively, example fits to the barrel-barrel, barrel-endcap and endcap-endcap spectra of the difference between reconstructed and true mass, obtained from DY samples for the different mass ranges, with the fit of a DCB function to the peak. The same is shown in Figure 6.13 for example spectra of the Z'_ψ and Z'_{SSM} signal samples. The fits for all mass ranges can be found in Appendix A.

The resolutions obtained from the simulated samples and the extra contribution from the difference between data and simulation at the Z peak are shown in Figure 6.14 for the three event topologies. The fit of the mass resolution model to the resolutions is also shown in the plots.

The resolution improves towards higher invariant masses and reaches a plateau above about 700 GeV. A rising trend in resolution that can be seen above 1.8 TeV in the barrel-barrel channel in Figure 6.14, which is related to the fact that the resolution and also the scale are not constant over the pseudorapidity. Since the resolution is better in the low $|\eta|$ region of the barrel and the electrons are more central for higher masses, a better resolution is expected at higher invariant masses. However, the trend towards high invariant masses shows a worsening of the resolution. A drift of the mean of the $m_{\text{RECO}} - m_{\text{true}}$ peak away from zero is observed as function of the mass, and is different for high and low $|\eta|$ regions in the barrel, which widens the peak of the combined spectrum and can explain the slightly worse resolution at higher invariant mass. This is shown in the plots in Figure 6.15, where the resolution and the bias of the DCB function for three different event topologies in the ECAL barrel are

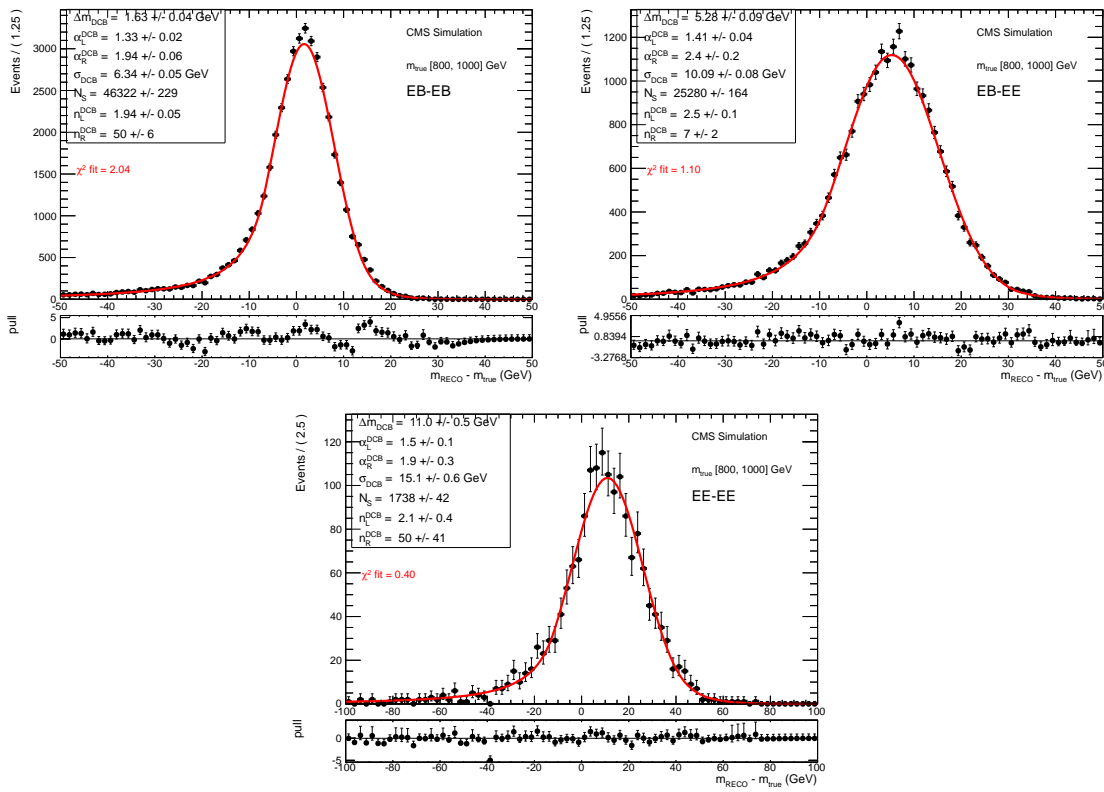


Figure 6.12 – Fit of a DCB function to $m_{\text{RECO}} - m_{\text{true}}$ for, barrel-barrel (EB-EB) (top left plot), barrel-endcap (EB-EE) (top right plot) and endcap-endcap (EE-EE) (bottom plot) dielectron events, selected from DY samples.

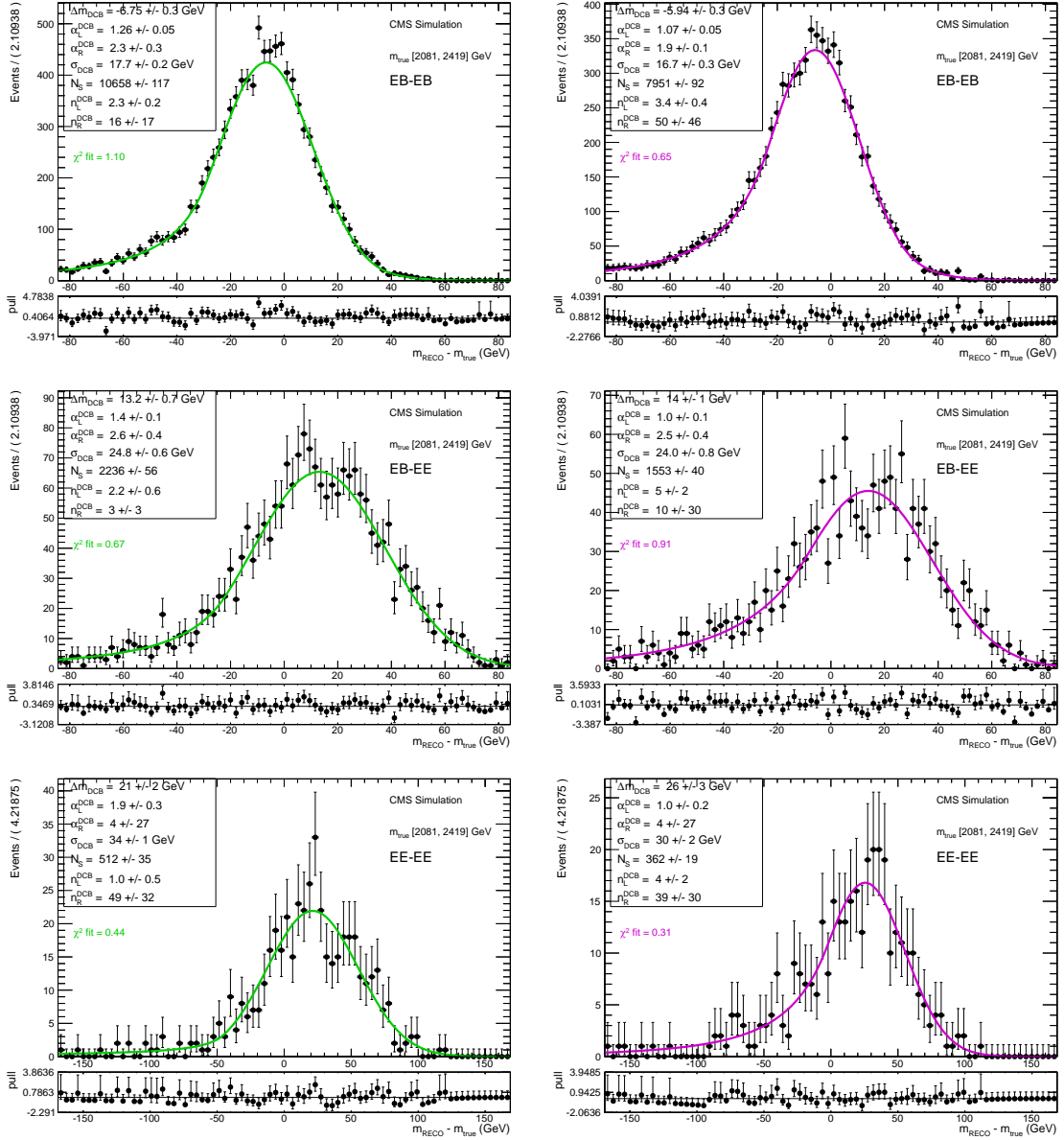


Figure 6.13 – Fit of a DCB function to $m_{\text{RECO}} - m_{\text{true}}$ for, barrel-barrel (EB-EB) (top plots), barrel-endcap (EB-EE) (middle plots) and endcap-endcap (EE-EE) (bottom plots) dielectron events. The left column shows spectra from Z'_{ψ} samples and the right column from Z'_{SSM} samples.

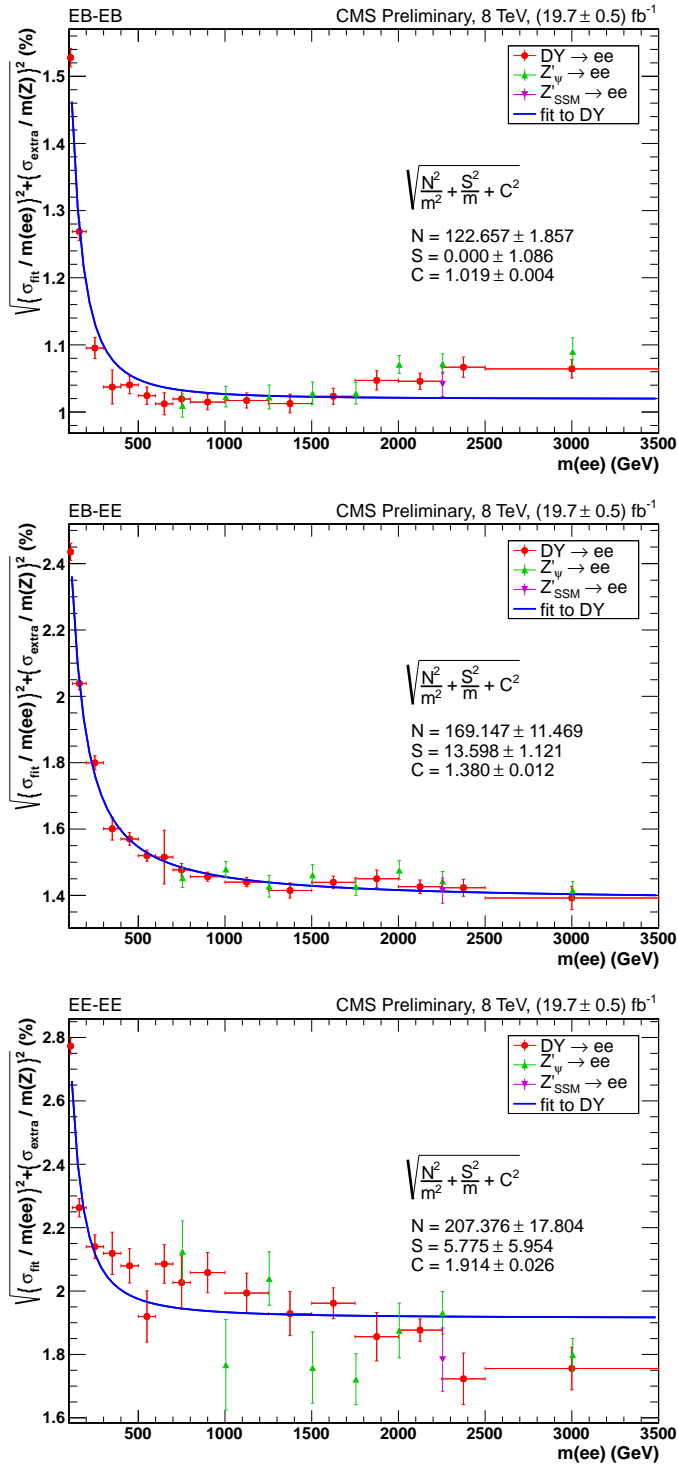


Figure 6.14 – Resolutions measured from simulated samples, with extra smearing from the data to simulation difference, as a function of the true invariant mass and a fit of the resolution parametrisation function to the resolutions obtained from the DY samples. Top plot: barrel-barrel (EB-EB) resolution. Middle plot: barrel-endcap (EB-EE) resolution. Bottom plot: endcap-endcap (EE-EE) resolution.

compared. If the barrel-barrel events are split with both HEEP electron candidates above or below $|\eta| = 0.7$, or with one candidate below and one above $|\eta| = 0.7$, the rise of the resolution towards high invariant masses does not occur. The different behaviour of the bias of the DCB, for the centre and forward regions of the barrel, can be seen by comparing the middle plots of Figure 6.15. For HEEP electron candidates with $|\eta| < 0.7$, the peak of the $m_{\text{RECO}} - m_{\text{true}}$ distribution (Δm_{DCB}) lies below zero towards high invariant masses, while the opposite is observed for HEEP electron candidates with $|\eta| \geq 0.7$. This means that HEEP electron candidates with $|\eta| < 0.7$

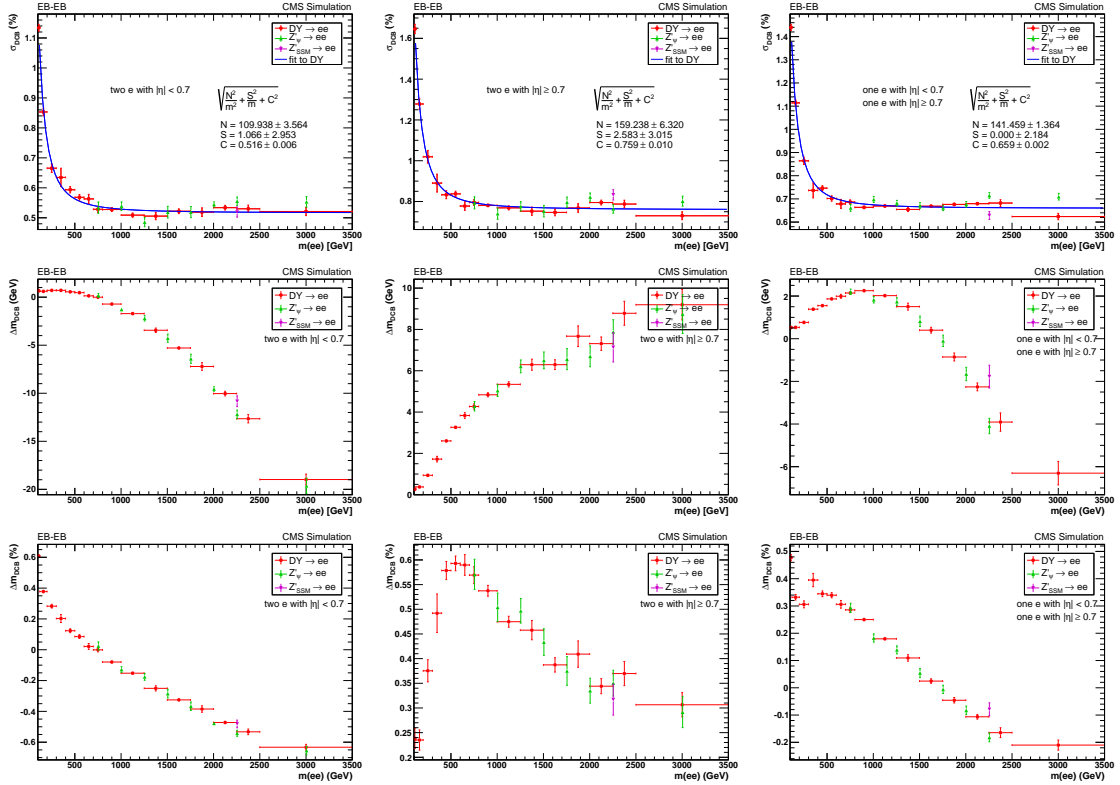


Figure 6.15 – Top row: Resolutions in the ECAL barrel, measured from simulated samples as a function of the true invariant mass. Middle row: Bias of the DCB function in the ECAL barrel. Bottom row: Relative bias of the DCB function in the ECAL barrel. The left plots show events with both HEEP electron candidates with $|\eta| < 0.7$. The middle plots show events with both HEEP electron candidates with $|\eta| \geq 0.7$ and the right plots are for events with one HEEP electron candidate with $|\eta| < 0.7$ and the other with $|\eta| \geq 0.7$.

have a tendency of having less reconstructed energy than true energy towards high dielectron invariant mass. The reason for this can be that the shower cannot be fully contained in the crystal of the ECAL anymore and energy is also deposited in the HCAL tower behind the crystal. Figure 6.16 shows the H/E distributions as a function of the dielectron invariant mass for events with both HEEP electron candidates below and above $|\eta| = 0.7$, respectively. The red points indicate the mean

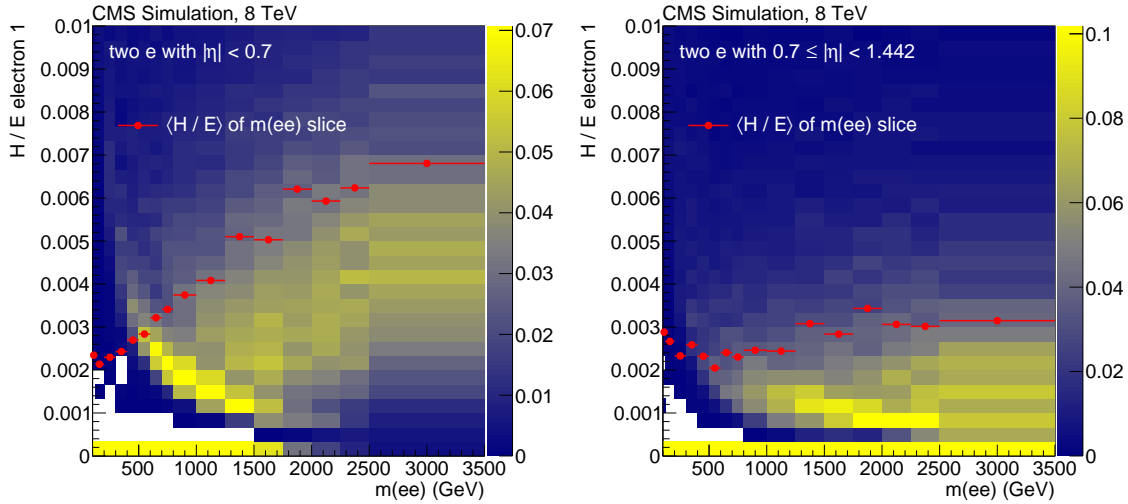


Figure 6.16 – H/E distributions for the highest energy HEEP electron candidate as a function of the dielectron mass. The left plot is for events with both HEEP electron candidates with $|\eta| < 0.7$, and on the right plot both candidates have $0.7 \leq |\eta| < 1.442$. The distributions are normalised in each mass slice. White bins contain no entries. The red markers indicate the mean of the H/E distribution in one mass slice.

of the H/E distribution in a mass slice. For the left plot, where both HEEP electron candidates have $|\eta| < 0.7$, the mean reaches higher values at high dielectron invariant mass than in the right plots, where both candidates have $0.7 \leq |\eta| < 1.442$. This indicates that indeed more energy is lost at the back of the crystal for more central electrons, which ultimately leads to the worsening of the mass resolution in the barrel for high invariant masses.

6.4 Backgrounds

Three categories of backgrounds for the search for new resonances with dielectrons can be identified. The most important background comes from the Drell–Yan process with an electron and a positron in the final state, which account for approximately 85% of all background events with invariant masses above 120 GeV. This background has the same final state as the signal and is, thus, irreducible. Another background contribution comes from events with jets that are misidentified as HEEP electron candidates. This happens significantly often because of the high cross section for multijet events. Events from SM processes that have, among eventual other particles, two isolated electrons in the final state form the third background category. These backgrounds are described below.

6.4.1 Drell–Yan background

The irreducible DY background is estimated from simulated NLO samples listed in Table 6.2. The NLO cross sections are reweighted with a K-factor calculated from the ratio between the NNLO cross section, obtained with the FEWZ calculator [83], and the generator NLO cross section of the sample with $M_{\text{ij}} > 20$ GeV. The samples are normalised to the event yield around the Z peak in a window from 60 – 120 GeV. The normalisation factor from the barrel-barrel channel is used both for the barrel-barrel and barrel-endcap channels. Both normalisation factors were measured to be in agreement within the uncertainty.

The barrel-barrel factor has the smaller uncertainty of 0.7%, including a 0.25% statistical uncertainty. The uncertainty in the barrel-barrel channel mainly comes from the E_{T} threshold of the trigger, which affects the shape of the Z peak and, thus, the energy scale. The uncertainty is estimated by varying the E_{T} threshold of the HEEP electron candidate selection up to 40 GeV and down to 20 GeV, from the nominal 35 GeV, and measuring the impact on the normalisation. For this, the same trigger as for the energy scale measurement in Section 6.2 is used, since it has lower thresholds than the signal trigger.

A larger uncertainty of 3% is taken for the normalisation factor in the barrel-endcap channel. Two contributions are responsible for the larger uncertainty: the worse agreement of the energy scale between data and simulation in the barrel-endcap channel, and the larger efficiency scale factor for electron energies around the Z resonance, due to a mismodeling of bremsstrahlung in the simulation. Both uncertainties amount to 2%, which are added in quadrature.

For the search for a narrow resonance, the absolute value of the background has only a small impact in any case.

6.4.2 Jet background

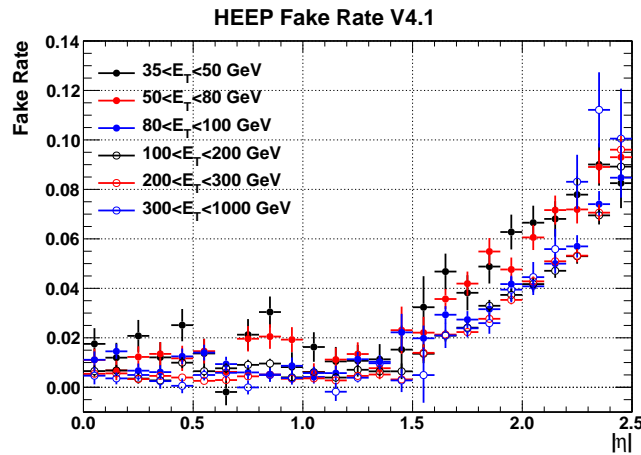
The jet background consists of events where one or more jet(s) are misidentified as HEEP electron candidates. This includes three types of processes: the multijet background, where two jets are misidentified as HEEP electron candidates, the W+jets background, where the W gives an electron and one jet is misreconstructed as a HEEP electron candidate, and the γ +jets background, where the photon converts and is reconstructed as a HEEP electron candidate, and the jet is misreconstructed as a HEEP electron candidate.

The three backgrounds are estimated with a data driven technique using the fake-rate (FR) method. A data driven estimation is favoured over the estimation from simulations, since the FR is very small and only a tiny fraction of the simulated events would be selected for the invariant mass spectrum, even if an electromagnetic enriched sample is used. It is difficult to verify if these events are well handled by the simulation and, furthermore, owing to the many jets, the normalisation of the jets sample would be difficult as well.

The FR method consists of two steps: first the probability of a jet to be misreconstructed as a HEEP electron candidate is estimated in bins of $|\eta|$ and E_{T} , then

Table 6.14 – Selection for the loose electron candidates forming the denominator of the FR calculation.

Variable	Barrel	Endcap
$\sigma_{i\eta i\eta}$	< 0.013	< 0.034
H/E	< 0.15	< 0.10
Missing inner hits	≤ 1	≤ 1
$ d_{xy} $	< 0.02	< 0.05

Figure 6.17 – Measured FR as a function of $|\eta|$ for several E_T bins [91].

the FR is applied to a set of dijet candidate events to obtain the multijet background contribution to the dielectron invariant mass spectrum.

Estimation of the fake-rate

In practice, the FR is estimated from a jets sample, for which already some loose electron selection is applied. The jets sample is built from events that pass one of the single photon triggers in Table 6.4 and do not have more than one reconstructed ECAL-driven GSF electron candidate with $E_T > 10$ GeV. The one GSF electron candidate only requirement reduces the contamination from $DY \rightarrow ee$ events of the sample. The events are weighted by the smallest prescale of the selecting triggers. The GSF electron candidates have to pass a loose selection defined in Table 6.14. The FR is defined as the ratio of loose electron candidates that pass the HEEP selection, to the total number of loose electron candidates. Contaminations to the FR measurement come from W +jets and γ +jets, but also from $t\bar{t}$, tW , $DY \rightarrow \tau\tau$ and WW events. These contaminations are subtracted from estimations from simulations.

The measured FR for various E_T ranges as a function of η is shown in Figure 6.17. In the barrel region ($|\eta| < 1.442$) the FR stays flat for all E_T ranges and in the endcaps a linear increase with respect to $|\eta|$ is observed. Figure 6.18 shows the measured FR as a function of E_T in the barrel region and in the region $1.8 < |\eta| < 2.0$. Three functions are fitted to the measurement in the low, medium and high E_T regions and the

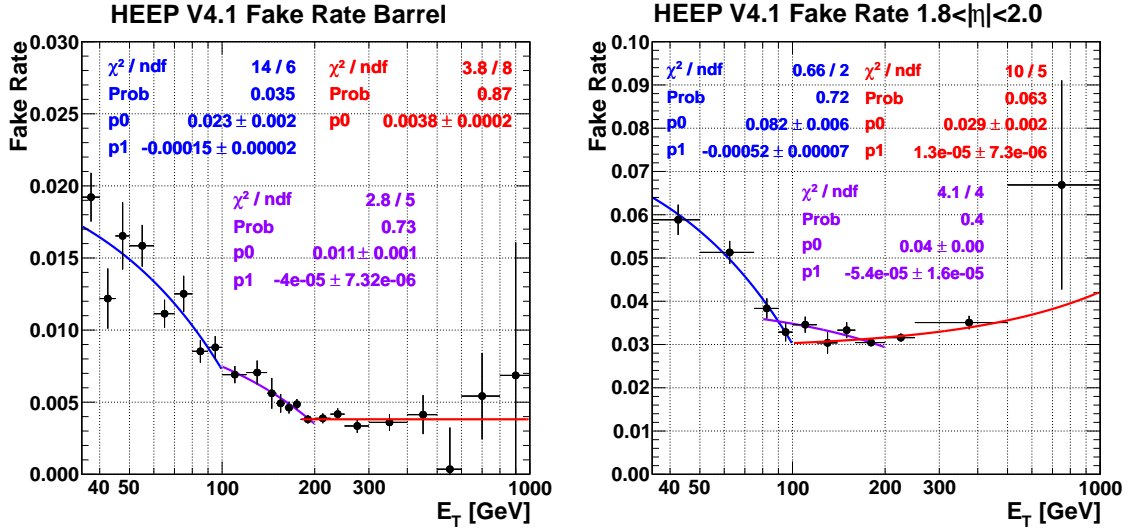


Figure 6.18 – Measured FR as a function of E_T for the barrel (left) and for the region $1.8 < |\eta| < 2.0$ (right). Polynomials are fitted to the measured data in different E_T ranges [91].

Table 6.15 – Functional form of the FR for the barrel and endcap regions [91].

Detector region	E_T in GeV	Fake-rate parametrisation
Barrel	$35 \leq E_T < 98.0$	$0.0226 - 1.53 \times 10^{-4} \frac{E_T}{\text{GeV}}$
	$98.0 \leq E_T < 191.9$	$0.0115 - 3.98 \times 10^{-5} \frac{E_T}{\text{GeV}}$
	$E_T \geq 191.9$	0.00382
Endcap	$35 \leq E_T < 89.9$	$0.0823 - 5.22 \times 10^{-4} \frac{E_T}{\text{GeV}} + 0.065 \times (\eta - 1.9)$
	$89.9 \leq E_T < 166.4$	$0.0403 - 5.45 \times 10^{-5} \frac{E_T}{\text{GeV}} + 0.065 \times (\eta - 1.9)$
	$E_T \geq 166.4$	$0.0290 + 1.32 \times 10^{-5} \frac{E_T}{\text{GeV}} + 0.065 \times (\eta - 1.9)$

intersection of the fits are taken as the boundary between two regions. The functional form for the FR is given in Table 6.15. For the endcap, the $|\eta|$ dependence of the parametrisation is extrapolated from the measurement in the region $1.8 < |\eta| < 2.0$, assuming a linear increase with $|\eta|$.

Validation of the fake-rate

For the validation of the FR the dijet component of the dielectron invariant mass spectrum is estimated for events where one electron candidate passes the HEEP selection and one fails it but passes the loose electron candidate selection. The value for the FR is defined by the loose electron candidate that fails the HEEP selection. The events are weighted by the factor $\text{FR}/(1 - \text{FR})$ to apply the FR, taking into account that events with two HEEP electron candidates are not selected. The resulting invariant mass spectra are plotted in Figure 6.19 for the barrel-barrel, barrel-endcap and endcap-endcap channels. The W +jets and γ +jets backgrounds are estimated

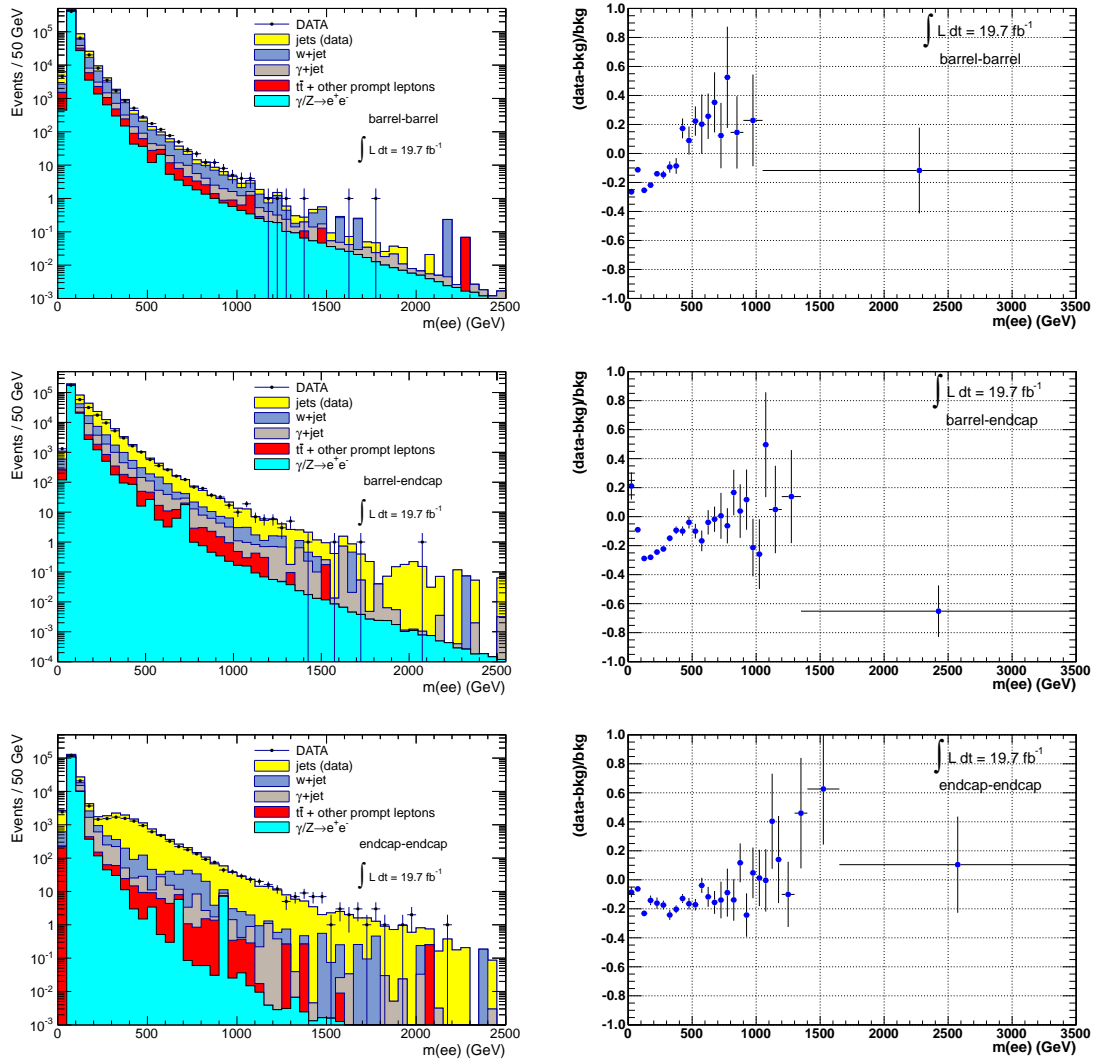


Figure 6.19 – Mass spectra of events with one HEEP electron candidate and one loose electron candidate in the left row, and the corresponding data minus background over background distribution in the right row. Top: barrel-barrel events. Middle: barrel-endcap events. Bottom: endcap-endcap events [91].

from simulations. The endcap-endcap spectrum has the largest relative dijet contribution and offers the best test for the FR estimate, followed by the barrel-endcap spectrum. Based on these plots, the uncertainty on the absolute contribution of the jet background to the invariant mass spectrum is taken to be 40%.

Estimation of the jet background contribution

To obtain the absolute contribution of the jet background to the invariant mass spectrum, the FR is applied once to a sample of events with one HEEP electron candidate and one loose electron candidate that does not pass the HEEP selection (1-pass-1-fail). The loose electron candidate that fails the HEEP selection defines the value of the FR. Since the loose electron candidate must fail the HEEP selection, the event has to be weighted by a factor $1/(1 - \text{FR})$. The obtained contribution to the invariant mass spectrum estimates the W +jets and γ +jets backgrounds, but overestimates the dijet background by a factor of two because of combinatorial counting.

To correct this overestimation, a sample of events, where both electron candidates pass the loose selection only (2-fail), is selected and the FR is applied for both loose electrons. Each event in the 2-fail sample has to be weighted by a factor $1/(1 - \text{FR}_{e_1}) \times 1/(1 - \text{FR}_{e_2})$, since both loose electron candidates must fail the HEEP selection. The invariant mass spectrum obtained from the 2-fail sample is then subtracted from the 1-pass-1-fail estimation.

The 1-pass-1-fail spectrum has a remaining contamination from $DY \rightarrow ee$ events at the Z peak, which is corrected from simulated events. Finally, around the Z peak, the 2-fail estimation is used solely, normalised to the jet background estimate one both sides of the Z peak. This is done to prevent the jet background estimation from becoming negative in this region, when the $DY \rightarrow ee$ contamination is subtracted.

6.4.3 Reducible dielectron background

The third category of background events includes processes that have two isolated electrons in the final state. The dominant process of this group is the $t\bar{t}$ process, where the top / antitop quark decays involve a W^+ / W^- boson, respectively, which subsequently decay to a positron and an electron. Another process is the tW process, where the top again decays to a W boson and the two bosons decay to electrons. The dilepton decays from WW , WZ and ZZ diboson production can also lead to final states with at least two electrons. Finally, the $DY \rightarrow \tau\tau$ process with the taus decaying to electrons contributes as well to this category. Since all these processes involve additional particles in their decays, which could be used to veto such events, they are part of the reducible dielectron background. For this analysis however, the approach is to keep the selection as inclusive as possible and use simulated samples for the estimation of the reducible background contributions. The samples used are listed in Table 6.2 with their NLO or NNLO cross sections. For the high mass $t\bar{t}$ samples an NNLO/NLO K-factor is calculated from the inclusive $t\bar{t}$ samples NLO cross section and the theoretical NNLO calculation [84].

In order to validate the reducible background samples, a data driven method called the $e\mu$ method, described in detail in Section 6.5, is used, which compares the samples with the data by looking at the $e\mu$ invariant mass spectrum.

6.4.4 Background fit

For the limit setting, an analytic function is used to describe the background shape in the search region above 200 GeV. The function that was found to fit the shape of the combined backgrounds from SM processes, as described in the previous sections, well is

$$f_{bkg}(m|p_0, p_1, p_2, p_3) = e^{p_0 + p_1 \cdot m + p_2 \cdot m^2} \cdot m^{p_3}, \quad (6.8)$$

which was fitted for the barrel-barrel and barrel-endcap channels, separately, in the range $200 \text{ GeV} < m_{ee} < 3500 \text{ GeV}$. The background spectra together with the fitted function can be seen in Figure 6.20.

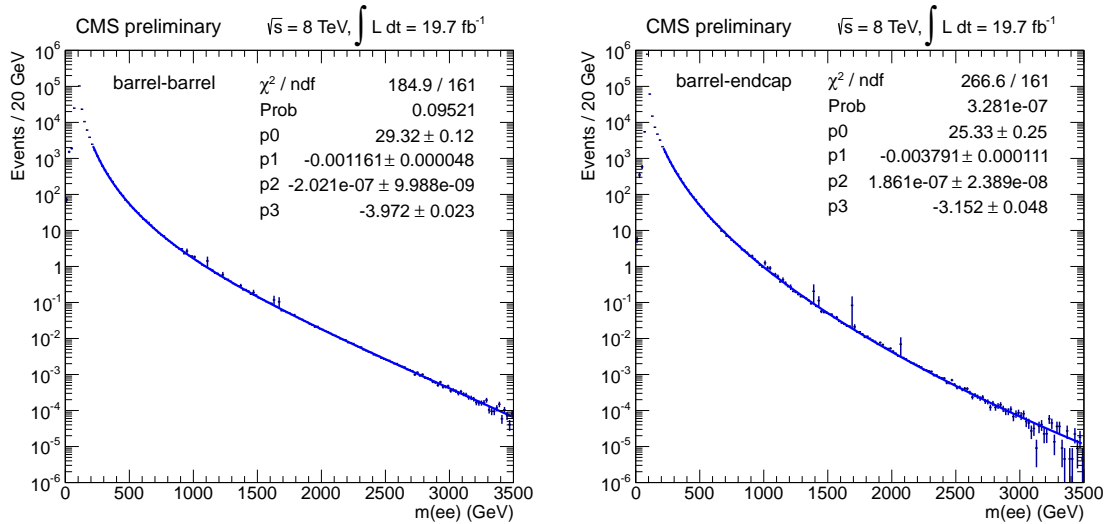


Figure 6.20 – The left plot shows the fit of the function from Equation (6.8) to the estimated total background in the barrel-barrel channel, and the right plot shows the fit in the barrel-endcap channel [87].

6.5 $e\mu$ method

The $e\mu$ method is used to validate, using the data, the simulation of the reducible background with two isolated electrons in the final state. The idea is to make use of the lepton universality and assume that the decay to an electron is just as likely as the decay to a muon. The invariant mass spectrum from $e\mu$ events should yield twice as many events for the reducible background processes as the ee spectrum. Verifying the compatibility of data and background estimation from the simulated samples allows to validate the samples for the $t\bar{t}$, diboson, tW and DY processes.

Because of different reconstruction efficiencies for electrons and muons, the measured $e\mu$ invariant mass spectrum does not have exactly twice as many events as the ee spectrum, and a correction needs to be applied in the validation process.

Figures 6.21 to 6.23 show some of the Feynman diagrams for the dominant SM processes having two isolated electrons in the final state.

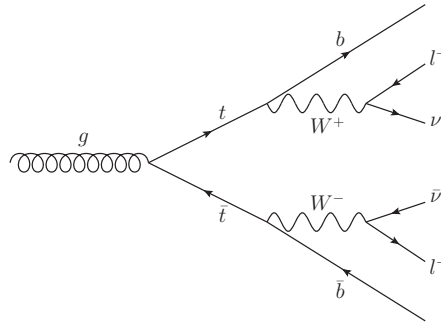


Figure 6.21 – Feynman diagram of a $t\bar{t}$ process decaying to leptons.

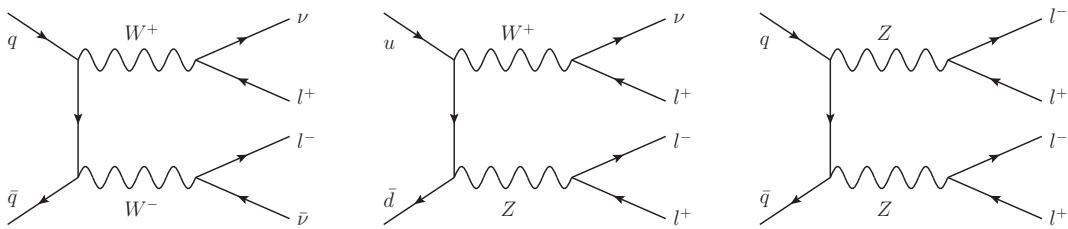


Figure 6.22 – Feynman diagrams for diboson production and subsequent decays to leptons.

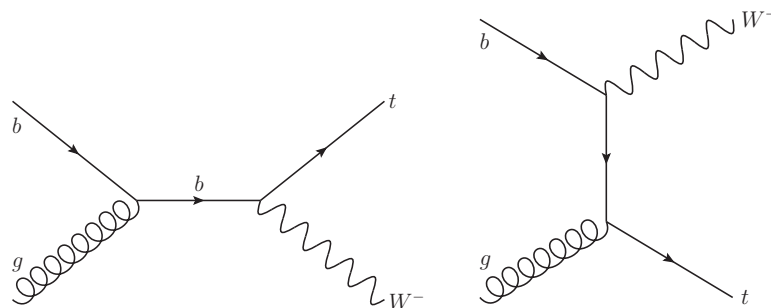


Figure 6.23 – Feynman diagrams for tW production

Table 6.16 – Estimated efficiencies and data to simulation scale factors for the HLT_Mu22_Photon22_CaloIdL trigger for different pseudorapidity regions [97].

	Efficiency			Data / simulation scale factor
	L1	electron	muon	
$ \eta < 0.9$	99%	100%	92.9%	0.976
$0.9 \leq \eta < 1.2$	99%	100%	83.1%	0.954
$1.2 \leq \eta $	99%	100%	80.3%	0.983

6.5.1 Event selection

Dataset and simulated samples

The MuEG datasets listed in Table 6.1 are used for the analysis, with a total integrated luminosity of $19.7 \pm 0.5 \text{ fb}^{-1}$. For the backgrounds the same samples as for the ee invariant mass spectrum are used, which are listed in Table 6.2.

Trigger

The trigger HLT_Mu22_Photon22_CaloIdL used for the event selection requires an online reconstructed muon candidate and a photon candidate with $p_T > 22 \text{ GeV}$ and $E_T > 22 \text{ GeV}$, respectively. Requiring a photon candidate and not an electron candidate is a looser requirement since no track matching to the SC is necessary. The trigger was unrescaled for the complete period of data taking. The efficiency for the trigger is estimated from the combination of efficiencies of other triggers that have parts in common with the muon-photon trigger. The efficiency of the L1_Mu3p5_EG12 trigger, seeding the muon-photon trigger, is taken to be the same as for an electron L1 trigger, with 99%. The photon part of the trigger is assumed to be fully efficient, and the efficiency for the muon part of the trigger is taken from the HLT_Mu40_eta2p1 single muon trigger and ranges from 80% to 93%, depending on the pseudorapidity. The scale factor between data and simulation for the HLT_Mu40_eta2p1 trigger was measured to range from 0.95 to 0.98 [97], depending on pseudorapidity, and the muon-photon triggers scale factor adopts these values, despite the lower online muon p_T threshold. Table 6.16 lists the estimated values for the trigger efficiency and data to simulation scale factor.

Electron candidate selection

Electron candidates are selected from reconstructed GSF electron candidates, using the same HEEP selection as the main analysis. The criteria for the HEEP selection are listed in Table 6.8.

The efficiency scale factors for the GSF electron candidate reconstruction were measured by the electron/photon object subgroup of CMS, with the tag-and-probe method for different pseudorapidity regions and electron E_T ranges. Since the focus lies on the high invariant mass $e\mu$ spectrum, the scale factors for $E_T > 50 \text{ GeV}$ were

taken for all GSF electron candidates. Table 6.17 lists the GSF electron candidate reconstruction efficiency scale factors.

The efficiency scale factors for the HEEP selection are listed in Table 6.9.

Table 6.17 – Scale factors for the GSF electron candidate reconstruction efficiency, measured by the CMS electron/photon object group with the tag-and-probe method.

	Scale factor \pm stat. \pm syst.
$ \eta < 0.8$	$0.990 \pm 0.001 \pm 0.004$
$0.8 \leq \eta < 1.4442$	$0.991 \pm 0.001 \pm 0.004$
$1.4442 \leq \eta < 1.566$	$0.974 \pm 0.009 \pm 0.006$
$1.566 \leq \eta < 2.0$	$0.990 \pm 0.003 \pm 0.004$
$2.0 \leq \eta < 2.5$	$0.998 \pm 0.004 \pm 0.004$

Muon candidate selection

Muon candidates are selected using criteria optimised for muons with high transverse momentum. The selection is similar to the one used for the search for new physics using dimuons [97].

- Muon candidate tracks must be reconstructed globally from hits in the inner tracker and the muon stations, and as tracker muon tracks from the inner tracker only.
- The global muon track fit must include hits from ≥ 6 tracker layers.
- The global muon track fit must have ≥ 1 hit in the pixel detector.
- The global muon track fit must have ≥ 1 hit in the muon system.
- The tracker muon track is required to be matched to at least two muon station segments.
- The transverse impact parameter of the tracker muon track with respect to the primary vertex must be smaller than 2 mm.
- $|\eta| < 2.4$
- $p_T > 35$ GeV
- Relative transverse momentum uncertainty $\delta p_T/p_T < 0.3$.
- Tracker isolation: The sum of the p_T of all tracks, except the muon candidates tracker track, within a cone of $\Delta R < 0.3$ must be smaller than 10% of the muons p_T . Tracks have to be within 2 mm on the z -axis of the muon tracks primary vertex to be counted in the isolation.

For the track fit selection the Tune P algorithm described in Section 5.2.5 is used.

The efficiencies and data to simulation scale factors of the muon selection were measured by the muon object group of CMS, from data with a tag-and-probe technique, using muons from the Z decay. The resulting values for the scale factors, which are constant up to a p_T of 500 GeV, are listed in Table 6.18. A systematic uncertainty of 0.57% has to be added to the statistic uncertainties listed in the table.

Table 6.18 – Muon selection data to simulation scale factors measured for different pseudorapidity ranges, by the muon object group of CMS.

	Scale factor
$ \eta < 0.9$	0.9896 ± 0.0003
$0.9 \leq \eta < 1.2$	0.9917 ± 0.0006
$1.2 \leq \eta < 2.1$	0.9946 ± 0.0004
$2.1 \leq \eta < 2.4$	0.9920 ± 0.0012

$e\mu$ event selection

An $e\mu$ event is selected if it contains at least one electron candidate passing the HEEP selection, and at least one muon candidate passing the high- p_T muon selection. The event must be triggered by the muon-photon trigger described in Section 6.5.1. Muons that deposit some of their energy in the ECAL can be misreconstructed as electron candidates that pass the HEEP selection. Since, in such a case, the HEEP electron candidate and the muon candidate have essentially the same direction, the invariant mass calculated from such events peaks at zero. In order to suppress this, HEEP electron candidates are vetoed if there is a muon candidate with $p_T > 5$ GeV within $\Delta R < 0.1$. In case that there are more than one HEEP electron candidate or muon candidate in the event, the lepton candidate with the, respectively, highest E_T or p_T is chosen.

6.5.2 SM signals and backgrounds

For the $e\mu$ method the $t\bar{t}$, diboson and tW SM processes, decaying with at least one isolated electron and at least one isolated muon in the final state, are considered as the signal, since the aim is to validate the simulation of those samples. Also DY events that decay to taus and subsequently to electrons and muons are falling into this category. However, the contribution from this process is suppressed by the small branching fraction and only plays a role around the mass of the Z peak.

Backgrounds for the $e\mu$ method are processes with misreconstructed leptons. The two most important ones are the contribution from W +jets events and the one from multijet events, where the jet(s) are misreconstructed as electrons or muons. DY events decaying to one of the first two lepton families also give a small contribution, when additional lepton candidates are in the event. The DY and the W +jets backgrounds are estimated from simulated samples.

The simulated samples are weighted depending on the number on primary vertices, according to the difference between the simulated PU distribution to the measured PU distribution shown in Figure 3.7.

The relative normalisation of the background samples comes from the SM cross sections listed in Table 6.2. For the absolute normalisation the normalisation factors are obtained from the normalisation of the backgrounds to the yield at the Z peak in the dielectron spectrum. For $e\mu$ events with the HEEP electron candidate in the barrel of the detector the factor is 0.997 and for events where the HEEP electron candidate is in the endcap it is 0.934.

The uncertainties on the cross sections for the simulated samples are listed in Table 6.19. They are extracted from the theoretical cross sections obtained with different calculators, depending on the process, as discussed in Section 6.1.2. At the time the analysis was performed, uncertainties for cross sections at $\sqrt{s} = 8$ TeV were not yet available for many of the processes, so that the uncertainties from $\sqrt{s} = 7$ TeV collisions were taken from [98]. The exception are the uncertainties for $t\bar{t}$ and tW cross sections, which were already calculated for $\sqrt{s} = 8$ TeV and could be taken from [99].

Table 6.19 – Uncertainty on the theory cross section for the simulated processes, taken from [98, 99]. The samples corresponding to the processes are listed in Table 6.2.

Process	Uncertainty
$t\bar{t}$	3.6%
$DY \rightarrow \tau\tau$	5.4%
WW	3.5%
WZ	3.8%
ZZ	2.5%
$tW, \bar{t}W$	6.9%
$DY \rightarrow ee$	5.4%
$DY \rightarrow \mu\mu$	5.4%
W+jets	5.0%

Multijet background

Estimating the multijet background from simulated samples is not feasible because of the small misreconstruction rate for the jets. Instead, the invariant mass spectrum is obtained from the same-sign $e\mu$ spectrum, where the electron and muon have the same charge. All the SM processes, except WZ or ZZ production, giving two leptons in the final state lead to oppositely charged $e\mu$ pairs. For the multijet background however, the spectrum for the same-sign or opposite-sign $e\mu$ pair should be the same. To estimate the multijet background, the contributions of the other SM processes, estimated from simulations, are subtracted from the data spectrum, and the remaining spectrum is taken to come from multijet events. In the case that the data yield in one bin of the same-sign invariant mass histogram is already smaller than the combined

yield of all SM processes, the yield for the multijet background is set to zero. Since this overestimates the total yield of the multijet background, the obtained spectrum is scaled by a factor of 0.995, derived from the ratio of 1210 expected versus 1216 found multijet events when bins below zero are suppressed. The multijet background spectrum from same-sign events is used as the estimation for the multijet background for the opposite-sign spectrum.

6.5.3 $e\mu$ invariant mass spectrum

The invariant mass spectra for $e\mu$ pairs are presented in Figure 6.24 and the cumulative spectra in Figure 6.25. The plots show the spectra for all $e\mu$ pairs, for opposite-sign $e\mu$ pairs, where the multijet background estimation comes from the same-sign spectrum, and for same-sign $e\mu$ pairs. The binning of the histograms follows the resolution in the high mass region and has a minimal bin width in the low mass region, where the resolution would otherwise dictate a very small bin width. The error bars shown for the data are 68% Poisson intervals. By construction, the agreement between the data and simulation plus multijet background is almost perfect in the same-sign spectrum, for bins where the data yield is higher than the yield from simulations without the multijet background. The event yields above certain masses for data and the SM expectations are listed in Tables 6.20 to 6.22 for all, same-sign, and opposite-sign $e\mu$ pairs, respectively. The event yields and statistical uncertainties in the tables are extracted from the histograms, with the exception of the multijet contribution. The systematic uncertainties for the simulated samples contain the uncertainties on the cross section listed in Table 6.19, the uncertainty on the muon efficiency scale factor and the uncertainties on the electron efficiency scale factor, depending on the electron candidates p_T and η . For the multijet contribution only the event yield is taken from the histograms. The multijet uncertainties in each column are calculated by adding in quadrature the uncertainties from the SS data and the other SS samples, based on the formula

$$N_{\text{multijet}} = N_{\text{data}}^{SS} - (N_{\text{t}\bar{\text{t}}\text{-like}}^{SS} + N_{\text{other cont.}}^{SS}) , \quad (6.9)$$

where the $\text{t}\bar{\text{t}}$ -like contribution includes the SS yields from $\text{t}\bar{\text{t}}$, $\text{DY} \rightarrow \tau\tau$, diboson and tW processes and the other contaminations include the SS yields from $\text{DY} \rightarrow \mu\mu$, $\text{DY} \rightarrow \text{ee}$ and W+jets . An additional correction factor taking into account the small difference between the multijet event yield from the histogram and the multijet event yield calculated from the SS data yield and the other SS samples from the table is applied to the multijet uncertainties. The multijet yields and uncertainties from the SS table are used in the OS table and doubled in the combined table. For the rows showing the total contamination, which is the combination of $\text{DY} \rightarrow \mu\mu$, $\text{DY} \rightarrow \text{ee}$, W+jets and multijet background the uncertainties are calculated based

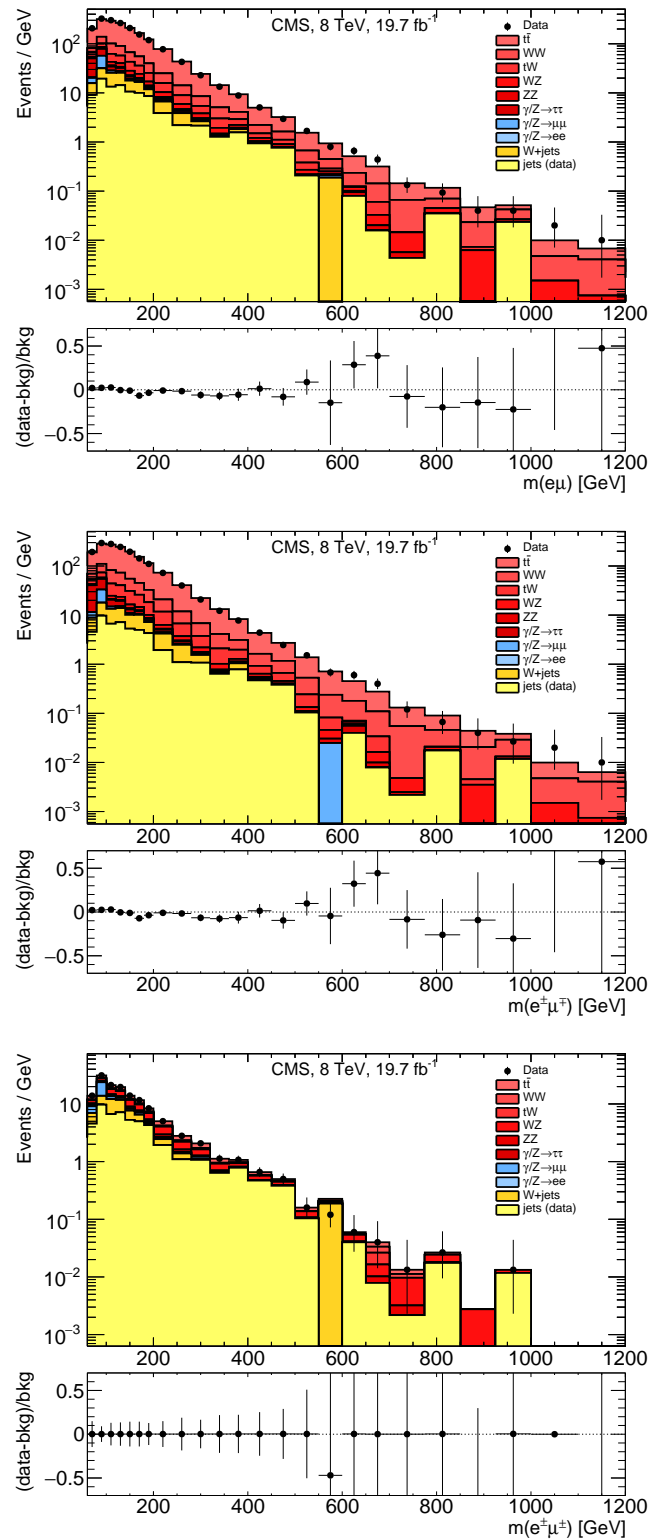


Figure 6.24 – Invariant mass spectra of selected $e\mu$ pairs. Top: All $e\mu$ pairs. Middle: opposite-sign $e\mu$ pairs. Bottom: same-sign $e\mu$ pairs. Below the histograms, the data minus background over background distribution is plotted.

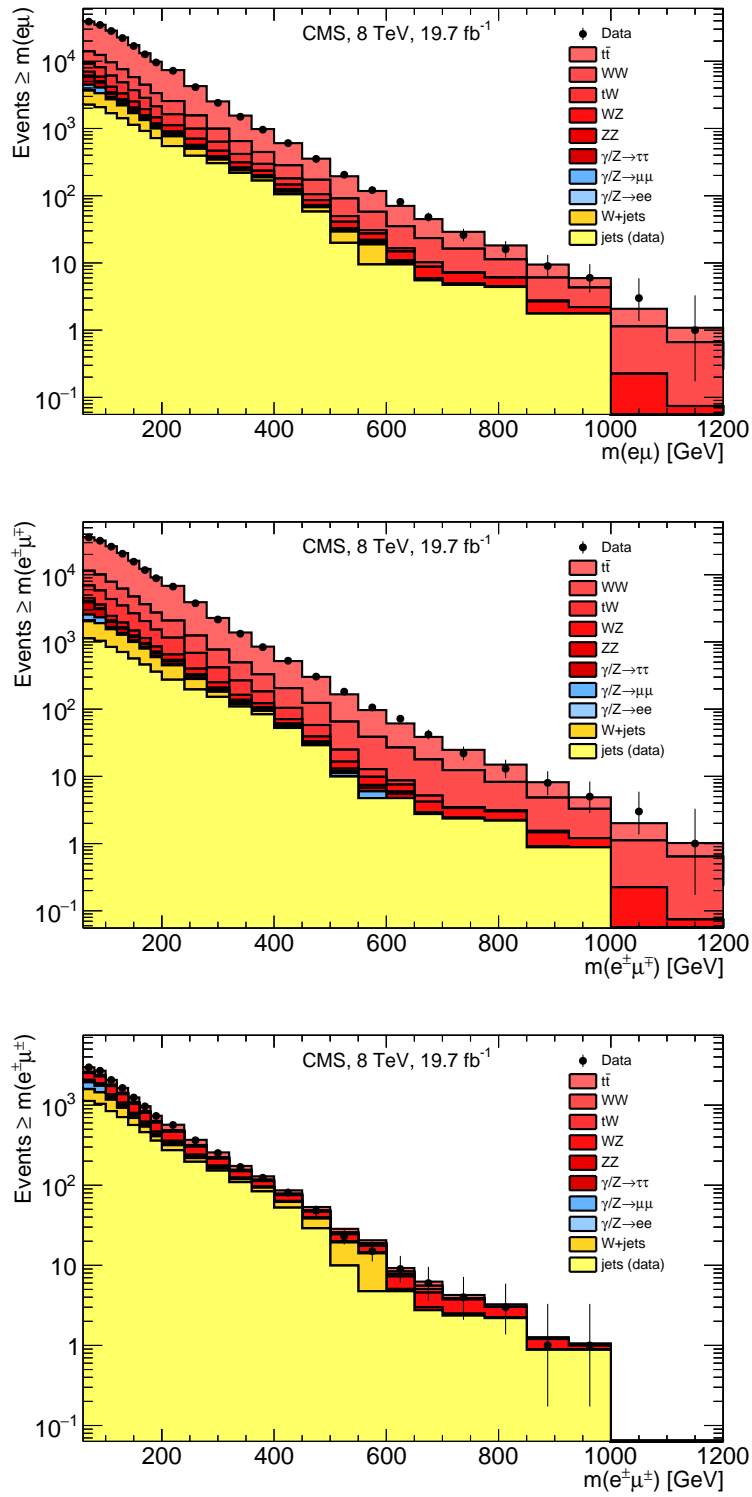


Figure 6.25 – Cumulated invariant mass spectra of selected $e\mu$ pairs. Top: All $e\mu$ pairs. Middle: opposite-sign $e\mu$ pairs. Bottom: same-sign $e\mu$ pairs.

Table 6.20 – Number of $e\mu$ events with different mass thresholds for data and SM expectations, with statistic and systematic uncertainties.

Source	Number of events			
	$m_{e\mu} > 60$ GeV	$m_{e\mu} > 120$ GeV	$m_{e\mu} > 200$ GeV	$m_{e\mu} > 400$ GeV
Data	38842	22151	7221	606
$t\bar{t}$	$24979.3 \pm 65.7 \pm 939.9$	$15087.5 \pm 49.9 \pm 570.0$	$4836.6 \pm 26.1 \pm 184.5$	$322.4 \pm 4.8 \pm 12.4$
WW	$4590.9 \pm 23.2 \pm 167.9$	$2751.3 \pm 17.9 \pm 100.9$	$934.3 \pm 10.5 \pm 34.6$	$103.0 \pm 3.5 \pm 3.9$
tW	$2478.8 \pm 34.3 \pm 173.3$	$1546.0 \pm 27.1 \pm 108.2$	$509.1 \pm 15.6 \pm 35.7$	$33.8 \pm 4.0 \pm 2.4$
WZ	$890.1 \pm 8.0 \pm 35.1$	$591.9 \pm 6.5 \pm 23.4$	$217.1 \pm 3.9 \pm 8.6$	$21.8 \pm 1.2 \pm 0.9$
ZZ	$226.8 \pm 2.9 \pm 6.2$	$143.5 \pm 2.3 \pm 3.9$	$46.6 \pm 1.3 \pm 1.3$	$4.0 \pm 0.4 \pm 0.1$
DY $\rightarrow \tau\tau$	$1367.7 \pm 32.8 \pm 75.1$	$223.4 \pm 13.3 \pm 12.3$	$49.4 \pm 6.1 \pm 2.7$	$3.0 \pm 1.4 \pm 0.2$
Total $t\bar{t}$ -like	$34533.6 \pm 84.7 \pm 973.9$	$20343.5 \pm 61.4 \pm 589.5$	$6593.2 \pm 33.0 \pm 191.3$	$488.1 \pm 7.4 \pm 13.2$
DY $\rightarrow \mu\mu$	$795.4 \pm 25.2 \pm 43.7$	$137.8 \pm 10.6 \pm 7.6$	$36.1 \pm 5.6 \pm 2.0$	$3.2 \pm 1.8 \pm 0.2$
DY $\rightarrow ee$	$19.4 \pm 4.2 \pm 1.1$	$10.7 \pm 3.0 \pm 0.6$	$1.7 \pm 1.2 \pm 0.1$	-
W+jets	$1402.5 \pm 118.2 \pm 71.6$	$783.4 \pm 88.2 \pm 40.0$	$217.1 \pm 46.3 \pm 11.1$	$9.3 \pm 9.3 \pm 0.5$
multijet	$2252.2 \pm 177.3 \pm 74.9$	$1415.5 \pm 125.9 \pm 37.3$	$546.6 \pm 64.7 \pm 11.9$	$104.8 \pm 29.1 \pm 1.7$
Total contamination	$4469.5 \pm 164.5 \pm 77.2$	$2347.4 \pm 121.7 \pm 42.9$	$801.5 \pm 68.2 \pm 14.4$	$117.4 \pm 22.6 \pm 1.4$
Total SM exp.	$39003.0 \pm 183.5 \pm 977.6$	$22690.9 \pm 135.0 \pm 591.0$	$7394.7 \pm 74.4 \pm 191.8$	$605.5 \pm 22.0 \pm 13.5$

Table 6.21 – Number of SS $e\mu$ events with different mass thresholds for data and SM expectations, with statistic and systematic uncertainties.

Source	Number of SS events			
	$m_{e\mu} > 60$ GeV	$m_{e\mu} > 120$ GeV	$m_{e\mu} > 200$ GeV	$m_{e\mu} > 400$ GeV
Data	2967	1638	565	81
$t\bar{t}$	$371.2 \pm 7.9 \pm 14.0$	$217.4 \pm 5.8 \pm 8.2$	$83.4 \pm 3.3 \pm 3.2$	$8.1 \pm 0.8 \pm 0.3$
WW	$54.1 \pm 2.5 \pm 2.0$	$39.3 \pm 2.1 \pm 1.4$	$16.7 \pm 1.4 \pm 0.6$	$2.3 \pm 0.5 \pm 0.1$
tW	$31.7 \pm 3.9 \pm 2.2$	$17.6 \pm 2.9 \pm 1.2$	$5.2 \pm 1.6 \pm 0.4$	$0.8 \pm 0.6 \pm 0.1$
WZ	$445.2 \pm 5.6 \pm 17.6$	$295.5 \pm 4.6 \pm 11.7$	$106.1 \pm 2.8 \pm 4.2$	$11.5 \pm 0.9 \pm 0.5$
ZZ	$109.9 \pm 2.0 \pm 3.0$	$71.3 \pm 1.6 \pm 1.9$	$24.0 \pm 1.0 \pm 0.7$	$1.7 \pm 0.3 \pm 0.0$
DY $\rightarrow \tau\tau$	$30.3 \pm 4.8 \pm 1.7$	$7.4 \pm 2.4 \pm 0.4$	$3.2 \pm 1.6 \pm 0.2$	-
Total $t\bar{t}$ -like	$1042.5 \pm 11.9 \pm 22.9$	$648.4 \pm 8.8 \pm 14.5$	$238.6 \pm 5.2 \pm 5.4$	$24.4 \pm 1.4 \pm 0.6$
DY $\rightarrow \mu\mu$	$334.0 \pm 16.4 \pm 18.3$	$62.3 \pm 7.1 \pm 3.4$	$13.3 \pm 3.2 \pm 0.7$	$0.1 \pm 0.1 \pm 0.0$
DY $\rightarrow ee$	$9.6 \pm 3.0 \pm 0.5$	$4.9 \pm 2.1 \pm 0.3$	$1.7 \pm 1.2 \pm 0.1$	-
W+jets	$455.2 \pm 66.8 \pm 23.2$	$216.9 \pm 46.6 \pm 11.1$	$42.4 \pm 20.2 \pm 2.2$	$9.3 \pm 9.3 \pm 0.5$
multijet	$1126.1 \pm 88.7 \pm 37.4$	$707.8 \pm 63.0 \pm 18.7$	$273.3 \pm 32.3 \pm 5.9$	$52.4 \pm 14.5 \pm 0.8$
Total contamination	$1924.9 \pm 55.8 \pm 22.9$	$991.9 \pm 41.5 \pm 14.6$	$330.7 \pm 24.6 \pm 5.4$	$61.9 \pm 10.0 \pm 0.6$
Total SM exp.	$2967.4 \pm 54.5 \pm 0.0$	$1640.3 \pm 40.5 \pm 0.0$	$569.3 \pm 24.0 \pm 0.0$	$86.3 \pm 9.6 \pm 0.0$

on the following formulas for the yields

$$\begin{aligned}
N_{\text{cont.}}^{SS} &= N_{\text{multijet}} + N_{\text{other cont.}}^{SS} = N_{\text{data}}^{SS} - N_{\text{t}\bar{\text{t}}\text{-like}}^{SS} \\
N_{\text{cont.}}^{OS} &= N_{\text{multijet}} + N_{\text{other cont.}}^{OS} = N_{\text{data}}^{SS} - N_{\text{t}\bar{\text{t}}\text{-like}}^{SS} - N_{\text{other cont.}}^{SS} + N_{\text{other cont.}}^{OS} \\
N_{\text{cont.}} &= 2N_{\text{multijet}} + N_{\text{other cont.}}^{SS} + N_{\text{other cont.}}^{OS} \\
&= 2(N_{\text{data}}^{SS} - N_{\text{t}\bar{\text{t}}\text{-like}}^{SS}) - N_{\text{other cont.}}^{SS} + N_{\text{other cont.}}^{OS}.
\end{aligned} \tag{6.10}$$

Table 6.22 – Number of OS $e\mu$ events with different mass thresholds for data and SM expectations, with statistic and systematic uncertainties.

Source	Number of OS events			
	$m_{e\mu} > 60$ GeV	$m_{e\mu} > 120$ GeV	$m_{e\mu} > 200$ GeV	$m_{e\mu} > 400$ GeV
Data	35875	20513	6656	525
$t\bar{t}$	$24608.1 \pm 65.2 \pm 926.0$	$14870.1 \pm 49.5 \pm 561.8$	$4753.2 \pm 25.9 \pm 181.3$	$314.3 \pm 4.7 \pm 12.1$
WW	$4536.8 \pm 23.0 \pm 165.9$	$2712.0 \pm 17.8 \pm 99.5$	$917.7 \pm 10.4 \pm 34.0$	$100.7 \pm 3.4 \pm 3.8$
tW	$2447.1 \pm 34.1 \pm 171.0$	$1528.4 \pm 27.0 \pm 107.0$	$503.9 \pm 15.5 \pm 35.4$	$33.1 \pm 4.0 \pm 2.3$
WZ	$444.8 \pm 5.6 \pm 17.5$	$296.4 \pm 4.6 \pm 11.7$	$111.0 \pm 2.8 \pm 4.4$	$10.2 \pm 0.8 \pm 0.4$
ZZ	$116.9 \pm 2.1 \pm 3.2$	$72.2 \pm 1.7 \pm 2.0$	$22.6 \pm 0.9 \pm 0.6$	$2.3 \pm 0.3 \pm 0.1$
DY $\rightarrow \tau\tau$	$1337.4 \pm 32.5 \pm 73.5$	$216.0 \pm 13.1 \pm 11.9$	$46.2 \pm 5.9 \pm 2.6$	$3.0 \pm 1.4 \pm 0.2$
Total $t\bar{t}$ -like	$33491.1 \pm 83.9 \pm 959.1$	$19695.1 \pm 60.8 \pm 580.8$	$6354.6 \pm 32.6 \pm 187.9$	$463.7 \pm 7.2 \pm 12.9$
DY $\rightarrow \mu\mu$	$461.4 \pm 19.2 \pm 25.3$	$75.5 \pm 7.9 \pm 4.2$	$22.8 \pm 4.5 \pm 1.3$	$3.1 \pm 1.8 \pm 0.2$
DY $\rightarrow ee$	$9.8 \pm 2.9 \pm 0.5$	$5.8 \pm 2.2 \pm 0.3$	-	-
W+jets	$947.2 \pm 97.5 \pm 48.4$	$566.5 \pm 74.9 \pm 29.0$	$174.7 \pm 41.7 \pm 8.9$	-
multijet	$1126.1 \pm 88.7 \pm 37.4$	$707.8 \pm 63.0 \pm 18.7$	$273.3 \pm 32.3 \pm 5.9$	$52.4 \pm 14.5 \pm 0.8$
Total contamination	$2544.5 \pm 133.2 \pm 66.2$	$1355.5 \pm 98.2 \pm 34.7$	$470.8 \pm 53.1 \pm 10.9$	$55.5 \pm 14.6 \pm 0.8$
Total SM exp.	$36035.6 \pm 157.4 \pm 977.6$	$21050.6 \pm 115.4 \pm 591.0$	$6825.4 \pm 62.0 \pm 191.7$	$519.1 \pm 15.2 \pm 13.4$

For the rows showing the total SM expectation the formulas used are

$$\begin{aligned}
N_{\text{tot}}^{SS} &= N_{\text{multijet}} + N_{t\bar{t}\text{-like}}^{SS} + N_{\text{other cont.}}^{SS} = N_{\text{data}}^{SS} \\
N_{\text{tot}}^{OS} &= N_{\text{multijet}} + N_{t\bar{t}\text{-like}}^{OS} + N_{\text{other cont.}}^{OS} \\
&= N_{\text{data}}^{SS} - N_{t\bar{t}\text{-like}}^{SS} - N_{\text{other cont.}}^{SS} + N_{t\bar{t}\text{-like}}^{OS} + N_{\text{other cont.}}^{OS} \quad (6.11) \\
N_{\text{tot}} &= 2N_{\text{multijet}} + N_{t\bar{t}\text{-like}} + N_{\text{other cont.}} \\
&= 2N_{\text{data}}^{SS} - N_{t\bar{t}\text{-like}}^{SS} - N_{\text{other cont.}}^{SS} + N_{t\bar{t}\text{-like}}^{OS} + N_{\text{other cont.}}^{OS} .
\end{aligned}$$

The yields in the tables are taken from the histograms, and correction factors for the difference between the yields in the table and the yields from the formulas are applied to the uncertainties. The statistic uncertainties of these yields are all uncorrelated so that the statistic uncertainties can be added in quadrature. The systematic uncertainties between the SS and OS samples are taken to be fully correlated, so that the uncertainties from the SS and OS components are added.

The agreement between the data and the simulated samples is good, which justifies the use of the simulated samples as the $t\bar{t}$ -like background for the dielectron analysis.

6.6 Invariant mass spectrum

The invariant mass spectra for dielectron events, selected as described in Section 6.1, is shown in Figure 6.26 for all selected events, barrel-barrel events and barrel-endcap events. The SM background estimations are obtained from simulations and from data, following the methods explained in Section 6.4. In the high mass region the binning of the x -axis is according to the resolution. The error bars drawn on the data points indicate the 68% Poisson intervals. Figure 6.27 shows cumulated versions of the invariant mass spectra, with each bin containing the number of events with an invariant mass greater or equal the bin mass. The plots in Figure 6.28 show the

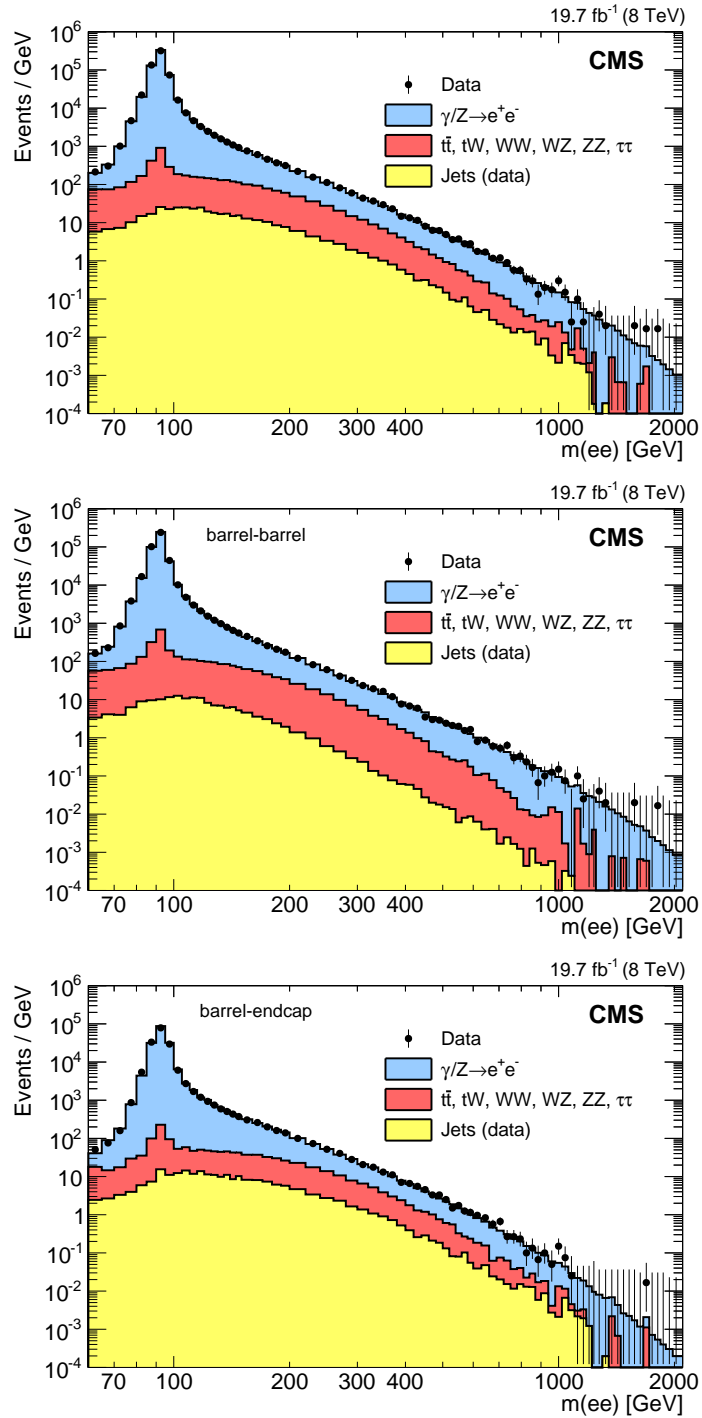


Figure 6.26 – Invariant mass spectra of selected dielectron pairs. Top: all selected pairs. Middle: barrel-barrel dielectron pairs. Bottom: barrel-endcap dielectron pairs [1].

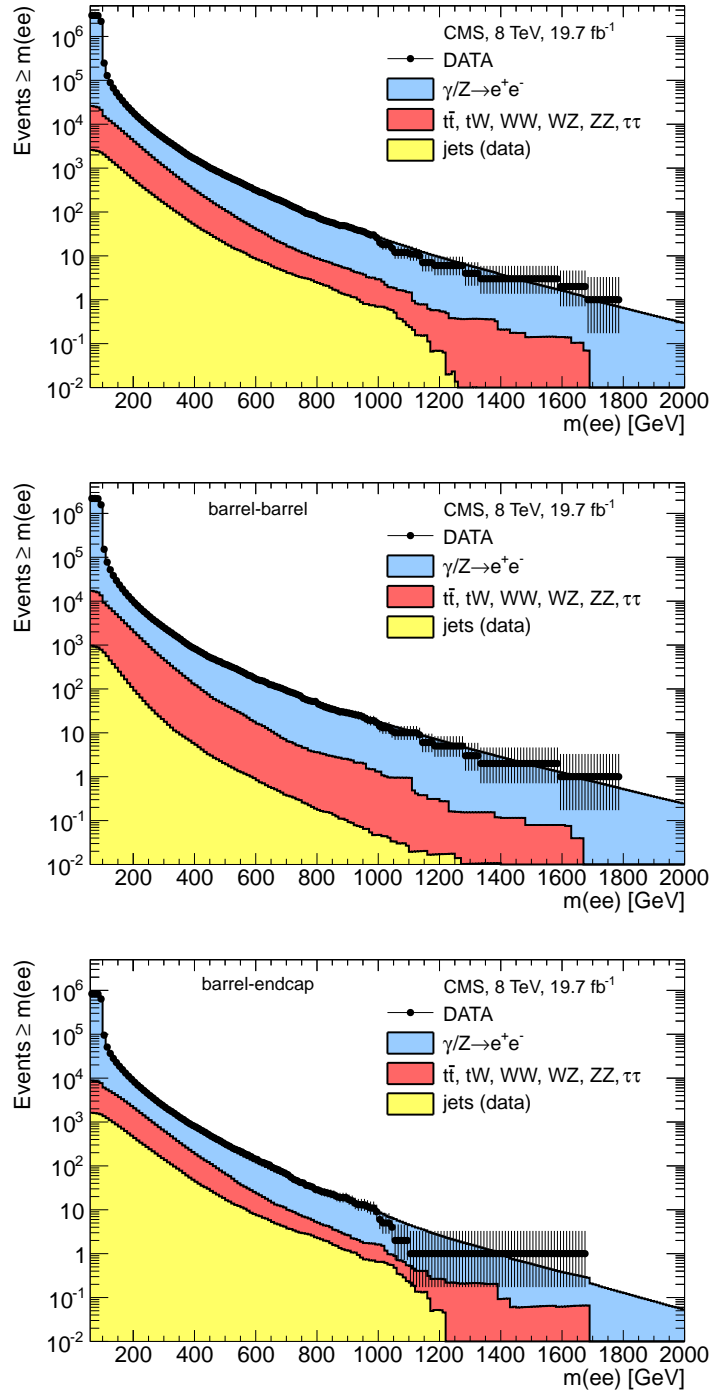


Figure 6.27 – Cumulated invariant mass spectra of selected dielectron pairs. Top: all selected pairs. Middle: barrel-barrel dielectron pairs. Bottom: barrel-endcap dielectron pairs [91].

Table 6.23 – Input for the Z cross section calculation and the resulting measured cross section.

Variable	Barrel-barrel	Barrel-endcap
N_{data}	2138549	798481
N_{bkg}	10318 ± 689	3745 ± 300
$A \times \epsilon$	0.0973 ± 0.0010	0.0382 ± 0.0004
ϵ_{trg}	0.9930 ± 0.0004	0.9926 ± 0.0003
sf_{ϵ}	0.994 ± 0.014	0.976 ± 0.014
\mathcal{L}_{int} (fb $^{-1}$)	19.7 ± 0.5	
σ_Z (pb)	$1125 \pm 15(\text{syst.}) \pm 29(\text{lumi.})$	$1090 \pm 15(\text{syst.}) \pm 28(\text{lumi.})$
σ_Z^{theory} (pb)	1117	

data minus background estimation over the background estimation, for the control region from invariant masses from 120 GeV to 200 GeV and for the search region with invariant masses greater than 200 GeV, respectively. In both, the control and the signal regions, the distributions can be fitted with a constant term that is compatible with zero.

The event with the highest invariant mass selected has $m(ee) = 1776$ GeV and an event display is shown in Figure 6.29.

A Z cross section measurement is performed in the region from $60 < M_{ee} < 120$ GeV, to further compare the measurement with the theory prediction. The cross section is defined as

$$\sigma_Z = \frac{N_{\text{data}} - N_{\text{bkg}}}{A \times \epsilon \cdot \epsilon_{\text{trg}} \cdot sf_{\epsilon} \cdot \mathcal{L}_{\text{int}}}, \quad (6.12)$$

where N_{data} and N_{bkg} are the event yields for data and the non-DY backgrounds, $A \times \epsilon$ is the acceptance times efficiency at the Z mass, ϵ_{trg} is the trigger efficiency, sf_{ϵ} is the selection efficiency scale factor for dielectrons obtained from Table 6.9 and \mathcal{L}_{int} is the integrated luminosity. The input values for the measurement and the resulting cross sections for the barrel-barrel and barrel-endcap event topologies are listed in Table 6.23. The difference of 3% between the barrel-barrel and barrel-endcap cross section can be partially explained with the energy scale shift between data and simulation in the barrel-endcap case. Compensating for the shift lowers the acceptance times efficiency in the barrel-endcap case by 2%, at which point the two cross sections agree within the uncertainties. Both results agree with the theoretical prediction for the cross section of 1117 pb [83], with a 5% uncertainty according to Table 6.19.

6.7 Statistical interpretation

No excesses over the SM expectation are seen in the invariant mass spectra that would indicate new physics. In this case, upper limits on the ratio of cross sections of a new resonance to the Z resonance are calculated.

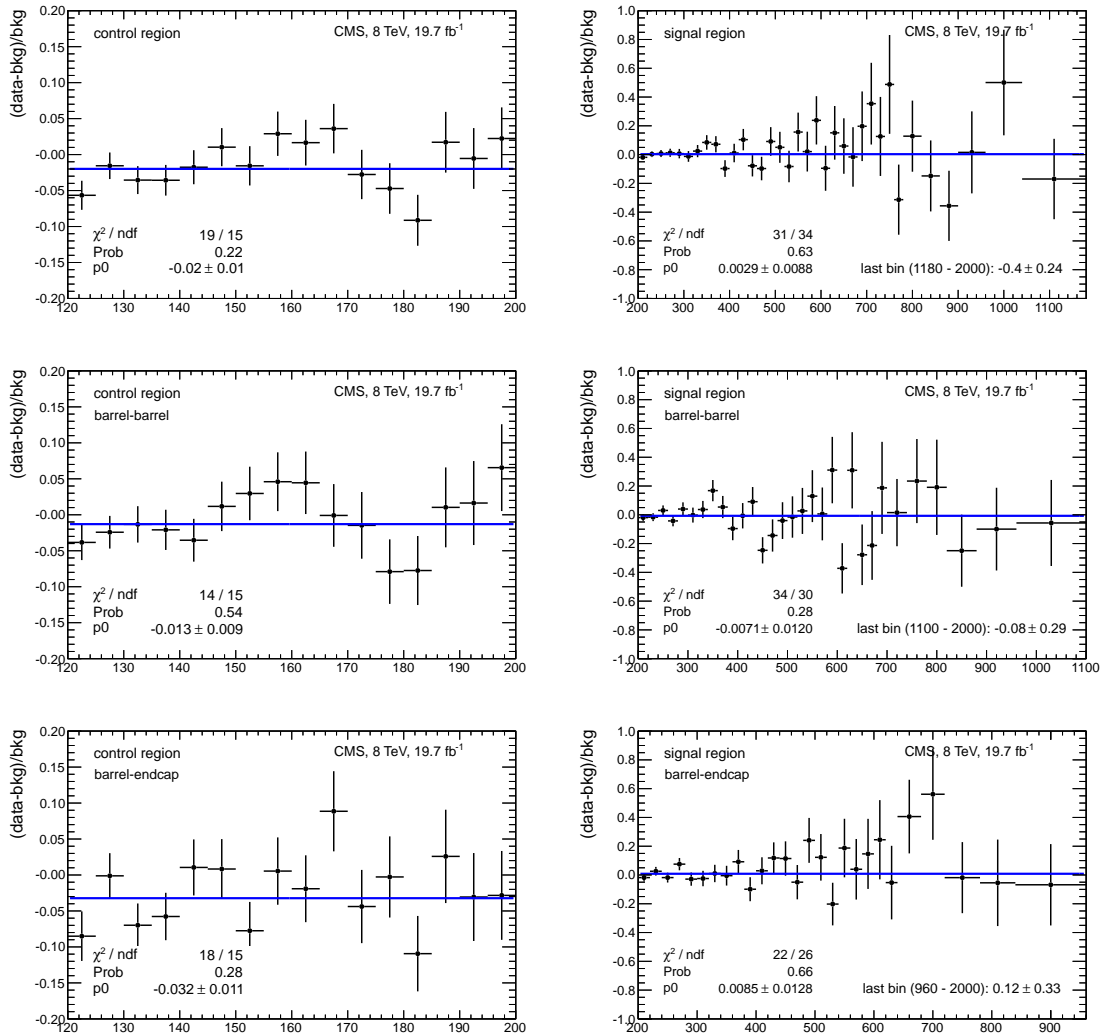


Figure 6.28 – Data minus background over background distribution for the selected dielectron pairs as a function of the dielectron invariant mass in GeV, in the control region (left) and the search region (right). Top: all selected pairs. Bottom left: barrel-barrel dielectron pairs. Bottom right: barrel-endcap dielectron pairs [91].

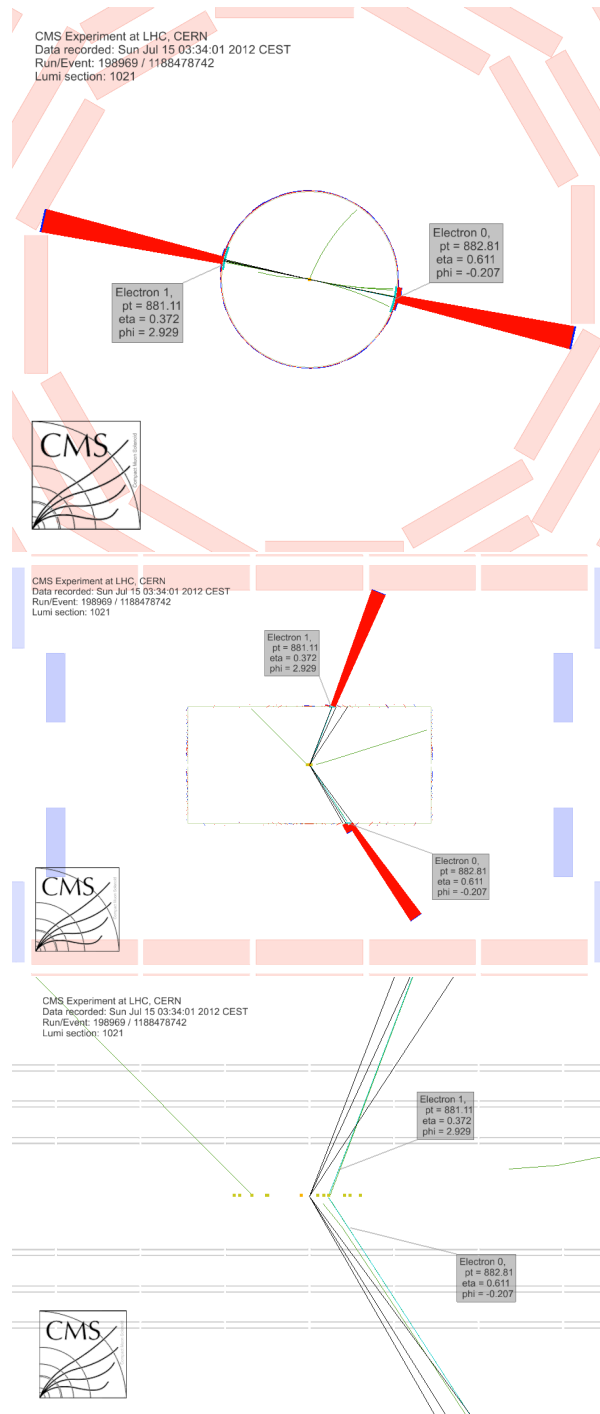


Figure 6.29 – Event display of the highest invariant mass event selected, with a mass of $m(ee) = 1776$ GeV. The top plot shows the event in the ρ - ϕ plane of the detector and the middle plot shows the ρ - z plane. The red (blue) bars indicate the energy in the ECAL (HCAL). Tracks with a $p_T > 3$ GeV are shown. The bottom plot shows magnified the interaction region in the ρ - z plane with the reconstructed primary vertices as dots. The horizontal lines indicate the position of the pixel detector layers. The two HEEP electron candidates tracks originate from one primary vertex.

6.7.1 Limit setting method

For the statistical procedure to set limits on new physics a Bayesian approach with an unbinned likelihood is chosen [3, 74]. The probability density function (pdf) is modeled as the sum of a resonant signal pdf and a steeply falling background pdf

$$f(m|\boldsymbol{\theta}, \boldsymbol{\nu}) = q_1(\boldsymbol{\theta}, \boldsymbol{\nu}) \cdot f_{\text{sig}}(m|\boldsymbol{\nu}) + (1 - q_1(\boldsymbol{\theta}, \boldsymbol{\nu})) \cdot f_{\text{bkg}}(m|\boldsymbol{\nu}), \quad (6.13)$$

where the observable is the measured invariant dielectron mass m , $\boldsymbol{\theta}$ is a vector of parameters of interest and $\boldsymbol{\nu}$ is a vector of nuisance parameters. The probability of a signal event is given by q_1 .

The signal pdf is modeled as the convolution of a non-relativistic Breit–Wigner shape, describing the natural shape of the resonance, and a Gaussian shape modeling the detector resolution

$$f_{\text{sig}}(m|\Gamma, \sigma) = \text{BW}(m|\Gamma) \otimes \text{Gauss}(m|\sigma), \quad (6.14)$$

where Γ is the width of the BW and σ the width of the Gaussian. The non-relativistic BW shape is defined as

$$\text{BW}(m|\Gamma) = A \cdot \frac{\Gamma}{m^2 + \left(\frac{\Gamma}{2}\right)^2}, \quad (6.15)$$

with A being a normalisation factor.

The background pdf shape was discussed in Section 6.4.4 and takes the form of Equation (6.8).

The only parameter of interest used for this analysis is the ratio between the cross section times branching fraction (BF) to dielectrons of a new resonance, and the cross section times BF of the Z resonance in the mass region of ± 30 GeV about the Z peak

$$R_\sigma = \frac{\sigma_{Z'} \cdot \text{BF}(Z' \rightarrow ee)}{\sigma_Z \cdot \text{BF}(Z \rightarrow ee)}. \quad (6.16)$$

This choice has the advantage that certain known uncertainties, and also possible unknown uncertainties that are the same or similar between the signal and the Z, cancel or at least are reduced. One example is the uncertainty on the integrated luminosity. The ratio from Equation (6.16) is connected to the signal event yield via the formula

$$\mu_{\text{sig}} = R_\sigma \frac{(A \times \epsilon)_{Z'}}{(A \times \epsilon)_Z} N_Z, \quad (6.17)$$

where $(A \times \epsilon)_{Z'}$ and $(A \times \epsilon)_Z$ are, respectively, the acceptance times efficiency of the Z' and the Z, and N_Z is the number of selected Z events defined in the mass region of ± 30 GeV around the Z peak.

The unbinned likelihood is defined as

$$\mathcal{L}(\mathbf{m}|R_\sigma, \boldsymbol{\nu}) = \prod_{i=1}^N f(m_i|R_\sigma, \boldsymbol{\nu}), \quad (6.18)$$

where the product is over the number of events in the dataset and \mathbf{m} is a vector of corresponding dielectron masses. Inserting the signal and background models, the equation is

$$\mathcal{L}(\mathbf{m}|R_\sigma, \boldsymbol{\nu}) = \frac{\mu(R_\sigma, \boldsymbol{\nu})^N e^{-\mu(R_\sigma, \boldsymbol{\nu})}}{N!} \prod_{i=1}^N \left(\frac{\mu_{\text{sig}}(R_\sigma, \boldsymbol{\nu})}{\mu(R_\sigma, \boldsymbol{\nu})} f_{\text{sig}}(m_i|\boldsymbol{\nu}) + \frac{\mu_{\text{bkg}}(\boldsymbol{\nu})}{\mu(R_\sigma, \boldsymbol{\nu})} f_{\text{bkg}}(m_i|\boldsymbol{\nu}) \right) \quad (6.19)$$

with $\mu(R_\sigma, \boldsymbol{\nu}) = \mu_{\text{sig}}(R_\sigma, \boldsymbol{\nu}) + \mu_{\text{bkg}}(\boldsymbol{\nu})$ being the event yield as a sum of the event yield from signal and background.

The nuisance parameters in the vector $\boldsymbol{\nu}$ have uncertainties that are taken into account by modeling the nuisance parameter as

$$\nu = \hat{\nu}(1 + \delta\nu)^\beta, \quad (6.20)$$

where $\hat{\nu}$ is the estimate of ν , $\delta\nu$ is the systematic uncertainty on ν and β is random number drawn from a Gaussian at the origin with a width equal to one. The likelihood is weighted by $\text{Gauss}(\beta|0, 1)$ for each nuisance parameter, which results in a Log-normal constraint of the nuisance parameter, giving

$$\mathcal{L}(\mathbf{m}|R_\sigma, \boldsymbol{\nu}) = \prod_j \left[\mathcal{L}(\mathbf{m}|R_\sigma, \hat{\nu}_j(1 + \delta\nu_j)^{\beta_j}) \cdot \frac{1}{\sqrt{2\pi}} e^{-\frac{\beta_j^2}{2}} \right], \quad (6.21)$$

where the product is over the nuisance parameters. Since the barrel-barrel and barrel-endcap channels have different parameters and, consequently, different likelihoods, the likelihood of a combination can be obtained by multiplying the two likelihoods.

With the likelihood function 95% confidence level (C.L.) upper limits are calculated using Bayes theorem

$$p(R_\sigma|\mathbf{m}) \cdot p(\mathbf{m}) = \mathcal{L}(\mathbf{m}|R_\sigma) \cdot p(R_\sigma), \quad (6.22)$$

that links the posterior pdf $p(R_\sigma|\mathbf{m})$ to the flat prior pdf $p(R_\sigma)$ using the likelihood function. Here, the nuisance parameters $\boldsymbol{\nu}$ are already integrated over. For the posterior pdf, it follows that

$$p(R_\sigma|\mathbf{m}) = \frac{\mathcal{L}(\mathbf{m}|R_\sigma) \cdot p(R_\sigma)}{p(\mathbf{m})} = \frac{\mathcal{L}(\mathbf{m}|R_\sigma) \cdot p(R_\sigma)}{\int \mathcal{L}(\mathbf{m}|R_\sigma) \cdot p(R_\sigma) dR_\sigma}. \quad (6.23)$$

Once the posterior pdf is calculated, an integration over the parameter of interest up to an upper limit of R_σ^{95} gives a value of 0.95 as in

$$\int_0^{R_\sigma^{95}} p(R_\sigma|\mathbf{m}) dR_\sigma = 0.95. \quad (6.24)$$

R_σ^{95} is then the observed 95% C.L. upper limit on the parameter of interest. The Metropolis–Hastings algorithm [100, 101], a Markov Chain Monte Carlo (MCMC) method, is used for the integration.

Table 6.24 – Input parameters for the upper limit calculation. Masses are in GeV

Variable	Barrel-barrel	Barrel-endcap
$N_Z(60 - 120 \text{ GeV})$	2138549	798481
$(A \times \epsilon)_Z(60 - 120 \text{ GeV})$	0.0973 ± 0.0010	0.0382 ± 0.0004
f_{bkg}	$e^{29.32 - 1.16 \times 10^{-3} \cdot m - 2.02 \times 10^{-7} \cdot m^2} \cdot m^{-3.97}$	$e^{25.33 - 3.79 \times 10^{-3} \cdot m + 1.86 \times 10^{-7} \cdot m^2} \cdot m^{-3.15}$
Mass resolution	$\sqrt{\frac{122.7^2}{m^2} + 1.019^2}$	$\sqrt{\frac{169.1^2}{m^2} + \frac{13.60^2}{m} + 1.38^2}$
Spin 1 $A \times \epsilon$	$0.592 - \frac{2.91 \times 10^5}{m^2 + 7.45 \times 10^5}$	$0.0635 - \frac{159}{m + 345} + \frac{7.304 \times 10^5}{m^2 + 1.81 \times 10^6}$
Spin 2 $A \times \epsilon$	$0.571 - \frac{2.97 \times 10^4}{m^2 + 1.32 \times 10^5}$	$-0.238 - \frac{1.16 \times 10^4}{m + 3.52 \times 10^4} + \frac{6.58 \times 10^4}{m^2 + 7.54 \times 10^6}$

Expected limits

To calculate the expected limits under the assumption that there is no signal, pseudo-data are generated following the background shape. The 95% C.L. limit for this pseudo-data is then calculated as described above for the real data. The expected limit is defined as the median of the 95% C.L. limits of many randomly drawn pseudo-datasets. In addition to the expected limits, bands defining the $\pm 1\sigma$ and $\pm 2\sigma$ uncertainty on the expected limit are also calculated from the distribution of the 95% C.L. limits of the pseudo-datasets.

Pseudo-data are generated by drawing a random number for the event yield N from a Poisson distribution with mean

$$\mu_{bkg} = \hat{\mu}_{bkg} (1 + \delta\mu_{bkg})^{\beta_{bkg}}, \quad (6.25)$$

where β_{bkg} is a random number drawn from a normal distribution of width $\delta\mu_{bkg}$, and $\hat{\mu}_{bkg}$ is the integral over the background shape, normalised to data below 200 GeV. Then the actual vector of dielectron masses is generated by drawing N random numbers according to the background pdf f_{bkg} .

6.7.2 Input for the limit calculation

The input for the limit calculation is listed in Table 6.24. Events in a mass window of ± 6 times the mass resolution around the resonance mass hypothesis are counted in the likelihood, if the total number of events is above 400. In case it is below 400 the lower edge of the window is adjusted until at least 400 events are present, in order to keep the statistical uncertainty at a negligible level. The reason for choosing only events in a narrow window around the resonance mass is to limit the number of background events to the number around the resonance, since it would be dominated by the number from the low mass side of the spectrum otherwise. The width of the BW is taken to be the width of the Z'_ψ model of 0.6% of the resonance mass. This ensures that the narrow width approximation is maintained and the interference with the DY process at the Z' peak give negligible contributions.

Systematic uncertainties

The systematic uncertainties for the limit setting are listed in Table 6.25. They

Table 6.25 – Systematic uncertainties on the input parameters for the limit calculation.

Observable	Origin	Uncertainty (%)
$(A \times \epsilon)_{Z'}/(A \times \epsilon)_Z$	ID efficiency	4 (barrel-barrel), 6 (barrel-endcap)
Mass scale	Energy scale uncertainty	1
DY background	PDF	$4.15 + 1.83 \times 10^{-3} \cdot \frac{m}{\text{GeV}} + 2.68 \times 10^{-6} \cdot \left(\frac{m}{\text{GeV}}\right)^2$
DY background	NLO electroweak	$-1 + 4.2 \times 10^{-3} \cdot \frac{m}{\text{GeV}}$
Jet background	Jet background estimation	30
$t\bar{t}$ background	cross section	2.6

come mainly from the ratio of acceptance times efficiency between the Z' and the Z , from the uncertainty on the mass scale and from the uncertainty on the number of DY background events. The uncertainties on the jet background and the $t\bar{t}$ background can be neglected, since those backgrounds are sufficiently small in the total background that the uncertainties have no effect on the final result. The remaining uncertainties on the background events come from the mass dependent PDF uncertainties of the DY background, that are estimated with PDF4LHC [102], and the mass dependent next-to-leading-order electroweak uncertainties on the DY cross section, estimated with the HORACE event generator [103]. The total uncertainty on the background is calculated as the quadratic sum of the single uncertainties and ranges from 6% at 200 GeV to 46% at 3500 GeV for the barrel-barrel channel. However, since the signal is a narrow resonance and the background a continuous spectrum, even a large uncertainty on the background does not affect the calculated limits much, as this would just result in a change of the background shape on a wide mass range, which is not compatible with the signal. Furthermore, the uncertainty on the background is not important in high invariant mass regions, where the expected background contribution is small and no events are observed.

6.7.3 Limit results

With the methods described above the observed and expected upper limits on the ratio of the cross section of a new resonance to the cross section of the Z resonance can be calculated for resonances with spin 1 and spin 2. These limits can be translated in the lower limit on the resonance mass of a specific model. Resonance masses below the intersection of the theoretical onshell cross section ratio with the observed cross section ratio limit can be excluded at 95% C.L. Only the onshell cross section of the model has to be taken into account in the narrow width approximation, not including the low mass tails of resonances produced at the kinematic limit. As shown in [104], taking only events from a window of $\pm 0.05 \cdot \sqrt{s}$ around the resonance mass ensures that the narrow width approximation holds for many models.

Figure 6.30 shows the 95% C.L. upper limits on the cross section ratio of a spin 1 resonance, together with theoretical onshell production cross sections for a Z'_{SSM} and a Z'_{ψ} model. In Figure 6.31 the 95% C.L. upper limits on the cross section ratio of a spin 2 resonance are shown, with theoretical predictions for the cross section

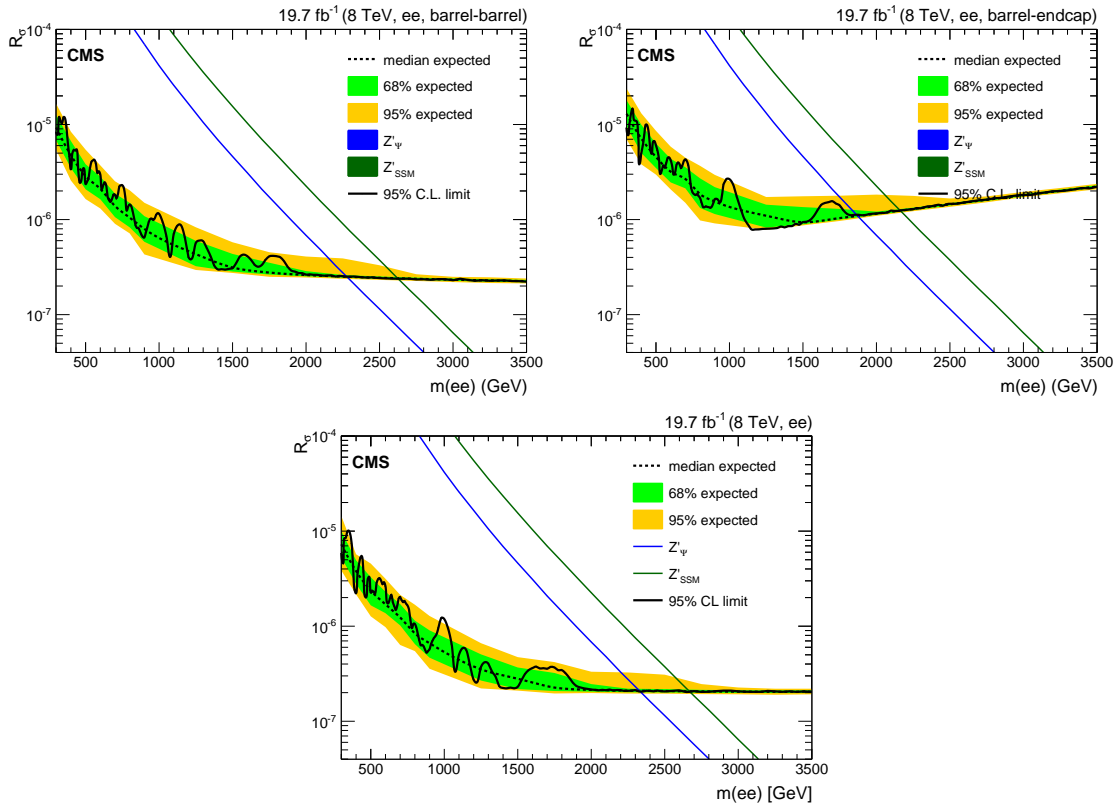


Figure 6.30 – 95% C.L. upper limits on R_σ for a spin 1 resonance in the barrel-barrel channel (top-left), the barrel-endcap channel (top-right) and for the combination of the two channels (bottom). The solid black line is the observed limit and the dashed black line shows the median expected limit. The two coloured bands indicate the 1σ and 2σ uncertainty band for the expected limit. The blue and green line represent the theoretical expectation for a Z'_ψ and Z'_{SSM} resonance, respectively [91].

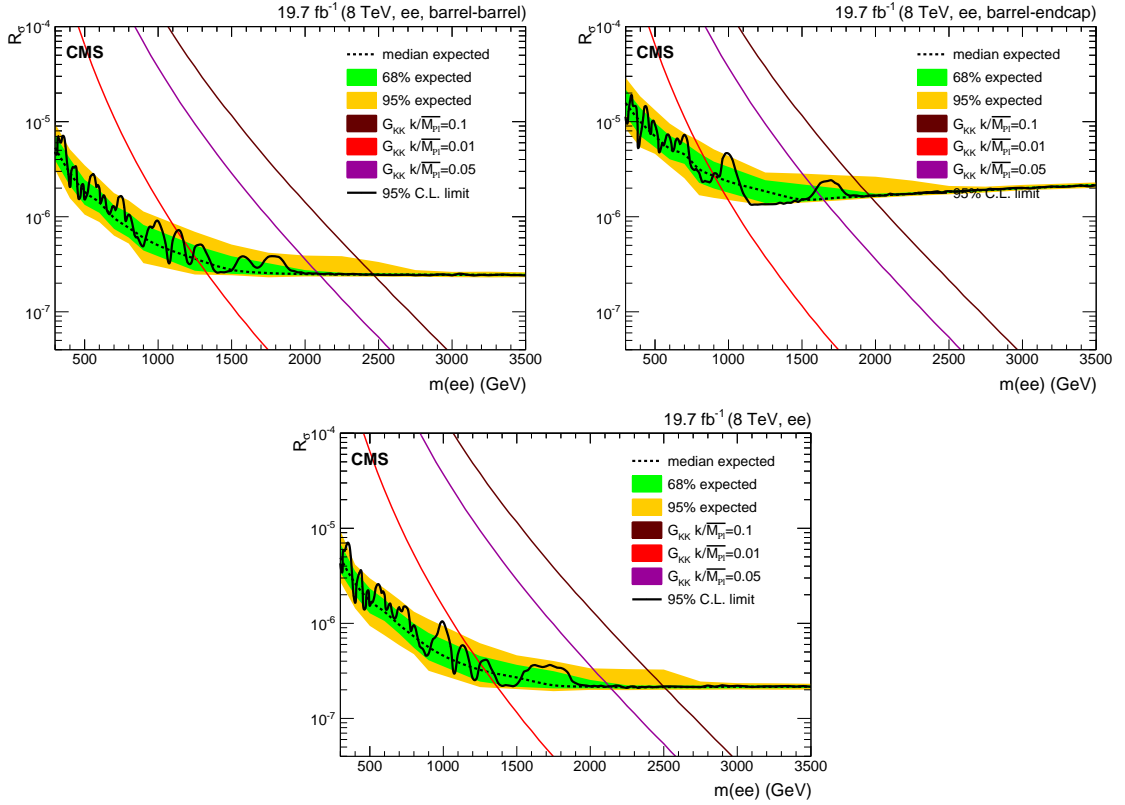


Figure 6.31 – 95% C.L. upper limits on R_σ for a spin 2 resonance in the barrel-barrel channel (top-left), the barrel-endcap channel (top-right) and for the combination of the two channels (bottom). The solid black line is the observed limit and the dashed black line shows the median expected limit. The two coloured bands indicate the 1σ and 2σ uncertainty band for the expected limit. The three steeply falling lines represent the theoretical expectation for an RS graviton with three different couplings [91].

Table 6.26 – Lower limit on the resonance mass for various spin 1 and spin 2 models. All masses are in GeV.

Model	barrel-barrel	barrel-endcap	dielectron	dielectron & dimuon
Z'_{SSM}	2630	2170	2670	2900
Z'_ψ	2280	1870	2340	2570
$G_{RS} k/M_{Pl} = 0.01$	1130	900	1250	1270
$G_{RS} k/M_{Pl} = 0.05$	2090	1590	2130	2350
$G_{RS} k/M_{Pl} = 0.1$	2470	1960	2500	2730

of an RS graviton with various couplings. The cross sections obtained from PYTHIA for the Z'_{SSM} and Z'_ψ models are reweighted with a mass dependent NNLO to LO K-factor obtained with the ZWPRODP calculator [105] for DY events. For the RS graviton cross section a constant K-factor of 1.3 is applied.

The comparison between the observed and the expected limits shows good agreement. Table 6.26 lists the lower limits on the resonance masses for the Z'_{SSM} and Z'_ψ spin 1 resonances and for an RS graviton spin 2 resonance with various couplings.

Combination with the dimuon resonance search

In parallel to the search for new resonances with dielectrons a similar search was performed using the dimuon invariant mass spectrum [1]. The sensitivity of the two searches is comparable and they are combined, with the assumption that the branching ratio to dielectrons and dimuons is the same. The resulting limits for a spin 1 and a spin 2 resonance are shown in Figure 6.32 and the last column of Table 6.26 gives the corresponding lower limits on the resonance masses for the various models considered.

6.8 Summary

In this chapter, the search for new massive narrow resonances with the dielectron invariant mass spectrum was introduced, using 19.7 fb^{-1} of data from pp collisions at 8 TeV.

The event selection for the search was optimised for final states with high energy electrons and with the goal to have a high efficiency whilst still rejecting background from jets well. As the selection efficiencies are different for the barrel and the endcaps, the dataset was split in events with two barrel electron candidates and events with one electron candidate emitted in the barrel and one in the endcap of the detector. Both channels were analysed separately. Events with both electron candidates emitted in the endcaps were not used in the analysis. The electron energy scale has been measured at the Z peak and the resolution at high mass was obtained from simulated DY samples.

Since the analysis was designed to be very inclusive in its events selection, a variety of backgrounds had to be considered. However, compared to the most important

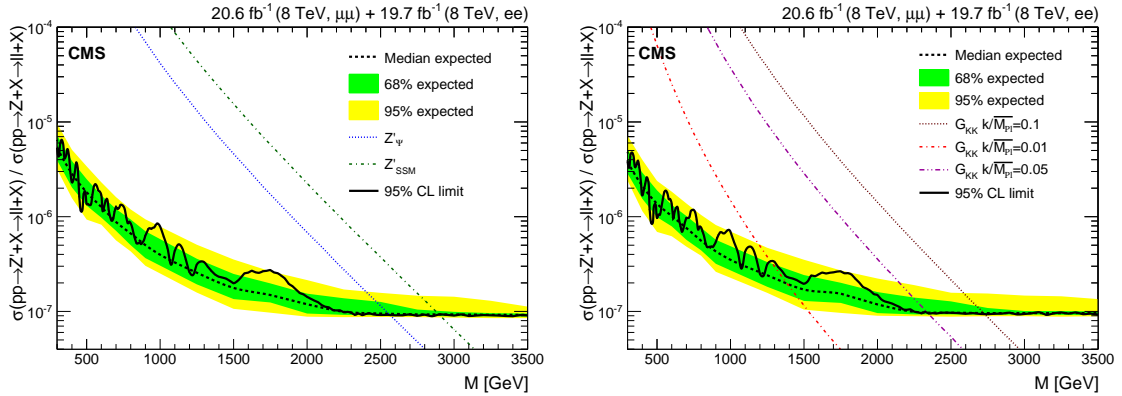


Figure 6.32 – Combined dielectron and dimuon 95% C.L. upper limits on R_σ for a spin 1 resonance (left) and a spin 2 resonance (right). The solid black line is the observed limit and the dashed black line shows the median expected limit. The two coloured bands indicate the 1σ and 2σ uncertainty band for the expected limit. The blue and green line in the left plot represent the theoretical expectation for a Z'_ψ and Z'_{SSM} resonance, respectively and the three steeply falling lines in the right plot represent the theoretical expectation for an RS graviton with three different couplings [1].

background, the irreducible Drell–Yan background, all other backgrounds only contribute a fraction of approximately 15% to the total number of background events in the search region above 200 GeV. All backgrounds that involve two isolated electrons were taken from simulated samples. Their accuracy was validated with the $e\mu$ invariant mass spectrum for all backgrounds but the one from the DY process, which does not decay to $e\mu$ pairs. Backgrounds involving jets that were misidentified and selected as electron candidates were estimated from data.

No new signal has been observed in the data. A Bayesian method, using an unbinned likelihood for a narrow signal over a smooth falling background, was chosen to set upper limits on the ratio of cross section of a new resonance to the Z cross section at the peak. Lower limits for several benchmark models were set on the new resonance mass. For a Z'_{SSM} , resonance masses up to 2670 GeV can be excluded at 95% C.L., with the combined limit of the barrel-barrel and the barrel-endcap channels, and for a Z'_ψ the upper limit on the resonance mass is 2340 GeV. RS gravitons serve as benchmark model for spin 2 resonances and upper limits between 1250 GeV, for a coupling of 0.01, up to 2500 GeV, for a coupling of 0.1, could be set.

These results were combined with the limits from the search for new resonances using the dimuon invariant mass spectrum, and are part of a paper that has been submitted to JHEP for publication recently [1]. With the combination, the lower mass limits for the benchmark models could be improved to 2900 GeV for the Z'_{SSM} , 2570 GeV for the Z'_ψ and to 1270 GeV ($c = 0.01$), 2350 GeV ($c = 0.05$) and 2730 GeV ($c = 0.1$) for the RS graviton.

Chapter 7

Search for new physics in $e\mu$ events

In this chapter the search for new physics in the invariant mass spectrum of electron-muon pair events is presented. The analysis uses the dataset recorded by the CMS detector in 2012 of pp collisions at a center-of-mass energy of $\sqrt{s} = 8$ TeV.

With an electron and a muon in the final state, the new physics process must violate lepton flavour conservation that is present in the SM for charged leptons. In this thesis the focus lies on a particular lepton flavour violation model, described in Chapter 2, which predicts a neutral gauge boson Z' . This new boson would lead to a resonance peak in the high mass tail of the $e\mu$ invariant mass spectrum, that can be easily spotted in the otherwise smoothly falling SM background. However, as to not be biased towards one model, the analysis is designed to be generic to accommodate other models as well.

The datasets and simulated SM samples are described in Section 7.1 and the simulation of the signal sample is explained in Section 7.2. In Section 7.3 the event selection is presented and the $e\mu$ invariant mass resolution estimation is detailed in Section 7.4. The relevant backgrounds are introduced in Section 7.5. Section 7.6 shows control variables and in Section 7.7 the invariant mass spectra are shown. Finally, the systematic uncertainties are discussed in Section 7.8 and the statistical interpretation is described in Section 7.9.

7.1 Dataset and simulated background samples

7.1.1 Datasets

For the $e\mu$ analysis, the SingleMu datasets from run A to D recorded in 2012 and listed in Table 7.1 have been used. These represent the full dataset recorded at a center-of-mass energy of 8 TeV. The data were reconstructed in the 22Jan2013 re-reconstructing campaign with the 5.2.7.patch5/6 versions of the CMS software [75], and only runs satisfying the data quality criteria were used. The integrated luminosity of the dataset is measured to be $19.7 \pm 0.5 \text{ fb}^{-1}$ [76]. For cross check studies, the MuEG dataset listed in Table 6.1 for the $e\mu$ method has been used.

Table 7.1 – Reconstructed datasets used in the analysis together with the run range of the dataset.

Dataset	Run range
/SingleMu/Run2012A-22Jan2013-v1/AOD	190456 - 193621
/SingleMu/Run2012B-22Jan2013-v1/AOD	193834 - 196531
/SingleMu/Run2012C-22Jan2013-v1/AOD	198022 - 203742
/SingleMu/Run2012D-22Jan2013-v1/AOD	203777 - 208686

Table 7.2 – Simulated SM process samples used, with the corresponding cross sections. The first block lists centrally produced CMS samples, while the samples in the second block are not part of the official CMS production but produced privately.

Process	Criteria	Generator	PDF	Cross section (pb)
$t\bar{t}$	inclusive	POWHEG	CT10	245.8 (NNLO)
$t\bar{t}$	$700 < M_{t\bar{t}} < 1000$ GeV	POWHEG	CT10	18.2 (NLO \times 1.17)
$t\bar{t}$	$M_{t\bar{t}} \geq 1000$ GeV	POWHEG	CT10	3.4 (NLO \times 1.17)
$tW \rightarrow l\bar{l}$	-	POWHEG	CTEQ6M	1.17 (approx. NNLO)
$\bar{t}W \rightarrow l\bar{l}$	-	POWHEG	CTEQ6M	1.17 (approx. NNLO)
$WW \rightarrow 2l2\nu$	-	POWHEG	CTEQ6L1	5.88 (NLO)
$WZ \rightarrow 3l\nu$	$M_{ll}(\gamma^*/Z) > 12$ GeV	MADGRAPH5	CTEQ6L1	1.09 (NLO)
$ZZ \rightarrow 4l$	$M_{ll}(\gamma^*/Z) > 12$ GeV	MADGRAPH5	CTEQ6L1	0.18 (NLO)
$DY \rightarrow l\bar{l}$	$M_{ll}(\gamma^*/Z) > 12$ GeV	MADGRAPH5	CTEQ6L1	3531.9 (NNLO)
$W\gamma \rightarrow l\nu\gamma$	inclusive	MADGRAPH5	CTEQ6L1	461.6 (LO)
$W\gamma \rightarrow l\nu\gamma$	$30 < p_T^\gamma < 50$ GeV	MADGRAPH5	CTEQ6L1	20.4 (LO)
$W\gamma \rightarrow l\nu\gamma$	$50 < p_T^\gamma < 130$ GeV	MADGRAPH5	CTEQ6L1	3.3 (LO)
$W\gamma \rightarrow l\nu\gamma$	$p_T^\gamma > 130$ GeV	MADGRAPH5	CTEQ6L1	0.26 (LO)
$t\bar{t} \rightarrow b\bar{b}e\nu\mu\nu$	$M_{e\mu} > 600$ GeV	POWHEG BOX	CT10	5.0×10^{-3} (NLO \times 1.17)
$WW \rightarrow e^-\nu\mu^+\nu$	$M_{e\mu} > 600$ GeV	POWHEG BOX	CT10	1.7×10^{-3} (generator NLO \times 1.07)
$WW \rightarrow e^+\nu\mu^-\nu$	$M_{e\mu} > 600$ GeV	POWHEG BOX	CT10	1.7×10^{-3} (generator NLO \times 1.07)

7.1.2 Simulated SM samples

For the background estimation, centrally produced CMS simulated MC samples were used that were generated with the POWHEG [78] or MADGRAPH5 [77] event generators, with the CT10 [12] or CTEQ6 [18] PDF sets. For the parton shower simulation and the hadronisation the PYTHIA6 [80] generator was used. To model the decay of τ -leptons, the TAUOLA[81] package was used for $t\bar{t}$ and single top samples. In order to have more simulated events with the desired final state, high mass $t\bar{t} \rightarrow b\bar{b}e\nu\mu\nu$ and $WW \rightarrow e\nu\mu\nu$ samples were generated in addition to the officially produced CMS samples, using the POWHEG BOX [79] generator with the CT10 PDF set. The privately produced samples have a filter applied at generator level that selects only events with the desired final state and a minimal invariant mass of 600 GeV for the $e\mu$ pair. All samples used are listed in Table 7.2 with their cross section and eventual additional selection criteria. The inclusive $W\gamma$ samples is only used to validate the combination of the other $W\gamma$ samples. The NNLO K-factor applied to the high mass $t\bar{t}$ samples, with the assumption that it is not mass dependent, is obtained from the factor between the NLO cross section, coming from the inclusive $t\bar{t}$ POWHEG sample,

and the theoretical NNLO cross section [84]. The approximate NNLO cross section for the tW samples is taken from [106]. For the high mass WW samples, the K-factor is taken to be the factor between the generator cross section of the privately produced samples and the MCFM NLO cross section for the inclusive WW production [107], under the assumption that it is independent of the mass.

It was found that for the first production of the CMS samples the geometrical position of the barrel muon system of the CMS detector had been accidentally shifted upwards by 2 mm with respect to the inner tracker. This means that the geometry of the simulated detector differs from the measured geometry of the actual detector, which results in a worse muon p_T resolution at high p_T in the simulation. In order to improve the accuracy of the simulation, two new alignment scenarios, called C1 and C2, were introduced. In the C1 scenario, the unintentional upwards shift was corrected by shifting the muon barrel system downwards by 2 mm from the initial alignment. For the C2 scenario, the muon stations were randomly misaligned from the position in a perfectly aligned detector, according to the statistical uncertainty of their position measurement from 2011 data. As will be shown in Section 7.4, the C1 scenario represents a more conservative approach and was, therefore, chosen as the new alignment for later sample productions. However, since the re-reconstruction of the already produced samples was not feasible because of limitations in computing resources, all centrally produced samples in the analysis use the initial alignment. The privately produced samples were reconstructed with the C1 and the C2 alignment for resolution studies. The C1 alignment is used solely for the rest of the analysis.

7.2 Signal samples

The signal samples are generated with the MADGRAPH5 [77] event generator with the CTEQ6L1 PDF set and hadronised with PYTHIA6 [80]. The LFV Z' model was implemented in FEYNRULES [108], which is a MATHEMATICA package from which the model description for MADGRAPH5 can be generated.

The implemented model includes the new Z'_{LFV} resonance production and also the excited photon a'_{LFV} .

In a first step, the absolute decay width of the two particles is estimated with MADGRAPH5. These values are then added as parameters of the particles for the generation of the events, which is done with MADGRAPH5 as well.

The output of MADGRAPH5 is a file containing the generated events in the Les Houches event format. This generated sample is given as an input to the PYTHIA6 generator, which does the parton showering and hadronisation to complete the generation step. The detector and pileup simulation and the reconstruction is done with the standard CMS workflow described already in Section 6.1.2. In order to study the impact of the muon alignment on the $e\mu$ invariant mass resolution, the signal samples were reconstructed with the C1 and the C2 alignment scenario.

The generated signal samples are listed in Table 7.3. For each sample 10 000 events were generated, with the exception of the sample in which both particles have

Table 7.3 – Simulated signal samples used, with the corresponding cross sections. The first block lists the samples where the mass of the Z'_{LFV} and the one of the a'_{LFV} are the same, while the second block contains samples with different masses for Z'_{LFV} and a'_{LFV} .

Signal process	Z'_{LFV} mass	a'_{LFV} mass	Cross section (pb)
$Z'_{\text{LFV}}/a'_{\text{LFV}} \rightarrow e\mu$	250 GeV		9.53×10^{-4} (LO)
$Z'_{\text{LFV}}/a'_{\text{LFV}} \rightarrow e\mu$	500 GeV		2.39×10^{-4} (LO)
$Z'_{\text{LFV}}/a'_{\text{LFV}} \rightarrow e\mu$	750 GeV		8.956×10^{-5} (LO)
$Z'_{\text{LFV}}/a'_{\text{LFV}} \rightarrow e\mu$	1000 GeV		3.862×10^{-5} (LO)
$Z'_{\text{LFV}}/a'_{\text{LFV}} \rightarrow e\mu$	1250 GeV		1.781×10^{-5} (LO)
$Z'_{\text{LFV}}/a'_{\text{LFV}} \rightarrow e\mu$	1500 GeV		8.503×10^{-6} (LO)
$Z'_{\text{LFV}}/a'_{\text{LFV}} \rightarrow e\mu$	1750 GeV		4.127×10^{-6} (LO)
$Z'_{\text{LFV}}/a'_{\text{LFV}} \rightarrow e\mu$	2000 GeV		2.014×10^{-6} (LO)
$Z'_{\text{LFV}}/a'_{\text{LFV}} \rightarrow e\mu$	2500 GeV		4.735×10^{-7} (LO)
$Z'_{\text{LFV}}/a'_{\text{LFV}} \rightarrow e\mu$	3000 GeV		1.059×10^{-7} (LO)
$Z'_{\text{LFV}}/a'_{\text{LFV}} \rightarrow e\mu$	3500 GeV		2.197×10^{-8} (LO)
$Z'_{\text{LFV}}/a'_{\text{LFV}} \rightarrow e\mu$	4000 GeV		4.155×10^{-9} (LO)
$Z'_{\text{LFV}}/a'_{\text{LFV}} \rightarrow e\mu$	5000 GeV		1.293×10^{-10} (LO)
$Z'_{\text{LFV}}/a'_{\text{LFV}} \rightarrow e\mu$	1000 GeV	20000 GeV	1.018×10^{-5} (LO)
$Z'_{\text{LFV}}/a'_{\text{LFV}} \rightarrow e\mu$	20000 GeV	1000 GeV	2.764×10^{-5} (LO)

a mass of 1 TeV, for which 100 000 events were generated. In order to study events without interference between Z'_{LFV} and a'_{LFV} , two samples were generated where one of the two particles was chosen to have a much larger mass than the other.

As discussed in Section 2.3, the $e^-\mu^+$ final state yields about ten times more events than the $e^+\mu^-$ final state, because the valence quarks of the proton can be used for the production of the Z'_{LFV} or a'_{LFV} . To investigate the interference effects, comparisons of generated lepton p_T and η are made between the signal sample where both, the Z'_{LFV} and a'_{LFV} mass are 1 TeV, and the two samples where only one of the two particle types has a mass of 1 TeV.

Figure 7.1 shows the comparisons of generated lepton p_T , for the $e^\mp\mu^\pm$, $e^-\mu^+$ and $e^+\mu^-$ final states. The distributions show a peak at half the resonance mass. No difference can be seen between the sample with interference between Z'_{LFV} and a'_{LFV} , and the ones without interference.

The comparisons of generated lepton η are presented in Figure 7.2, for the $e^\mp\mu^\pm$, $e^-\mu^+$ and $e^+\mu^-$ final states. A deformation of the pseudorapidity spectrum of the electron and the muon due to the interference can be seen in the distributions of the $e^\mp\mu^\pm$, and $e^-\mu^+$ final states, whereas the $e^+\mu^-$ shows no such feature. The pseudorapidity distribution of the electron shows a double peak structure and the distribution of the muon is more narrow than without interference, in the $e^-\mu^+$ final state. The distributions for the $e^\mp\mu^\pm$ final state show a similar shape since the $e^-\mu^+$ final state has approximately ten times more events than the $e^+\mu^-$ final state. The effects of the interference can be studied in the $\cos\theta^*$ distribution, where θ^* is defined

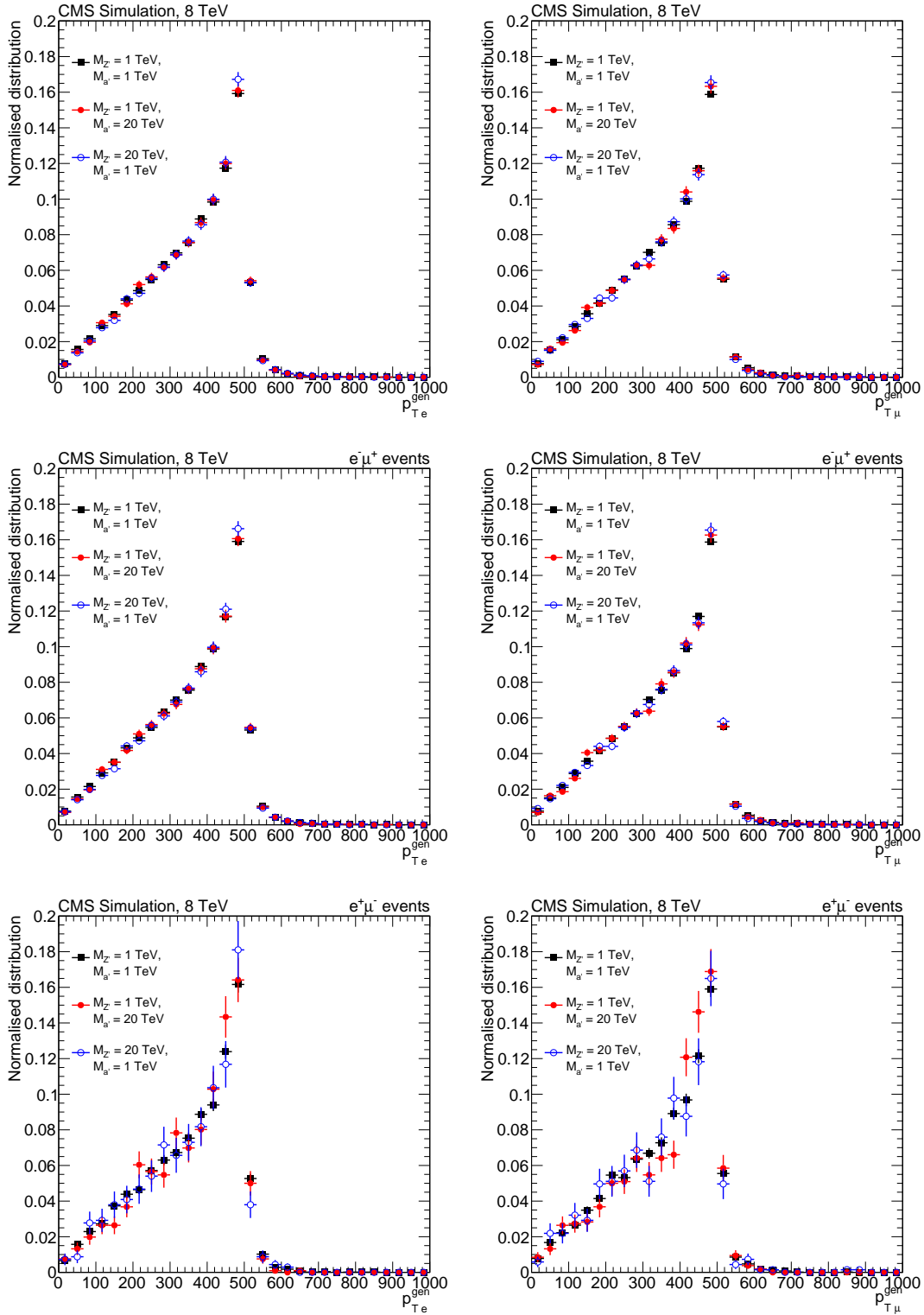


Figure 7.1 – Normalised p_T distribution for the generated electron (left column) and the generated muon (right column). The top row shows all $e^\mp\mu^\pm$ events, while the middle row and the bottom row show $e^-\mu^+$ events and $e^+\mu^-$ events, respectively.

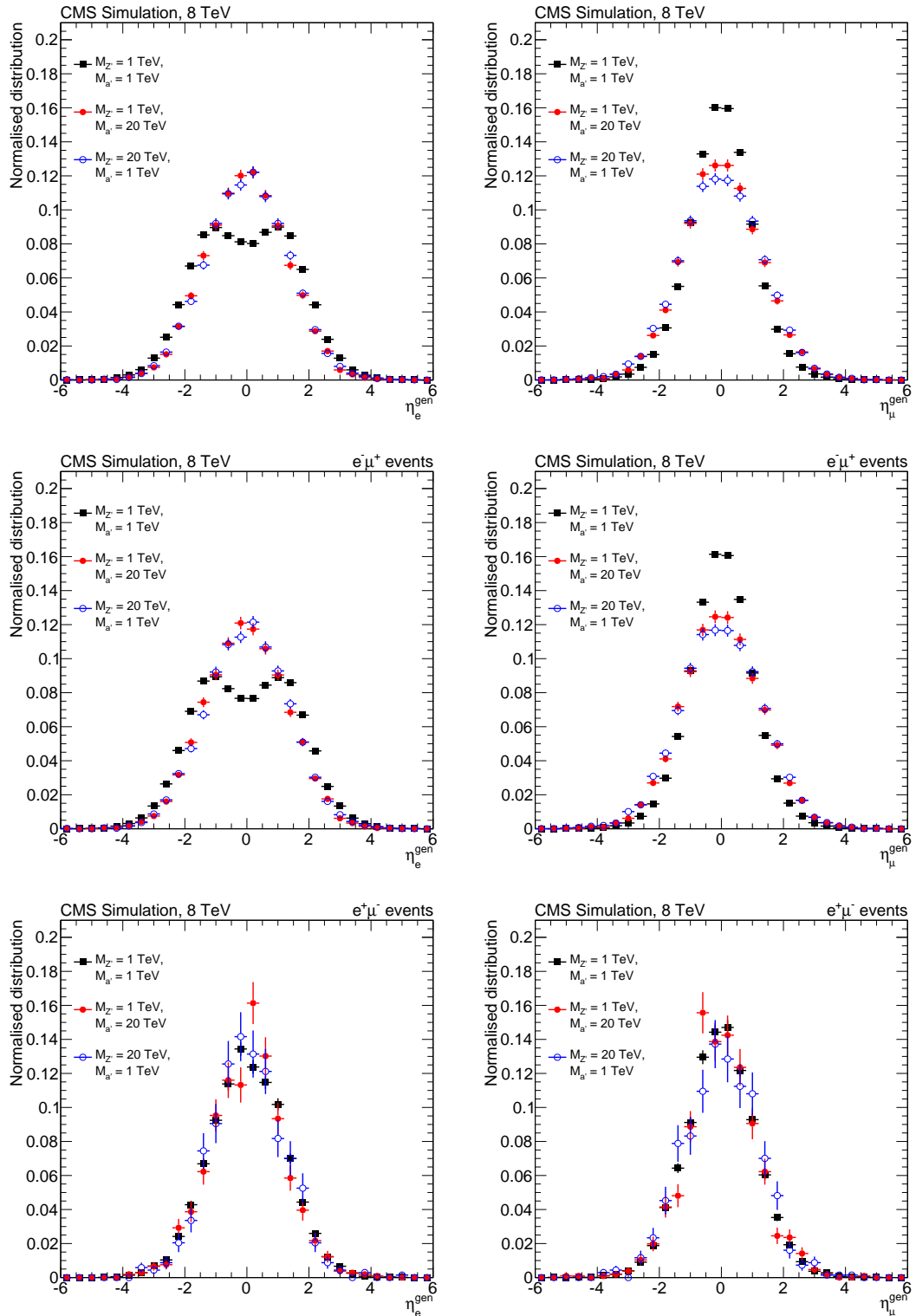


Figure 7.2 – Normalised η distribution for the generated electron (left column) and the generated muon (right column). The top row shows all $e^{\pm}\mu^{\pm}$ events, while the middle row and the bottom row show $e^{-}\mu^{+}$ events and $e^{+}\mu^{-}$ events, respectively.

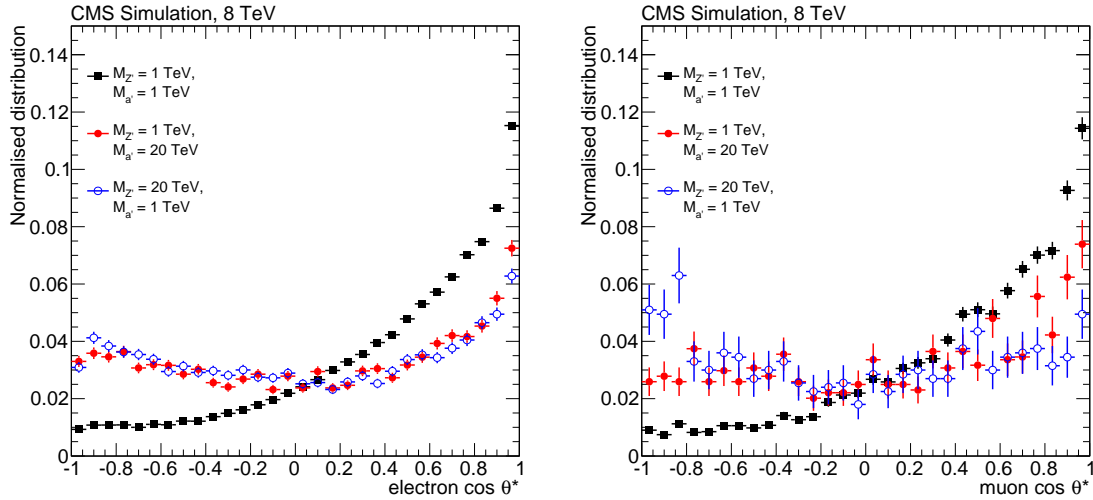


Figure 7.3 – Normalised $\cos \theta^*$ distributions in the $q\bar{q}$ center-of-mass frame, for the generated electron (left) in $e^-\mu^+$ events and the generated muon (right) in $e^+\mu^-$ events.

as the angle between the quark direction and the lepton direction in the $q\bar{q}$ center-of-mass frame. Figure 7.3 shows the $\cos \theta^*$ distributions for the generated electron in $e^-\mu^+$ events and the generated muon in $e^+\mu^-$ events, for the sample with interference and the two samples without interference. Both, the electron and the muon $\cos \theta^*$ distributions, indicate that the lepton flies more in the direction of the quark for the sample with interference.

An event display of a generated event from the sample with $M_{Z'_{\text{LFV}}/a'_{\text{LFV}}} = 1 \text{ TeV}$ is shown in Figure 7.4.

7.3 Event selection

The event selection for the search for new resonances in the $e\mu$ spectrum has to be optimised for high energy electrons and muons. The criteria for the leptons are essentially the same as for the analysis that search for new resonances in the dielectron and the dimuon channels [1]. The event selection has also many similarities with the $e\mu$ method described in Section 6.5.

7.3.1 Trigger

Two unrescaled triggers, a single muon trigger and a muon-photon trigger, were studied for the analysis. They are listed in Table 7.4. An online muon candidate with $p_T > 40 \text{ GeV}$ and $|\eta| < 2.1$ is required for the single muon trigger, while the muon-photon trigger fires with an online muon candidate with $p_T > 22 \text{ GeV}$ and a photon candidate with $E_T > 22 \text{ GeV}$. The L1 triggers that seed the single muon and the muon-photon HLT triggers require, respectively, an L1 muon candidate with

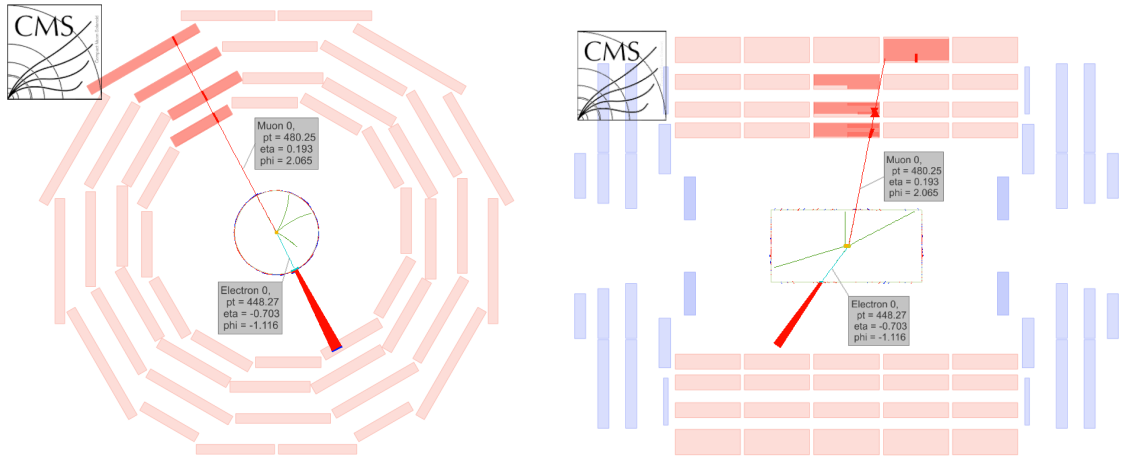


Figure 7.4 – Event display of an event from the signal sample with $M_{Z'_{\text{LFV}}/a'_{\text{LFV}}} = 1$ TeV, decaying in an $e\mu$ pair. The left display shows the event in the x - y -plane of the detector and the right display shows the y - z -plane. The tracks shown have $p_T > 3$ GeV.

$p_T > 16$ GeV and $|\eta| < 2.1$, and an L1 muon candidate with $p_T > 3.5$ GeV together with a localised energy deposit in the ECAL of $E_T > 12$ GeV. The restriction on η is a disadvantage of the single muon trigger since events with muons in the forward range of the muon system are not triggered on.

Studies with the simulated signal samples show that the trigger acceptance times efficiency, defined as the number of events passing the trigger over the total number of generated events that include a Z'_{LFV} or a'_{LFV} , as a function on the invariant mass, is better for the single muon trigger in the mass region up to 2.5 TeV, as can be seen in Figure 7.5. The trigger efficiency of the two triggers as a function of the generated lepton p_T and η is shown in Figures 7.6 and 7.7. As can be seen in the left plot in Figure 7.7, the acceptance times efficiency of the muon-photon trigger shows a small drop for barrel electrons, compared to endcap electrons, coming from the L1 filter of the trigger. It is necessary that the behaviour of the simulated samples is well understood, as the analysis relies on them. Since the single muon trigger does not show this drop in acceptance times efficiency, it was chosen as the signal trigger for the analysis. The muon-photon trigger was used for cross checks.

In addition, the use of the single muon trigger has the advantage that the scale factors and efficiencies for the trigger could be taken directly from the measurements with tag-and-probe on data at the Z peak, that were performed by the CMS muon

Table 7.4 – The triggers used by the analysis.

Trigger	L1 seed
HLT_Mu40_eta2p1	L1_SingleMu16er
HLT_Mu22_Photon22_CaloIdL	L1_Mu3p5_EG12

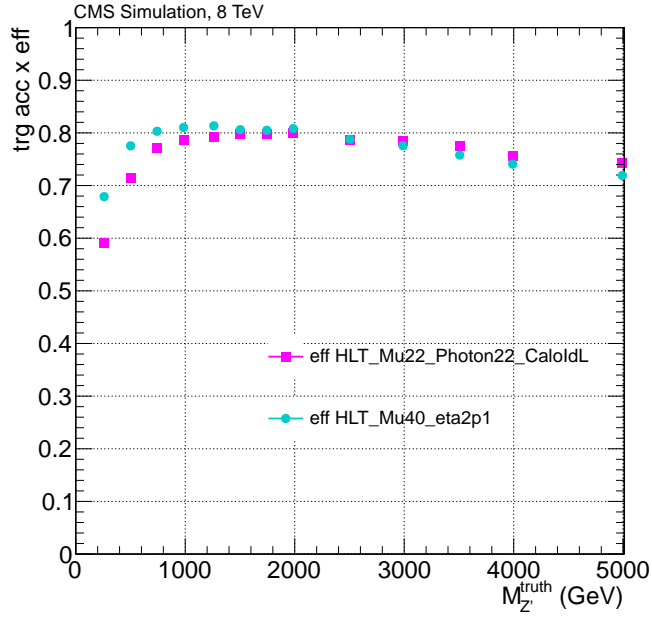


Figure 7.5 – Comparison of the trigger acceptance times efficiency of the single muon trigger and the muon-photon trigger as a function of the mass of the new resonance.

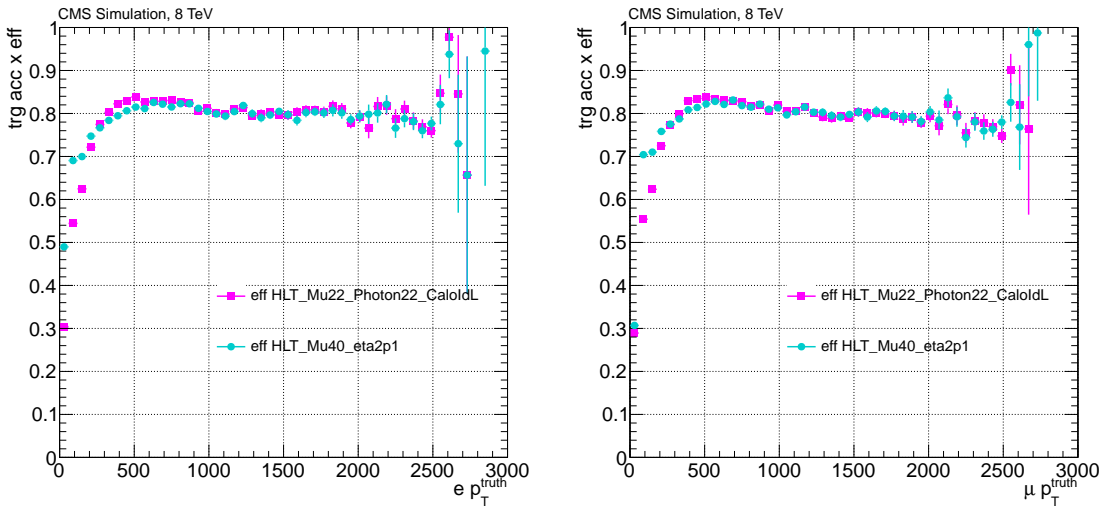


Figure 7.6 – Comparison of the trigger acceptance times efficiency of the single muon trigger and the muon-photon trigger as a function of generated electron p_T (left) and generated muon p_T (right) from signal samples.

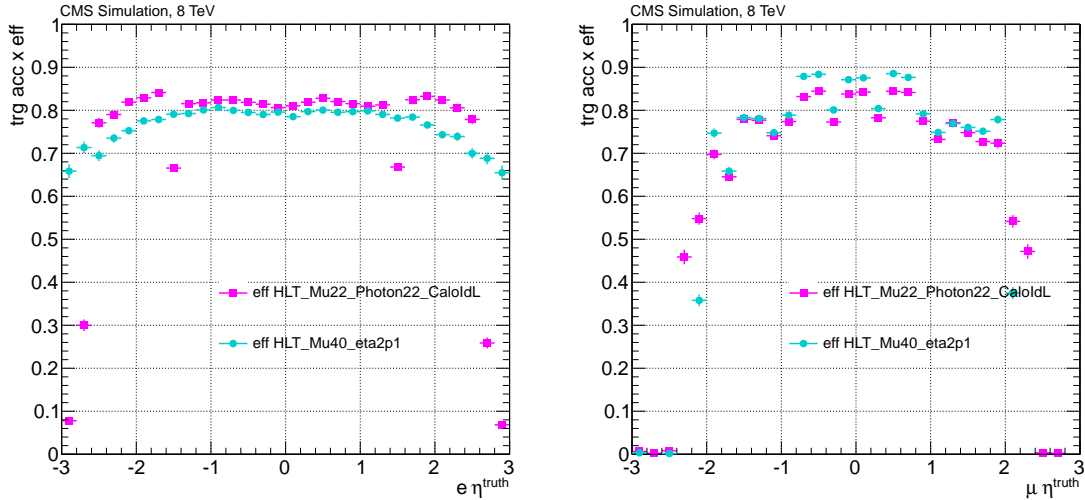


Figure 7.7 – Comparison of the trigger acceptance times efficiency of the single muon trigger and the muon-photon trigger as a function of η of the generated electron (left) and the generated muon p_T (right) from signal samples.

object group. Two sets of efficiencies and scale factors for the muon probe were measured: one with a fine binning in η and only one bin in p_T , and a second one with several bins in muon p_T , but a coarser binning in η . For the Z'_{LFV}/a'_{LFV} signal samples, the used efficiencies and scale factors are the ones that were measured in a fine binning in η , for all muon probes in a p_T range from 45 GeV to 500 GeV. The scale factor ranges between 0.93 and 1.01 and is chosen according to the reconstructed η of the selected muon candidate. For all other samples, the efficiencies and scale factors used are the ones that were measured in a coarser binning in η , but in several different bins of p_T . For the region $|\eta| < 0.9$ the scale factor ranges between 0.97 and 0.99, for the region $0.9 < |\eta| < 1.2$ the range is from 0.95 to 0.96, and for the region from $1.2 < |\eta| < 2.1$ the scale factor lies between 0.97 and 0.99.

7.3.2 Electron selection

The electron candidate selection for the analysis is the same as the HEEP electron candidate selection also used for the search for new resonances in the dielectron spectrum. The starting point for the HEEP selection is a reconstructed GSF electron candidate. Details on the HEEP selection are given in Section 6.1.4 and the criteria are summarised in Table 6.8.

The data to simulation scale factors for the reconstruction of the GSF electron candidates were measured by the electron/photon object subgroup of CMS, with a tag-and-probe method for different η and E_T bins. For the analysis, the scale factors for $E_T > 50$ GeV are taken, which are listed in Table 6.17.

The efficiency of the selection was measured with the tag-and-probe method at the Z peak, and the data to simulation scale factor is listed in Table 6.9.

7.3.3 Muon selection

The muon candidate selection is almost identical to the one used in the $e\mu$ method in the search for new resonances with dielectrons. The selection criteria listed in Section 6.5.1 are also used for this analysis, with the exception of the maximal $|\eta|$ and the p_T threshold. Since the single muon trigger was chosen for this analysis the selected muon candidate must have $|\eta| < 2.1$ and $p_T > 45$ GeV. Furthermore, an additional requirement on the longitudinal impact parameter of the tracker muon track with respect to the primary vertex, was introduced. This variable must be smaller than 5 mm.

The data to simulation scale factors for the muon candidate selection were measured by the muon object group of CMS, with a tag-and-probe technique at the Z peak. The scale factors are found to be constant up to $p_T = 500$ GeV and listed in Table 6.18. The uncertainties listed in the table are statistical, to which a systematic uncertainty of 0.57% has to be added.

7.3.4 Electron-muon pair selection

To be selected for the analysis, an event has to have at least one HEEP electron candidate and one muon candidate passing the high- p_T muon selection. Only events that were triggered by the single muon trigger described in Section 7.3.1 are considered. HEEP electron candidates that have a muon candidate with $p_T > 5$ GeV within $\Delta R < 0.1$ are not considered, in order to suppress muon induced fake HEEP electron candidates. This can happen if a muon deposits some of its energy in the ECAL, and can lead to an invariant mass peak around zero, since the muon candidate and the fake HEEP electron candidate have the same direction. Figure 7.8 shows a simulated signal event with a muon being misreconstructed also as GSF electron candidate. While the event shown has a second reconstructed GSF electron candidate, that would be favoured by the event selection, a problem can arise in cases where the electron is not in the detector acceptance or does not pass the HEEP selection.

In the case where more than one good HEEP electron candidate or muon candidate are found in an event, the pair giving the highest invariant mass is chosen. There is no selection criterion on the charge of the two leptons.

Furthermore, the event must have an offline reconstructed primary vertex with at least four tracks associated to it, and must lie within $|r| < 2$ cm and $|z| < 24$ cm of the nominal interaction point. Events which have more than ten tracks, but less than 25% of them marked as high purity tracks, are filtered out as well.

7.3.5 Acceptance times efficiency

The fraction of events within the detector acceptance combined with the reconstruction and selection efficiency is estimated from the simulated signal samples. Counted in the acceptance are also the p_T and η thresholds for the electron candidate and the muon candidate. The acceptance times efficiency is used to set limits

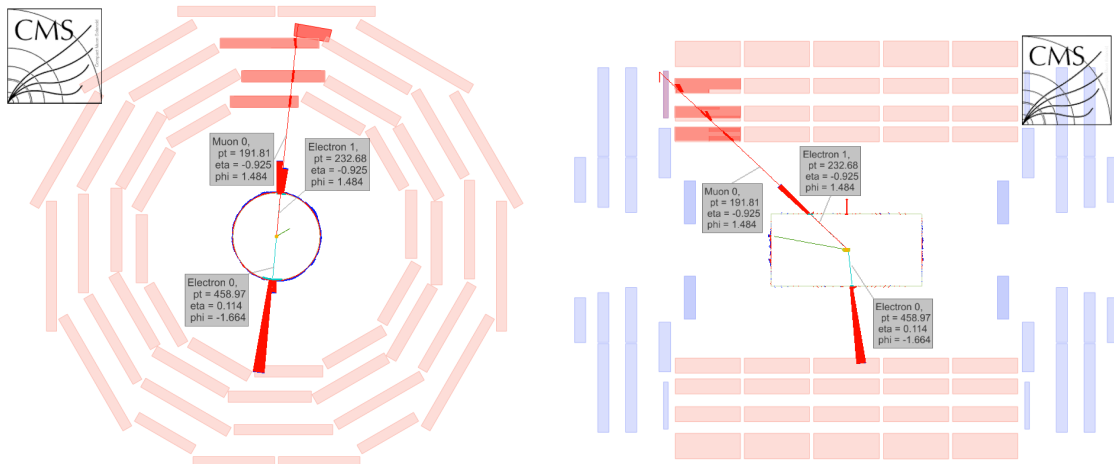


Figure 7.8 – Event display of an event from the sample with $M_{Z'_{LFV}/a'_{LFV}} = 1 \text{ TeV}$, showing a muon that is also reconstructed as a GSF electron candidate (Electron 1). The left display shows the event in the x - y -plane of the detector and the right display shows the y - z -plane. The tracks shown have $p_T > 3 \text{ GeV}$.

on the cross section for the signal model. Figure 7.9 shows the obtained acceptance times efficiency for the Z'_{LFV} signal model, together with a fit in the range $200 \text{ GeV} < M_{Z'_{LFV}/a'_{LFV}} < 2500 \text{ GeV}$. After a turn on coming from the acceptance, a plateau of about 61% is reached for Z'_{LFV}/a'_{LFV} masses above 1 TeV. The functional form of the fit is given as

$$A \times \epsilon(M_{Z'}) = 0.74 - \frac{141.3}{165.6 + \frac{M_{Z'}}{\text{GeV}}} - 2.70 \times 10^{-5} \cdot \frac{M_{Z'}}{\text{GeV}}. \quad (7.1)$$

7.4 Muon p_T and $e\mu$ mass resolution

7.4.1 Muon p_T resolution

At high mass, the muon p_T resolution has the largest impact on the $e\mu$ invariant mass resolution. The muon p_T is measured by tracking detectors and, owing to the limited bending power of the magnet, the tracks become very straight for high p_T muons, which makes the p_T measurement difficult. As was explained in Section 7.1.2, the initial geometry for the simulation samples had the barrel muon system shifted upwards, giving a worse p_T resolution compared to data. Two new geometries, named C1 and C2, were introduced to compensate this shift and the resolution estimation for both new geometries were studied.

The resolution is estimated from simulated signal samples, with masses for the new particles ranging from 250 GeV to 4000 GeV. For several bins in the generated muon p_T from 35 GeV to 2400 GeV, Gaussian fits are performed to the distribution of $R = (1/p_T^{\mu \text{ reco}} - 1/p_T^{\mu \text{ gen}})/(1/p_T^{\mu \text{ gen}})$. A first fit is performed in the range ± 1 RMS around the maximum bin of the distribution. With the width obtained from the first

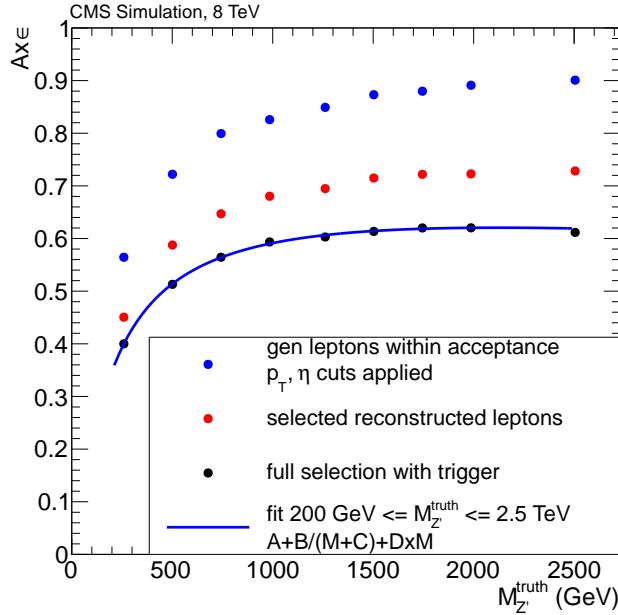


Figure 7.9 – Acceptance times efficiency estimated from simulated signal samples as a function of the LFV resonance mass is shown as the black dots. The blue dots indicate the fraction of events with generated electrons and muons in the acceptance. The red dots show the fraction of selected events without the trigger applied. The statistical uncertainties are too small to be visible in this plot. The blue line represents the fit to the acceptance times efficiency.

fit, a second Gaussian is fitted to the distribution, in the range defined by twice the width obtained from the first fit, around the mean of the first fit. In case the distribution contains less than 400 entries the width for the second fit is increased to three times the width of the second fit. The width of the second Gaussian is taken as an estimation for the muon p_T resolution.

The muon p_T resolution is estimated for the C1 and the C2 alignment, and examples for the fits are shown in Figure 7.10. Fits to distributions of the rest of the generated muon p_T bins can be found in Appendix B.1.

Figure 7.11a shows the estimated muon p_T resolution as a function of the generated muon p_T . For the C1 alignment scenario a functional form given by

$$\sigma(R) = 0.014 + 0.55 \left[1 - \exp \left(\frac{-1}{6231} \frac{p_T^{\mu \text{gen}}}{\text{GeV}} \right) \right], \quad (7.2)$$

is the result of a fit to the $p_T^{\mu \text{gen}}$ dependent resolutions.

The absolute value of the relative difference between the muon p_T resolutions, obtained with the C1 and C2 alignment scenarios, are shown in Figure 7.11b, fitted with a second order polynomial.

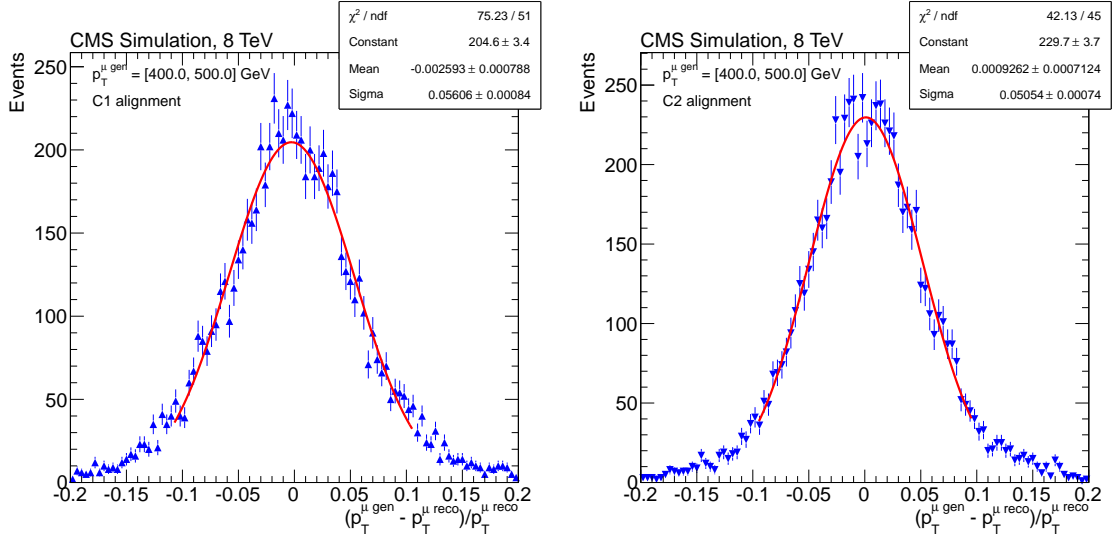


Figure 7.10 – Fits of a Gaussian function to the relative muon p_T difference $(p_T^{\mu \text{ gen}} - p_T^{\mu \text{ reco}})/p_T^{\mu \text{ reco}}$, for $400 \text{ GeV} < p_T^{\mu \text{ gen}} < 500 \text{ GeV}$ with the C1 muon alignment scenario (left) and the C2 muon alignment scenario (right).

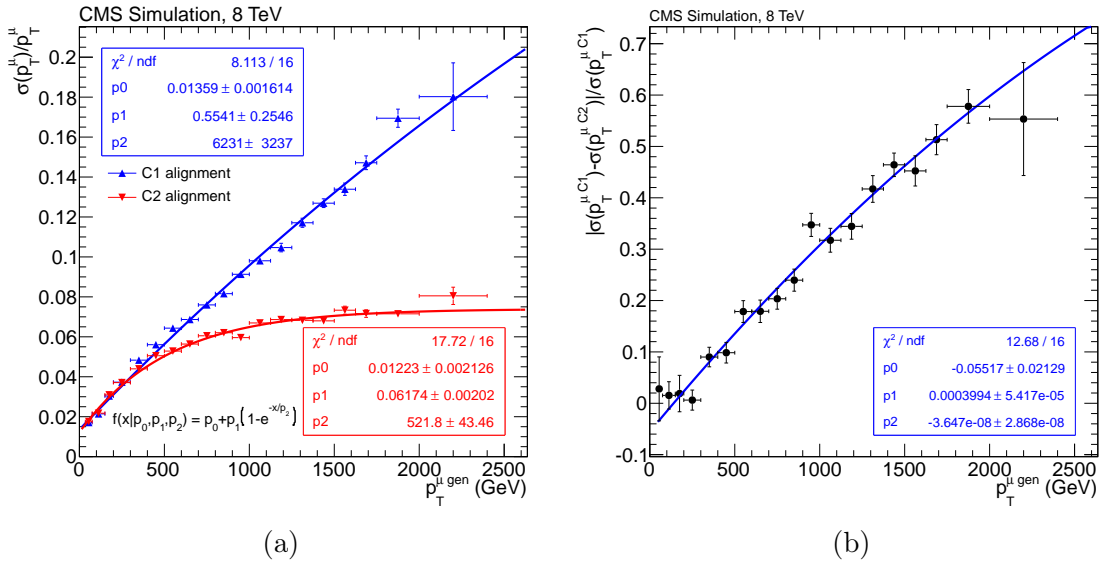


Figure 7.11 – The estimated muon p_T resolution as a function of the generated muon p_T , for the C1 and the C2 alignment scenarios (a). The absolute value of the relative difference between the muon p_T resolutions obtained with the C1 and C2 alignments, fitted with a second order polynomial (b).

7.4.2 $e\mu$ mass resolution

The estimation of the $e\mu$ mass resolution is similar to one for the muon p_T resolution. Two Gaussian functions are fitted, subsequently, to the spectrum of the relative difference between the reconstructed invariant mass and the true invariant mass $(M_{e\mu}^{\text{reco}} - M_{e\mu}^{\text{gen}})/M_{e\mu}^{\text{gen}}$. The first fit is performed in the range of ± 1 RMS around the maximum of the full distribution. The second fit uses a fit range of 1.8 times the width of the Gaussian obtained in the first fit, centered around the mean of the first fit. Performing two subsequent fits is more robust in the cases where the mean of the distribution is not at zero. Indeed, only the core of the distribution is fitted in the second fit. Figure 7.12 shows examples for the fits to the relative invariant mass difference for the two geometries. The fits for other $Z'_{\text{LFV}}/a'_{\text{LFV}}$ masses can be found in Appendix B.2.

The invariant mass resolution as a function of the $Z'_{\text{LFV}}/a'_{\text{LFV}}$ mass is shown in Figure 7.13 for the two geometries. A strong dependence of the invariant mass resolution to the alignment scenario can be observed, with the two studied scenarios diverging at high invariant mass. For the C1 alignment, the relative invariant mass resolution ranges from 1.6% at $M_{e\mu} = 200$ GeV, over 2.7% at $M_{e\mu} = 1000$ GeV to 5% at $M_{e\mu} = 2500$ GeV. The relative invariant mass resolution for the C2 alignment ranges from 1.7% at $M_{e\mu} = 200$ GeV, over 2.6% at $M_{e\mu} = 1000$ GeV to 3.7% at $M_{e\mu} = 2500$ GeV. The more conservative estimation for the invariant mass resolution, coming from the C1 alignment, is chosen to model the signal shape. The functional form of the relative invariant mass resolution is given as

$$\frac{\sigma(M_{e\mu})}{M_{e\mu}} = 0.013 + 1.4 \times 10^{-5} \cdot \frac{M_{e\mu}}{\text{GeV}} + 3.3 \times 10^{-10} \cdot \left(\frac{M_{e\mu}}{\text{GeV}} \right)^2. \quad (7.3)$$

As a measure for the uncertainty of the mass resolution, the relative difference between the mass resolution estimation obtained with the C1 and the C2 alignment is used. Figure 7.14 shows the relative difference of the two measured mass resolutions. For the parametrisation of the uncertainty of the signal resolution, fits of a constant and a second order polynomial to the relative difference are performed, respectively, in the lower mass region up to 700 GeV and above 600 GeV. The intersection between the two curves separates the two parametrisation regions. The resulting parametrisation is given in Table 7.5

Table 7.5 – Parametrisation of the relative difference between the invariant mass resolution obtained from the C1 and C2 alignment scenario.

$M_{e\mu}$	Functional form
$M_{e\mu} < 687.8 \text{ GeV}$	0.018
$M_{e\mu} > 687.8 \text{ GeV}$	$-0.0117 + 2.10 \times 10^{-4} \left(\frac{M_{e\mu}}{\text{GeV}} \right) - 1.79 \times 10^{-8} \left(\frac{M_{e\mu}}{\text{GeV}} \right)^2$

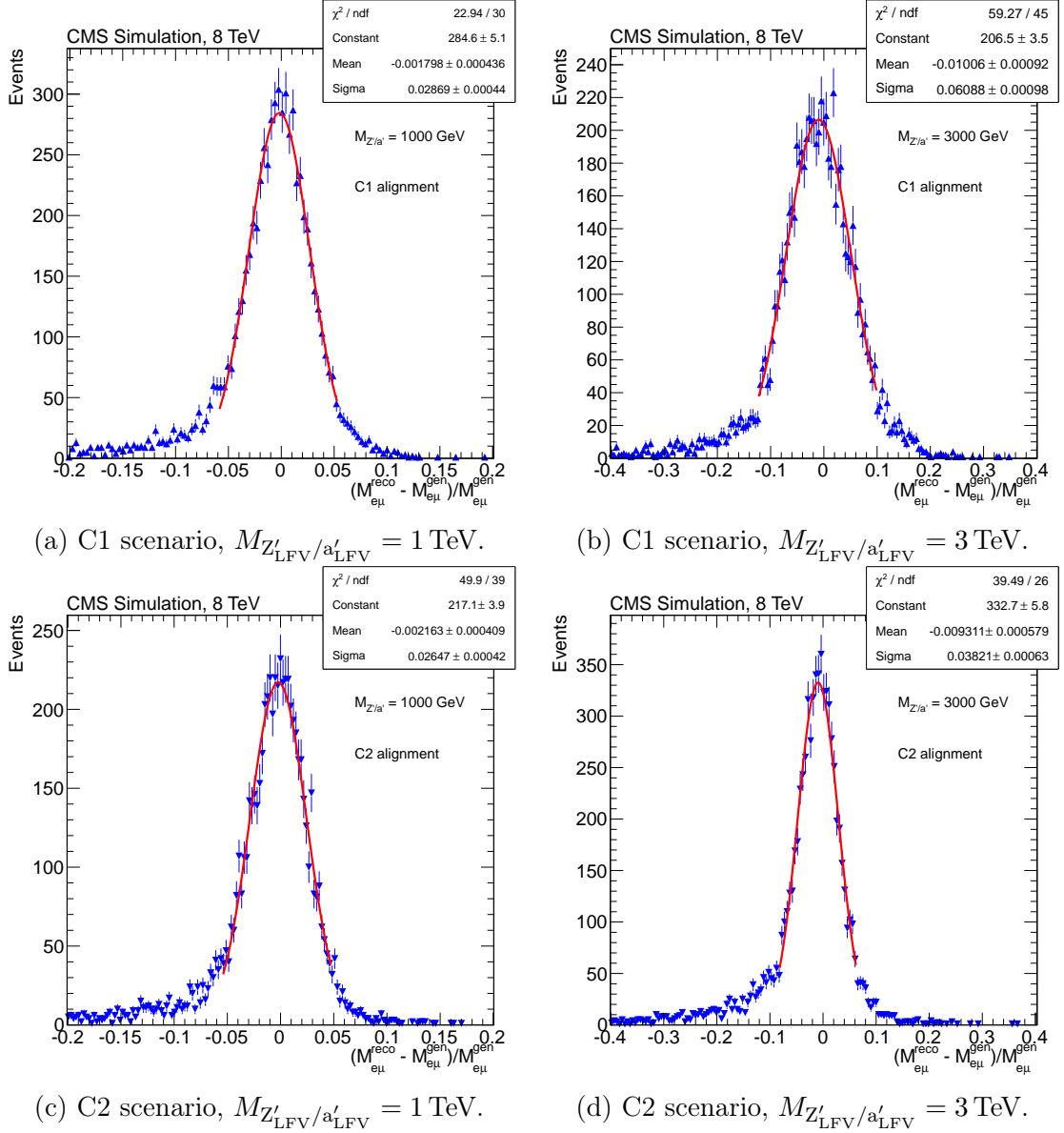


Figure 7.12 – Fits of Gaussian functions to the relative invariant mass difference $(M_{e\mu}^{\text{reco}} - M_{e\mu}^{\text{gen}})/M_{e\mu}^{\text{gen}}$, with the C1 muon alignment scenario (a, b) and the C2 muon alignment scenario (c, d), for two mass hypothesis: $M_{Z'_{LFV}}/a'_{LFV} = 1$ TeV (a, c) and $M_{Z'_{LFV}}/a'_{LFV} = 3$ TeV (b, d).

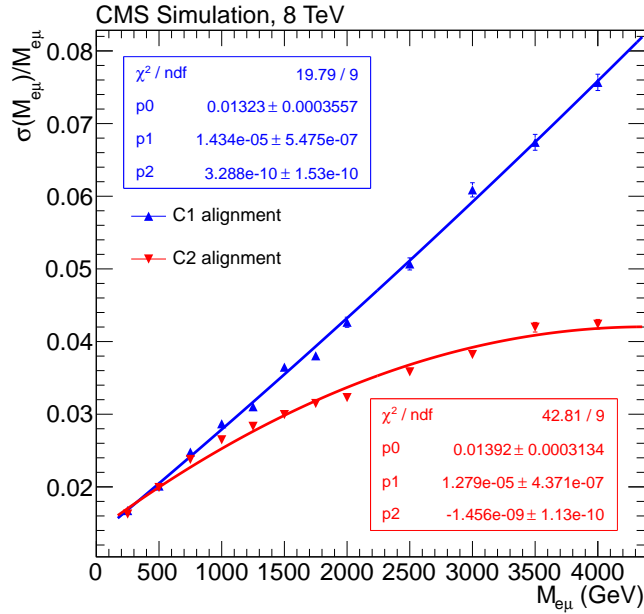


Figure 7.13 – The relative invariant mass resolution as a function of the $e\mu$ invariant mass, as estimated from simulated signal samples (markers). Also shown are the second order polynomials fitted to the measurements for the two scenarios.

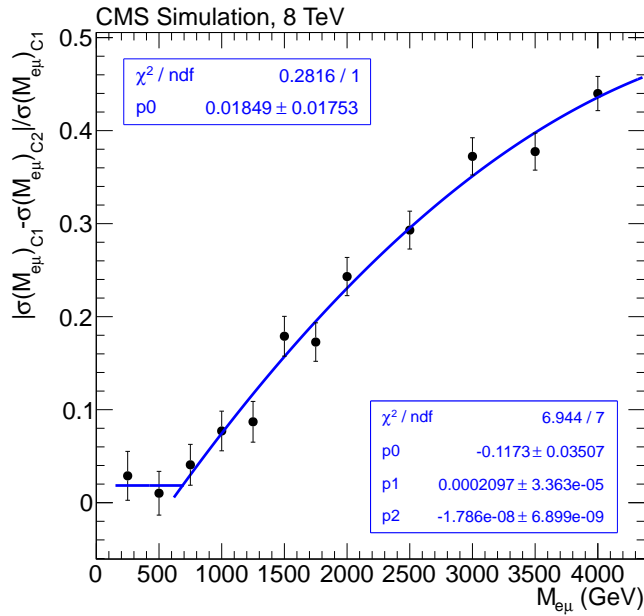


Figure 7.14 – The relative difference between the invariant mass resolutions obtained for the C1 and C2 alignment scenarios. The blue curve is the result of the fits of a constant in the low mass region, and a second order polynomial in the high mass region, to the relative difference.

7.5 Backgrounds

Backgrounds of two categories must be considered for the search for new physics with the $e\mu$ invariant mass spectrum. The first category is made of SM processes that have isolated electrons and isolated muons in the final state. Processes that have final states which can be misidentified as electrons or muons form the second category. Most of the backgrounds are estimated from simulated MC samples and normalised to the integrated luminosity of the dataset. The events of the simulated samples are weighted in order to obtain the same distribution for the number of primary vertices as seen in data.

7.5.1 Prompt lepton background

The prompt lepton background comes from SM processes which have at least one isolated electron and one isolated muon in the final state. The dominant contribution comes from $t\bar{t}$ production with subsequent decay to b quarks and W bosons, that decay leptonically, as shown in the Feynman diagram in Figure 6.21. Diboson production, especially the WW process, but also the WZ and ZZ processes contribute to the prompt lepton background as well, if the bosons decay leptonically. Furthermore, single top production in the tW channel does also contribute. Feynman diagrams for these processes are shown in Figures 6.21 to 6.23. DY events that decay to taus, which then decay leptonically, give a small contribution, because of the small branching fraction of the tau decay to leptons and this contribution is located mainly at low mass. The Feynman diagrams for the DY process are shown in Figure 1.3.

While the $t\bar{t}$ background is the most significant in the mass region below 1 TeV, it loses its relative share on the total background in favour of the WW background towards higher invariant masses. Above $M_{e\mu} = 1$ TeV they contribute approximately the same amount. The reason for the lowering of the $t\bar{t}$ background fraction towards higher masses is that the jet from the b-quark is more often in the isolation cone of the electron candidate, resulting in it failing the HEEP criteria for isolation.

The contributions from all processes contributing to the prompt lepton background are estimated from the simulated samples listed in Table 7.2 and normalised to the measured integrated luminosity of the dataset. In the high mass region, where the search for new physics takes place, the number of simulated events is limited. For the $t\bar{t}$ process and the WW process privately produced samples, containing only events with generated $M_{e\mu} > 600$ GeV, were produced to improve the statistical uncertainty in this region, as described in Section 7.1.2. To combine the $t\bar{t}$ samples, a cut on generated mass $M_{e\mu}$ is applied, so that for generated $M_{e\mu} > 600$ GeV only events from the privately produced sample are taken. For generated $M_{e\mu} < 600$ GeV the events are taken from one of the three centrally produced $t\bar{t}$ samples, according to the generated $t\bar{t}$ mass region. Plots that show the combined $t\bar{t}$ spectra as a function of the reconstructed $e\mu$ mass, the generated $t\bar{t}$ mass and the generated $e\mu$ mass, are shown in Figure 7.15. The resulting spectra after the combination are compared to the spectra of the inclusive $t\bar{t}$ sample.

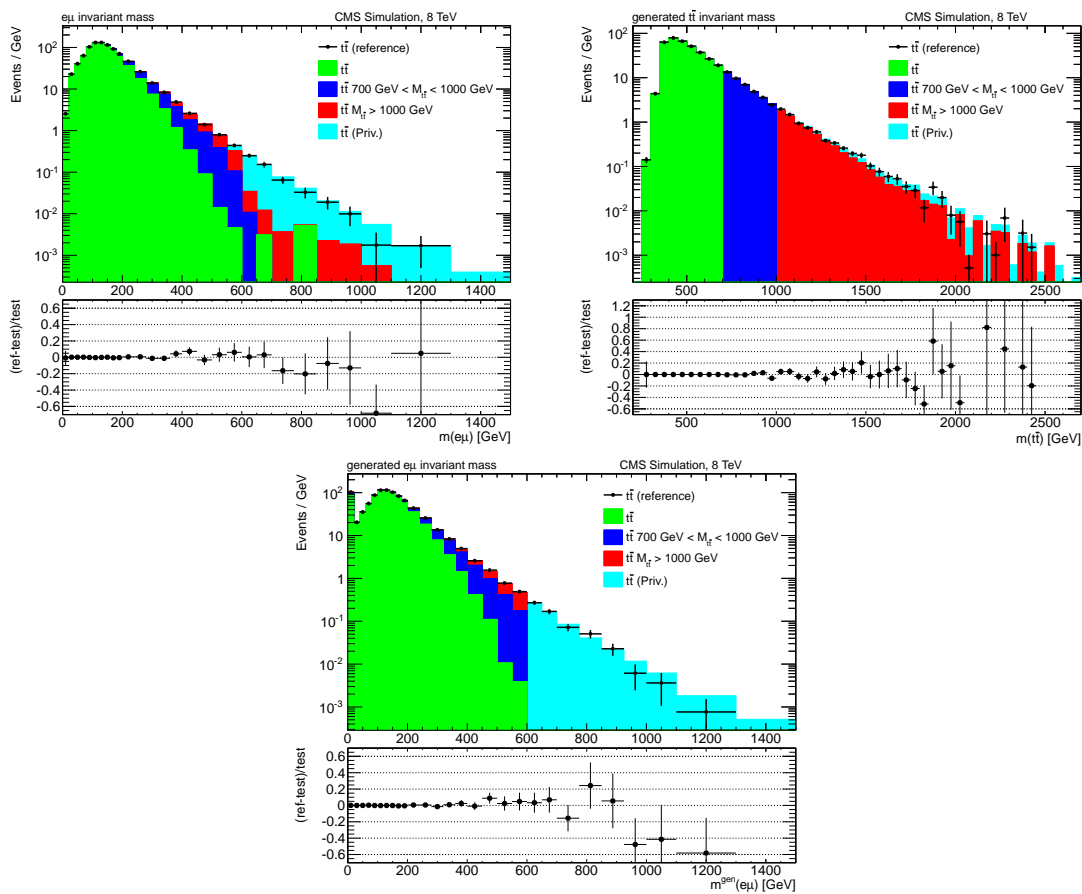


Figure 7.15 – Comparison of the inclusive $t\bar{t}$ sample (reference) with the truncated combination of all $t\bar{t}$ samples, as a function of the reconstructed $e\mu$ invariant mass (top left), the invariant mass of the generated $t\bar{t}$ pair (top right), and the generated $e\mu$ invariant mass (bottom).

For the combination of the WW samples the centrally produced one is used below generated $e\mu$ masses of 600 GeV, and the privately produced samples are used for generated $M_{e\mu} > 600$ GeV. Figure 7.16 shows the comparison of the spectra of the centrally produced WW sample with the spectra resulting from the combination of the samples, as a function of the reconstructed $e\mu$ mass and the generated $e\mu$ mass.

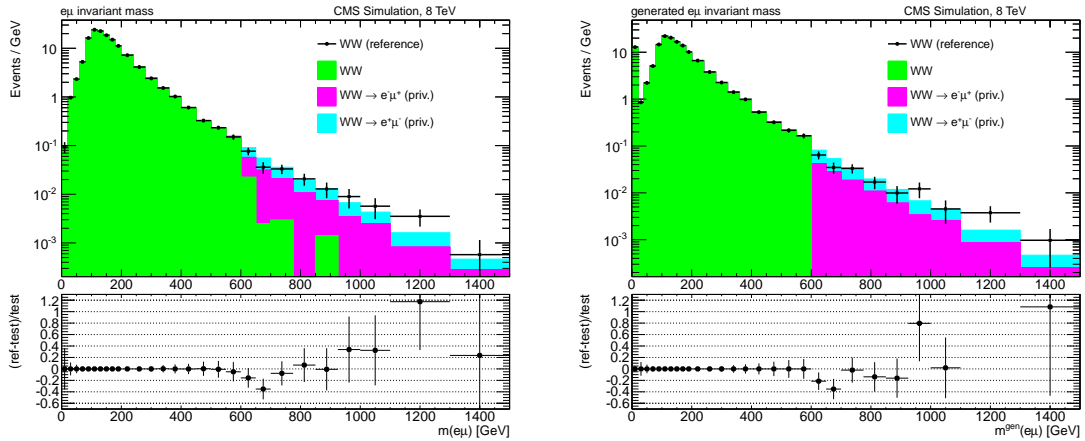


Figure 7.16 – Comparison of the centrally produced WW sample (reference) with the truncated combination of all WW samples, as a function of the reconstructed $e\mu$ invariant mass (left), and the generated $e\mu$ invariant mass (right).

7.5.2 Background with misidentified leptons

For the backgrounds that involve misidentified leptons several processes contribute. For DY events that decay to dielectrons or dimuons, one lepton can be misidentified as being of the other flavour. Naturally, this background is concentrated around the Z resonance peak. The contribution from DY to dimuon events is expected to be much larger than the contribution from DY to dielectron events, since it is more likely that additional jets in DY to dimuon events are misidentified as electron candidates, than that jets are misidentified as muons in DY to dielectron events. The DY background with misidentified leptons is estimated from a DY sample with dilepton decays. This sample also contains ditau events where the taus decay and give electrons and muons in the final state.

Another process that contributes is the $W\gamma$ process, where the W decays to a muon and the photon converts to electrons. This background is taken from simulated samples which are binned in photon p_T , and normalised to the integrated luminosity of the dataset. Since the $W\gamma$ samples are binned in p_T^γ , they can be combined without any truncation. The resulting $e\mu$ invariant mass spectrum and the spectrum of the HEEP electron candidate E_T are shown in Figure 7.17, in comparison with the spectra from an inclusive $W\gamma$ sample. Since the cross sections of the samples are only known at leading order and the uncertainty of the simulation of the photon

conversion has to be taken into account as well, a conservative 50% uncertainty is assigned to the estimated $W\gamma$ yield.

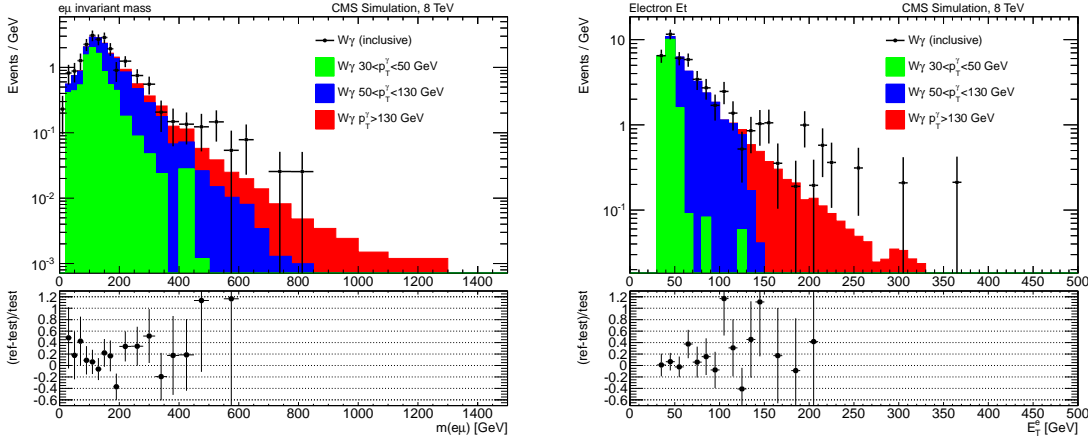


Figure 7.17 – Comparison of the inclusive $W\gamma$ sample with the combination of the p_T^γ -binned samples, as a function of the reconstructed $e\mu$ invariant mass (left), and the E_T of the HEEP electron candidate (right).

Jet background

The most important background with misidentified leptons comes from processes that include jets that are misidentified as electron candidates passing the HEEP selection. A data driven technique is used for the estimation of the background, using the fake-rate (FR) for electrons described in Section 6.4.2. The parametrisation of the fake-rate as a function of electron candidate E_T is listed in Table 6.15. For the estimation of the jet background contribution in the $e\mu$ invariant mass spectrum, the fake-rate is applied to an event sample with at least one selected muon candidate, and a GSF electron candidate passing the loose selection listed in Table 6.14, but not the HEEP selection. The requirement that the loose electron candidates must not pass the HEEP selection makes it necessary to compensate for the lost electron candidates with a correction factor $1/(1 - \text{FR})$. Since the selection of a muon candidate plus a loose electron candidate contains still a significant contribution from DY , $t\bar{t}$ and also $W\gamma$ events, the contributions from those processes are subtracted using the estimations from the simulated samples. For simplicity, only the inclusive $t\bar{t}$ sample is used for the subtraction.

Estimating the jet background in this way includes multijet and $W + \text{jets}$ processes. In order to validate the estimation for the jet background, the obtained spectrum is compared to the one that is obtained from the same-sign $e\mu$ invariant mass spectrum as described in Section 6.5.2. The jet background spectrum obtained there does not contain the contribution from $W + \text{jets}$ events, while the one from the fake-rate does contain $W + \text{jets}$. Therefore, the $W + \text{jets}$ contribution is added from simulated samples to the spectrum from the same-sign method. Figure 7.18 shows the

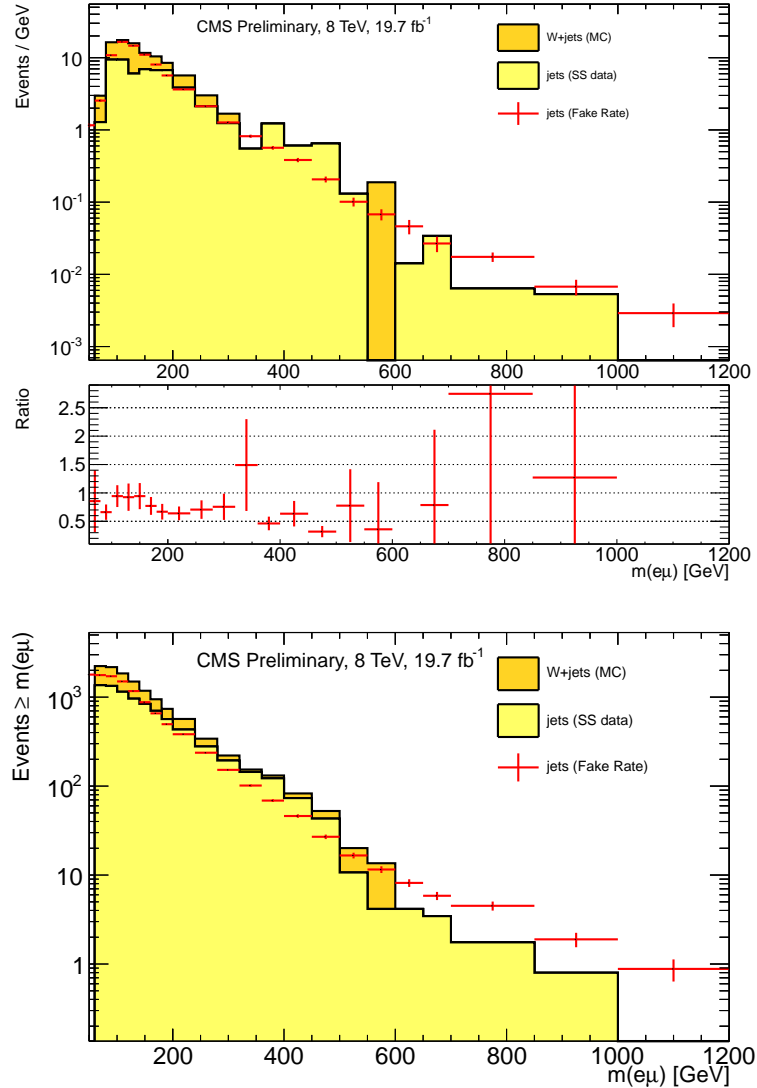


Figure 7.18 – Comparison of the jet background estimations taken from the fake-rate method and the same-sign method from Section 6.5.2. The histogram labeled ‘SS data’ is the spectrum obtained with the same-sign method, and the red markers indicate the spectrum resulting from the the fake-rate method. The $W + \text{jets}$ contribution that is not included in the same-sign spectrum but in the fake-rate method spectrum is added to the SS spectrum from a simulated MC sample to achieve comparability. On the top plot the spectrum as a function of $e\mu$ mass is shown on top, with the ratio between the same-sign plus $W + \text{jets}$ spectrum and the fake-rate method spectrum below. On the bottom plot a cumulated spectrum is shown, with each bin containing all events that have $M_{e\mu} \geq M_{\text{bin}}$.

comparison between the two spectra. The systematic uncertainty assigned to the jet background estimation obtained with the fake-rate method is taken to be 30%, taken from the comparison to the jet background spectrum estimation from the same-sign $e\mu$ invariant mass spectrum.

7.6 Comparisons between data and simulation

This section contains comparison distributions between data and the expected backgrounds. The expected backgrounds are introduced in Section 7.5: the jet background contribution is estimated from data, the other backgrounds are taken from simulations. For all distributions presented in this section, the final event selection, described in Section 7.3, has been applied. The simulations are normalised to the luminosity of the data sample.

7.6.1 Number of primary vertices

When the simulated samples are produced, they have in general a different distribution for the number of primary vertices than the data. The events of the simulated samples are weighted according to their generated number of primary vertices, in order to reproduce the number of primary vertex distribution of the data.

The weights for a certain number of generated primary vertices are calculated by comparing the measured primary vertex distribution, obtained for the dataset used, from a set of CMS runs defined specially for this measurement, with the generated primary vertex distribution of the simulated sample. The measured primary vertex distribution is obtained from minimum bias events, which have a minimal set of trigger requirements, for the used CMS runs of the single muon dataset. Figure 7.19 shows the comparison between data and expected background as a function of the number of primary vertices.

7.6.2 Lepton kinematics

Figure 7.20 shows the comparisons between the data and the background distributions for the HEEP electron candidates E_T and the muon candidates p_T . The spectra agree within the uncertainties, but a negative slope can be seen in the p_T spectrum of the muon candidate: a difference of about 10% is observed in the mass range of 100 GeV to 200 GeV for the muon p_T . This effect has been studied in the CMS top object working group, and can be compensated by a reweighting of the simulated $t\bar{t}$ events according to the top/antitop p_T . The weight is calculated with the generated top and antitop p_T with the formula

$$w = \sqrt{e^{0.159-0.00141 \cdot p_T^t} + e^{0.159-0.00141 \cdot p_T^{\bar{t}}}}, \quad (7.4)$$

where the numerical values were calculated by the top object working group, based on the differential top cross section measurement in the lepton+jets channel at $\sqrt{s} =$

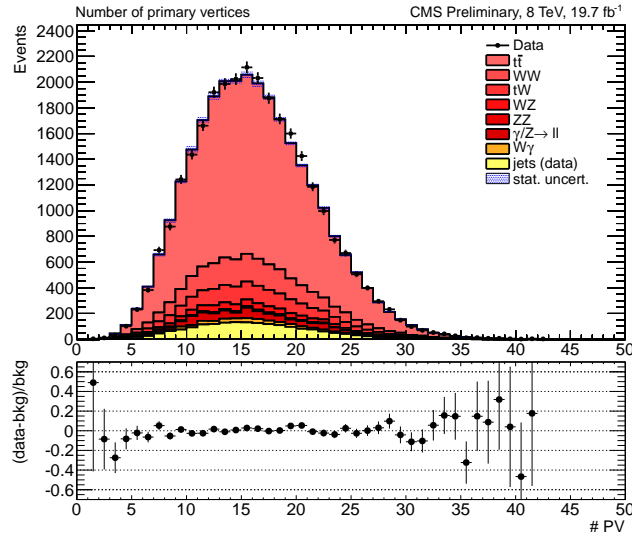


Figure 7.19 – Comparison between data and expected background after the simulated background events have been weighted to have the same distribution of number of primary vertices.

8 TeV [109]. The spectra with the top/antitop p_T reweighting applied are shown in Figure 7.21. They indicate an improvement of the agreement between data and the estimated background contributions, in the HEEP electron candidate E_T and the muon candidate p_T distribution, respectively, in the range up to 200 GeV.

However, this reweighting procedure is only commissioned for top p_T up to 400 GeV, which is exceeded for many events in the high $e\mu$ invariant mass tail. Applying the reweighting parametrisation for higher values of top p_T would underestimate the high mass $t\bar{t}$ spectrum, since the mean of the scale factor lies well below one for such events. Therefore, no reweighting of the $t\bar{t}$ samples was performed, and instead, the impact of the reweighting on the shape of the $t\bar{t}$ invariant mass spectrum is taken as a systematic uncertainty.

Data to expectation comparisons for the η and ϕ distributions of the selected lepton candidates are shown in Figures 7.22 and 7.23. These plots show a good agreement within the uncertainties between data and expected background.

Further comparison plots for the HEEP electron and muon candidate selection variables, as well as other variables of interest, can be found in Appendix C.

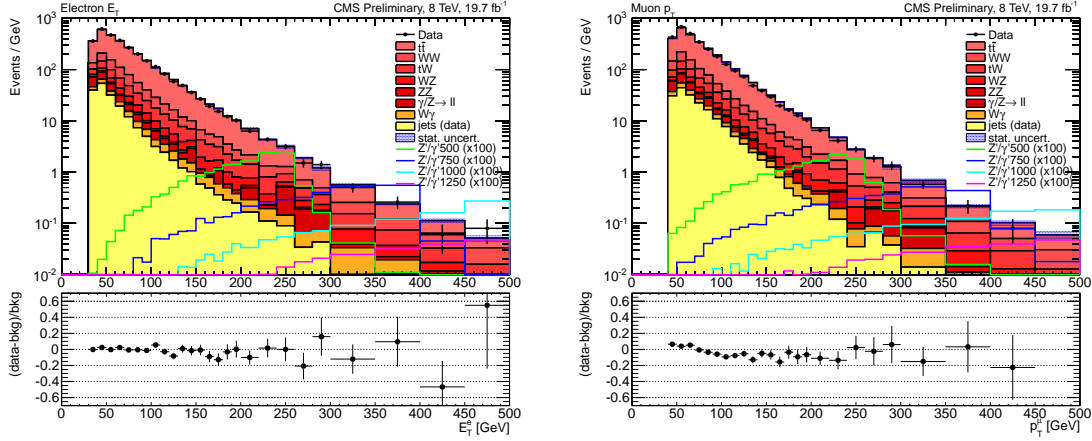


Figure 7.20 – Data to expectation comparisons for the E_T of the HEEP electron candidates on the left plot and the p_T of the selected muon candidates on the right plot. The bottom plots show the data minus background over background distributions.

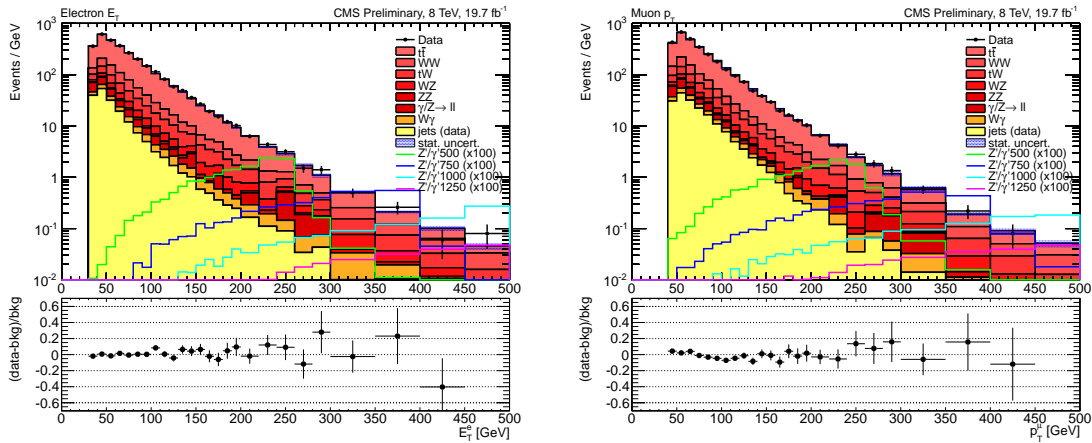


Figure 7.21 – Data to expectation comparisons, with the top/antitop p_T reweighting applied, for the E_T of the HEEP electron candidates on the left plot and the p_T of the selected muon candidates on the right plot. The bottom plots show the data minus background over background distributions.

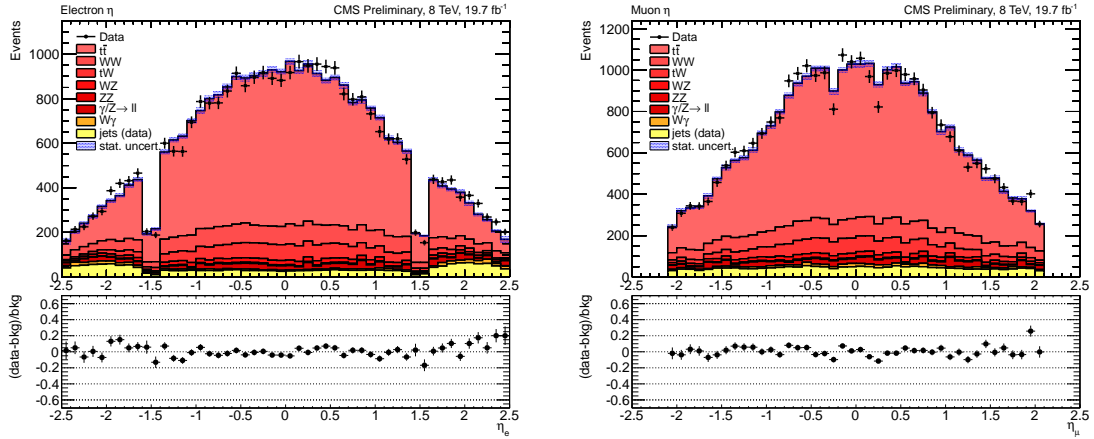


Figure 7.22 – Data to expectation comparisons for the η of the selected lepton candidates. The left plot shows the distribution for the HEEP electron candidates and the right plot the one for the muon candidates. The bottom plots show the data minus background over background distributions.

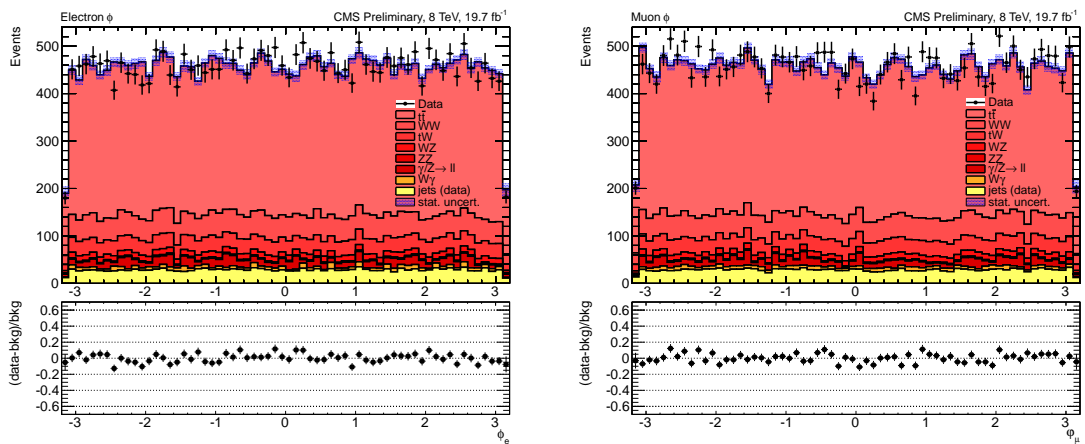


Figure 7.23 – Data to expectation comparisons for the ϕ of the selected lepton candidates. The left plot shows the distribution for the HEEP electron candidates and the right plot the one for the muon candidates. The bottom plots show the data minus background over background distributions.

7.7 Invariant mass spectrum

The invariant mass distribution of the selected $e\mu$ events is shown in Figure 7.24. Shown are the spectra from the selected events from data, the expectation for the SM background processes and examples for LFV signal spectra with different resonance masses. Above an invariant mass of 60 GeV, 27034 events are selected. The expected SM backgrounds are taken from simulated samples and normalised to the integrated luminosity, with the exception of the background from $W + \text{jets}$ and multijet events, which is estimated using a data driven method described in Section 7.5.2. Figure 7.25 shows the cumulated invariant mass spectrum for the selected $e\mu$ pair events.

The event yield for data and the expected yield for the total background are listed in Table 7.6. Table 7.7 lists the relative contributions of the SM processes from the total background expectation, for different $e\mu$ invariant mass ranges. While the $t\bar{t}$ background is dominant for $e\mu$ invariant masses below 500 GeV, the contributions are more evenly spread for high $M_{e\mu}$, with $t\bar{t}$, WW and processes with jets taking a similar share.

The invariant mass spectra and the corresponding cumulated distributions of the selected $e^\mp\mu^\pm$ and $e^\pm\mu^\pm$ events are shown in Figures 7.26 and 7.27, respectively. Figure 7.28 shows the invariant mass spectra for events where the HEEP electron candidate is in the barrel only or in the endcap only.

The selected event with the highest invariant mass has $m(e\mu) = 1046$ GeV, and an event display is shown in Figure 7.29.

7.7.1 Opposite sign mass spectrum asymmetry

In the LFV model described in Section 2.3 the event yield for $e^-\mu^+$ pairs should be approximately ten times larger than the one for $e^+\mu^-$ pairs. The reason for this is that in the first case valence quarks of the proton can be involved in the production, while in the second case only sea quarks can contribute. Since all SM background processes are symmetric in the $e^-\mu^+$ and $e^+\mu^-$ final states, a subtraction of the two spectra should result in a distribution centered around zero. In the case of the LFV signal however, a residual $e^-\mu^+$ excess should remain. While the rest of the analysis is set up to be as model independent as possible, using the asymmetry of the opposite-sign $e\mu$ spectra represents a strong focus on the LFV model. In the case

Table 7.6 – Event yield from data and expected yield for the total background. The listed uncertainties are the statistical and the systematic uncertainty.

Mass range	Data	Total background \pm stat. \pm syst.
$M_{e\mu} < 200$ GeV	22712	$22580 \pm 74 \pm 1916$
$200 \text{ GeV} < M_{e\mu} < 500$ GeV	6009	$6055 \pm 30 \pm 484$
$500 \text{ GeV} < M_{e\mu} < 1000$ GeV	174	$170 \pm 4 \pm 16$
$1000 \text{ GeV} < M_{e\mu} < 1500$ GeV	1	$3.5 \pm 0.3 \pm 0.5$
$M_{e\mu} > 1500$ GeV	0	$0.24 \pm 0.08 \pm 0.04$

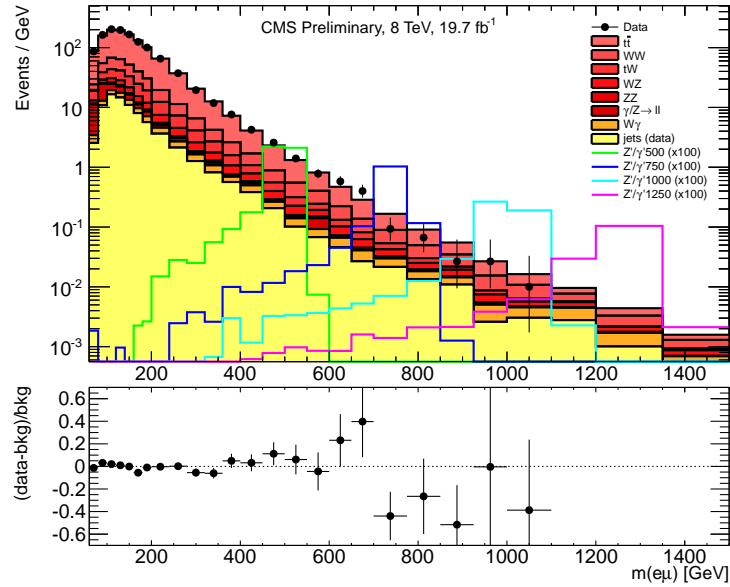


Figure 7.24 – Invariant mass spectrum of the selected $e\mu$ pair events. The data are represented by the points with error bars, while the histograms show the expected contributions from SM processes. The error bars on the data points represent the statistical uncertainties. Also shown are four curves that represent the 100 times enhanced expected spectra from the LFV model for a $Z'_{\text{LFV}}/a'_{\text{LFV}}$ with different masses. The bottom plot shows the data minus background over background distribution.

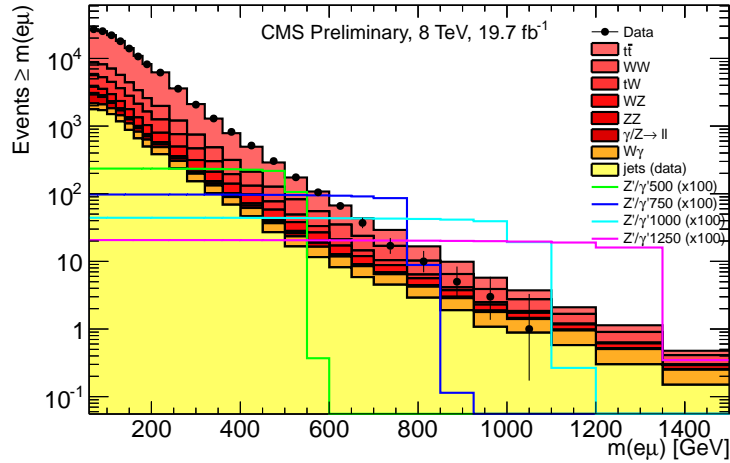


Figure 7.25 – Cumulated distribution of the $e\mu$ invariant mass spectrum, where all the events above the mass on the x -axis are summed. The data are represented by the points with error bars, while the histograms show the expected contributions from SM processes. The error bars on the data points represent the statistical uncertainties. Also shown are four curves that represent the 100 times enhanced expected spectra from the LFV model for a $Z'_{\text{LFV}}/a'_{\text{LFV}}$ with different masses.

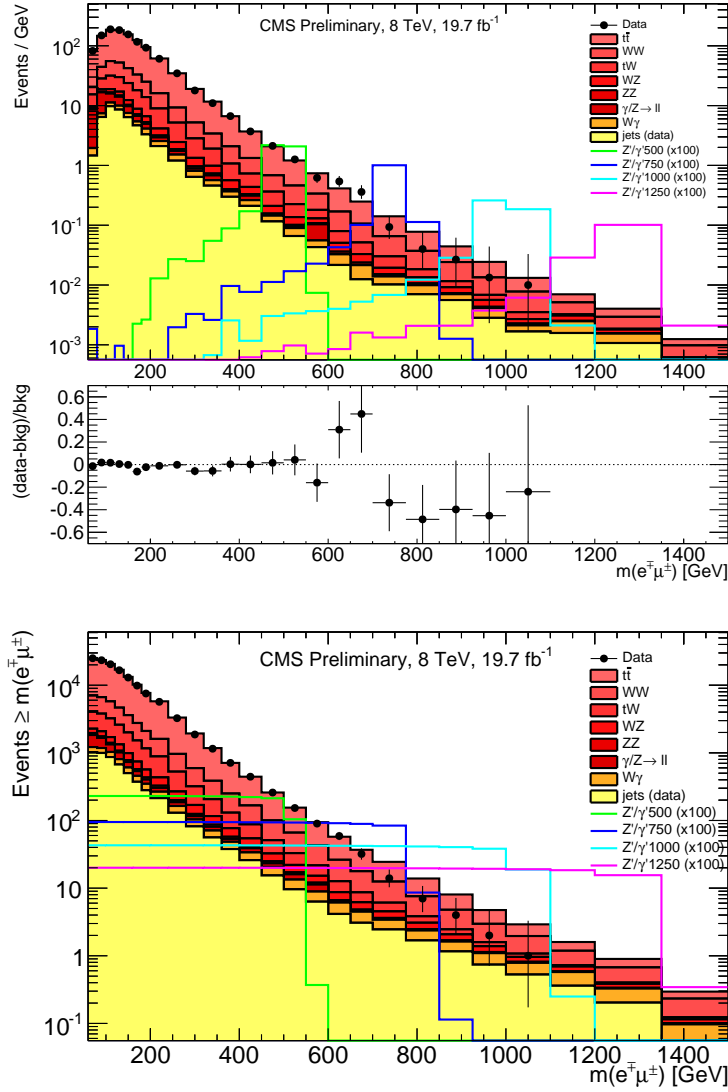


Figure 7.26 – Invariant mass spectrum of the selected $e^\pm\mu^\pm$ pair events on the top plot, and the cumulated distribution, where all the events above the mass on the x -axis are summed on the bottom plot. The data are represented by the points with error bars, while the histograms show the expected contributions from SM processes. The error bars on the data points represent the statistical uncertainties. Also shown are four curves that represent the 100 times enhanced expected spectra from the LFV model for a Z'_{LFV}/a'_{LFV} with different masses. The bottom distribution on the top plot shows the data minus background over background distribution.

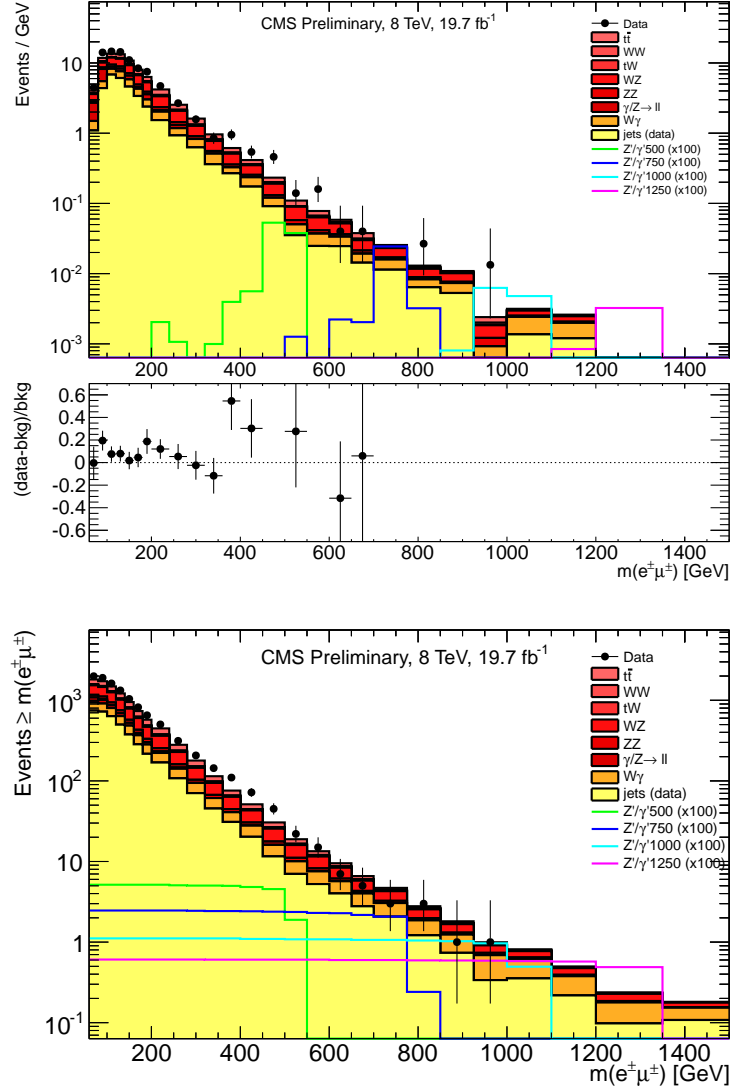


Figure 7.27 – Invariant mass spectrum of the selected $e^\pm\mu^\pm$ pair events on the top plot, and the cumulated distribution, where all the events above the mass on the x -axis are summed on the bottom plot. The data are represented by the points with error bars, while the histograms show the expected contributions from SM processes. The error bars on the data points represent the statistical uncertainties. Also shown are four curves that represent the 100 times enhanced expected spectra from the LfV model for a $Z'_{\text{LFV}}/a'_{\text{LFV}}$ with different masses. The bottom distribution on the top plot shows the data minus background over background distribution.

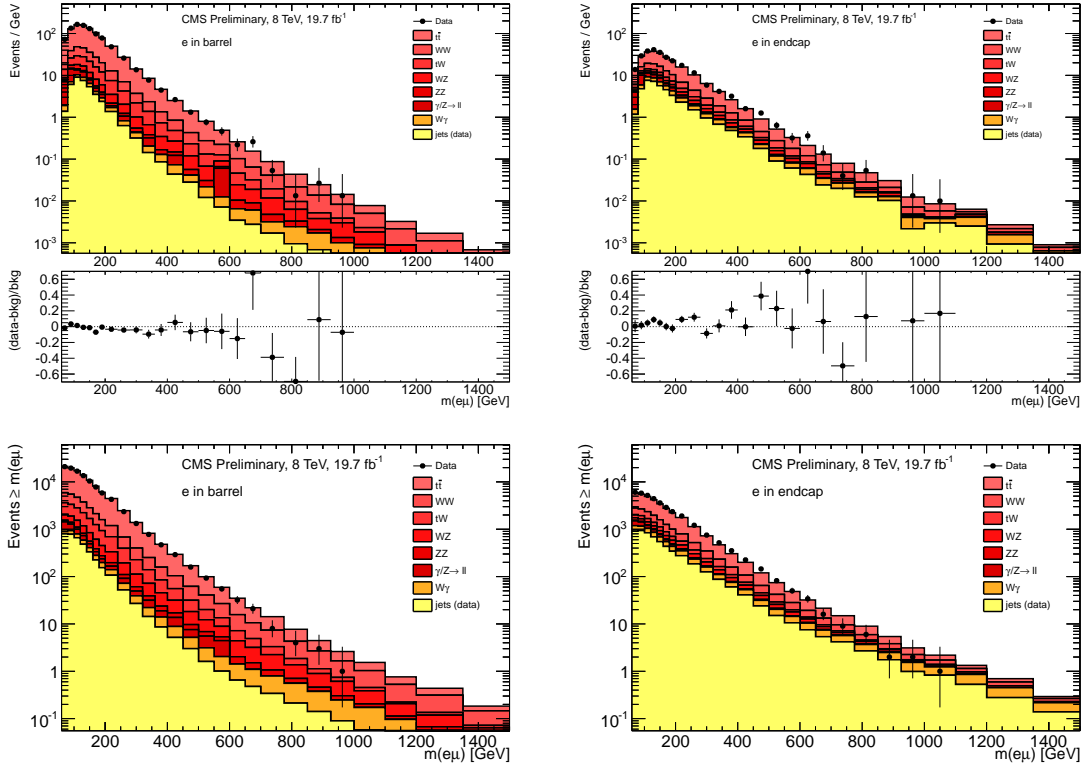


Figure 7.28 – Invariant mass spectrum of the selected $e\mu$ pair events where the HEEP electron candidate is in the barrel (top left) and in the endcap (top right) of the detector. The data are represented by the points with error bars, while the histograms show the expected contributions from SM processes. The error bars on the data points represent the statistical uncertainties. The bottom distribution on the top plots shows the data minus background over background distribution. The plots at the bottom show the corresponding cumulated distributions, where all the events above the mass on the x -axis are summed.

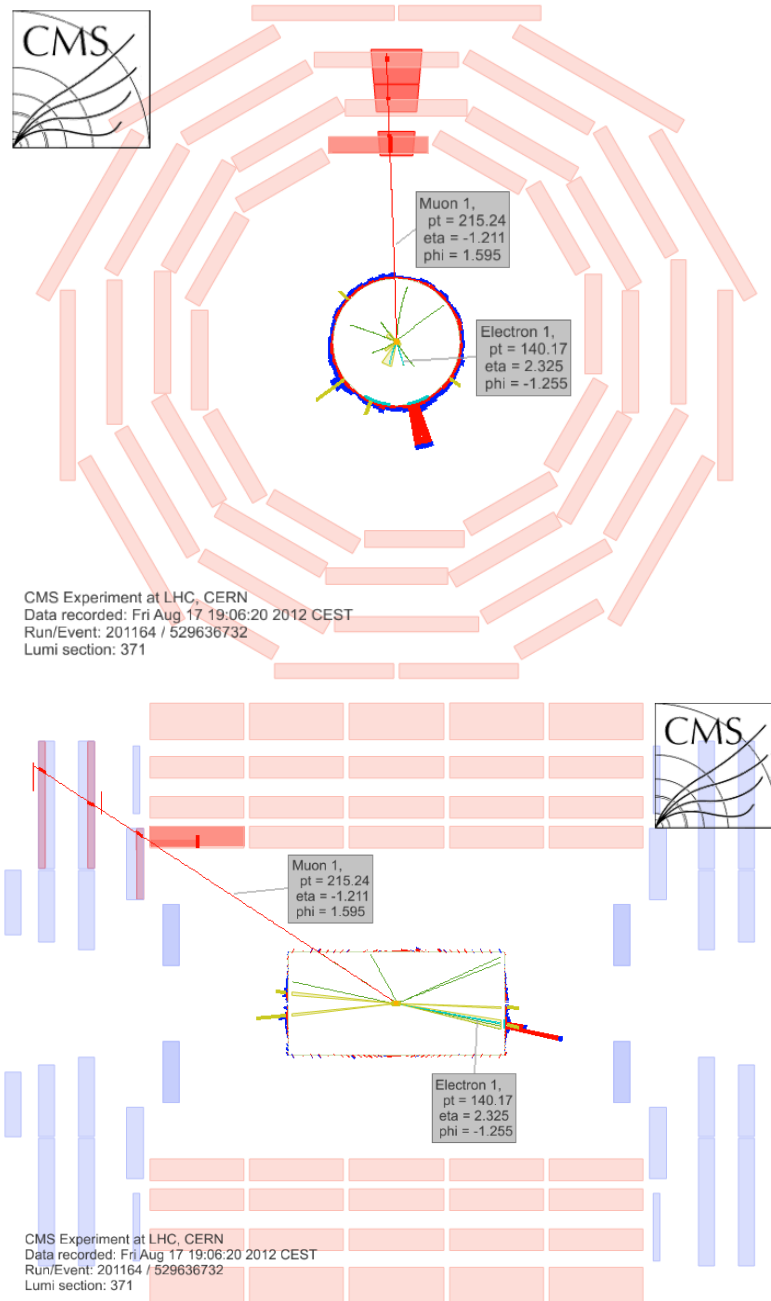


Figure 7.29 – Event display of the highest invariant mass event selected, with a mass of $m(e\mu) = 1046$ GeV. The top plot shows the event in the ρ - ϕ plane of the detector and the bottom plot shows the ρ - z plane. The red (blue) bars indicate the energy in the ECAL (HCAL). Tracks with a $p_T > 3$ GeV and reconstructed jets with $p_T > 20$ GeV are shown.

Table 7.7 – Composition of the expected SM background in three $e\mu$ invariant mass ranges.

Process	$M_{e\mu} < 500$ GeV	500 GeV $< M_{e\mu} < 1000$ GeV	1000 GeV $< M_{e\mu} < 1500$ GeV
$t\bar{t}$	69%	53%	28%
WW	11%	19%	24%
tW	7%	6%	3%
W+jets, multijets	6%	9%	22%
WZ, ZZ	3%	7%	9%
DY	3%	2%	-
$W\gamma$	1%	4%	14%

that a new resonance is found in the $e\mu$ spectrum, the asymmetry could be used to test if the signal behaves like predicted by the LFV model, or if a different theory, symmetric in the yield for $e^-\mu^+$ and $e^+\mu^-$, describes the observations better.

The invariant mass spectra for $e^-\mu^+$ and $e^+\mu^-$ events are shown in the two plots in Figure 7.30, with the SM expectations and example shapes for LFV signals. As expected, the signal yield in the left plot is much larger than in the right plot. The data and the expected background contribution in the two plots have a compatible yield. The subtraction of the $e^+\mu^-$ spectrum from the $e^-\mu^+$ spectrum results in the distributions shown in Figure 7.31. The two plots in the figure are identical with the exception of the axis ranges. It has to be noted that, because of the subtraction, an excess in the distribution can come either from an excess in the $e^-\mu^+$ spectrum, or from a deficit in the $e^+\mu^-$ spectrum.

The fluctuations of the background expectation around zero, left by the subtraction of the SM background expectations, remain larger than the expected signal peak from the LFV model. Therefore, the asymmetry of the opposite-sign invariant mass spectra is not used to improve the sensitivity of a search for new LFV resonances.

7.8 Uncertainties

Various systematic uncertainties have to be taken into account for the background and the signal estimations. Some uncertainties affect the normalisation of the background, while others change the shape of the $e\mu$ invariant mass distribution. In the later case the impact of the uncertainty is estimated by varying the parameter up and down by one standard deviation, if not stated otherwise, and observing the effects for the invariant mass spectrum.

7.8.1 Systematic uncertainties on the background

For the background the following uncertainty sources are considered:

Luminosity A 2.6% uncertainty is assigned to the measurement of the integrated luminosity to which the simulated samples are normalised [76].

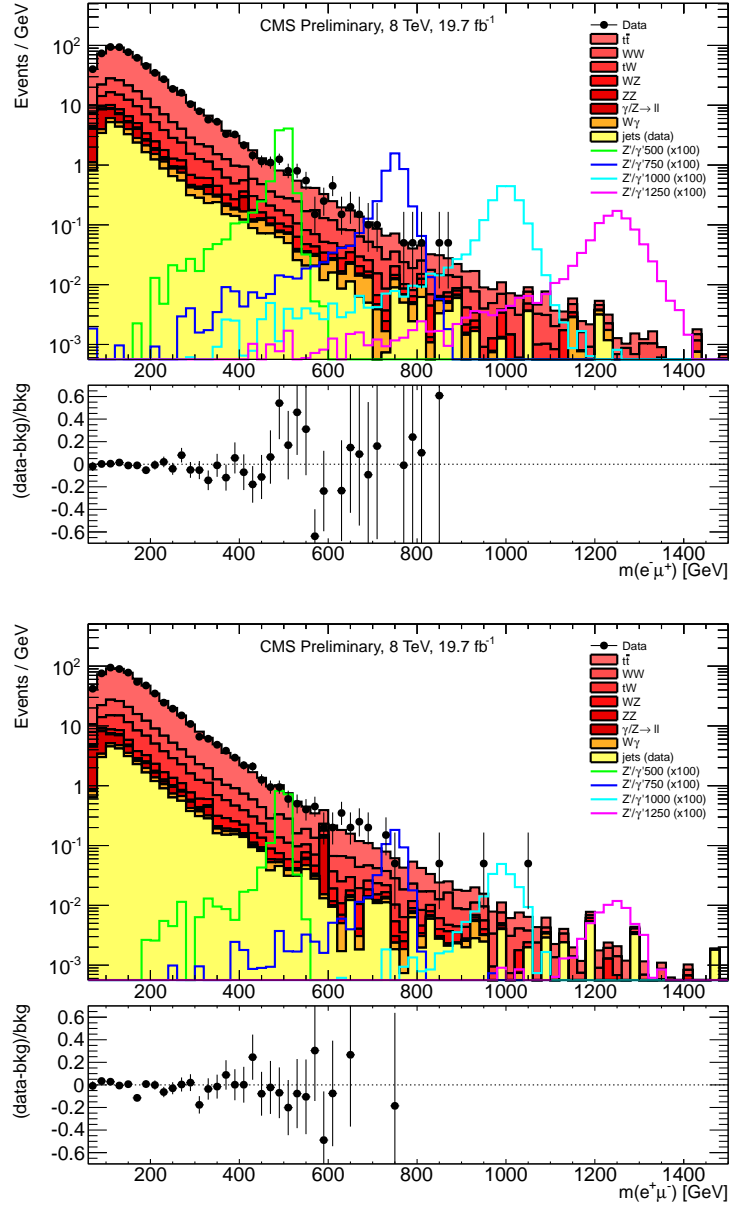


Figure 7.30 – Invariant mass spectra of the selected $e^-\mu^+$ pair events on the top plot, and $e^+\mu^-$ pair events on the bottom plot. The data are represented by the points with error bars, while the histograms show the expected contributions from SM processes. The error bars on the data points represent the statistical uncertainties. Also shown are four curves that represent the 100 times enhanced expected spectra from the LFV model for a $Z'_{\text{LFV}}/a'_{\text{LFV}}$ with different masses. The plots below the spectra show the data minus background over background distribution.

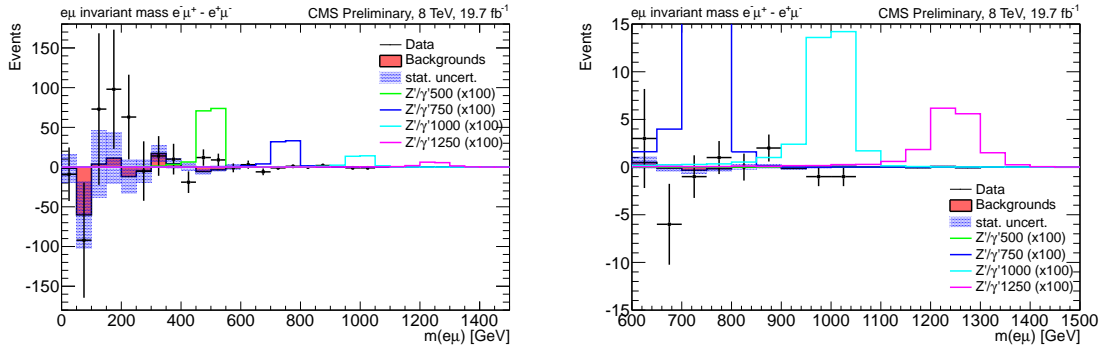


Figure 7.31 – The distribution of the $e^- \mu^+$ subtracted by the $e^+ \mu^-$ invariant mass spectrum. The data are represented by the points with error bars, while the histogram shows the expected contributions from SM processes. The error bars on the data points represent the statistical uncertainties. The statistical uncertainty on the background estimation is shown as dotted area. Also shown are four curves that represent the 100 times enhanced expected spectra from the LFV model for a $Z'_{\text{LFV}}/a'_{\text{LFV}}$ with different masses. The two plots distinguish themselves only by the ranges of the axes.

Sample cross section The uncertainties on the theoretical cross sections for the simulated sample process are given below. They are taken from the CMS cross section table [110] if not stated otherwise. For most of the processes these are taken to be constant, but for the WW process an additional mass dependent uncertainty from higher order corrections is considered. In case of the uncertainty on the $W\gamma$ process, the modeling of the photon conversion has to be considered as well.

- $t\bar{t}$: 5%
- WW: An uncertainty of 4% from the renormalisation and factorisation scale, to which a 10%/TeV mass dependent uncertainty from higher order corrections [111] is added in quadrature, is used.
- WZ: 4%
- ZZ: 3%
- tW: 3%
- DY: 1%
- $W\gamma$: The LO cross section calculated with MADGRAPH5 is used, to which the photon misreconstruction as electron candidates has to be added. A 50% uncertainty is assumed for this process.

Jet background The uncertainty on the jet background estimation with the electron fake rate is taken to be 30% as explained in Section 7.5.2.

PDF The evaluation of the PDF uncertainties is performed with the PDF4LHC recipe [102]. The CT10 [112], MSTW2008 [11] and NNPDF23 [19] NLO PDF

sets are used, and the uncertainties arising from the parametrisation of the PDF fit, plus the different choice of the strong coupling constant α_S in the PDFsets, are included. The upper and lower bounds of contours for the different PDF sets, $\Delta_{\text{PDF}}^{\pm i}(M_{e\mu})$, are defined by the relative difference between the number of all simulated background events in a mass bin, with a $\pm 1\sigma$ variation of the parameters of the PDF set i , $N_{\sigma\pm}^i(M_{e\mu})$, and the number obtained for the nominal set, $N(M_{e\mu})$.

$$\Delta_{\text{PDF}}^{+i}(M_{e\mu}) = \frac{N_{\sigma+}^i(M_{e\mu}) - N(M_{e\mu})}{N(M_{e\mu})}, \quad (7.5)$$

$$\Delta_{\text{PDF}}^{-i}(M_{e\mu}) = \frac{N_{\sigma-}^i(M_{e\mu}) - N(M_{e\mu})}{N(M_{e\mu})}. \quad (7.6)$$

The envelope of these three contours is taken. A fit of a second order polynomial below $M_{e\mu} = 1.4 \text{ TeV}$, to the mean from to upper and lower bound of the PDF4LHC envelope on the total background event yield, gives

$$\delta(M_{e\mu}) = 0.045 + 3.4 \times 10^{-5} \cdot \frac{M_{e\mu}}{\text{GeV}} + 1.5 \times 10^{-8} \cdot \left(\frac{M_{e\mu}}{\text{GeV}}\right)^2. \quad (7.7)$$

This function is used to extrapolate the PDF uncertainty to higher $M_{e\mu}$. Figure 7.32 shows the fitted function. For the total simulated background the uncertainty rises from 5% at $M_{e\mu} = 100 \text{ GeV}$, to 10% at an invariant mass of 1.5 TeV.

Efficiency scale factors The electron efficiency scale factors are measured at the Z peak, and the uncertainty of the evolution to high invariant mass has a value of 2% for barrel electrons and 4% for endcap electrons [1]. The muon efficiency scale factors range from 1% at an invariant mass of 1 TeV to 3.5% at 3 TeV [97]. A 5% uncertainty due to the efficiency scale factors is assumed at masses above the Z peak.

Electron energy scale ECAL detector performance measurements [113] show an uncertainty of 0.6% for electron candidates in the barrel, and 1.5% for electron candidates in the endcaps. This uncertainty is taken as an uncertainty on the background shape in the limit calculations.

Muon momentum scale From cosmic data a curvature bias of $+0.05/\text{TeV}$ is measured for muons with $p_T > 200 \text{ GeV}$, with the cosmic endpoint method described in [66]. The uncertainty is taken as a background shape affecting uncertainty in the limit calculations.

Invariant mass resolution The uncertainty on the invariant mass resolution is dominated by the uncertainty on the muon momentum resolution. An additional Gaussian smearing of 30% of the muon p_T resolution taken from Equation (7.2) is applied on the $1/p_T$ distribution of the muon to estimate the uncertainty on the background shape.

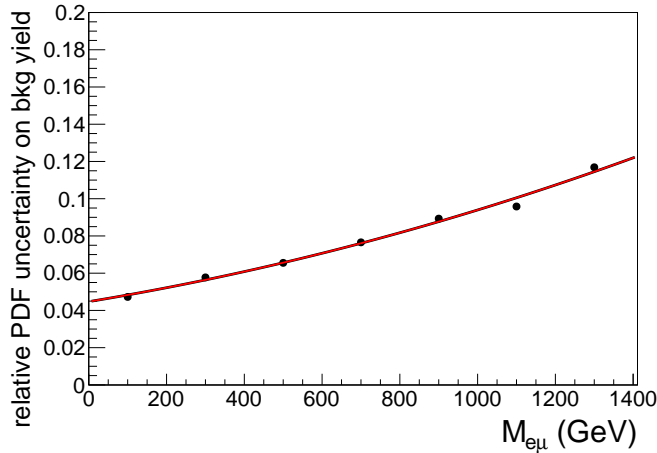


Figure 7.32 – Fit of a second order polynomial, to the mean from to upper and lower bound of the PDF4LHC envelope on the total background event yield, as a function of $M_{e\mu}$ [115].

$t\bar{t}$ top p_T reweighting and aNNLO corrections The $t\bar{t}$ background shape uncertainty is estimated differently for the downward and the upward fluctuating shape. The downward shape is estimated using the top/antitop p_T reweighting. This reweighting is not performed in the analysis, as explained in Section 7.6.2. However, the difference of the invariant mass spectra with and without the reweighting is taken as an estimation for the downward fluctuating shape uncertainty for the $t\bar{t}$ background.

For the upward fluctuating shape uncertainty, the difference of the invariant mass spectra, with and without the aNNLO-to-NLO K-factor from Figure 3 in [114] applied, is taken as an estimate. The K-factor is parametrised as

$$\begin{aligned}
 k(p_T^t) &= 1 && \text{for } p_T^t < 300 \text{ GeV}, \\
 k(p_T^t) &= 1 + 1.2 \cdot \left(\frac{p_T^t - 300 \text{ GeV}}{700 \text{ GeV}} \right) && \text{for } p_T^t \geq 300 \text{ GeV}. \quad (7.8)
 \end{aligned}$$

At $M_{e\mu} = 1500$ GeV, this leads to a ratio of about 1.5 between the number of expected $t\bar{t}$ events with the K-factor applied and the NLO simulation.

7.8.2 Systematic uncertainties on the signal

For the signal the considered systematic uncertainties are:

Luminosity A 2.6% uncertainty is assigned to the measurement of the integrated luminosity to which the simulated samples are normalised [76].

Acceptance times efficiency An uncertainty of 5%, coming from the evolution of the efficiency scale factors to high invariant masses, is used.

PDF The PDF uncertainty for the signal, is estimated with a similar method than for the background, but with the acceptance instead of the event yield as observable. Choosing the acceptance as observable instead of the event yield as for the background has the advantage that it is a more model independent approach. PDF uncertainties affecting the cross section of a specific model can then be added as an uncertainty on the theoretical cross section estimation. The uncertainties on the acceptance from varying the PDF range from 1.5% at a mass of 200 GeV to 0.5% above masses of 1500 GeV, and are subleading to the 5% uncertainty on the acceptance times efficiency [115]. The falling trend of the uncertainty can be explained by the fact that the leptons are emitted more centrally for higher invariant masses, and are, thus, further away from the acceptance limits in η .

Invariant mass resolution The uncertainty on the muon momentum resolution dominates the uncertainty on the invariant mass resolution. Since the signal width is much smaller than the resolution, the shape of the signals $e\mu$ invariant mass spectrum is directly affected by the uncertainty on the mass resolution. For the estimation of the uncertainty on the mass resolution the difference between the C1 and the C2 muon system alignment scenarios, shown in Figure 7.14, is taken. Table 7.5 lists the parametrisation of this difference. It is used to widen and narrow the signal shape for the upward and downward shape fluctuations, respectively, for the limit calculation.

7.8.3 Statistical uncertainties

In addition to the systematic uncertainties also the statistical uncertainties become important in the high invariant mass region, where the number of simulated events for the background processes becomes low. Beyond $M_{e\mu} \sim 1.4$ TeV the statistical uncertainty becomes larger than the total systematic uncertainty. For the limit calculation the statistical uncertainty is taken into account as well.

7.9 Statistical interpretation

No significant excess over the SM expectation is observed in the $e\mu$ invariant mass spectrum shown in Figure 7.24. Therefore, 95% C.L. upper limits on the signal cross section times the branching ratio of a new narrow resonance are calculated.

7.9.1 Limit calculation

For the calculation of the 95% C.L. upper limits on the cross section times branching fraction of a new resonance a Bayesian approach was chosen [3]. A uniform prior is used for the signal cross section and the integration is carried out with a Markov Chain Monte Carlo procedure. The Metropolis–Hastings algorithm is used as MCMC method. The nuisance parameters from systematic uncertainties that affect the normalisation, and the statistical uncertainty on the background event yield of the simulated samples, are taken into account with a Log-normal prior. Another class of uncertainties changes the shape of the background distribution. These are taken into account from template histograms of the expected background, that have the nuisance parameter varied according to the estimation of its uncertainty, as described in Section 7.8. Like this, each background histogram that is affected by a certain uncertainty comes with two corresponding shape histograms that represent an up and down variation of the background, because of the uncertainty of the nuisance parameter.

The limit calculation for each mass hypothesis is done as a multibin counting experiment, using 1 GeV binned histograms as input for the data, and for the signal and background estimation. The search window, for a given mass of the $Z'_{\text{LFV}}/a'_{\text{LFV}}$ boson of the signal, is ± 6 times the invariant mass resolution around the $Z'_{\text{LFV}}/a'_{\text{LFV}}$ mass. For $M_{e\mu} \geq 800$ GeV the upper limit on the search window is dropped and all events up to $M_{e\mu} = 3$ TeV are counted.

In order to be able to normalise the template histograms for the uncertainties that affect the shape of the background mass spectrum, the histograms have to contain at least one entry if the nominal histogram for the background contains more than zero entries. In the high invariant mass region, the samples used can run out of simulated events, so that while e.g. the nominal histogram still contains entries, one of the template histograms can have these events not selected or shifted out of the search window. The vice versa case, where the nominal histogram is empty, can also happen and has to be treated as well. To avoid such cases, the upper or lower edge of the search window is adjusted in $\pm 1\%$ steps of the initial 6σ of the invariant mass resolution, to widen or narrow the search window. The window is widened in the case where the nominal histogram contains entries and one of the shape histograms does not, and narrowed in the case where the nominal histogram is empty in the beginning but one or more of the shape histograms contain entries. The widening or narrowing of the search window is done until the nominal histogram and all corresponding shape histograms contain at least one entry, or all contain no entries. A maximum of a 6% enlargement and a 5% narrowing is necessary for the input histograms used in the

limit calculation. It is to be noted, however, that for most invariant mass points, no adjustment is required.

7.9.2 Signal model

The LFV model under study results in a narrow resonance in the invariant mass spectrum, with an intrinsic width Γ much smaller than the detector mass resolution. Therefore, the signal is modeled with a Gaussian function centered at the mass of the $Z'_{\text{LFV}}/a'_{\text{LFV}}$ boson, and with the width taken from the mass resolution measurement in Section 7.4. The functional form of the invariant mass resolution is given in Equation (7.3).

Since the limit calculation is based on binned histograms, a random distribution is generated according to the Gaussian signal pdf and normalised to the number of expected signal events. The number of expected signal events is calculated by multiplying the integrated luminosity with the signal cross section times branching ratio to $e^\mp\mu^\pm$, and the acceptance times efficiency for the given resonance mass hypothesis. To arrive at a parametrisation for the signal cross section times branching ratio to $e^\mp\mu^\pm$ a fit is performed to the LO cross sections obtained from MADGRAPH5 for the samples listed in Table 7.3. The result of the fit can be seen in Figure 7.33 and the corresponding parametrisation is

$$\sigma(M_{Z'_{\text{LFV}}/a'_{\text{LFV}}}) = 3.984 \times 10^{-4} e^{-\frac{M_{Z'_{\text{LFV}}/a'_{\text{LFV}}} + \frac{323.6}{M_{Z'_{\text{LFV}}/a'_{\text{LFV}}} - \frac{\left(M_{Z'_{\text{LFV}}/a'_{\text{LFV}}}\right)^2}{1.050 \times 10^7}}}{397.4}}. \quad (7.9)$$

The corresponding shape histograms related to the invariant mass resolution uncertainty are created in the same way, with wider or narrower Gaussian distributions according to the invariant mass resolution uncertainty.

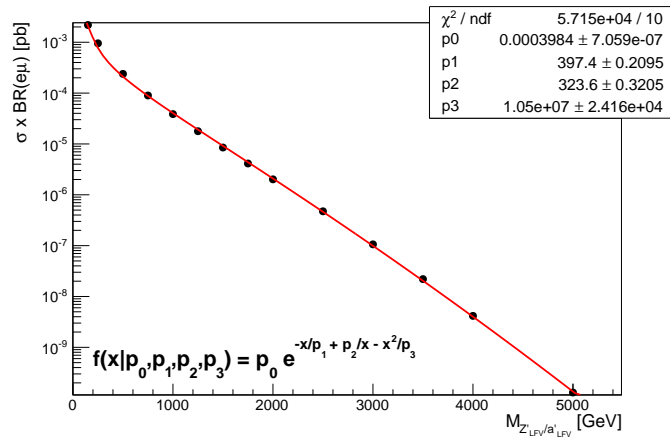


Figure 7.33 – A fit to the LO cross section times branching ratios for the MADGRAPH5 signal samples, which are represented by the dots.

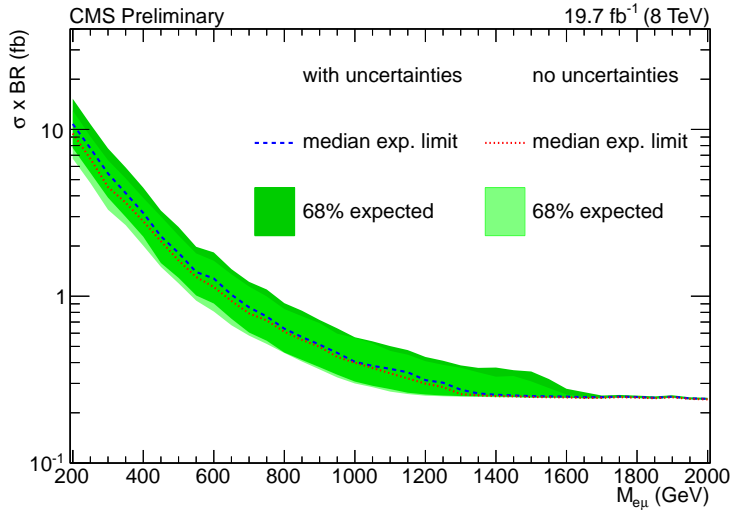


Figure 7.34 – Comparison of the 95% C.L. expected limits on the signal cross section times branching ratio (BR), with and without uncertainties taken into account for the limit calculation. The lines show the median expected limits and the two green coloured bands indicate the 1σ uncertainty bands for the two cases.

7.9.3 Background model

The background expectation is taken from simulated samples for the $t\bar{t}$, WW, WZ, ZZ, tW, $W\gamma$ and DY processes, and from the data driven estimation with the electron fake rate for the estimation of the W + jet and multijet contribution, as described in Section 7.5. The uncertainties associated to the background expectation are discussed in Section 7.8.

In order to see the impact of the uncertainties on the expected limits a plot is shown in Figure 7.34, comparing the expected 95% upper limits with the inclusion of the uncertainties to the result where the uncertainties are not taken into account. Without uncertainties the expected limits would be 11%, 4% and 5% better at $e\mu$ masses of 400 GeV, and 800 GeV and 1200 GeV, respectively.

7.9.4 Limit results

With the input given above, 95% C.L. upper limits on the signal cross section times branching ratio for the Z'_{LFV}/a'_{LFV} model are calculated. The resulting limit plot is shown in Figure 7.35, together with the expected limits and the curve indicating the cross section times branching ratio predicted by the LFV model, with the bounds from low energy experiments [45]. The observed 95% C.L. limits obtained are 3.9 fb, 0.60 fb and 0.26 fb at $e\mu$ invariant masses of 400 GeV, 800 GeV and 1200 GeV, respectively. The corresponding expected values are 3.2 fb, 0.64 fb and 0.31 fb. Since the search is not optimised for a certain topology, these results are model independent limits for a narrow $e\mu$ resonance. The result represents the first direct search for a

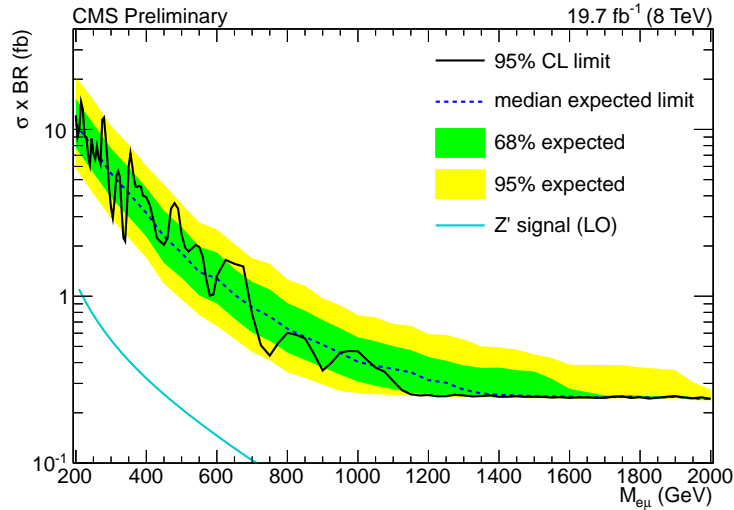


Figure 7.35 – 95% C.L. upper limits on the signal cross section times branching ratio (BR) to $e^\mp\mu^\pm$ for the LFV Z' model. The solid black line is the observed limit and the dashed black line shows the median expected limit. The two coloured bands indicate the 1σ and 2σ uncertainty band for the expected limit. The line below the limit curve represents the theory expectation for the LFV Z' model with the model parameters from [45].

narrow $e\mu$ resonance with the CMS detector.

In the case of an interpretation of the results in the LFV model, the analysed integrated luminosity is not sufficient to improve the bounds already existing. The inclusive search achieves a sensitivity in the expected limits, of approximately ten times the predicted cross section times branching ratio of the LFV model. The cross section times branching ratio of the LFV model is 0.32 fb, 0.075 fb and 0.022 fb at masses of 400 GeV, 800 GeV and 1200 GeV, respectively.

Apart from the search for a narrow resonance in the context of a LFV Z' model, also a search for a narrow resonance coming from an R -parity violating Supersymmetry model [22, 116] and a search for deviations of the spectrum coming from quantum black hole models [117] have been performed with the $e\mu$ invariant mass spectrum. The results of the searches are described in a paper that is currently in preparation [2]. A search for new physics, in the context of R -parity violating Supersymmetry, using also the $e\mu$ final state was performed by the ATLAS experiment for a pp center-of-mass energy of 7 TeV [50].

7.10 Summary

In this chapter, the search for a new massive resonance decaying to an electron-muon pair was described. This channel violates the lepton flavour conservation of the SM. For the search, the full dataset corresponding to $19.7 \pm 0.5 \text{ fb}^{-1}$, recorded by the CMS experiment during the 2012 data taking at a pp center-of-mass energy of 8 TeV, was analysed.

The event selection requires a high energy electron candidate and a high p_T muon candidate. The invariant mass resolution at high lepton energies is dominated by the muon p_T resolution, and was estimated with simulated signal samples for a realistic alignment scenario of the muon system. The analysis was designed to be inclusive in its event selection in order to allow for searches for different signals. This approach leaves contributions from several background processes in the spectrum, that had to be considered. The most important background process is the $t\bar{t}$ production, but towards higher invariant masses the WW and the jet induced background become more and more important. All background estimations, except the one for the jet induced background, were taken from simulated samples. Contributions from background processes involving jets that were misidentified and selected as electron candidates were estimated from data.

The obtained $e\mu$ invariant mass spectrum does not show any deviations from the SM expectation that could point to new physics. A Bayesian multibin limit calculation was performed with the selected events from the $e\mu$ invariant mass spectrum, to set 95% C.L. upper limits on the cross section times branching ratio of a new resonance. With the strong constraints from low energy experiments for the LFV Z' model under study, the analysed dataset was too small to improve the existing bounds. This analysis represents, however, the most sensitive result for the search of a LFV heavy boson that decays to the $e^\mp\mu^\pm$ final state.

Conclusions

The standard model of elementary particle physics is a very successful theory and describes well all the measurements performed. It is known, however, that it is not a complete theory, and new physics is expected to be lying undiscovered beyond the edges of what can be explained by the SM. In this context, the thesis at hand presented the searches for new physics, that manifests itself as new massive, narrow resonances decaying to dielectrons or electron-muon pairs, with the CMS detector. Two independent but related analyses were performed for the two different final states. The former represents an important search channel for new physics, studied already by experiments predating the LHC, and is considered an analysis of high priority within the CMS collaboration. The later signal comes from a process that breaks the lepton flavour conservation of the SM. Both searches benefit from the never before achieved center-of-mass energy of the proton-proton collisions at the LHC, which increases the production cross section for heavy resonances significantly compared to previous accelerators. This made it possible to probe for new resonances in mass regions never studied before. The full dataset of proton-proton collisions at $\sqrt{s} = 8 \text{ TeV}$, recorded in 2012 and accumulating $19.7 \pm 0.5 \text{ fb}^{-1}$, was analysed for both searches.

The thesis gave a brief introduction to the SM of elementary particle physics, and discussed its shortcomings. Beyond the SM theories, that aim at resolving some of these shortcomings, were introduced. Grand unified theories and theories with extra dimensions are relevant, since they predict heavy resonances at the TeV scale.

The LHC and the CMS detector, with its subdetectors and trigger system, were described. The reconstruction of electron and muon candidates was presented, since these are the key particles used in both analysis final states. The reconstruction of jets and the missing transverse energy variable, which are used as control variables in the analysis, were explained as well.

The search for new heavy resonances in the dielectron invariant mass spectrum was described in detail. It uses an electron selection that was optimized for high efficiency at high electron energies. The most important background for the search comes from the Drell–Yan process, which accounts for about 85% of the events in the search region. The DY background estimation was taken from simulations. Other backgrounds with prompt leptons in the final state include $t\bar{t}$ and WW production, and were also taken from simulations. A data driven verification of the simulation for these processes was performed, using the electron-muon invariant mass spectrum. The jet background, contributing to the dielectron mass spectrum, was estimated

from data. The analysis was performed separately for events with both electron candidates in the detector barrel, and for events where one electron candidate was registered in one detector endcap. Events with both electron candidates registered in the detector endcaps were not considered. The two channels were combined for the final dielectron limit calculation. The measured invariant mass spectra fit the ones predicted by the SM well. With a shape based Bayesian limit calculation, 95% confidence level upper limits could be set on the ratio of cross section times branching ratio of a new resonance to the one from the Z resonance. Using the ratio as a parameter of interest cancels or suppresses some systematic uncertainties. Notably, the uncertainty on the measured integrated luminosity does not have an impact on the result. With the measured upper limit on the cross section ratio, lower limits on the resonance masses, for particles predicted by various models, could be set. For spin 1 resonances, masses below 2.67 TeV, for a Z'_{SSM} from the sequential standard model, and below 2.34 TeV for a Z'_ψ from Grand unified theories, could be excluded with the dielectron channel alone. Excluded masses for the spin 2 Randall–Sundrum graviton range from 1.25 TeV for a coupling of $c = 0.01$, to 2.50 TeV for a coupling of $c = 0.1$. When combined with the analysis in the dimuon channel, which is not described in detail in this thesis, masses below 2.90 TeV and 2.57 TeV could be excluded for the Z'_{SSM} and the Z'_ψ , respectively. For the Randall–Sundrum graviton the excluded masses range from 1.27 TeV to 2.73 TeV for couplings between $c = 0.01$ and $c = 0.1$.

The second analysis presented in this thesis is the search for new resonances in the electron-muon invariant mass spectrum. The same electron candidate selection as for the dielectron analysis was used, in combination with a muon candidate selection optimised for muons with a high transverse momentum. A simple event selection was chosen in order to be as model independent as possible. The most important backgrounds come from $t\bar{t}$ production, and towards higher invariant masses also from the WW process and from jet induced background events. Simulated samples, normalised to the integrated luminosity, were used for all background processes, except for the jet induced background, which was estimated from data with a similar method like for the dielectron analysis. The agreement between the measured invariant mass spectrum and the SM prediction shows no sign of new physics. A Bayesian technique was used for the calculation of 95% confidence level upper limits on the production cross section times the branching ratio to an electron-muon pair, of a spin 1 heavy resonance. Observed limits are 3.9 fb, 0.60 fb and 0.26 fb at $e\mu$ invariant masses of 400 GeV, 800 GeV and 1200 GeV, respectively. This resonance search gives the most sensitive result, obtained with CMS data, in the electron-muon final state. The limits can be interpreted in a particular model that predicts a lepton flavour violating Z' boson. In this interpretation, the existing bounds from low energy experiments, could not be improved with the amount of data that were analysed.

After being upgraded since 2013, the LHC is scheduled to restart in 2015, with a higher collision energy of 13 TeV in the proton-proton center-of-mass. A further increase to a center-of-mass energy of 14 TeV is planned until the end of the next LHC run. Since the cross section for heavy resonances increases with the collision energy, higher mass regions than before will be available for new physics searches.

With only a few months of data taking, the sensitivity of the searches presented in this thesis can already be reached. With the full dataset of an integrated luminosity of about 300 fb^{-1} , that is expected to be collected until the next long shutdown of the LHC, the discovery potential can reach resonance masses beyond 4.5 TeV [118]. An active program is undertaken since the end of the first LHC run, to adapt the dielectron analysis to the new data taking conditions in 2015, which will be even more challenging than the conditions in 2012. The search for new physics in the electron-muon invariant mass spectrum will benefit as well from the increased collision energy. It is therefore important that an analysis, like the one presented in this thesis, is also performed with the data collected in the upcoming LHC run. With an integrated luminosity of 300 fb^{-1} at a pp center-of-mass energy of 14 TeV, the search could start to probe the lepton flavour violating model, that was described in this thesis. Furthermore, improvements of the discovery potential will also be possible for other models that predict a resonance, or a deformation of the electron-muon invariant mass spectrum.

It is known that new physics has to be lying beyond of what the SM can describe, but where exactly the new physics lies we can not know until we discover it. With the CMS experiment at the LHC, we have the ability to probe further the uncharted regions, and find a new piece to our understanding of the universe.

Appendix A

Dielectron invariant mass resolution fits

Fits of a DCB function to $m_{\text{RECO}} - m_{\text{true}}$ for DY and Z' signal samples. Figures A.1 to A.3 show the plots obtained with the DY samples in the barrel-barrel, barrel-endcap and endcap-endcap case, respectively. Figures A.4 to A.6 show the plots obtained with Z'_ψ signal samples and a Z'_{SSM} signal sample, in the barrel-barrel, barrel-endcap and endcap-endcap case, respectively. See also Section 6.3 for a detailed description.

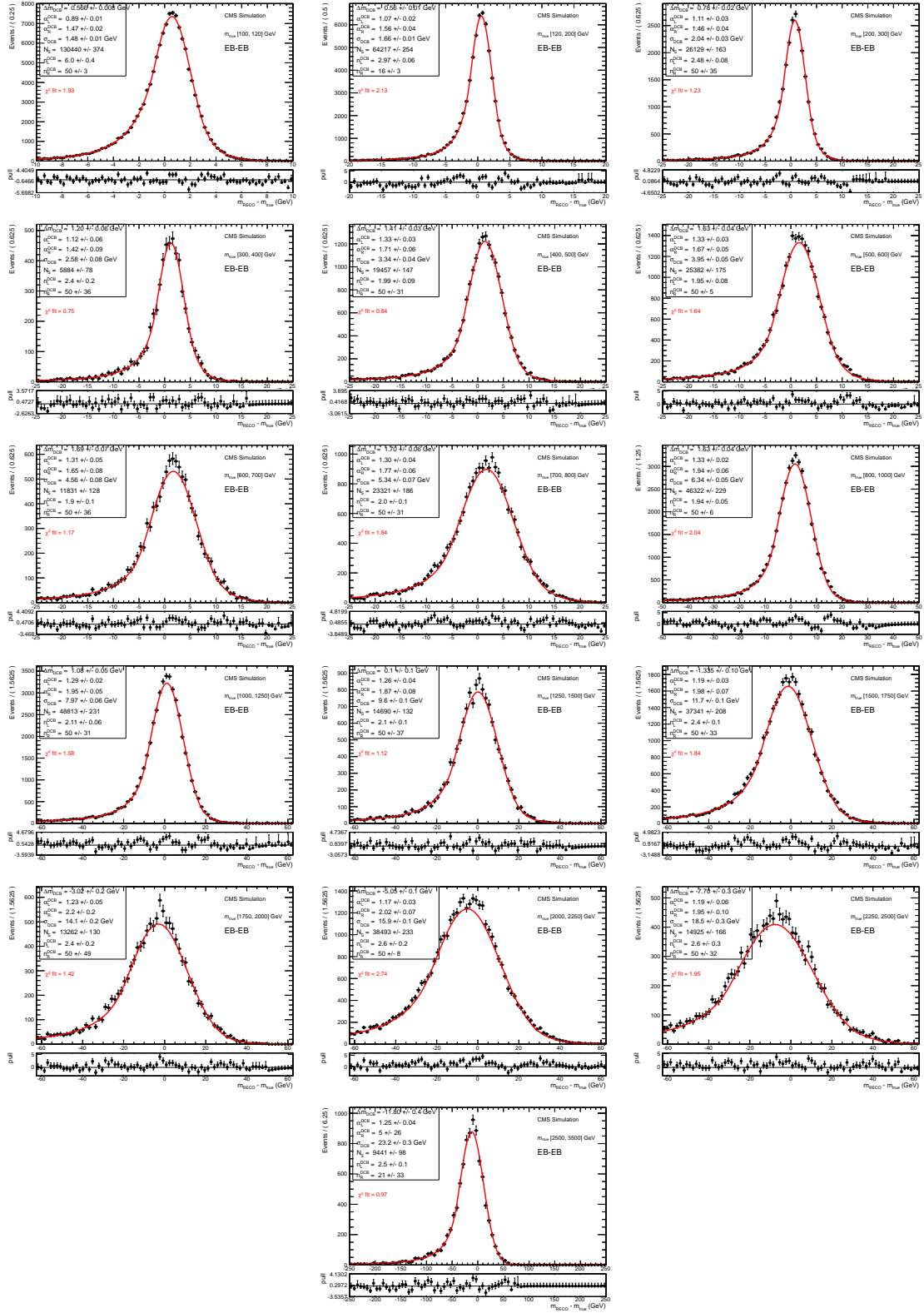


Figure A.1 – Fit of a DCB function to $m_{\text{RECO}} - m_{\text{true}}$ for barrel-barrel dielectron events selected from DY samples.

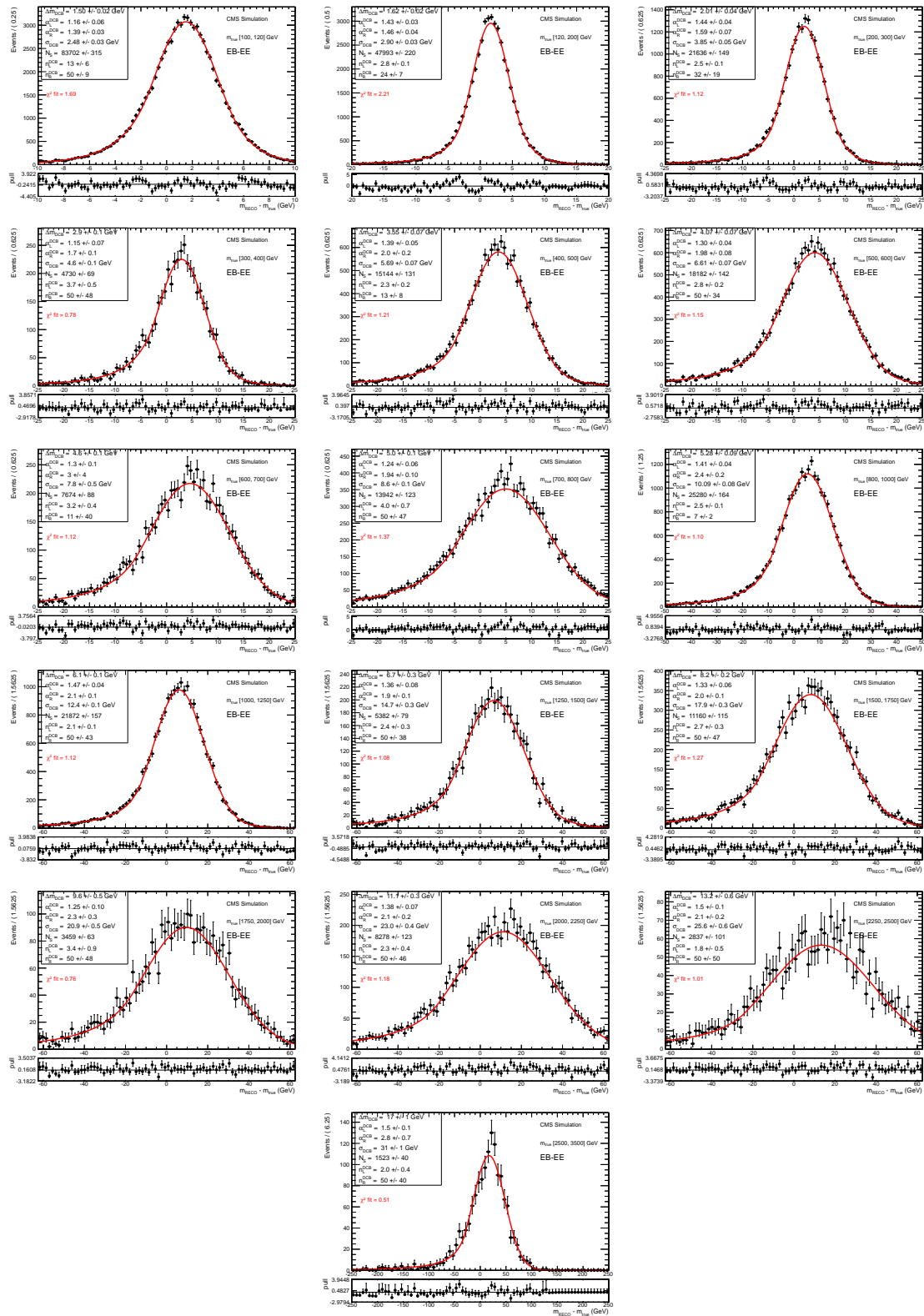


Figure A.2 – Fit of a DCB function to $m_{\text{RECO}} - m_{\text{true}}$ for barrel-endcap dielectron events selected from DY samples.

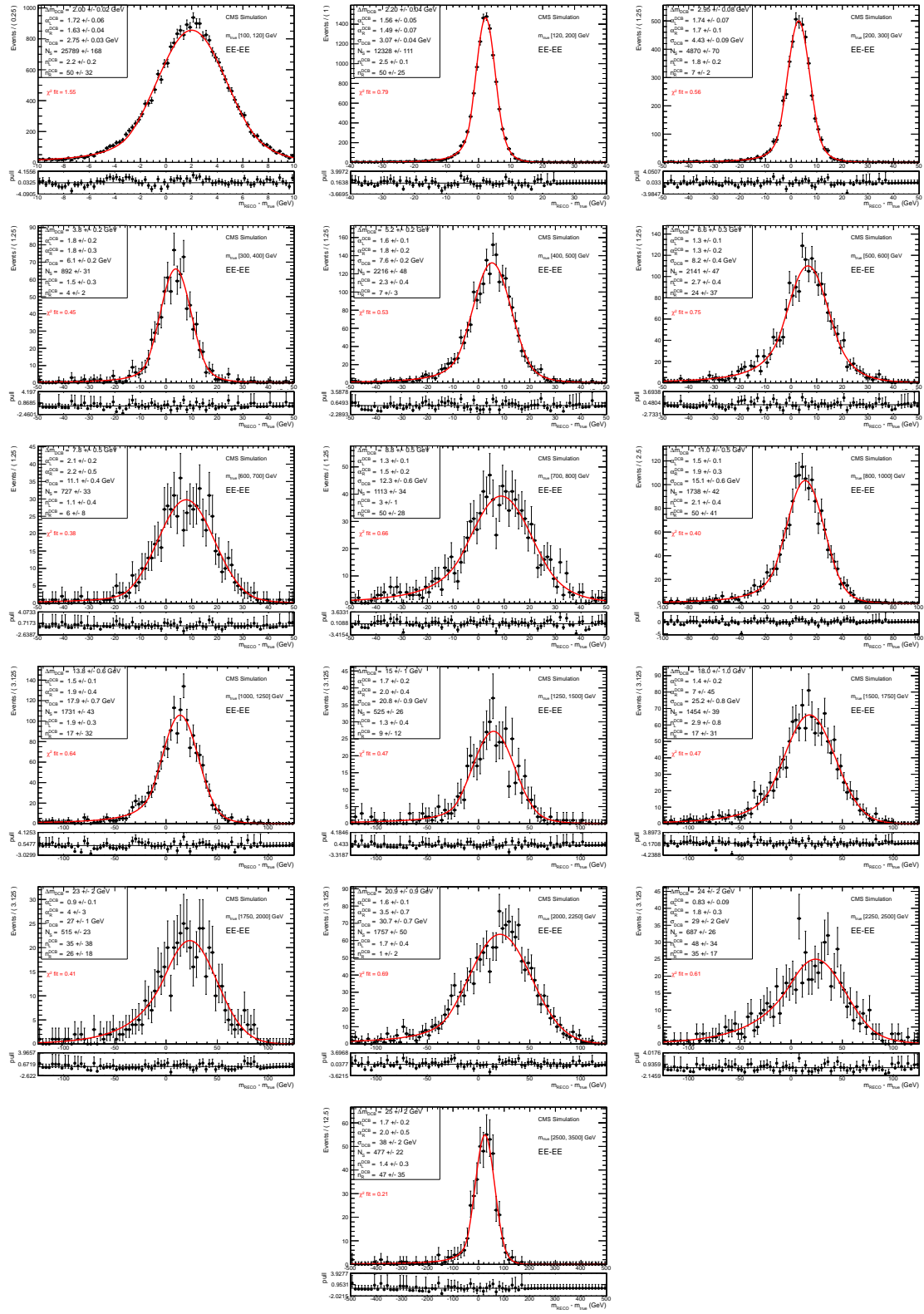


Figure A.3 – Fit of a DCB function to $m_{\text{RECO}} - m_{\text{true}}$ for endcap-endcap dielectron events selected from DY samples.

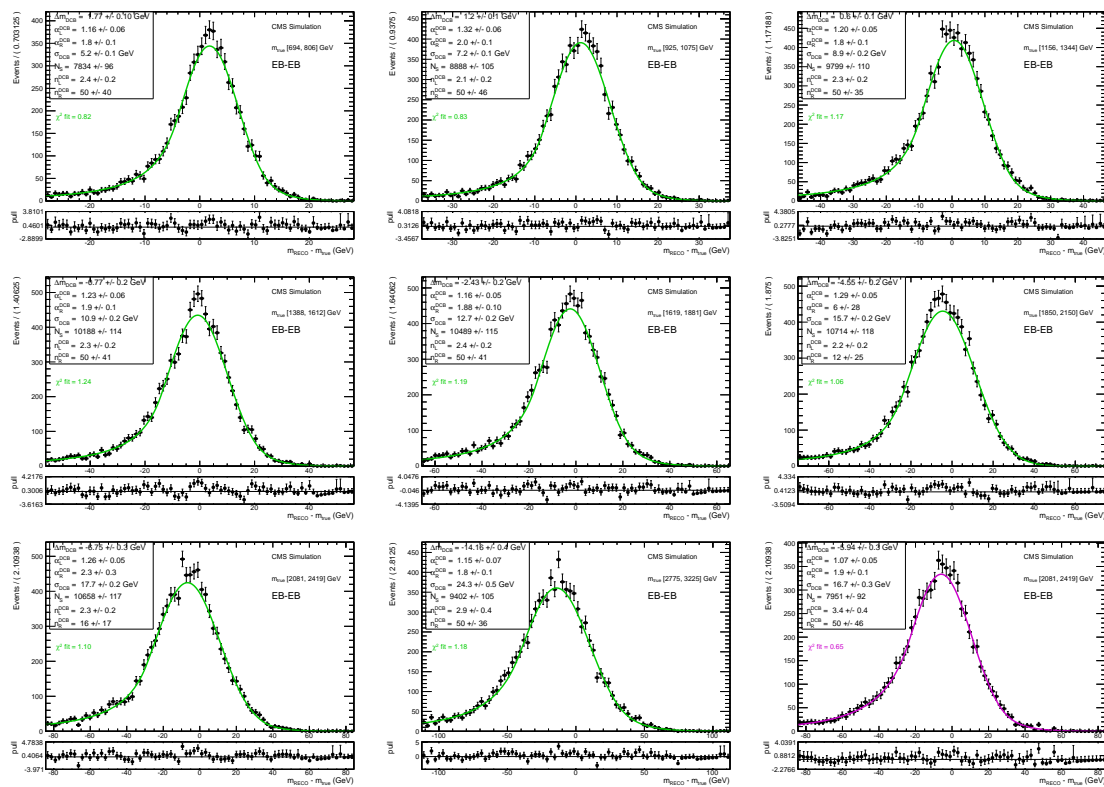


Figure A.4 – Fit of a DCB function to $m_{\text{RECO}} - m_{\text{TRUE}}$ for barrel-barrel dielectron events selected from Z'_{ψ} samples (first 8 plots) and a Z'_{SSM} sample (bottom right plot).

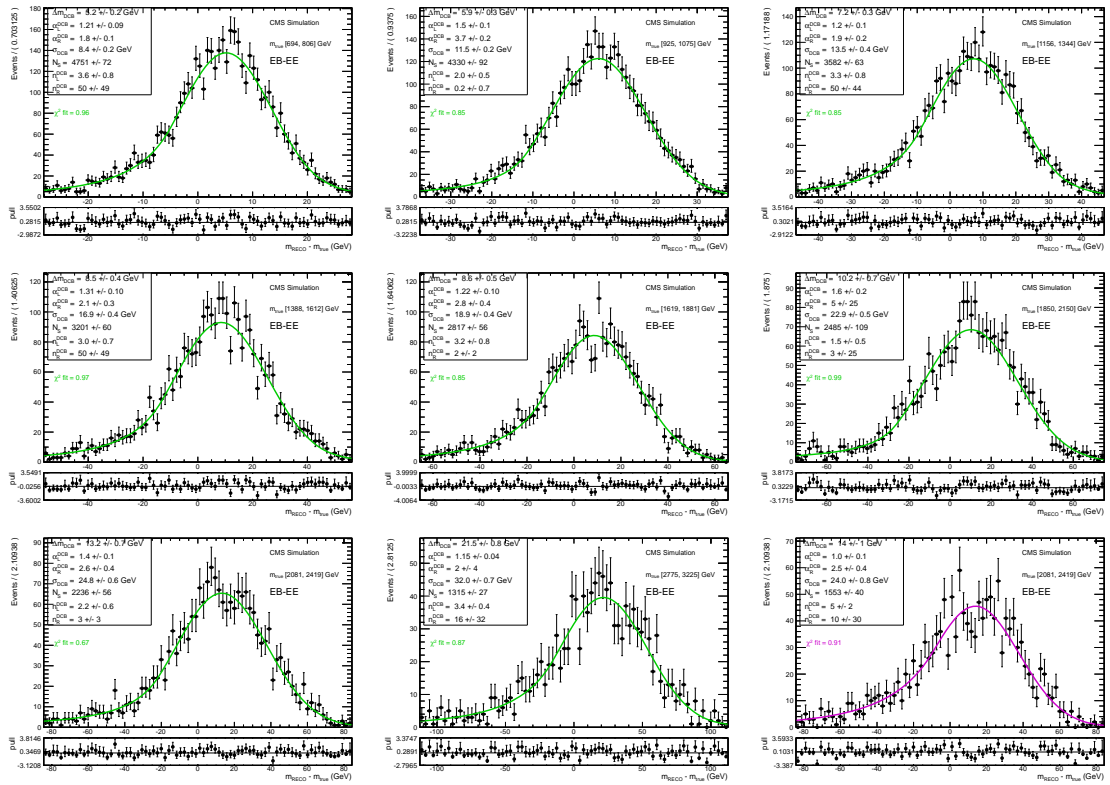


Figure A.5 – Fit of a DCB function to $m_{\text{RECO}} - m_{\text{true}}$ for barrel-endcap dielectron events selected from Z'_{ψ} samples (first 8 plots) and a Z'_{SSM} sample (bottom right plot).

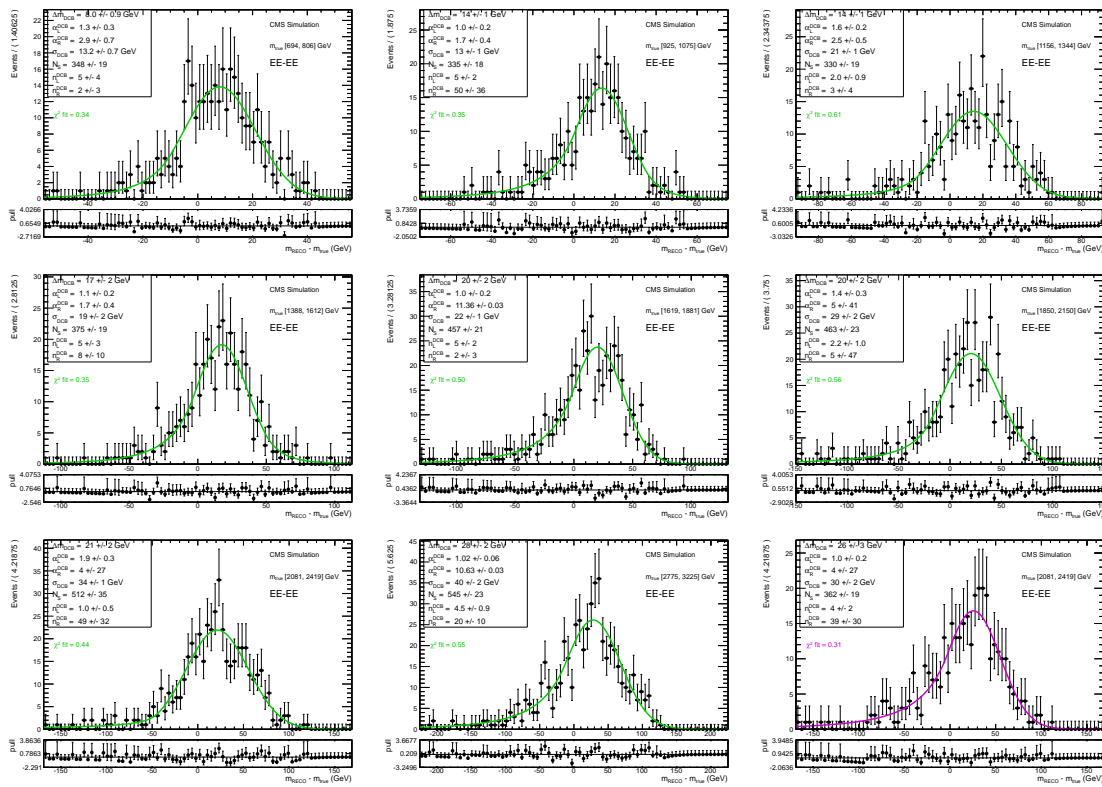


Figure A.6 – Fit of a DCB function to $m_{\text{RECO}} - m_{\text{true}}$ for endcap-endcap dielectron events selected from Z'_ψ samples (first 8 plots) and a Z'_{SSM} sample (bottom right plot).

Appendix B

Muon p_T and $e\mu$ invariant mass resolution fits

This appendix shows fits for muon p_T resolution and the $e\mu$ invariant mass resolution estimation in Chapter 7.

B.1 Muon p_T resolution fits

Figures B.1 and B.2 show, respectively for different muon system alignments, the fits of a Gaussian function to the distribution $R = (1/p_T^{\mu\text{reco}} - 1/p_T^{\mu\text{gen}})/(1/p_T^{\mu\text{gen}})$ for different p_T ranges, as explained in Section 7.4.1.

B.2 $e\mu$ mass resolution fits

Figures B.3 and B.4 show, respectively for different muon system alignments, the fits of a Gaussian function to the $(M_{e\mu}^{\text{reco}} - M_{e\mu}^{\text{gen}})/M_{e\mu}^{\text{gen}}$ spectra for different $Z'_{\text{LFV}}/a'_{\text{LFV}}$ masses. See also Section 7.4.2 for a detailed description.

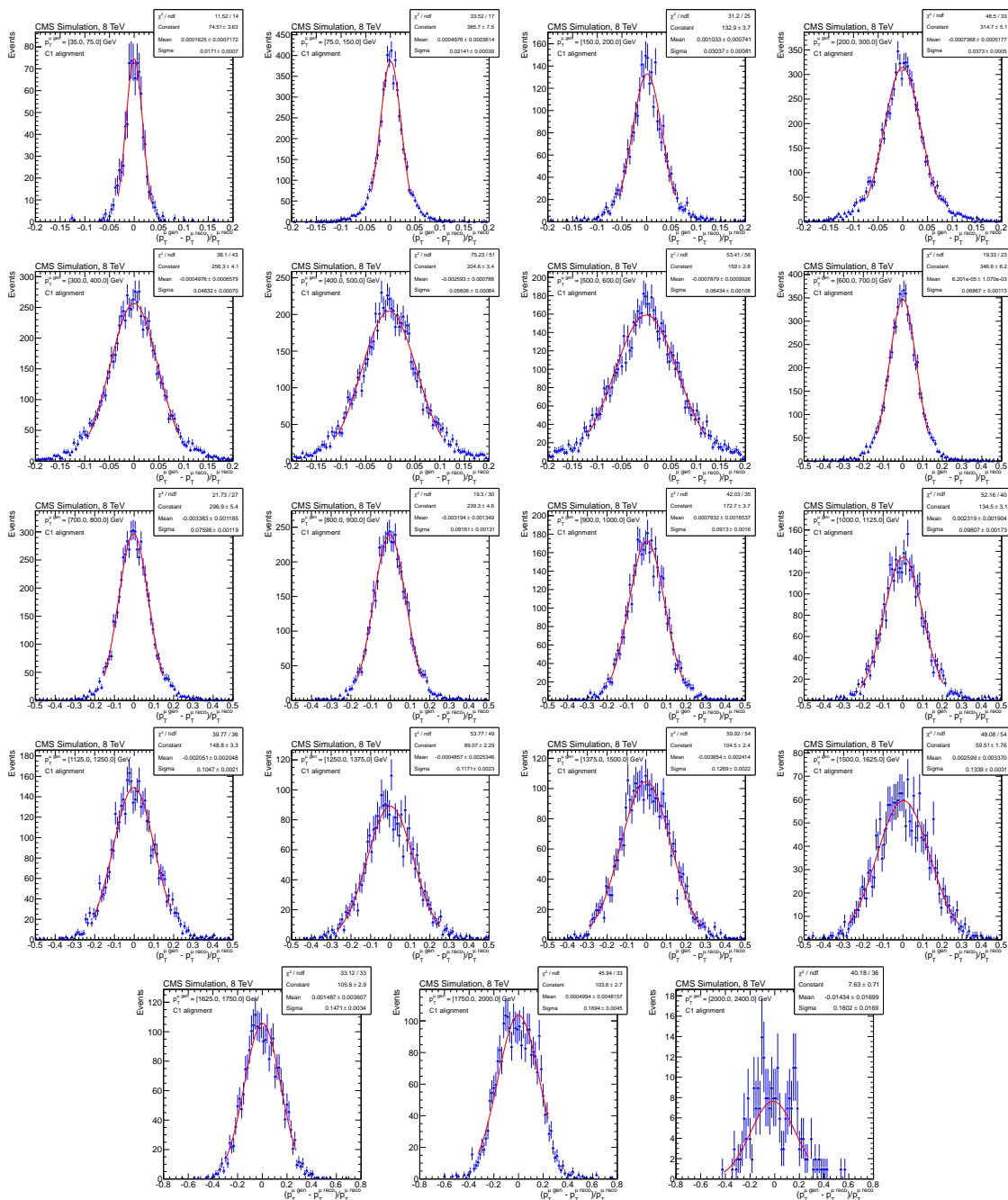


Figure B.1 – Fits of a Gaussian function to the relative muon p_T difference R , for different p_T ranges, with the C1 muon alignment scenario.

172 APPENDIX B. MUON P_T AND $e\mu$ INVARIANT MASS RESOLUTION FITS

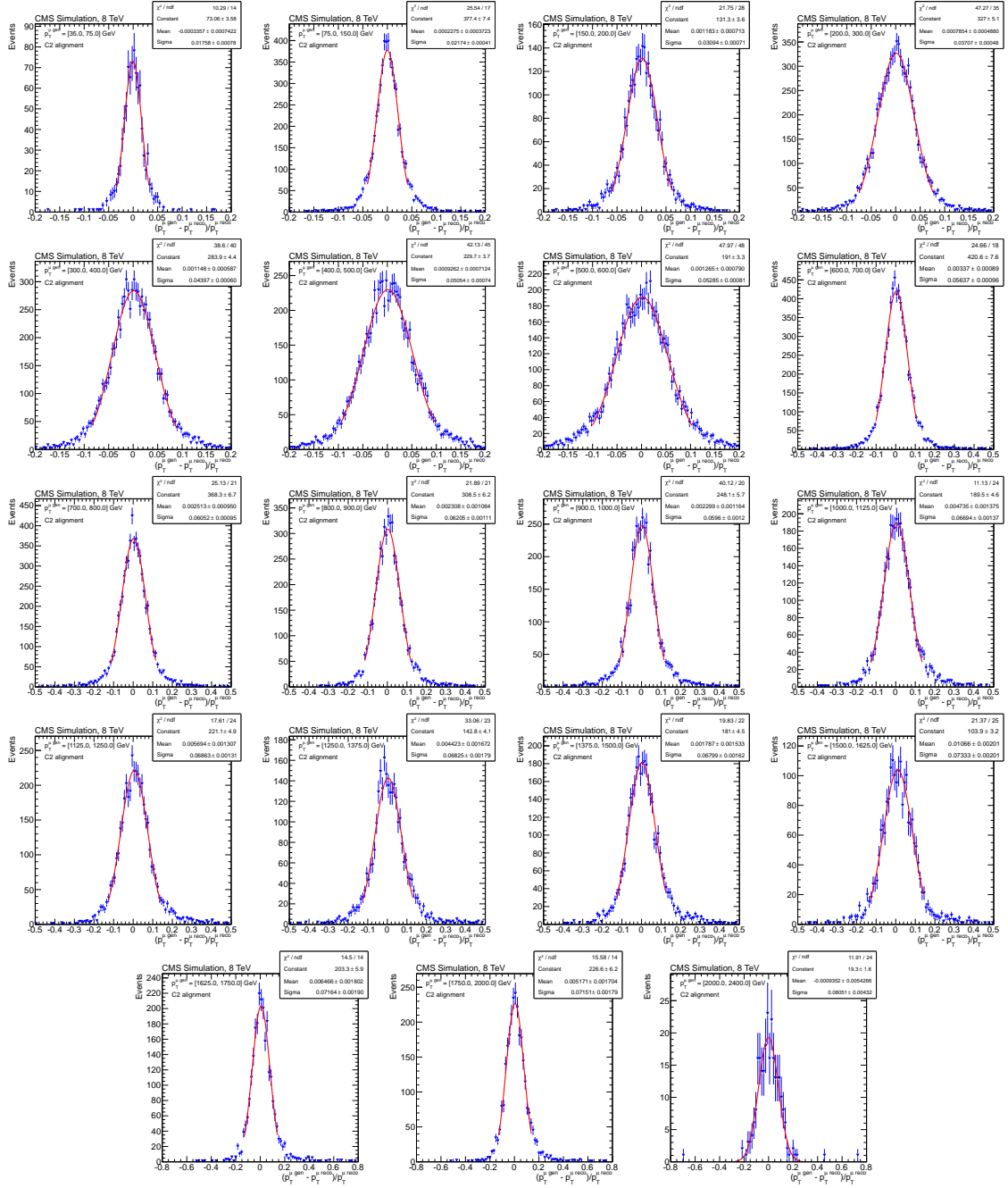


Figure B.2 – Fits of a Gaussian function to the relative muon p_T difference R , for different p_T ranges, with the C2 muon alignment scenario.

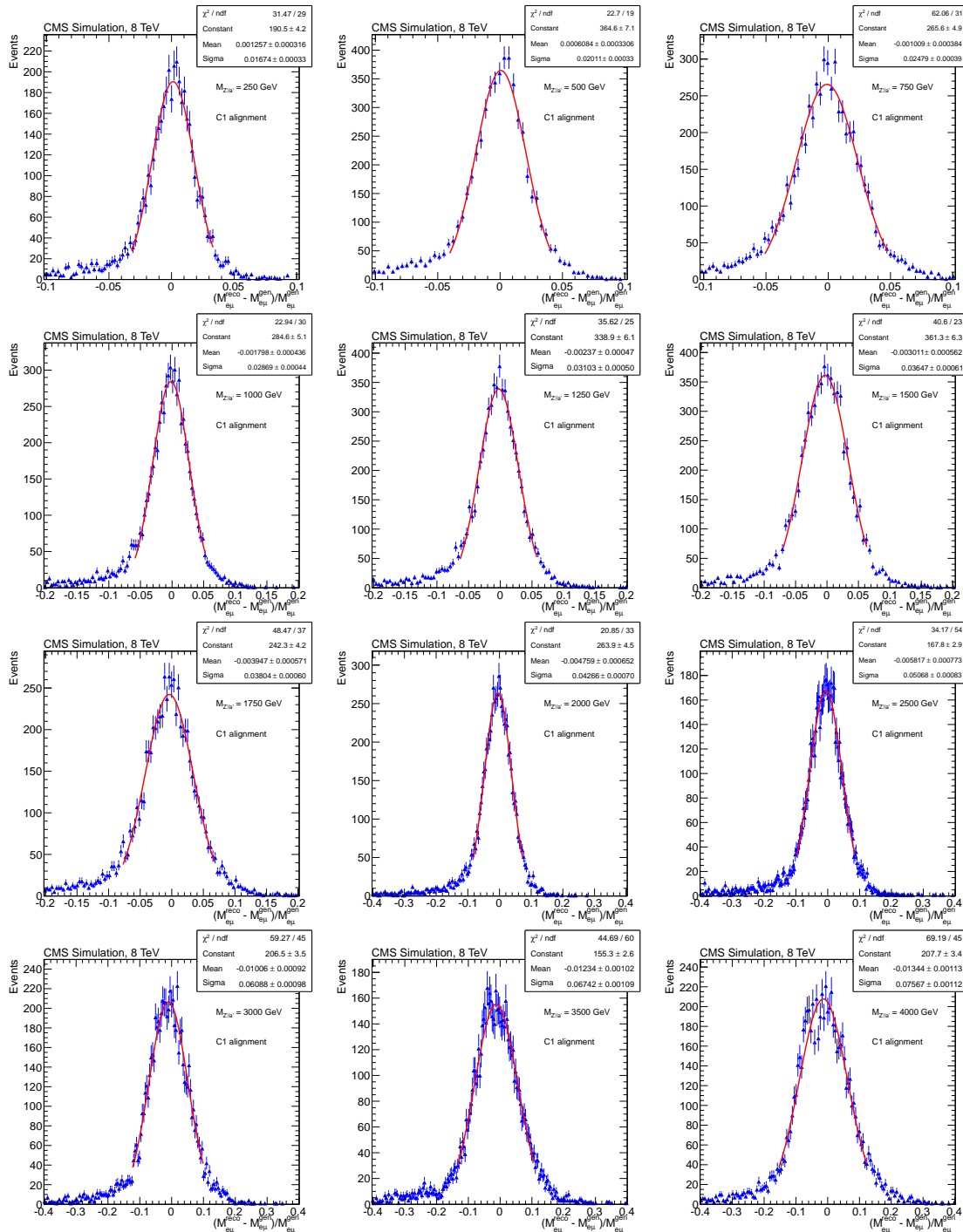


Figure B.3 – Fits of Gaussian functions to the relative invariant mass difference $(M_{e\mu}^{\text{reco}} - M_{e\mu}^{\text{gen}})/M_{e\mu}^{\text{gen}}$, with the C1 muon alignment scenario.

174 APPENDIX B. MUON P_T AND $e\mu$ INVARIANT MASS RESOLUTION FITS

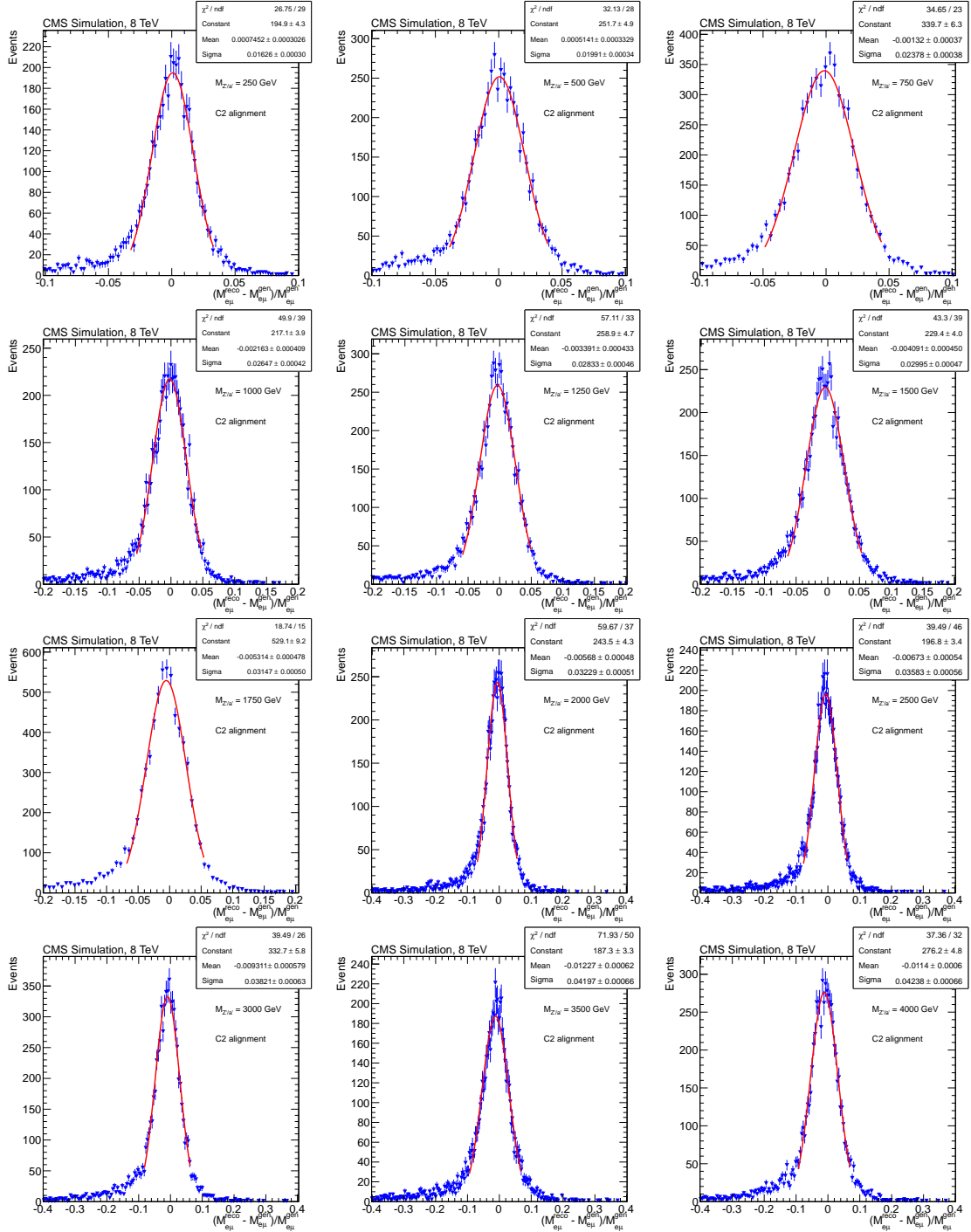


Figure B.4 – Fits of Gaussian functions to the relative invariant mass difference $(M_{e\mu}^{\text{reco}} - M_{e\mu}^{\text{gen}})/M_{e\mu}^{\text{gen}}$, with the C2 muon alignment scenario.

Appendix C

Electron and muon selection variables

This appendix shows comparisons for lepton selection variables, as well as other variables of interest, for the $e\mu$ analysis presented in Chapter 7.

C.1 High Energy Electron Pair selection variables

Figures C.1 to C.3 show the spectrum in data and the background expectation for several variables of the selected electron candidates.

C.2 High- p_T muon selection variables

Figures C.4 and C.5 show the spectrum in data and the background expectation for several variables of the selected muon candidates.

C.3 Additional variables

Figures C.6 and C.7 show the spectrum in data and the background expectation for additional variables for selected $e\mu$ events.

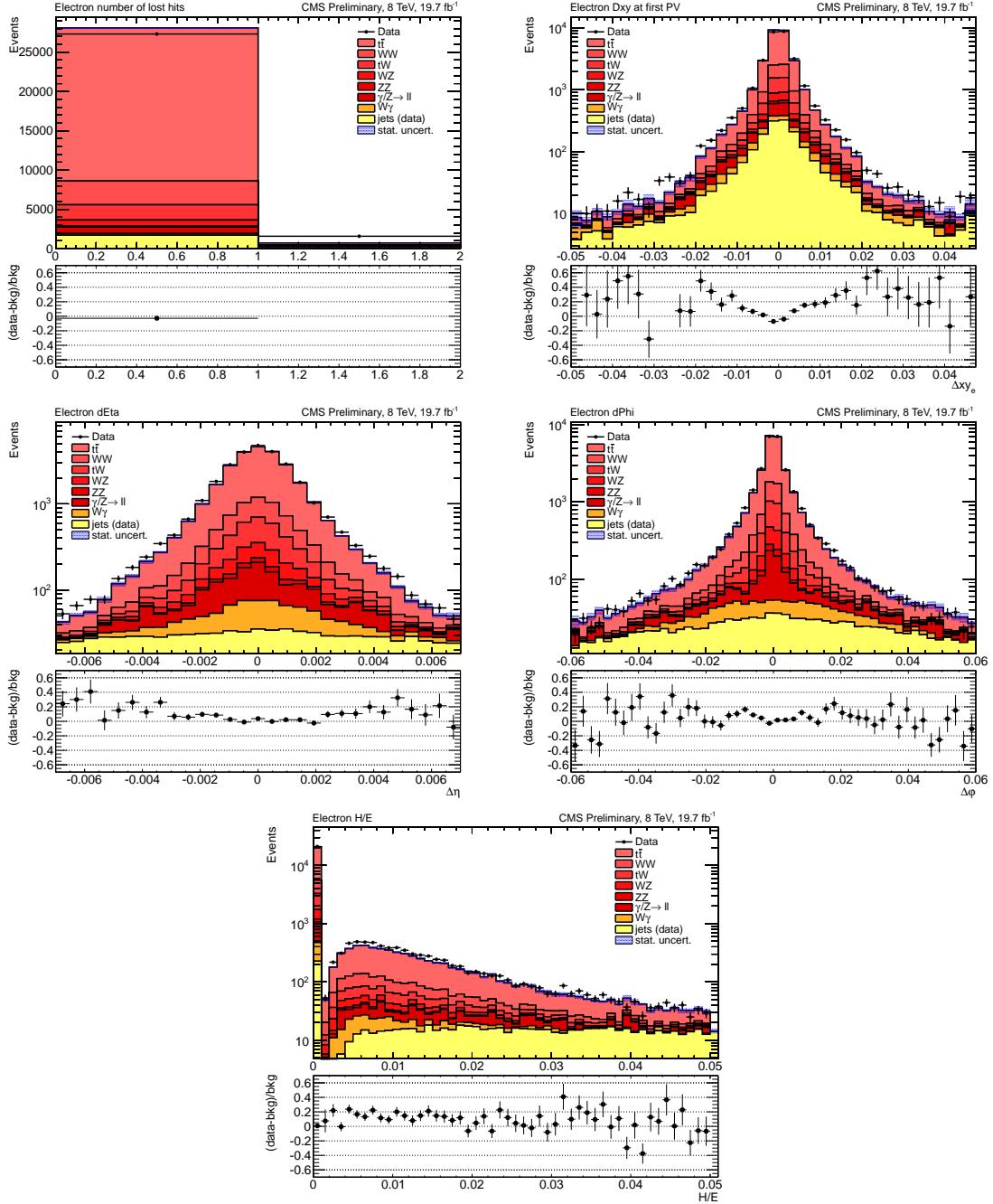


Figure C.1 – Data to expectation comparisons for HEEP selection variables. From top left to bottom right: Missing inner hits, $|d_{xy}|$, $\Delta\eta_{in}$, $\Delta\phi_{in}$, H/E . See Section 6.1.4 for definition of, and Table 6.8 for thresholds on the variables. The plots below the distributions show the data minus background over background.

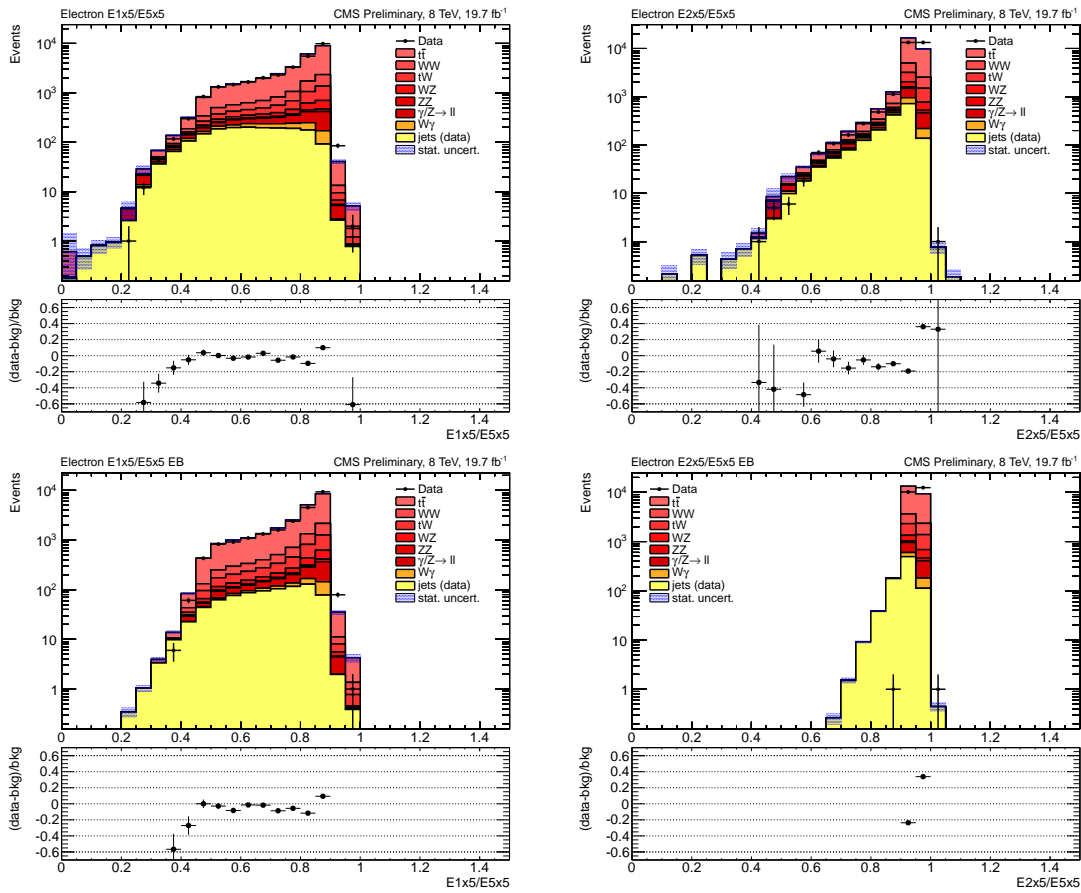


Figure C.2 – Data to expectation comparisons for HEEP selection variables. From top left to bottom right: $E^{1 \times 5}$, $E^{2 \times 5}$, $E^{1 \times 5}$ for events with the electron in the barrel, $E^{2 \times 5}$ for events with the electron in the barrel. See Section 6.1.4 for definition of, and Table 6.8 for thresholds on the variables. The plots below the distributions show the data minus background over background.

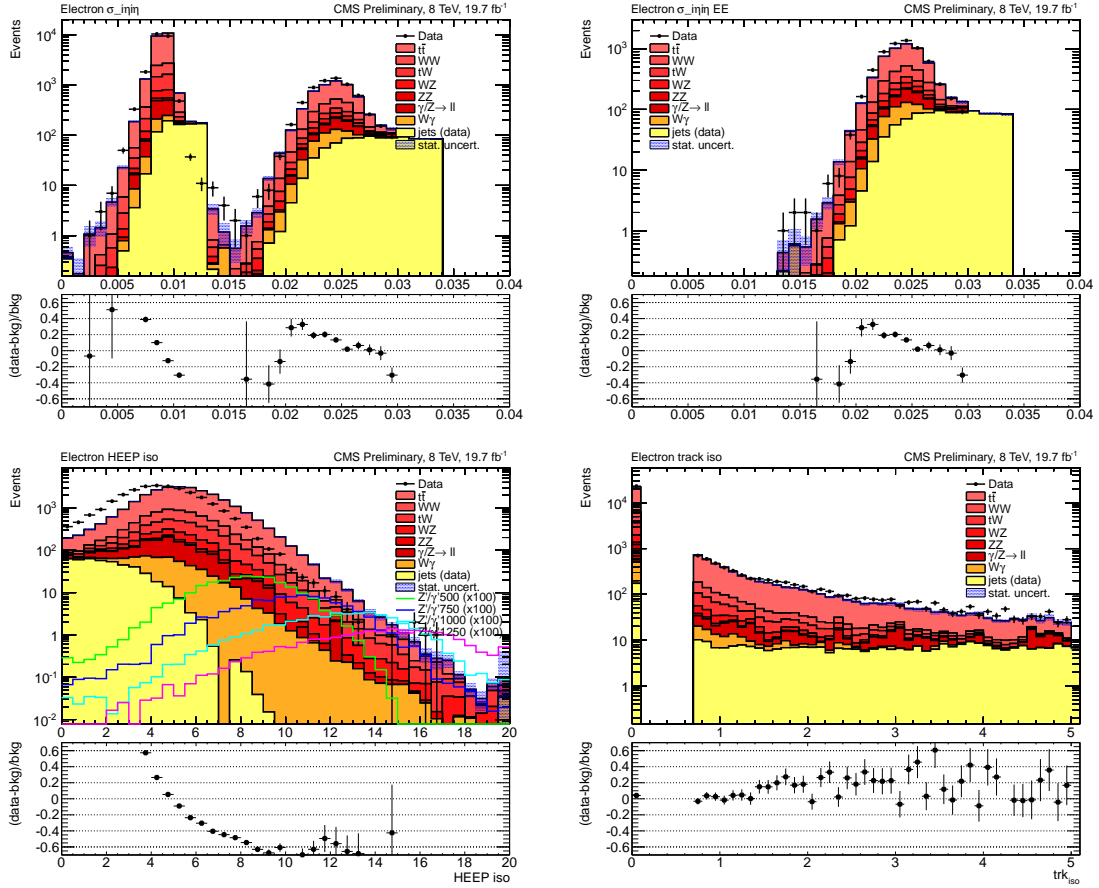


Figure C.3 – Data to expectation comparisons for HEEP selection variables. From top left to bottom right: σ_{inj} , σ_{inj} for events with the electron in the endcap, ECAL + HCAL Depth 1, Track isolation. See Section 6.1.4 for definition of, and Table 6.8 for thresholds on the variables. The plots below the distributions show the data minus background over background.

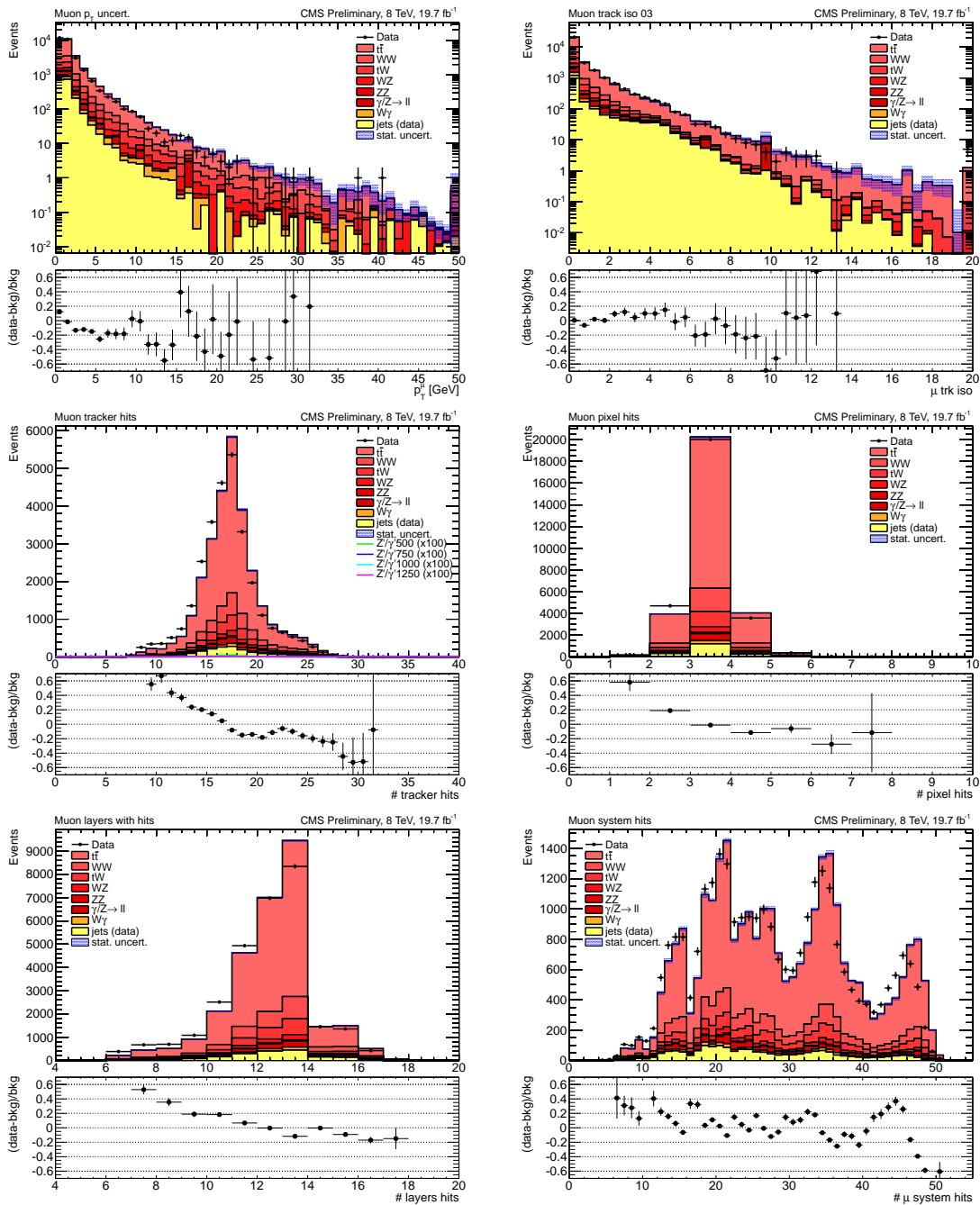


Figure C.4 – Data to expectation comparisons for the high- p_T muon selection variables. From top left to bottom right: Uncertainty on muon p_T measurement δp_T , tracker isolation, number of track hits, number of hits in the pixel detector, number of hits in the muon system, number of tracker layers with hits, number of matched muon stations. See Sections 6.5.1 and 7.3.3 for further definitions of, and threshold values on the variables. The plots below the distributions show the data minus background over background.

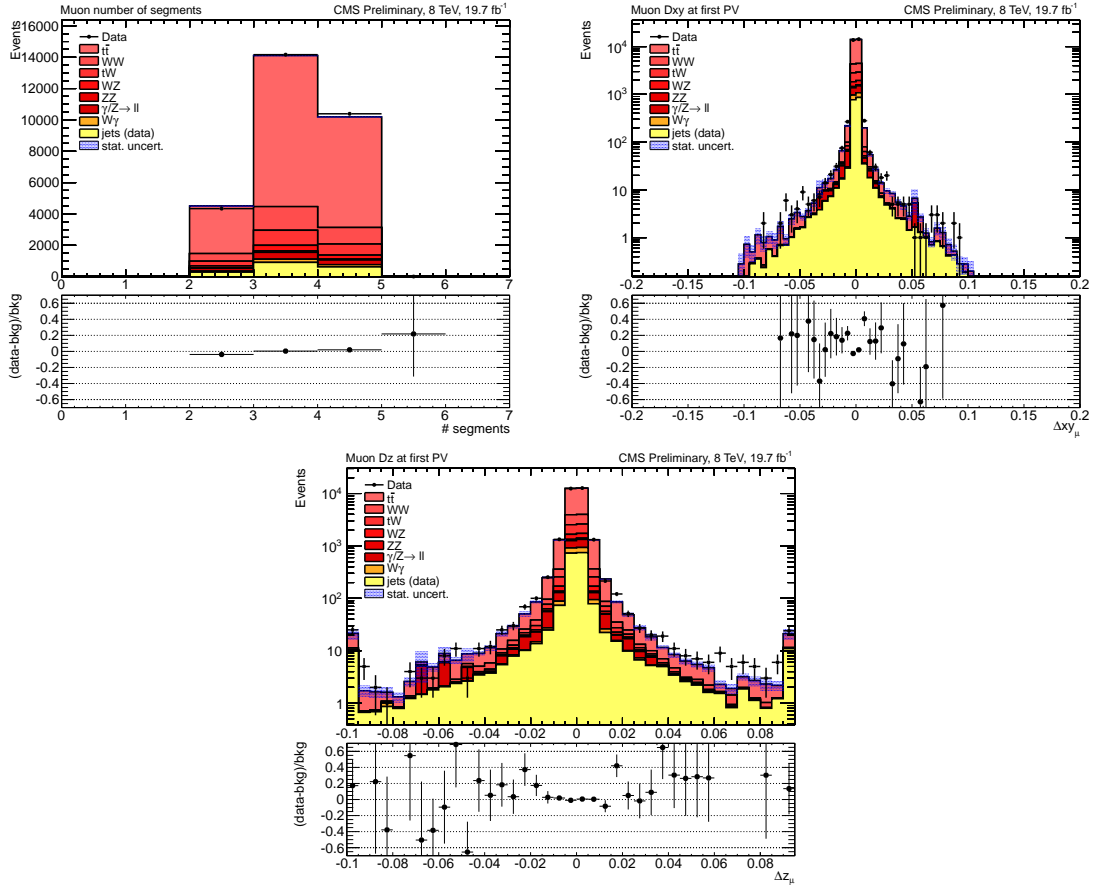


Figure C.5 – Data to expectation comparisons for the high- p_T muon selection variables. Top left: Number of muon station segments matched to tracker track. Top right: Transverse impact parameter with respect to primary vertex. Bottom: Longitudinal impact parameter with respect to primary vertex. See Sections 6.5.1 and 7.3.3 for further definitions of, and threshold values on the variables. The plots below the distributions show the data minus background over background.

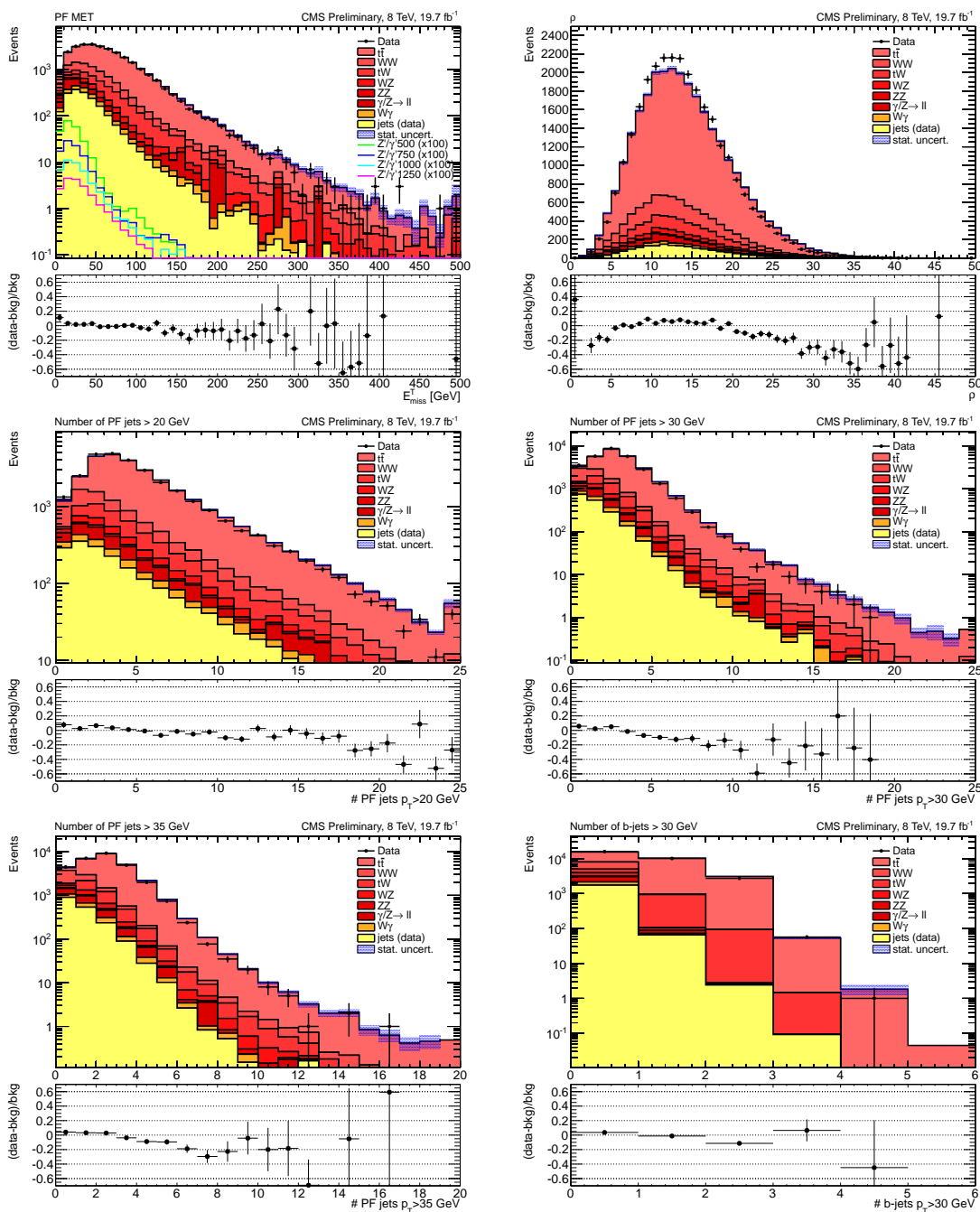


Figure C.6 – Data to expectation comparisons for additional variables of selected $e\mu$ events. From top left to bottom right: PF E_T^{miss} , ρ variable (described in Section 6.1.4), PF jet multiplicity for jets with $p_T > 20$ GeV, > 30 GeV, > 35 GeV and number of b-jets with $p_T > 30$ GeV. The plots below the distributions show the data minus background over background.

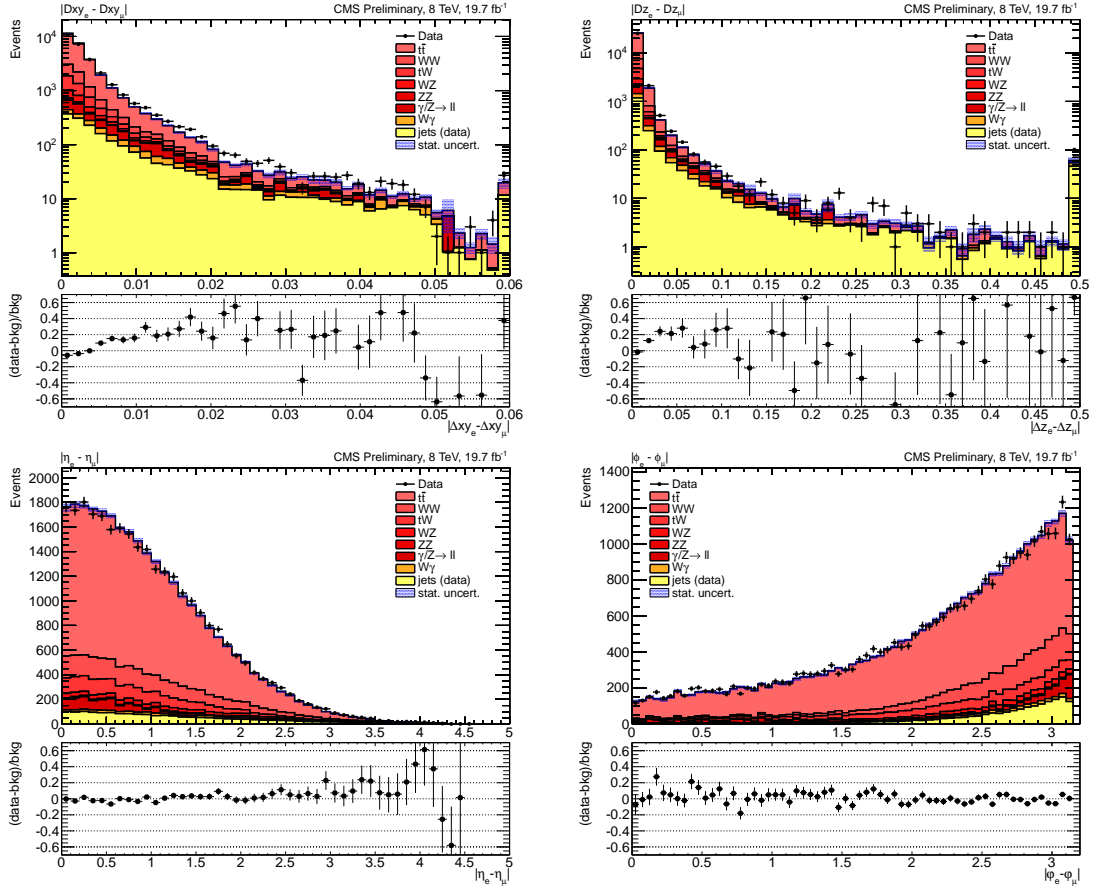


Figure C.7 – Data to expectation comparisons for additional variables of selected $e\mu$ events. Shown are the absolute difference between the electron and the muon track in the $x-y$ plane (top left) and in z direction (top right), and the absolute difference between the electron and the muon η (bottom left) and ϕ (bottom right). The plots below the distributions show the data minus background over background.

Bibliography

- [1] CMS Collaboration, “Search for physics beyond the standard model in dilepton mass spectra in proton-proton collisions at $\sqrt{s} = 8$ TeV”, [arXiv:1412.6302](#).
- [2] CMS Collaboration, “Search for Lepton Flavour Violating Decays of Heavy States to $e\mu$ Pairs in pp Collisions at $\sqrt{s} = 8$ TeV”, CMS-EXO-13-002, 2014. Publication in preparation.
- [3] Particle Data Group, “Review of Particle Physics (RPP)”, *Phys.Rev.* **D86** (2012) 010001, [doi:10.1103/PhysRevD.86.010001](#).
- [4] CMS Collaboration, “Precise determination of the mass of the Higgs boson and tests of compatibility of its couplings with the standard model predictions using proton collisions at 7 and 8 TeV”, [arXiv:1412.8662](#).
- [5] CMS Collaboration, “Constraints on the Higgs boson width from off-shell production and decay to Z-boson pairs”, *Phys.Lett.* **B736** (2014) 64, [doi:10.1016/j.physletb.2014.06.077](#), [arXiv:1405.3455](#).
- [6] CMS Collaboration, “Observation of a new boson at a mass of 125 GeV with the CMS experiment at the LHC”, *Phys.Lett.* **B716** (2012) 30–61, [doi:10.1016/j.physletb.2012.08.021](#), [arXiv:1207.7235](#).
- [7] ATLAS Collaboration, “Observation of a new particle in the search for the Standard Model Higgs boson with the ATLAS detector at the LHC”, *Phys.Lett.* **B716** (2012) 1–29, [doi:10.1016/j.physletb.2012.08.020](#), [arXiv:1207.7214](#).
- [8] F. Englert and R. Brout, “Broken Symmetry and the Mass of Gauge Vector Mesons”, *Phys. Rev. Lett.* **13** (Aug, 1964) 321–323, [doi:10.1103/PhysRevLett.13.321](#).
- [9] P. W. Higgs, “Broken symmetries, massless particles and gauge fields”, *Phys.Lett.* **12** (1964) 132–133, [doi:10.1016/0031-9163\(64\)91136-9](#).
- [10] E. Noether, “Invariante Variationsprobleme”, *Nachr. v. d. Ges. d. Wiss. zu Göttingen* **1918** (1918) 235–257.

- [11] A. Martin, W. Stirling, R. Thorne, and G. Watt, “Parton distributions for the LHC”, *Eur.Phys.J.* **C63** (2009) 189–285, doi:10.1140/epjc/s10052-009-1072-5, arXiv:0901.0002.
- [12] H.-L. Lai et al., “New parton distributions for collider physics”, *Phys.Rev.* **D82** (2010) 074024, doi:10.1103/PhysRevD.82.074024, arXiv:1007.2241.
- [13] “The Durham HepData Project - PDF plotter”.
<http://hepdata.cedar.ac.uk/pdf/pdf3.html>. Accessed: 2014-12-13.
- [14] H1 and ZEUS Collaboration, “Combined Measurement and QCD Analysis of the Inclusive $e^{\pm}p$ Scattering Cross Sections at HERA”, *JHEP* **1001** (2010) 109, doi:10.1007/JHEP01(2010)109, arXiv:0911.0884.
- [15] Y. L. Dokshitzer, “Calculation of the Structure Functions for Deep Inelastic Scattering and e^+e^- Annihilation by Perturbation Theory in Quantum Chromodynamics.”, *Sov.Phys.JETP* **46** (1977) 641–653.
- [16] V. Gribov and L. Lipatov, “Deep inelastic $e p$ scattering in perturbation theory”, *Sov.J.Nucl.Phys.* **15** (1972) 438–450.
- [17] G. Altarelli and G. Parisi, “Asymptotic Freedom in Parton Language”, *Nucl.Phys.* **B126** (1977) 298, doi:10.1016/0550-3213(77)90384-4.
- [18] J. Pumplin et al., “New generation of parton distributions with uncertainties from global QCD analysis”, *JHEP* **0207** (2002) 012, doi:10.1088/1126-6708/2002/07/012, arXiv:hep-ph/0201195.
- [19] R. D. Ball et al., “Parton distributions with LHC data”, *Nucl.Phys.* **B867** (2013) 244–289, doi:10.1016/j.nuclphysb.2012.10.003, arXiv:1207.1303.
- [20] S. Drell and T.-M. Yan, “Massive Lepton Pair Production in Hadron-Hadron Collisions at High-Energies”, *Phys.Rev.Lett.* **25** (1970) 316–320, doi:10.1103/PhysRevLett.25.316.
- [21] M. E. Peskin, “Beyond the standard model”, arXiv:hep-ph/9705479.
- [22] R. Barbier et al., “R-parity violating supersymmetry”, *Phys.Rept.* **420** (2005) 1–202, doi:10.1016/j.physrep.2005.08.006, arXiv:hep-ph/0406039.
- [23] G. Altarelli, B. Mele, and M. Ruiz-Altaba, “Searching for New Heavy Vector Bosons in $p\bar{p}$ Colliders”, *Z.Phys.* **C45** (1989) 109, doi:10.1007/BF01552335, 10.1007/BF01556677.
- [24] A. Leike, “The Phenomenology of extra neutral gauge bosons”, *Phys.Rept.* **317** (1999) 143–250, doi:10.1016/S0370-1573(98)00133-1, arXiv:hep-ph/9805494.

- [25] J. L. Hewett and T. G. Rizzo, “Low-Energy Phenomenology of Superstring Inspired E(6) Models”, *Phys.Rept.* **183** (1989) 193, doi:10.1016/0370-1573(89)90071-9.
- [26] L. Randall and R. Sundrum, “An Alternative to compactification”, *Phys.Rev.Lett.* **83** (1999) 4690–4693, doi:10.1103/PhysRevLett.83.4690, arXiv:hep-th/9906064.
- [27] L. Randall and R. Sundrum, “A Large mass hierarchy from a small extra dimension”, *Phys.Rev.Lett.* **83** (1999) 3370–3373, doi:10.1103/PhysRevLett.83.3370, arXiv:hep-ph/9905221.
- [28] H. Georgi and S. Glashow, “Unity of All Elementary Particle Forces”, *Phys.Rev.Lett.* **32** (1974) 438–441, doi:10.1103/PhysRevLett.32.438.
- [29] N. Arkani-Hamed, S. Dimopoulos, and G. Dvali, “The Hierarchy problem and new dimensions at a millimeter”, *Phys.Lett.* **B429** (1998) 263–272, doi:10.1016/S0370-2693(98)00466-3, arXiv:hep-ph/9803315.
- [30] ALEPH, DELPHI, L3, OPAL, LEP Electroweak, “Electroweak Measurements in Electron-Positron Collisions at W-Boson-Pair Energies at LEP”, *Phys.Rept.* **532** (2013) 119–244, doi:10.1016/j.physrep.2013.07.004, arXiv:1302.3415.
- [31] CDF Collaboration, “Search for High-Mass e^+e^- Resonances in $p\bar{p}$ Collisions at $\sqrt{s} = 1.96$ TeV”, *Phys.Rev.Lett.* **102** (2009) 031801, doi:10.1103/PhysRevLett.102.031801, arXiv:0810.2059.
- [32] D0 Collaboration, “Search for a heavy neutral gauge boson in the dielectron channel with 5.4 fb^{-1} of $p\bar{p}$ collisions at $\sqrt{s} = 1.96$ TeV”, *Phys.Lett.* **B695** (2011) 88–94, doi:10.1016/j.physletb.2010.10.059, arXiv:1008.2023.
- [33] CDF Collaboration, “Search for New Dielectron Resonances and Randall-Sundrum Gravitons at the Collider Detector at Fermilab”, *Phys.Rev.Lett.* **107** (2011) 051801, doi:10.1103/PhysRevLett.107.051801, arXiv:1103.4650.
- [34] D0 Collaboration, “Search for Randall-Sundrum gravitons in the dielectron and diphoton final states with 5.4 fb^{-1} of data from $p\bar{p}$ collisions at $\sqrt{s}=1.96$ TeV”, *Phys.Rev.Lett.* **104** (2010) 241802, doi:10.1103/PhysRevLett.104.241802, arXiv:1004.1826.
- [35] ATLAS Collaboration, “Search for high-mass resonances decaying to dilepton final states in pp collisions at $\sqrt{s} = 7$ TeV with the ATLAS detector”, *JHEP* **1211** (2012) 138, doi:10.1007/JHEP11(2012)138, arXiv:1209.2535.

- [36] CMS Collaboration, “Search for narrow resonances in dilepton mass spectra in pp collisions at $\sqrt{s} = 7$ TeV”, *Phys.Lett.* **B714** (2012) 158–179, doi:10.1016/j.physletb.2012.06.051, arXiv:1206.1849.
- [37] CMS Collaboration, “Search for heavy narrow dilepton resonances in pp collisions at $\sqrt{s} = 7$ TeV and $\sqrt{s} = 8$ TeV”, *Phys.Lett.* **B720** (2013) 63–82, doi:10.1016/j.physletb.2013.02.003, arXiv:1212.6175.
- [38] ATLAS Collaboration, “Search for high-mass dilepton resonances in pp collisions at $\sqrt{s} = 8$ TeV with the ATLAS detector”, *Phys.Rev.* **D90** (2014), no. 5, 052005, doi:10.1103/PhysRevD.90.052005, arXiv:1405.4123.
- [39] ATLAS Collaboration, “Search for contact interactions and large extra dimensions in the dilepton channel using proton-proton collisions at $\sqrt{s} = 8$ TeV with the ATLAS detector”, *Eur.Phys.J.* **C74** (2014), no. 12, 3134, doi:10.1140/epjc/s10052-014-3134-6, arXiv:1407.2410.
- [40] CMS Collaboration, “Search for Large Extra Spatial Dimensions in Dielectron Production with the CMS Detector”, CMS-PAS-EXO-12-031, CERN, Geneva, 2013.
- [41] CMS Collaboration, “Search for Extra Dimensions in Dimuon Events in pp Collisions at $\sqrt{s} = 8$ TeV”, CMS-PAS-EXO-12-027, CERN, Geneva, 2013.
- [42] J. M. Frère, M. V. Libanov, E. Y. Nugaev, and S. V. Troitsky, “Fermions in the vortex background on a sphere”, *JHEP* **0306** (2003) 009, doi:10.1088/1126-6708/2003/06/009, arXiv:hep-ph/0304117.
- [43] J. Frère, M. Libanov, E. Nugaev, and S. V. Troitsky, “Flavor violation with a single generation”, *JHEP* **0403** (2004) 001, doi:10.1088/1126-6708/2004/03/001, arXiv:hep-ph/0309014.
- [44] J.-M. Frère, M. Libanov, S. Mollet, and S. Troitsky, “Exploring variations in the gauge sector of a six-dimensional flavour model”, arXiv:1411.6539.
- [45] J. M. Frère, M. V. Libanov, E. Y. Nugaev, and S. V. Troitsky, “Searching for family number conserving neutral gauge bosons from extra dimensions”, *JETP Lett.* **79** (2004) 598–601, doi:10.1134/1.1790014, arXiv:hep-ph/0404139.
- [46] CDF Collaboration, “Search for high-mass resonances decaying to $e \mu$ in $p\bar{p}$ collisions at $\sqrt{s} = 1.96$ -TeV.”, *Phys.Rev.Lett.* **96** (2006) 211802, doi:10.1103/PhysRevLett.96.211802, arXiv:hep-ex/0603006.
- [47] ATLAS Collaboration, “Search for a heavy neutral particle decaying into an electron and a muon using 1 fb^{-1} of ATLAS data”, *Eur.Phys.J.* **C71** (2011) 1809, doi:10.1140/epjc/s10052-011-1809-9, arXiv:1109.3089.

- [48] CDF Collaboration, “Search for R-parity Violating Decays of τ sneutrinos to $e\mu$, $\mu\tau$, and $e\tau$ Pairs in $p\bar{p}$ Collisions at $\sqrt{s} = 1.96$ TeV”, *Phys.Rev.Lett.* **105** (2010) 191801, doi:10.1103/PhysRevLett.105.191801, arXiv:1004.3042.
- [49] D0 Collaboration, “Search for sneutrino production in $e\mu$ final states in 5.3 fb^{-1} of $p\bar{p}$ collisions at $\sqrt{s} = 1.96$ TeV”, *Phys.Rev.Lett.* **105** (2010) 191802, doi:10.1103/PhysRevLett.105.191802, arXiv:1007.4835.
- [50] ATLAS Collaboration, “Search for a heavy narrow resonance decaying to $e\mu$, $e\tau$, or $\mu\tau$ with the ATLAS detector in $\sqrt{s} = 7$ TeV pp collisions at the LHC”, *Phys.Lett.* **B723** (2013) 15–32, doi:10.1016/j.physletb.2013.04.035, arXiv:1212.1272.
- [51] V. Dero, “Recherche de nouvelle physique au LHC par l’étude du spectre de masse des paires de leptons à 7 TeV dans CMS”. PhD thesis, Université Libre de Bruxelles, 2011.
- [52] L. Evans and P. Bryant, “LHC Machine”, *JINST* **3** (2008) S08001, doi:10.1088/1748-0221/3/08/S08001.
- [53] J.-L. Caron, “Accelerator complex of CERN: an overview of all accelerators of CERN. Vue d’ensemble de tous les accélérateurs du CERN”, CERN-DI-0107024, 2001.
- [54] ATLAS Collaboration, “The ATLAS Experiment at the CERN Large Hadron Collider”, *JINST* **3** (2008) S08003, doi:10.1088/1748-0221/3/08/S08003.
- [55] CMS Collaboration, “The CMS experiment at the CERN LHC”, *JINST* **3** (2008) S08004, doi:10.1088/1748-0221/3/08/S08004.
- [56] ALICE Collaboration, “The ALICE experiment at the CERN LHC”, *JINST* **3** (2008) S08002, doi:10.1088/1748-0221/3/08/S08002.
- [57] LHCb Collaboration, “The LHCb Detector at the LHC”, *JINST* **3** (2008) S08005, doi:10.1088/1748-0221/3/08/S08005.
- [58] M. Lamont, “The First Years of LHC Operation for Luminosity Production”, in *Proceedings, 4th International Particle Accelerator Conference (IPAC 2013)*, Z. Dai, C. Petit-Jean-Genaz, V. R. Schaa, and C. Zhang, eds., p. 6. June, 2013.
- [59] CMS Collaboration, “CMS Luminosity - Public Results”. <https://twiki.cern.ch/twiki/bin/view/CMSPublic/LumiPublicResults>. Accessed: 2014-11-04.
- [60] W. J. Stirling, “Private communication”. http://www.hep.ph.ic.ac.uk/~wstirlin/plots/crosssections2012_v5.pdf. Accessed: 2014-12-17.

- [61] T. Sakuma and T. McCauley, “Detector and Event Visualization with SketchUp at the CMS Experiment”, *Journal of Physics: Conference Series* **513** (2014), no. 2, 022032, doi:10.1088/1742-6596/513/2/022032.
- [62] CMS Collaboration, “The performance of the CMS muon detector in proton-proton collisions at $\sqrt{s} = 7$ TeV at the LHC”, *JINST* **8** (2013) P11002, doi:10.1088/1748-0221/8/11/P11002, arXiv:1306.6905.
- [63] CMS Collaboration, “Description and performance of track and primary-vertex reconstruction with the CMS tracker”, *JINST* **9** (2014), no. 10, P10009, doi:10.1088/1748-0221/9/10/P10009, arXiv:1405.6569.
- [64] CMS Collaboration, G. L. Bayatian et al., “CMS Physics: Technical Design Report Volume 1: Detector Performance and Software”. Technical Design Report CMS. CERN, Geneva, 2006.
- [65] P. Adzic et al., “Energy resolution of the barrel of the CMS electromagnetic calorimeter”, *JINST* **2** (2007) P04004, doi:10.1088/1748-0221/2/04/P04004.
- [66] CMS Collaboration, “Performance of CMS muon reconstruction in pp collision events at $\sqrt{s} = 7$ TeV”, *JINST* **7** (2012) P10002, doi:10.1088/1748-0221/7/10/P10002, arXiv:1206.4071.
- [67] CMS Collaboration, “Performance of electron reconstruction and selection with the CMS detector in proton-proton collisions at $\sqrt{s}=8$ TeV”, arXiv:1502.02701.
- [68] S. Baffioni et al., “Electron reconstruction in CMS”, *Eur.Phys.J.* **C49** (2007) 1099–1116, doi:10.1140/epjc/s10052-006-0175-5.
- [69] CMS Collaboration, “Particle-Flow Event Reconstruction in CMS and Performance for Jets, Taus, and MET”, CMS-PAS-PFT-09-001, CERN, Geneva, 2009.
- [70] H. Bethe and W. Heitler, “On the Stopping of fast particles and on the creation of positive electrons”, *Proc.Roy.Soc.Lond.* **A146** (1934) 83–112, doi:10.1098/rspa.1934.0140.
- [71] M. Cacciari, G. P. Salam, and G. Soyez, “The anti- k_t jet clustering algorithm”, *JHEP* **0804** (2008) 063, doi:10.1088/1126-6708/2008/04/063, arXiv:0802.1189.
- [72] CMS Collaboration, “Determination of Jet Energy Calibration and Transverse Momentum Resolution in CMS”, *JINST* **6** (2011) P11002, doi:10.1088/1748-0221/6/11/P11002, arXiv:1107.4277.

- [73] CMS Collaboration, “Missing transverse energy performance of the CMS detector”, *JINST* **6** (2011) P09001, doi:10.1088/1748-0221/6/09/P09001, arXiv:1106.5048.
- [74] CMS Collaboration, “Search for Resonances in the Dilepton Mass Distribution in pp Collisions at $\sqrt{s} = 7$ TeV”, *JHEP* **1105** (2011) 093, doi:10.1007/JHEP05(2011)093, arXiv:1103.0981.
- [75] CMS Collaboration, “CMS offline software”.
<https://github.com/cms-sw/cmssw>. Accessed: 2014-11-04.
- [76] CMS Collaboration, “CMS Luminosity Based on Pixel Cluster Counting - Summer 2013 Update”, CMS-PAS-LUM-13-001, CERN, Geneva, 2013.
- [77] J. Alwall et al., “MadGraph 5 : Going Beyond”, *JHEP* **1106** (2011) 128, doi:10.1007/JHEP06(2011)128, arXiv:1106.0522.
- [78] S. Frixione, P. Nason, and C. Oleari, “Matching NLO QCD computations with Parton Shower simulations: the POWHEG method”, *JHEP* **0711** (2007) 070, doi:10.1088/1126-6708/2007/11/070, arXiv:0709.2092.
- [79] S. Alioli, P. Nason, C. Oleari, and E. Re, “A general framework for implementing NLO calculations in shower Monte Carlo programs: the POWHEG BOX”, *JHEP* **1006** (2010) 043, doi:10.1007/JHEP06(2010)043, arXiv:1002.2581.
- [80] T. Sjostrand, S. Mrenna, and P. Z. Skands, “PYTHIA 6.4 Physics and Manual”, *JHEP* **0605** (2006) 026, doi:10.1088/1126-6708/2006/05/026, arXiv:hep-ph/0603175.
- [81] N. Davidson et al., “Universal Interface of TAUOLA Technical and Physics Documentation”, *Comput.Phys.Commun.* **183** (2012) 821–843, doi:10.1016/j.cpc.2011.12.009, arXiv:1002.0543.
- [82] GEANT4 Collaboration, “GEANT4: A Simulation toolkit”, *Nucl.Instrum.Meth.* **A506** (2003) 250–303, doi:10.1016/S0168-9002(03)01368-8.
- [83] R. Gavin, Y. Li, F. Petriello, and S. Quackenbush, “FEWZ 2.0: A code for hadronic Z production at next-to-next-to-leading order”, *Comput.Phys.Commun.* **182** (2011) 2388–2403, doi:10.1016/j.cpc.2011.06.008, arXiv:1011.3540.
- [84] N. Kidonakis, “Differential and total cross sections for top pair and single top production”, doi:10.3204/DESY-PROC-2012-02/251, arXiv:1205.3453.
- [85] J. M. Campbell, R. K. Ellis, and C. Williams, “MCFM - Monte Carlo for FeMtobarn processes”. <http://mcfm.fnal.gov/>. Accessed: 2014-12-23.

- [86] T. Binoth, J. Guillet, E. Pilon, and M. Werlen, “A Next-to-leading order study of photon pion and pion pair hadro production in the light of the Higgs boson search at the LHC”, *Eur.Phys.J.direct* **C4** (2002) 7, doi:10.1007/s1010502c0007, arXiv:hep-ph/0203064.
- [87] L. Thomas, “Search for new heavy narrow resonances decaying into a dielectron pair with the CMS detector”. PhD thesis, Université Libre de Bruxelles, 2014.
- [88] CMS Collaboration, “Measuring Electron Efficiencies at CMS with Early Data”, CMS-PAS-EGM-07-001, CERN, Geneva, 2008.
- [89] CMS Collaboration, “Measurements of Inclusive W and Z Cross Sections in pp Collisions at $\sqrt{s} = 7$ TeV”, *JHEP* **1101** (2011) 080, doi:10.1007/JHEP01(2011)080, arXiv:1012.2466.
- [90] B. Clerbaux et al., “Search for High Mass Resonances Decaying to Electron Pairs at 8 TeV with the Full 2012 dataset”, CMS-AN-12-415, 2012. CMS internal note.
- [91] B. Clerbaux et al., “Update of the $Z' \rightarrow ee$ analysis with Jan 22 re-recoed data”, CMS-AN-13-359, 2013. CMS internal note.
- [92] M. Cacciari and G. P. Salam, “Pileup subtraction using jet areas”, *Phys.Lett.* **B659** (2008) 119–126, doi:10.1016/j.physletb.2007.09.077, arXiv:0707.1378.
- [93] M. Cacciari, G. P. Salam, and G. Soyez, “FastJet User Manual”, *Eur.Phys.J.* **C72** (2012) 1896, doi:10.1140/epjc/s10052-012-1896-2, arXiv:1111.6097.
- [94] ALEPH Collaboration, DELPHI Collaboration, L3 Collaboration, OPAL Collaboration, SLD Collaboration, LEP Electroweak Working Group, SLD Electroweak Group, SLD Heavy Flavour Group, “Precision electroweak measurements on the Z resonance”, *Phys.Rept.* **427** (2006) 257–454, doi:10.1016/j.physrep.2005.12.006, arXiv:hep-ex/0509008.
- [95] W. Verkerke and D. P. Kirkby, “The RooFit toolkit for data modeling”, *eConf* **C0303241** (2003) MOLT007, arXiv:physics/0306116.
- [96] I. Antcheva et al., “ROOT: A C++ framework for petabyte data storage, statistical analysis and visualization”, *Comput.Phys.Commun.* **182** (2011) 1384–1385, doi:10.1016/j.cpc.2011.02.008.
- [97] G. Alverson et al., “Search for High-Mass Resonances Decaying to Muon Pairs in pp Collisions at $\sqrt{s} = 8$ TeV”, CMS-AN-12-422, 2012. CMS internal note.

- [98] CMS Collaboration, “Standard Model Cross Sections for CMS at 7 TeV”.
<https://twiki.cern.ch/twiki/bin/viewauth/CMS/StandardModelCrossSections?rev=27>. CMS internal twiki page. Accessed: 2015-02-08.
- [99] CMS Collaboration, “Standard Model Cross Sections for CMS at 8 TeV”.
<https://twiki.cern.ch/twiki/bin/viewauth/CMS/StandardModelCrossSectionsat8TeV?rev=26>. CMS internal twiki page. Accessed: 2015-02-08.
- [100] N. Metropolis et al., “Equation of state calculations by fast computing machines”, *J.Chem.Phys.* **21** (1953) 1087–1092, doi:10.1063/1.1699114.
- [101] W. Hastings, “Monte Carlo Sampling Methods Using Markov Chains and Their Applications”, *Biometrika* **57** (1970) 97–109, doi:10.1093/biomet/57.1.97.
- [102] M. Botje et al., “The PDF4LHC Working Group Interim Recommendations”, arXiv:1101.0538.
- [103] C. Carloni Calame, G. Montagna, O. Nicrosini, and A. Vicini, “Precision electroweak calculation of the production of a high transverse-momentum lepton pair at hadron colliders”, *JHEP* **0710** (2007) 109, doi:10.1088/1126-6708/2007/10/109, arXiv:0710.1722.
- [104] E. Accomando et al., “Z’ at the LHC: Interference and Finite Width Effects in Drell-Yan”, *JHEP* **1310** (2013) 153, doi:10.1007/JHEP10(2013)153, arXiv:1304.6700.
- [105] R. Hamberg, W. van Neerven, and T. Matsuura, “A Complete calculation of the order $\alpha - s^2$ correction to the Drell-Yan K factor”, *Nucl.Phys.* **B359** (1991) 343–405, doi:10.1016/0550-3213(91)90064-5.
- [106] N. Kidonakis, “Differential and total cross sections for top pair and single top production”, doi:10.3204/DESY-PROC-2012-02/251, arXiv:1205.3453.
- [107] J. M. Campbell, R. K. Ellis, and C. Williams, “Vector boson pair production at the LHC”, *JHEP* **1107** (2011) 018, doi:10.1007/JHEP07(2011)018, arXiv:1105.0020.
- [108] N. D. Christensen and C. Duhr, “FeynRules - Feynman rules made easy”, *Comput.Phys.Commun.* **180** (2009) 1614–1641, doi:10.1016/j.cpc.2009.02.018, arXiv:0806.4194.
- [109] CMS Collaboration, “Measurement of differential top-quark pair production cross sections in the lepton+jets channel in pp collisions at 8 TeV”, CMS-PAS-TOP-12-027, CERN, Geneva, 2013.

- [110] CMS Collaboration, “Standard Model Cross Sections for CMS at 8 TeV”.
<https://twiki.cern.ch/twiki/bin/viewauth/CMS/StandardModelCrossSectionsat8TeV?rev=31>. CMS internal twiki page.
Accessed: 2015-02-08.
- [111] A. Bierweiler, T. Kasprzik, J. H. Kühn, and S. Uccirati, “Electroweak corrections to W-boson pair production at the LHC”, *JHEP* **1211** (2012) 093, doi:10.1007/JHEP11(2012)093, arXiv:1208.3147.
- [112] J. Gao et al., “CT10 next-to-next-to-leading order global analysis of QCD”, *Phys.Rev.* **D89** (2014), no. 3, 033009, doi:10.1103/PhysRevD.89.033009, arXiv:1302.6246.
- [113] CMS Collaboration, “ECAL Detector Performance, 2011 Data”, CMS-DP-2012-007, CERN, Geneva, 2012.
- [114] N. Kidonakis, “NNLO soft-gluon corrections for the top-quark p_T and rapidity distributions”, arXiv:1411.2633.
- [115] B. Clerbaux et al., “Search for Lepton Flavour Violating Decays of Heavy States to $e\mu$ Pairs in pp Collisions at $\sqrt{s} = 8$ TeV”, CMS-AN-13-422, 2014. CMS internal note.
- [116] H. K. Dreiner, C. Luhn, and M. Thormeier, “What is the discrete gauge symmetry of the MSSM?”, *Phys.Rev.* **D73** (2006) 075007, doi:10.1103/PhysRevD.73.075007, arXiv:hep-ph/0512163.
- [117] X. Calmet, “A Review of Quantum Gravity at the Large Hadron Collider”, *Mod.Phys.Lett.* **A25** (2010) 1553–1579, doi:10.1142/S0217732310033591, arXiv:1005.1805.
- [118] CMS Collaboration, “Projected Performance of an Upgraded CMS Detector at the LHC and HL-LHC: Contribution to the Snowmass Process”, arXiv:1307.7135.